All-optical switching of spintronic devices

David Salomoni

THÈSE

Pour obtenir le grade de

DOCTEUR DE L'UNIVERSITÉ GRENOBLE ALPES

École doctorale : PHYS - Physique
Spécialité : Nanophysique
Unité de recherche : Spintronique et Technologie des Composants

Ecriture toute optique de dispositifs spintroniques

All-optical switching of spintronic devices

Présentée par :

David SALOMONI

Direction de thèse :

Liliana BUDA-PREJBEANU PROFESSEURE DES UNIVERSITES, GRENOBLE INP	Directrice de thèse
Ioan-Lucian PREJBEANU DIRECTEUR DE RECHERCHE, CEA CENTRE DE GRENOBLE	Co-directeur de thèse

Rapporteurs :

JÖRG WUNDERLICH
PROFESSEUR, UNIVERSITÄT REGENSBURG
OXANA CHUBYKALO-FESENKO
SENIOR SCIENTIST, CSIC

Thèse soutenue publiquement le **31 janvier 2024**, devant le jury composé de :

MICHEL HEHN, PROFESSEUR DES UNIVERSITES, UNIVERSITE DE LORRAINE	Président
JÖRG WUNDERLICH, PROFESSEUR, UNIVERSITÄT REGENSBURG	Rapporteur
OXANA CHUBYKALO-FESENKO, SENIOR SCIENTIST, CSIC	Rapporteure
REINOUD LAVRIJSEN, ASSOCIATE PROFESSOR, TECHNISCHE UNIVERSITEIT EINDHOVEN	Examinateur
LAURENT RANNO, MAITRE DE CONFERENCES HDR, UNIVERSITE GRENOBLE ALPES	Examinateur

Acknowledgements

This PhD thesis is a testament to the collaborative spirit and collective effort that made it possible. I extend my deepest gratitude to my supervisors, Liliana, Lucian, and Ricardo, whose support and guidance have been the cornerstone of my entire PhD journey. Their expertise and mentorship have profoundly influenced not only the research itself but also my personal growth. I am incredibly grateful for the collaborative efforts of my colleagues from Nancy. Gregory Malinowski, Michel Hehn, and Stéphane Mangin have all enriched the scope of my research. Additionally, a special acknowledgment goes to Yi Peng, whose exceptional contributions to our experimental work played a pivotal role in the success of our endeavors. I extend my sincere gratitude to Kevin Garello for consistently supporting me on the CSI committee. I also express my appreciation to Stéphane A. for his proficient execution of sputtering depositions, and to Laurent V. and Florian D. for their meticulous work in e-beam lithography. Furthermore, I am grateful to Guillaume G. and Valentine B. for their contributions to the ITO deposition process. The expertise of Elizaveta A. T. in atomistic spin simulations significantly advanced the theoretical aspects of my work. I would also like to express my appreciation to the ESRs from the COMRAD project: Timur, Aya, Jackson, Julian, Leo, Paul, Thodoris, Thomas, and Guillermo. Our time spent together at meetings across Europe fostered valuable connections. A heartfelt thanks goes to the entire MRAM team for transforming workdays into enjoyable experiences. I am especially grateful to Louis, Ariam, Hasan, Bruno, Libor, Alvaro, Daniel, Nuno, Michal, Javier, Marco M., Pedro, Marco B., Ilaria, Subham, Sergi, Hanna, and Anda for their outstanding teamwork and the strong bonds of friendship we've built. Last but not least, my deepest gratitude goes to my family and my girlfriend, Cami. Their unwavering support, understanding, and encouragement throughout this challenging journey have been my pillar of strength. Their love has fueled my determination to succeed.

This research was made possible through financial support from the Agence Nationale de la Recherche (ANR) UltraFast Opto-magneto-spintronics for Futur Nanotechnologies (UFO) project and the European Union Horizon 2020 research and innovation program under Marie Skłodowska-Curie Grant Agreement No. 861300 Cold Opto-Magnetism for Random Access Devices (COMRAD) project.

You better start swimming or sink like a stone.
For the times, they are a-changin'.
—Bob Dylan, "The Times They Are A-Changin'"

Summary

The evolution of computer memory has led to a multilevel hierarchy, balancing speed, storage density, and cost. As complementary metal oxide semiconductor (CMOS) memory limits are approached, interest grows in nonvolatile alternatives like magnetic random access memory (MRAM). Although perpendicular spin-transfer torque (p-STT-MRAM) is already in production, alternative technologies such as spin-orbit torque (SOT) are explored for high-speed and fast cache operation. However, SOT has drawbacks, such as a larger bit-cell area and the need for an applied magnetic field for deterministic switching. In the pursuit of faster, more efficient memory, all-optical switching (AOS) technology seeks to achieve magnetization reversal through energy-efficient ultrafast writing with single-femtosecond laser pulses. This Ph.D. thesis addresses the objective of merging helicity-independent HI-AOS with MRAM devices. The materials investigated are rare-earth transition-metal multilayer systems, with a particular focus on Tb/Co-based structures. Through a combination of experimental investigations and numerical simulations, we unraveled the intricate dynamics of HI-AOS and used them to develop functional nanometer-sized AOS magnetic tunnel junctions (AOS-MTJs). These results not only deepen our understanding of HI-AOS but also explore its applications in non-volatile data storage and energy-efficient computation at the nanoscale. The exploration of HI-AOS in thin films of rare-earth transition metal multilayer systems lays the foundation for reliable magnetization toggle reversal, exploring the response to different pulse durations and fluences. Key new findings include the observation of concentric rings with opposite magnetic orientations and the independence of fluence on pulse duration, challenging existing paradigms. A hypothesis emphasizing the role of local anisotropy decrease that favors a precessional type of HI-AOS is introduced. The development of a macrospin model, incorporating two-temperature model (2TM) principles, explains the precession-driven switching mechanism observed in the Tb/Co-based multilayer system. Simulations reveal dynamics influenced by parameters such as Gilbert damping, anisotropy tilt angle, and the quality factor Q. Atomistic simulations further validate the model's predictions, emphasizing the significance of temperature-dependent magnetization and anisotropy effects in the HI-AOS process. Practical applications require the fabrication and electrical characterization of MTJ devices. Optimization of tunnel magnetoresistance (TMR) values, reaching a maximum value of 74%, a significant improvement over previous demonstrations. The thesis main achievement was demonstrating field-free HI-AOS on 100 nm diameter patterned [Tb/Co] p-MTJ devices, using 50 fs laser pulses with an estimated absorbed energy of approximately 68.6 fJ per bit reversal. The research not only contributes to our understanding of HI-AOS but also opens future research paths. Recommendations for future directions include using atomistic and LLB models for a more comprehensive understanding, exploring alternative materials beyond Tb/Co, investigating deterministic switching using spin-transfer torque, and addressing device variability challenges. The thesis offers a comprehensive exploration of HI-AOS, from its fundamental mechanisms to practical applications in nonvolatile data storage and energy-efficient computation. The optimized TMR values and successful demonstration of AOS in nano-patterned devices are a first step toward a new memory technology. The use of both experimental and simulated methods strengthens the importance of the obtained results for further progress in this area. In summary, this doctoral research not only has expanded the knowledge of helicity-independent all-optical switching but has also laid the foundation for innovative applications in nano-scale technology. The ongoing integration of photonic and spintronic elements has the potential to bring about significant progress in data storage and computation.

Résumé

L'évolution de la mémoire des ordinatreurs conduit à plusieurs niveaux des applications, potentielles mariant vitesse, densité de stockage et coût. À mesure que les limites des mémoires CMOS (Complementary Metal Oxide Semiconductor) approchent, l'intérêt pour les alternatives non volatiles telles que la mémoire magnétique à accès aléatoire (MRAM) grandit. Dans la quête d'une mémoire plus rapide et plus efficace, la technologie de commutation tout-optique (AOS) cherche à réaliser le retournement de l'aimantation par une écriture ultrarapide à faible énergie avec une seul impulsion laser femto- ou picoseconde. Cette thèse a pour objectif d'utiliser des dispositifs AOS comme éléments mémoire MRAM. Les matériaux étudiés sont des systèmes multicouches de métaux de transition et terres rares, notamment les structures à base de Tb/Co. Grâce à une combinaison d'études expérimentales et de simulations numériques, nous avons élucidé la dynamique complexe de HI-AOS (écrtiture indépendante de l'helicité de l'impulsion laser) et l'avons utilisée pour développer des jonctions tunnel magnétiques AOS (AOS-MTJ) de taille nanométrique.

L'étude de HI-AOS dans des multicouches de métaux de transition et terres rares a démontré le renversement fiable de l'aimantation, en explorant la réponse à différentes durées d'impulsion et à différentes fluences. Parmi les nouveaux résultats clés, on peut citer notamment l'observation d'anneaux concentriques avec des orientations magnétiques altemantes et l'indépendance de la fluence par rapport à la durée de l'impulsion, ce qui remet en question les paradigmes existants. Le développement d'un modèle de macrospin, incorporant les principes du modèle à deux températures (2TM), explique le mécanisme de commutation par précession observé dans le système multicouche à base de Tb/Co. Les simulations révèlent une dynamique influencée par des paramètres tels que l'amortissement de Gilbert, l'angle d'inclinaison de l'anisotropie et le facteur de qualité Q. Les simulations atomistiques valident égalment les prédictions du modèle, soulignant l'importance des effets de l'aimantation et de l'anisotropie en fonction de la température dans le processus HI-AOS. Pour envisager des applications pratiques est nécessaire la fabrication et la caractérisation électrique des dispositifs MTJ. L'optimisation des valeurs de magnétorésistance tunnel (TMR), atteignant une valeur maximale de 74%, représente une amélioration significative par rapport aux démonstrations précédentes. La principale réalisation de la thèse a été la démonstration d'un retournement HI-AOS sans champ externe sur des dispositifs p-MTJ [Tb/Co] de 100 nm de diamètre, en utilisant des impulsions laser de 50 fs avec une énergie absorbée estimée à environ 68,6 fJ par bit. Ces études contribuent non seulement à notre compréhension du HI-AOS, mais ouvre également des pistes de recherche à l'avenir. Les prospectives pour les orientations futures comprennent l'utilisation de modèles atomistiques et LLB pour une compréhension plus complète, l'exploration de matériaux alternatifs au-delà du Tb/Co, l'étude de la commutation déterministe à l'aide du couple de transfert de spin, et l'investigation de la variabilité des dispositifs. La thèse propose une exploration complète de HI-AOS, de ses mécanismes fondamentaux à ses applications pratiques dans le domaine du stockage de données non volatiles et de la microelectronique à faible consommation d'énergie. Les valeurs optimisées de la TMR et la démonstration réussie de l'AOS dans des dispositifs nanometriques constituent un premier pas vers une nouvelle technologie mémoire. L'utilisation de méthodes expérimentales et simulées renforce l'importance des résultats obtenus pour les progrès futurs dans ce domaine. En résumé, cette recherche doctorale a non seulement élargi nos connaissances sur la commutation tout-optique indépendante de l'hélicité, mais a également posé les bases d'applications innovantes dans le domaine des technologies numérique à l'échelle nanométrique.

Table of Contents

List of Figures

List of Tables

List of Abbreviations

AF	Antiferromagnet(ic)
AOS	All-optical switching
AL	Analyzer layer
CMOS	Complementary Metal Oxide Semiconductor‘
DOS	Density of states
DW	Domain wall
DRAM	Dynamic Random Access Memory
FL	Free layer
FM	Ferromagnet(ic)
FMR	Ferromagnetic resonance
GMR	Giant magnetoresistance
HD-AOS	Helicity-Dependent All-optical switching
HI-AOS	Helicity-Independent All-optical switching
IBE	Ion beam etching
IP	In plane
LLG	Landau-Lifshitz-Gilbert
MCA	Magnetocrystalline anisotropy
MFM	Magnetic force microscopy
MOKE	Magneto-optical Kerr effect
MRAM	Magnetic random access memory
MTJ	Magnetic tunnel junction
NM	Non-magnet(ic)
PCM	Phase change memory
PHE	Planar Hall effect
PMA	Perpendicular magnetic anisotropy
PMR	Perpendicular magnetic recording
POL	Perpendicular polarizer
RIE	Reactive ion etching
RKKY	Ruderman-Kittel-Kasuya-Yosida
RRAM	Resistive random access memory
RT	Room temperature
SAF	Synthetic antiferromagnet(ic)
SEM	Scanning electron microscopy
SHE	Spin Hall effect
SOC	Spin-orbit coupling
SOT	Spin-orbit torque
SRAM	Static Random Access Memory
SQUID	Superconducting quantum interference device
STT	Spin-transfer torque
SOT	Spin-orbit torque
TMR	Tunnel magnetoresistance ratio
TCE	Transparent conductive electrode

VLSI	Very large scale integration
VSM	Vibrating sample magnetometry
XMCD	X-ray magnetic circular dichroism

Introduction

Motivation

In the realm of computer memory, a complex hierarchy has emerged to address the ever-growing demands of modern computing systems. This hierarchy takes into account factors such as operation speed, storage density, and cost. These considerations have given rise to a diverse range of memory technologies, each with its own set of advantages and limitations.

At the heart of this memory hierarchy are conventional complementary metal oxide semiconductor (CMOS) memories. CMOS memories, such as dynamic random access memory (DRAM) and static random access memory (SRAM), have long been the workhorses of computing because of their remarkable speed and efficiency. However, they have a critical drawback: They are volatile, meaning that they require a continuous supply of power to retain the data stored within them. As a result, once the power is cut off, all the information they hold is lost.

In this hierarchy, the top-tier memories, which are accessed most frequently, are placed closer to the processing unit, while the lower-tier memories, accessed less frequently, are located farther from the processor and have different requirements.

Memory in the upper tiers of the hierarchy, such as RAM and cache, prioritize high speed, low retention time rather than emphasizing memory capacity. On the contrary, the memories in the lower tiers of the hierarchy need not be as fast but require very high retention times and greater memory capacity. In terms of power consumption, the lower part of the hierarchy incorporates non-volatile memory technologies. These technologies consume power only when reading or writing data. In contrast, the upper part of the hierarchy utilizes the volatile memories mentioned that consume power even when in standby mode to achieve the necessary speed performance.

Over time, the challenge of improving both speed and density while managing costs within the CMOS framework has become more daunting. As technology has advanced and as the physical limits of CMOS memories are reached, there is a pressing need to explore alternative memory technologies capable of breaking through these constraints.

One compelling candidate that has garnered significant attention is magnetoresistive random access memory (MRAM) [1–3]. MRAM represents a departure from traditional volatile memory technologies. It possesses a unique attribute, nonvolatility. In other words, MRAM can retain data even when the power source is disconnected. This characteristic addresses the fundamental drawback of CMOS memories and opens up exciting possibilities for various computing applications.

MRAM relies on magnetoresistance principles to store and retrieve data. It uses the magnetic properties of materials to encode and access information quickly and efficiently. This magnetic

approach offers several advantages. In particular, MRAM can provide access times on par with volatile memories such as DRAM, making it an attractive choice for applications where speed is crucial.

The ongoing evolution of computer memory technologies has brought us to a pivotal point. The limitations of CMOS memories, with their volatile nature, have prompted a search for innovative solutions. MRAM, with its combination of nonvolatility and impressive performance characteristics, emerges as a promising contender. As the pursuit of faster, more efficient, and cost-effective memory technologies continues, MRAM remains a focal point in the quest for the next generation of computer memory.

Perpendicular spin-transfer torque (p-STT) MRAM, due to advantages such as reliable switching, low energy consumption, and easy integration with CMOS technology [1], is the most widely adopted spintronics-based memory adopted by the foundry [4–6]. High-performance STT magnetic tunnel junction (MTJ) cells are among the first MRAMs to have recently been commercialized as embedded flash memory and last-level cache replacements. The FeCoB/MgO/FeCoB system has become the basis of most MTJ designs, due to its high tunnel magnetoresistance ratio effect (TMR) [7,8], improved readability and scaling of interfacial perpendicular magnetic anisotropy (PMA) based devices [9,10]. Moreover, in STT cells the reading and writing paths are shared, enabling a compact design [11,12], however fast switching in the precessional regime requires switching voltages close to the barrier breakdown voltage.

Alternative spin-orbit torque (SOT) technology is more suitable for high-speed and low error rate operation [13,14]. The SOT three terminal devices with separate reading and writing paths enable better endurance combined with fast switching, creating a potential replacement for SRAM [15]. Its main drawback is the larger bit-cell area, and although switching pulses as short as 100 ps are possible, the application of a field is generally required to obtain deterministic switching, which complexifies the cell design.

The all-optical-switching (AOS) technology envisions further acceleration of the magnetization reversal process by enabling the cells to be written at femtosecond time scales. Single-pulse helicity independent all-optical switching (HI-AOS) is a phenomenon by which the magnetization of a nanostructure can be reversed by a single femtosecond laser pulse. The method is ultrafast and does not require the use of any applied field. Since its discovery in GdFeCo ferrimagnetic systems [16], single-pulse HI-AOS has been limited to Gd-based alloys or Gd/FM bilayers, where FM is a ferromagnetic layer [17,18]. Only recently few other material systems have shown switching driven by ultrashort single laser pulses: MnRuGa ferrimagnetic Heusler alloys [19], Tb/Co multilayers [20,21].

The utilization of all-optical switching as a writing mechanism in MRAM offers the potential for significantly faster write speeds, around two orders of magnitude quicker than electrical alternatives, with extremely low energy consumption (as low as 16 fJ/bit [3]) while maintaining nonvolatility. This advancement not only enhances speed and reduces power consumption, but also enables a more compact two-terminal design for STT devices, all without compromising endurance.

The first successful demonstration of AOS operation in a micron-sized p-MTJ cell was carried out by Chen et al., employing a GdFeCo alloy storage layer, resulting in a modest tunnel magnetoresistance ratio of 0.6%. Subsequent improvements by Wang et al. achieved switching in Co/Gd bilayer tunnel junctions with cell sizes as small as 3 µm lateral size and a remarkable TMR ratio

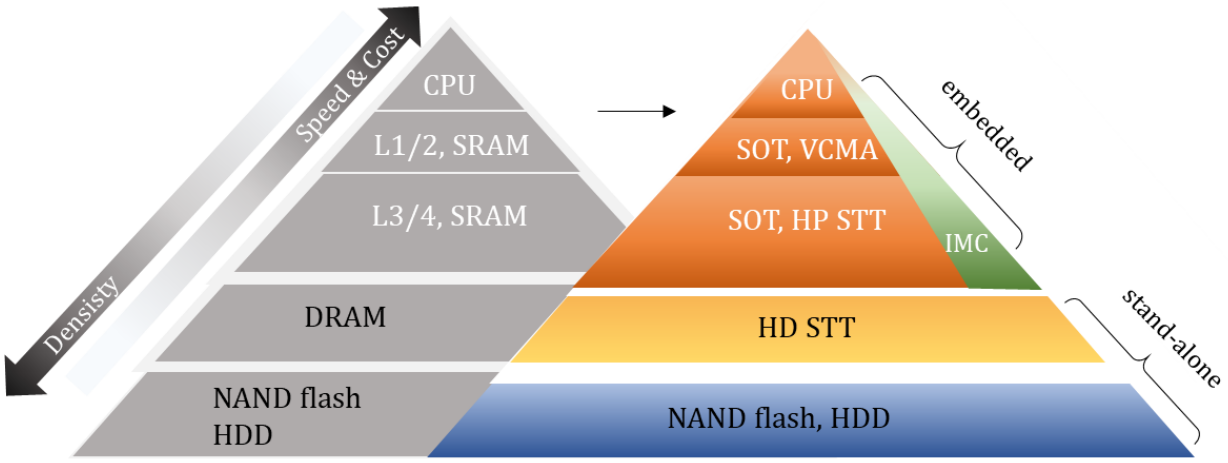

Fig. I.1: Memory hierarchy | Different memory types and prospective spintronic technologies that could replace them. L1-4 stands for different cache levels, SRAM and DRAM for static and dynamic random access memory, respectively, HDD for magnetic hard disk drives. HP and HD STT are high-performance and high-density STT-MRAM, respectively, IMC stands for in-memory computing. Adapted from [15]

of 34.7%. This enhancement was made possible by a clever design pioneered by Avilés-Félix et al., where an optically-switchable material is magnetically coupled to the FeCoB interface of the storage layer.

The initial reports of a storage layer based on $[Tb/Co]_N$ multilayers coupled to FeCoB showed the ability to adjust the Co/Tb composition to control the effective perpendicular anisotropy of magnetic tunnel junctions. Even after annealing at 250°C to achieve a 38% TMR ratio after patterning to nanometer sizes, the perpendicular anisotropy remained stable. Thin-film experiments with the same storage layer stacks confirmed HI-AOS of the magnetization using both 60 fs and 5 ps laser pulses for incident fluences as low as 3.5 mJ/cm2. However, reliable field-free AOS demonstrations on patterned devices and a comprehensive understanding of the switching mechanism in this system are still lacking.

Objective

The main objective of this thesis was to develop a fully functional AOS-MTJ. Our investigation primarily focused on stacks optimizing MTJ in order to enhance TMR values and allow for nano-fabrication at diameters below 100 nm. We explored the feasibility of achieving field-free, helicity-independent all-optical toggle switching using ultra-short 50 fs single light pulses both at thin-film level and on patterned [Tb/Co] based p-MTJ. During our experiments, we observed that certain features of the physical reversal phenomena did not align with existing theoretical explanations. Consequently, we delved deeper into these observations, employing both experiments and simulations to gain a more comprehensive understanding. Furthermore, we gained a deep understanding of the physical processes involved in all-optical switching within [Tb/Co] materials and similar systems. We evaluated the impact of patterning on the preservation of high anisotropy in the

Tb/Co-based electrode by comparing patterned devices with continuous films. We also examined the integration of a stable reference layer with minimal offset field to understand its influence on the properties of the AOS stack. Our study aimed to establish a correlation between the AOS behavior observed at the film level and the switching probability in the patterned device.

Outline This thesis is divided into five chapters and a conclusion chapter. Lists for all figures, tables, symbols, and abbreviations are provided. All links (figures, equations, chapter and section names, references) are clickable. The manuscript is organized as follows:

Chapter 1: Background: magnetic materials, spintronics, and all-optical switching This chapter serves as an introductory overview of the diverse topics discussed in this thesis. Its primary objective is to establish a groundwork in spintronics, ultrafast all-optical switching, and cutting-edge opto-spintronics devices. Within this chapter, we will explore the fundamental principles that form the basis of spintronics, provide a brief overview of the critical physical phenomena employed in this thesis, and provide a broader perspective on their relevance to MRAM technology. Although each of these fields is extensive on its own, we will focus exclusively on the concepts and findings pertinent to the systems and issues discussed in this thesis.

Chapter 2: Experimental techniques In this chapter, I present the experimental techniques central to our research, both for the growth of the layers and their magnetic characterisation. These methods are essential for understanding the magnetic properties and dynamics of the materials under investigation. Magnetron sputtering is employed for precise material deposition, which offers control over film thickness and composition. MOKE serves as a powerful tool for exploring magnetization in thin films, allowing us to characterize in-plane and out-of-plane magnetization properties. Furthermore, TR-MOKE, a cutting-edge approach, leverages ultrafast laser technology to investigate rapid and transient magnetization dynamics, enabling the study of dynamic processes and material responses to external stimuli. In the forthcoming chapters, I will unveil the results and insights derived from the application of these techniques, shedding light on the magnetic characteristics and behaviors of our system.

Chapter 3: All-optical switching in Tb/Co multilayer In this chapter, we explore the fundamental properties of RE-TM systems, providing essential insights necessary to comprehend the subsequent discussions on all-optical switching in Tb/Co multilayer systems. Subsequently, the results of HI-AOS in Tb/Co multilayer systems are presented, together with the magnetic characterization as a function of the layers thicknesses.

Chapter 4: Modelling of HI-AOS in multilayer systems In this chapter, we present the different theoretical approaches that have been used to understand the various physical phenomena presented in this thesis. Starting by exposing a theory of laser pulse absorption which is approximated as a simple heating effect in the two temperature model (2TM). Then the developed model that couples the 2TM to a macrospin algorithm is presented. It was utilized to phenomenologically simulate the optically driven magnetization reversal. After showing the obtained results a second investigation based on an atomistic spin solver is shown to complement the study.

Chapter 5: Nano-patterned all-optical switching spintronics devices This chapter serves a dual purpose: first, to provide an overview of the nano-fabrication processes central to the creation of these MTJ devices, encompassing the fabrication of magnetic pillars and the definition of the transparent and conductive electrodes; second, to delve into the critical aspects of device characterization and results. Particularly TMR values, coercivity mappings and the exciting potential of femtosecond laser pulse irradiation to achieve all-optical switching in nano-patterned spintronics devices.

Conclusions and perspectives In the concluding chapter, we distill the essence of our research by summarizing its main findings. We take a look at the future of research, suggesting interesting paths and directions that come from the knowledge gained in this study.

Chapter 1

Background: magnetic materials, spintronics, and all-optical switching

Contents

This chapter serves as an introductory overview of the diverse topics discussed in this thesis. Its primary objective is to establish a groundwork in spintronics, ultrafast all-optical switching, and cutting-edge opto-spintronics devices. Within this chapter, we will explore the fundamental principles that form the basis of spintronics, provide a brief overview of the critical physical phenomena employed in this thesis, and provide a broader perspective on their relevance to magnetic random-access memory (MRAM) technology. Although each of these fields is extensive on its own, we will focus exclusively on the concepts and findings pertinent to the systems and issues discussed in this thesis.

1.1 Magnetism

1.1.1 History

The exploration of magnetic properties in various materials traces its origins back to ancient times, with historical references to stones exhibiting the ability to attract iron in both Chinese and Greek cultures. Although it took physicists quite some time to develop accurate theories explaining the magnetization of materials, practical applications of magnetism emerged early on. Around 200 BC, China saw the creation of rudimentary compasses fashioned from magnetite, marking one of the earliest practical uses of magnetic properties [22]. However, it wasn't until the late 19th century that theoretical investigations began to provide qualitative and quantitative descriptions of magnetic materials.

In 1820, in Denmark, Hans-Christian Oersted stumbled upon a groundbreaking discovery; he accidentally found that a current-carrying wire could generate a magnetic field capable of deflecting a nearby compass needle, demonstrating the connection between electricity and magnetism [23]. In the wake of Oersted's discovery, André-Marie Ampère and Dominique-François Arago, working in Paris, rapidly followed suit. They wound wire into a coil and showed that a current-carrying coil acted as a magnet. In 1821, Michael Faraday introduced the concept of electric and magnetic fields and conducted experiments that led to the discovery of electromagnetic induction. He also demonstrated the principles of an electric motor using a combination of a steel magnet, a current-carrying wire, and a pool of mercury. Faraday's investigations further extended to the realm of optics, where he identified the magneto-optic Faraday effect in 1845, showcasing a connection between magnetism and light. In 1864 James Clerk Maxwell formulated his iconic set of equations, famously known as Maxwell's equations [24]. These equations provided a comprehensive framework for understanding the relationship between electric and magnetic fields in free space and their interaction with electric charge and current densities. A remarkable prediction arising from Maxwell's equations was that the physical constants ϵ_0 and μ_0, associated with electric and magnetic fields, respectively, are related by $\sqrt{\epsilon_0\mu_0} = 1/c$, where c represents the speed of light in a vacuum (approximately 2.998×10^8 m/s). This equation also establishes the ratio between the average values of electric and magnetic fields within an electromagnetic wave. Maxwell's equations exhibit an asymmetry between electric and magnetic fields, reflecting the absence of a magnetic counterpart to electric charge in nature. Despite these momentous achievements in electromagnetism, the enigma of ferromagnetism in solid materials persisted. Iron, for example, exhibited magnetization (M) equivalent to an exceedingly high surface current density. The idea of such colossal surface currents circulating around magnetized iron seemed implausible within classical physics. Finally, this long-standing puzzle found resolution in the twentieth century. George Uhlenbeck and Samuel Goudsmit's discovery of electron spin in 1925 unveiled that electrons possess quantized angular momentum and intrinsic spin. [25]

1.1.2 Quantum description

Isolated atoms

The advent of quantum mechanics in the early twentieth century offered a comprehensive explanation of electron dynamics and interactions. In this quantum framework, the mysterious behavior

of electrons within atoms is revealed through a set of mathematical functions known as wave functions. Solutions of Schrödinger's equation $H\psi = E\psi$, they describe the quantum state of a particle or system, providing information about the probability amplitude of finding the particle in various positions and states. For an electron in an atom, we call these wave functions **atomic orbitals**, each representing a distinct region in space where electrons are highly likely to be found. Each electron in an atom is described by different **quantum numbers**.

To understand how to evaluate the magnetic moment of an atom, one may start from the classical expression of the magnetic moment and convert it into a quantum mechanical one. With μ_0 representing the vacuum magnetic permeability and e, m_e the electron charge and mass respectively, classically we get $\mu = -\frac{e\mu_0}{2m_e}\mathbf{L}$. In quantum mechanics the expectation value of $\mathbf{L}$ cannot be observed, but only the component along a quantization axis, say z, is defined by an alignment field. Thus, we can only observe the expectation value $\langle \mathbf{L}_z \rangle$, which for a single electron $\langle \mathbf{L}_z \rangle = \hbar L_z$. In the last expression, we have specifically indicated that $\hbar L_z$ is the eigenvalue of the operator $\mathbf{L}_z$. The quantum mechanical expression for the measured magnetic moment along z is therefore given by

$$\langle \mu_z \rangle = -\frac{e\mu_0}{2m_e}\hbar L_z. \tag{1.1}$$

The quantum mechanical relation 1.1 is used to define the so-called Bohr magneton, μ_B. We can define the Bohr magneton as $\mu_B = \frac{e\hbar}{2m_e}$, with a value $\mu_B = 0.927 \times 10^{-23}\,\mathrm{Am}^2$.

As mentioned earlier the electron possess an intrinsic spin; therefore, the total magnetic moment of an atom is given by the sum of the orbital and spin magnetic moments, and when neglecting the anomalous correction to the g-factor, they can be expressed as

$$\langle \mu_o^z \rangle = -\mu_B \langle \mathbf{L}_z \rangle , \tag{1.2}$$

$$\langle \mu_s^z \rangle = -2\mu_B \langle \mathbf{S}_z \rangle \tag{1.3}$$

respectively, and thus the sum is given by it is

$$\langle \mu_{\mathrm{atom}}^z \rangle = -\mu_B \left(2 \langle \mathbf{S}_z \rangle + \langle \mathbf{L}_z \rangle\right) = -\mu_B \left(g_s \langle \mathbf{S}_z \rangle + g_l \langle \mathbf{L}_z \rangle\right), \tag{1.4}$$

we can associate a g-factor $g_s = 2$ with the spin moment and $g_l = 1$ with the orbital moment.

This sum depends on the filling of each subshell that is governed by Hund's and Pauli's rules.

In open shells, we need to consider rules for summing the spin and orbital angular momenta for all electrons in the open shell. Hund's rules allow us to describe the ground state multiplet and allow us to calculate the components of the orbital $\mathbf{L}$, spin $\mathbf{S}$, and total angular momenta $\mathbf{J} = \mathbf{L} + \mathbf{S}$ [26].

It should be noted that fully filled subshells ($J = 0$) do not contribute to magnetism because, in this case, all magnetic moments cancel out. In the case where the subshells are not fully filled, the atom is magnetic. This is the case for 79 pure elements.

Localized and itinerant magnetism

A material composed of magnetic atoms is not necessarily magnetic itself. We can define magnetization, M, as the average magnetic moment per unit volume:

$$\mathbf{M} = \frac{\langle \mu^z_{\text{atom}} \rangle_V}{V} \tag{1.5}$$

where V is the volume of the material. Indeed, the moments carried by each atom within the material can be ordered (ferromagnetism, antiferromagnetism, ferrimagnetism, etc.) or disordered (paramagnetism). This ordering depends on the energy of interaction between the moments.

An intuitive and elegant way to describe the manifestation of magnetic order on a macroscopic scale within a bulk material is the Heisenberg Exchange Theory [27]. It relies on the coupling of these atomic magnetic moments with their neighboring counterparts. This coupling arises from the quantum mechanical **exchange interaction** between electrons:

$$H_{\text{ex}} = -J_{\text{ex}} \sum_{i,j} \mathbf{S}_i \cdot \mathbf{S}_j \tag{1.6}$$

In this equation, J_{ex} represents the exchange coefficient and the sign of J_{ex} dictates the relative orientation of neighboring spins. When $J_{\text{ex}} > 0$, it favors parallel alignment, resulting in ferromagnetic ordering. On the contrary, when $J_{\text{ex}} < 0$, antiparallel spins dominate, leading to antiferromagnetic ordering. There is also a unique category, known as ferrimagnets, where nonequivalent ferromagnetic sublattices exhibit antiferromagnetic coupling, yielding a net nonzero magnetization; see Fig. 1.1.

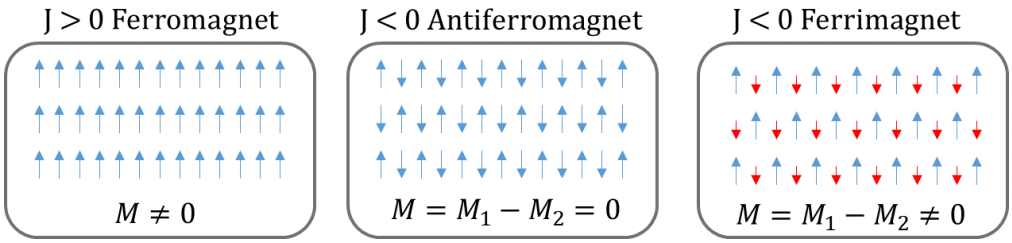

Fig. 1.1: Visual representation showcasing the three predominant magnetic order phenomena: ferromagnetism, antiferromagnetism, and ferrimagnetism. The symbol 'J' symbolizes the exchange interaction between adjacent magnetic moments.

When the coupling energy between magnetic moments exceeds the thermal agitation energy, the material becomes ordered and exhibits magnetism.

Ferromagnetic materials can be categorized into two groups: those with magnetic atoms possessing localized electron-based magnetic moments, such as rare earth's 4f electrons, and those with itinerant electron-based magnetism, as seen in the 3d transition metals. In the latter case, the electronic system is modeled by bands rather than orbitals.

In systems with significant atomic overlap of the electron wave functions, the energy and angular momentum states for these electrons are no longer discrete. Instead, energy levels form a continuum of states over a range of energies called energy bands; see Fig. 1.4(a). The distribution function for these energy levels is called the density of states.

The density of states (per unit volume), $g(E)$, is formally defined as $g(E)\,dE = \frac{1}{V}\frac{dN_E}{dE}\,dE$ such that the quantity $g(E)\,dE$ represents the number of electronic states in the energies range from (E) to (E + dE).

We integrate each density of states separately to yield a different number of electrons per unit volume in spin-up and spin-down bands, respectively:

$$n_\uparrow = \frac{N_\uparrow}{V} = \int_0^{E_F} g_\uparrow(E)\,dE; \quad n_\downarrow = \frac{N_\downarrow}{V} = \int_0^{E_F} g_\downarrow(E)\,dE \tag{1.7}$$

The magnetization, net dipole moment per unit volume, is then simply:

$$M = (n_\uparrow - n_\downarrow)\mu_B \tag{1.8}$$

The key to ferromagnetism lies in the existence of an energy shift between these two sub-bands, driven by the Pauli exclusion principle. This shift can be attributed to a repulsive energy (U) that arises because electrons with opposite spins repel each other more than electrons with the same spin. The system will distribute electrons to minimize the sum of kinetic and repulsive energy. Depending on the density of states at the Fermi level ($g(E_F)$) and the value of U, the system may maintain two symmetric sub-bands or exhibit a shift between them, see Fig. 1.4(a). The Stoner criterion [28,29] dictates that a material is ferromagnetic if $Ug(E_F) > 1$, typically observed in materials with a high density of states at the Fermi level.

The asymmetry in spin-dependent density of states results in a disparity in population between the two spin categories, $n_\uparrow - n_\downarrow$, giving rise to a magnetic moment of $(n_\uparrow - n_\downarrow)\mu_B$, see Fig. 1.4.

In these cases, exchange energy is often defined in terms of the exchange stiffness (A_{ex}) and gradients of magnetization:

$$E_{\text{ex}} = \int_V A_{\text{ex}} \left[(\nabla M_x)^2 + (\nabla M_y)^2 + (\nabla M_z)^2\right] \mathrm{d}V \tag{1.9}$$

The magnetic properties of materials are not solely determined by exchange interactions, but there is an array of energy contributions at play, and we will briefly discuss the main ones in the following.

Zeeman energy: The Zeeman effect, named after Pieter Zeeman, describes how the local magnetization ($\mathbf{M}$) of a material aligns itself with an external magnetic field ($\mathbf{H}_{\text{ext}}$). The Zeeman energy is expressed as a volume integral:

$$E_{\text{Zeeman}} = -\mu_0 \int_V \mathbf{M} \cdot \mathbf{H}_{\text{ext}}\,\mathrm{d}V \tag{1.10}$$

Here, μ_0 represents the vacuum magnetic permeability.

Magnetostatic interaction, (demagnetizing energy):

The concept of magnetostatic interaction, often referred to as demagnetizing energy, arises when dealing with magnetic materials. In a vacuum, where there is no magnetization, the magnetic field is simply described as $\mathbf{B} = \mu_0\mathbf{H}$. However, in the presence of a magnetized material, we need to consider the contribution from magnetization, leading to the equation $\mathbf{B} = \mu_0(\mathbf{H} + \mathbf{M})$. When the magnetization distribution within a material abruptly stops at its edges, it causes a divergence in the magnetic field, expressed as $\nabla \cdot \mathbf{H} = -\nabla \cdot \mathbf{M}$. This phenomenon means that the material

generates an additional magnetic field outside its physical boundaries as a result of its internal magnetization, and this field interacts with the material itself.

This self-interaction of magnetization, known as magnetostatic interaction, results in an energy term referred to as demagnetizing energy. With the *Macrospin approximation* that considers uniform magnetization such that the magnetic moment $\mathbf{m}$ of a given volume V is $\mathbf{m} = V\mathbf{M}$, one can express the demagnetizing energy as follows:

$$E_{\text{dem}} = -\frac{1}{2}\mu_0 \mathbf{M} \cdot \mathbf{H}_d = \frac{1}{2}\mu_0 \mathbf{M} \cdot (N\mathbf{M}) \tag{1.11}$$

Here, $\mathbf{H}_d = -N\mathbf{M}$ represents the demagnetizing field, and N is the demagnetizing tensor. This formulation of N is valid for ellipsoidal shapes, which are used as an approximation to describe the shape of uniformly magnetized materials for the purpose of applying the demagnetizing energy equation.

For simpler shapes, such as spheres, the diagonal elements of the demagnetizing tensor are all equal, e.g. $N_{xx} = N_{yy} = N_{zz} = \frac{1}{3}$. On the contrary, for a thin film with dimensions that are much larger in the lateral directions than in the thickness ($t \ll L$), we find $N_{xx} = N_{yy} \approx 0$ and $N_{zz} \approx 1$, where the z axis is perpendicular to the film's surface. This implies that in a homogeneously magnetized thin film, the demagnetizing energy E_{dem} is minimized when the magnetization vector $\mathbf{M}$ aligns along the longer dimension of the material, typically in the plane for an extended film. This aspect becomes crucial for the systems analyzed in this thesis.

Spin-orbit coupling (SOC) is a quantum relativistic effect that can be understood in a simplified manner as an interaction between the spin of an electron and the magnetic field created by its orbital motion. For hydrogen-like orbitals, the spin-orbit coupling energy, denoted as λ_{so}. The differing spin-orbit coupling energies observed for various elements, such as 3d transition metals and 4f rare earths, partly account for the variations in their magnetocrystalline anisotropy energies.

Spin-orbit coupling inherently links the electron's spin with the angular momentum of hybridized orbitals involved in atomic bonds within a crystal lattice. Consequently, magnetic moments tend to align preferentially with specific crystallographic directions, a property known as **magnetocrystalline anisotropy** (MCA). The variation in spin-orbit coupling energies observed between 3d transition metals (approximately $\lambda_{\text{so}} \approx 0.05$ eV) and 4f rare earths (approximately $\lambda_{\text{so}} \approx 0.2$ eV) partially accounts for the differences in the magnitudes of their respective magnetocrystalline anisotropy energies. Despite its quantum-mechanical origin, MCA can be described phenomenologically. The functional form of MCA reflects the crystal's symmetry and can be parameterized in terms of anisotropy constants K_i.

For example, a type of MCA often encountered in materials' volumes and interfaces is *uniaxial anisotropy*. It can be defined in the first order as:

$$E_{an} = -K_1(\hat{m} \cdot \hat{n})^2 = -K_1 \sin^2(\phi_M) \tag{1.12}$$

In this definition, K_1 represents the uniaxial anisotropy constant, $\hat{m}$ is the magnetization unit vector, $\hat{n}$ is the unit vector along the symmetry axis, and ϕ_M is the angle between $\hat{m}$ and $\hat{n}$. When K_1 is greater than zero, it results in an easy axis of magnetization along $\hat{n}$, known as easy-axis anisotropy. On the contrary, if K_1 is less than zero, $\hat{n}$ becomes the hard axis, and the magnetization

lies in the plane perpendicular to $\hat{n}$, referred to as the easy plane anisotropy.

Interfacial anisotropy: Another form of anisotropy, which is extensively employed in contemporary research, arises at the interface between a nonmagnetic material with high spin-orbit coupling and a ferromagnetic material. This type of anisotropy, originally predicted by Néel [30], can have various underlying causes, including broken inversion symmetry at the interface, magnetostriction, or orbital hybridization. In a significant number of cases, it exhibits an energy minimum oriented perpendicular to the material plane [31–33]. In these instances, this particular anisotropy is known as perpendicular magnetic anisotropy (PMA), and it typically competes with the shape anisotropy induced by the demagnetizing field, which results in an easy-plane bulk anisotropy. Due to this competition between perpendicular interfacial anisotropy and bulk easy-plane anisotropy, for film thicknesses below a critical value, the surface anisotropy components dominate over the shape anisotropy, leading to a net effective anisotropy oriented out of the plane. To account for this contribution, one can replace the term K_1 in equation 1.1.2 with a term that incorporates both contributions:

$$K_{\text{eff}} = K_u + \frac{K_S}{t} \tag{1.13}$$

Here, t represents the thickness of the ferromagnetic layer.

This type of anisotropy has been observed in various systems, including metal/ferromagnet combinations like Pt/Co or Au/Co [34,35], as well as oxide/ferromagnet multilayers such as Fe/MgO [36,37].

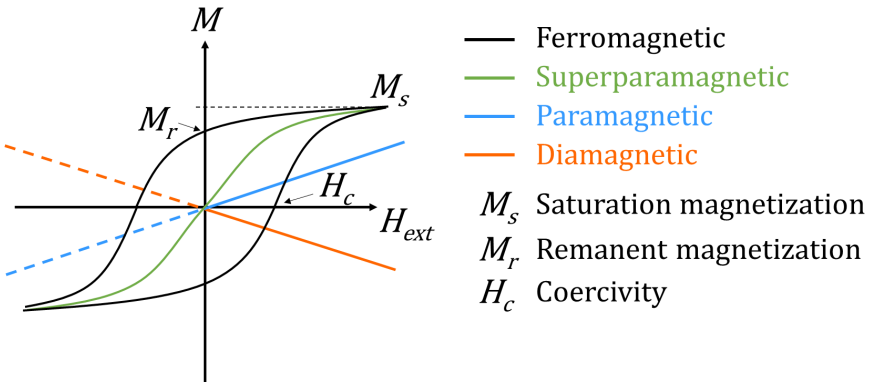

Fig. 1.2: Hysteresis loops of most common materials.

Now that the magnetization and the main interaction have been described, we can introduce a fundamental concept in the study of magnetism, the **hysteresis loop**. It describes the relationship between the magnetization of a material and an external applied magnetic field. When an external magnetic field is applied to a material, the magnetization of the material responds in different ways depending on its magnetic properties, see Fig. 1.2. It includes key parameters such as magnetization saturation (M_s), coercivity (H_c), and remanence (M_r), which vary depending on the magnetic properties of the material.

Ferromagnet: Ferromagnetic materials exhibit strong, spontaneous magnetization even without an external field. When an external field is applied, the magnetization increases until it reaches saturation (M_s), and if the field is removed, a remanence magnetization (M_r) appears. The coer-

civity (H_c) represents the field strength required to reduce the magnetication back to zero.

Superparamagnet: Superparamagnetic materials consist of small magnetic particles with no intrinsic magnetization. They align with an external field but lack coercivity or remanence because of their small size and absence of intrinsic anisotropy.

Paramagnet:Paramagnetic materials possess weak magnetization, proportional to the applied field strength. They lack spontaneous magnetization, have no coercivity, and exhibit a narrow, elongated hysteresis loop.

Diamagnet: Diamagnetic materials weakly oppose an external field due to the orbital motion of electrons. They do not exhibit spontaneous magnetization, have no coercivity, and display an almost absent hysteresis loop.

The magnetic properties of materials are intricately influenced by a complex interplay of the energy contributions presented earlier, each with its distinct role and characteristics. Understanding these contributions is fundamental to harnessing magnetism for various technological applications.

1.1.3 Ferrimagnets: rare-earth transition-metal (RE-TM) Systems

Ferrimagnetic materials are composed of two or more magnetic sublattices with opposing magnetization directions. One such class of materials that exhibits ferrimagnetic behavior are the Rare-Earth-Transition Metal (RE-TM) systems. Before discussing their properties, it is necessary to give an overview of the RE and TM atoms. The magneticrystalline anisotropy of 4f RE and 3d TM differs because of the relative weights of crystal-field and spin-orbit interactions on valence electrons. In RE, the 4f electrons are largely shielded from crystal-field effects by the outer shell, resulting in minimal quenching of orbital momentum. The strong spin-orbit interaction in RE, due to its high Z (atomic number), n (principal quantum number), and l (azimuthal quantum number), can be described using the single-ion model.

In this model, the anisotropy energy arises from the electrostatic interaction of the 4f shell charge distribution (effectively a quadrupole) with the crystal field, approximated by a point-charge model. The orientation of the magnetic easy axis is determined by the shape of the 4f orbital, which is governed by the filling of the 4f shell in the trivalent ions constituting the RE solids. In particular, the anisotropy constant can be written as $K_1 = -3Q_2A_2^0(2V_{RE})^{-1}$, where V_{RE} is the crystal volume per RE atom, Q_2 is the quadrupole moment (first non-vanishing anisotropic term describing the charge distribution), and A_2^0 is the crystal field parameter, details of the model can be found in [38]. In transition metals, the anisotropy constant $K_1 = \left(\sqrt{A^2 - 4\lambda_{so}^2} - A\right)/V_{TM}$ is small due to the dominance of the crystal field effect on the spin orbit coupling. The crystal field effect arises from the interaction between localized (3d) electrons and the surrounding crystal lattice, which causes the (3d) orbitals to split in energy. This crystal-field effect quenches the orbital angular momentum ($\mathbf{L}$) as electrons preferentially occupy lower energy orbitals. Consequently, the anisotropy constant K_1 is primarily determined by the crystal-field splitting term A, while the contribution from spin-orbit coupling (λ_{so}) is relatively weak in 3d transition metals and treated as a small perturbation [38].

In RE-TM systems, the interaction between atoms is exchange-driven. There are three types of interaction: TM-TM, RE-RE and RE-TM. Usually, for TM-TM and RE-RE interactions, the exchange integral is positive, resulting in ferromagnetic coupling. Instead, for RE-TM interactions, the exchange integral is negative, leading to antiferromagnetic coupling. It is worth noting that

the TM-TM coupling is relatively strong, around 0.01 to 0.1 eV, compared to the localized electron RE-RE which is an order of magnitude weaker. These systems can show complex magnetic behavior due to this interaction and the combination of strong magnetocrystalline anisotropy of the RE and the high magnetization (M_S) and Curie temperature (T_C) associated with the TM. They often can be modeled using two spin sublattices where the total magnetization ($\mathbf{M}_{\text{tot}}$) is the sum of these sublattice magnetizations:

$$\mathbf{M}_{\text{tot}} = \mathbf{M}_{\text{TM}} + \mathbf{M}_{\text{RE}} \tag{1.14}$$

The antiferromagnetic coupling leads to non-zero net magnetization due to differing magnetic moments of the sublattices, see Fig. 1.3.

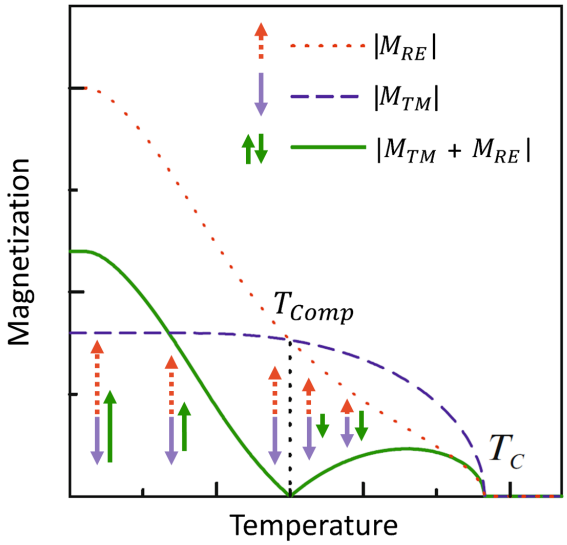

Fig. 1.3: Schematic illustration depicting the temperature-dependent variations in net magnetization (depicted by the green line), along with distinct sublattice-specific magnetization behaviors for the RE (highlighted in red) and TM (indicated in blue) sublattices. Image adapted from [39]

In alloys, the exchange interaction is strong enough to generate a common (T_{Curie}) for both sublattices, higher than the on one of the bulk RE. However, due to the distinct intrasublattice exchange strengths, the temperature dependence of magnetization differs for each sublattice. Consequently, the temperature-dependent magnetization of ferrimagnetic RE-TM alloys shows an important point: the **Magnetization Compensation Temperature (T_{Comp})**. Shown in Fig. 1.3, the T_{Comp} is the temperature at which the RE and TM sublattices have equal and opposite magnetization ($M_{RE}(T) = -M_{TM}(T)$), resulting in zero net magnetization. Here, the coercive field diverges and the system acts as an antiferromagnet. Additionally, another interesting point is the **angular momentum compensation temperature ($T_{A,C}$)** that is the temperature for which the RE and TM sublattices have equal and opposite angular momentum, resulting in zero net angular momentum, which can lead to interesting dynamics. Variations in the atomic environment of RE and TM may result in notable differences in their effective gyromagnetic ratios. Consequently, these differences could have an impact on the angular momentum compensation point. Effective gyromagnetic ratio γ_{eff} of ferrimagnets may be calculated following Kittel's model [40]:

$$\gamma_{\text{eff}} = \frac{M_{TM} + M_{RE}}{\frac{M_{TM}}{\gamma_{TM}}} \tag{1.15}$$

In the presence of an external field that is lower than the antiferromagnetic RE-TM coupling, the sublattice whose Zeeman energy and anisotropy energy sum are largest aligns parallel to the field, while the other sublattice aligns antiparallel. Intermediate situations can occur when the field is comparable to the interaction that couples the two sublattices, resulting in an inclined magnetization of each sublattice with respect to the applied field.

Ferrimagnets often experience spin reorientation transitions (SRT) because of competing contributions of RE and TM sublattices to magnetocrystalline anisotropy, affecting the magnetization ground state based on temperature. The importance of this reorientation in multilayers containing Tb or Dy will be addressed later in Chapter 4.

1.2 Spintronics

1.2.1 Spin-dependent transport phenomena

The theory that describes spin-dependent transport in ferromagnetic transition metals, initially proposed by Mott [41], provides a simple model for the electrical conductivity of two spin populations, denoted as ↑ for majority and ↓ for minority spins. In a ferromagnetic material, the total electrical resistivity is expressed as:

$$\rho_{TOT} = \frac{\rho_\uparrow \rho_\downarrow + \rho_{\uparrow\downarrow}(\rho_\uparrow + \rho_\downarrow)}{\rho_\uparrow + \rho_\downarrow + 4\rho_{\uparrow\downarrow}} \tag{1.16}$$

Here, $\rho_{\uparrow\downarrow}$ represents spin mixing resistivity, which accounts for the transfer of magnetic moments between the two spin populations due to spin-flip scattering events. In the low temperature approximation ($T << T_C$), this term can be considered negligible, leading to the simplified expression:

$$\rho_{TOT} = \frac{\rho_\uparrow \rho_\downarrow}{\rho_\uparrow + \rho_\downarrow}. \tag{1.17}$$

In this case, the resistivity of the ferromagnetic material results from the parallel combination of the resistivities of the two spin populations, as described in the two-current model.

The Drude-Sommerfeld model [42] is used to model the resistivity of each spin population:

$$\rho_{\uparrow(\downarrow)} = \frac{m_{\uparrow(\downarrow)}}{n_{\uparrow(\downarrow)} e^2 \tau_{\uparrow(\downarrow)}}. \tag{1.18}$$

Here, m, τ, and n represent the effective mass, relaxation time, and density of states at the Fermi level for the majority (minority) spin population. Since the density of states at the Fermi level differs for majority and minority spins in ferromagnetic materials, their resistivities also differ, with $\rho_\uparrow < \rho_\downarrow$.

This difference arises because s-electrons (conduction electrons) at the Fermi level have a higher probability of scattering on d-electrons (localized electrons). Consequently, in a uniformly magnetized ferromagnetic material, majority spin electrons (aligned with the magnetization) experience fewer scattering events than minority spin electrons.

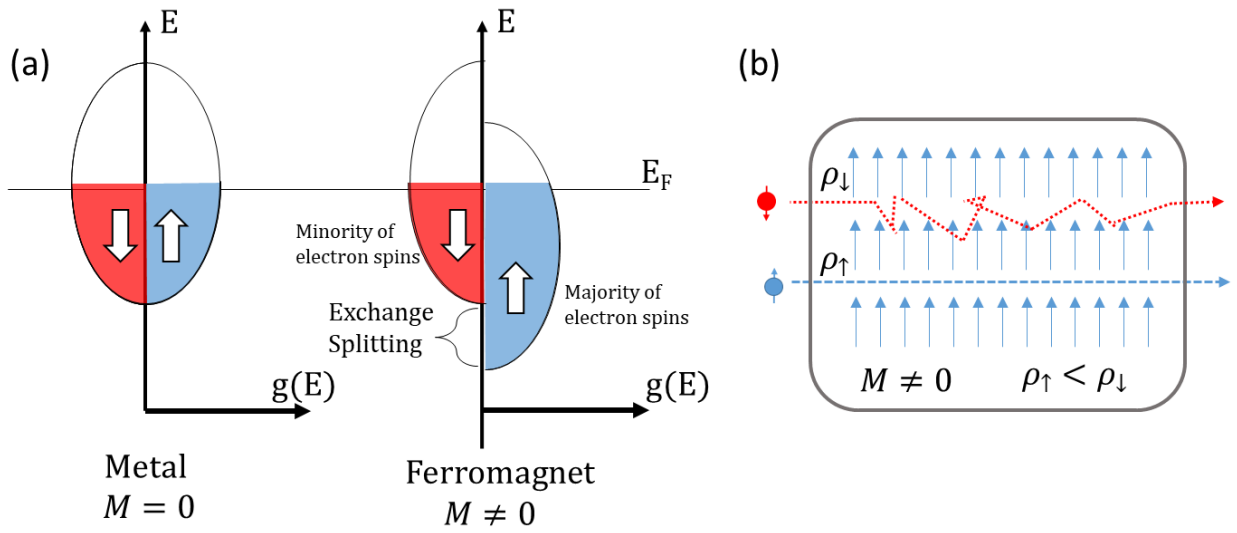

Fig. 1.4: Spin dependent transport | (a) Schematic of spin dependent DOS for a metal and a ferromagnet. (b) Schematic of spin dependent transport for majority and minority spin populations.

The experimental results obtained by Fert and Campbell on iron- and nickel-based alloys supported this model, demonstrating its effectiveness in describing spin-dependent transport [43–45].

This free-electron model can be used to understand various spin-dependent transport phenomena. One of these is the magnetoresistance effect, which refers to the change in resistance of a magnetic object depending on the direction of an applied magnetic field relative to the current direction. The anisotropic magnetoresistance (AMR) effect [46], first observed by Lord Kelvin in 1856, is a relatively small effect (a few percent at room temperature). Other magnetoresistance effects include giant magnetoresistance (GMR), tunneling magnetoresistance (TMR), colossal magnetoresistance (CMR) [47], and extraordinary magnetoresistance (EMR) [48]. GMR and TMR are commonly used in spintronics for various applications, including MRAM.

1.2.2 Tunnel magnetoresistance ratio (TMR)

The phenomenon of Tunnel magnetoresistance ratio (TMR), initially discovered by Julliére in 1975 [49], involves a trilayer structure consisting of two ferromagnetic materials separated by an insulating layer, later referred to as magnetic tunnel junctions (MTJ). Initially, the TMR effect was observed to be around 14% at 4.2K, and it did not gain much attention until the 1990s. It was only after the discovery of Giant Magnetoresistance (GMR) that two independent research groups in Japan and the USA measured TMR at room temperature in MTJ based on aluminum oxide (AlOx) [50,51].

Julliére's initial explanation for TMR involved the spin polarization of the two ferromagnetic materials. As discussed in the previous section, the transport of electrons near the Fermi level in ferromagnetic materials exhibits a significant difference in the Density of states (DOS) for the two spin populations, as illustrated in Fig. 1.5. Considering that the probability of tunneling depends on the density of final available states while the number of electrons available for tunneling depends on the density of initial filled states, Julliére estimated the TMR effect as:

$$TMR = \frac{R_{AP} - R_P}{R_P} \times 100 = \frac{2P_{F1}P_{F2}}{1 + P_{F1}P_{F2}} \times 100 \tag{1.19}$$

Here, P_{F1} and P_{F2} represent the spin polarization of the ferromagnetic materials F1 and F2, respectively, as shown in Fig. 1.5.

Initially, MTJs based on amorphous Al_2O_3 achieved TMR values of a few tens of percent. These values improved significantly through optimization of the composition of ferromagnetic materials, including the use of polycrystalline CoFe and amorphous CoFeB, and improvements in the quality of the tunnel barrier, leading to TMR values of 60% to 70% [52,53]. The introduction of post-deposition annealing also played a role in improving barrier quality and, consequently, the TMR amplitude [54]. In Julliére's model, the amplitude of TMR is primarily defined by the spin polarization of the magnetic electrodes near their interface with the barrier.

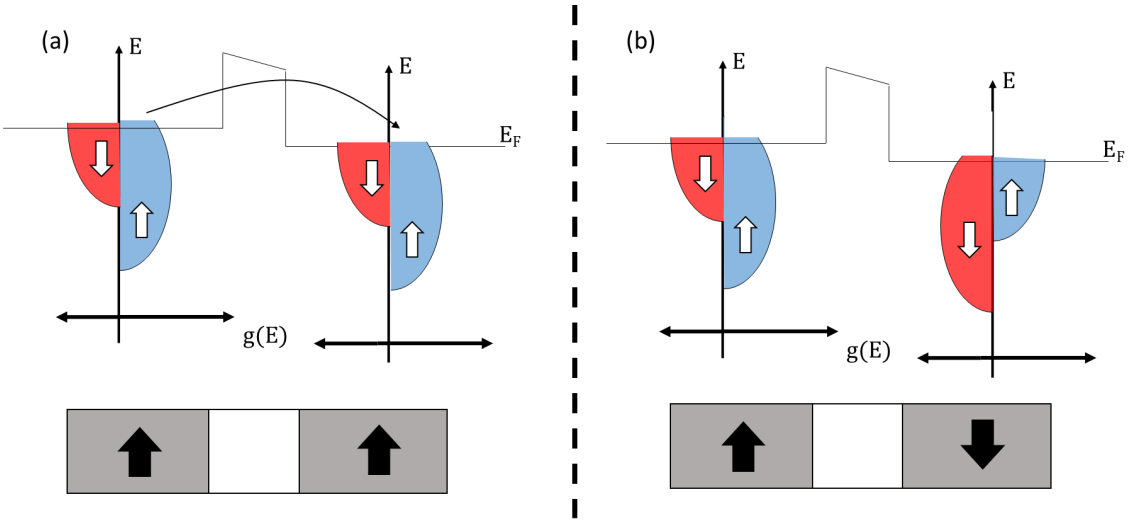

Fig. 1.5: Tunnel Magnetoresistance | **a.** Schematic of a spin dependent tunneling in a trilayer system (two ferromagnets F1 and F2 and the tunnel barrier B) in parallel configuration. The red arrows indicate the tunneling probability. **b.** As in a. but for the antiparallel configuration.

Subsequently, the composition of the tunneling barrier itself started to garner attention in the spintronics community. De Teresa et al. demonstrated that the choice of barrier material significantly influences the TMR amplitude [55]. Higher TMR values were predicted for highly textured materials, and this was experimentally confirmed by Bowen et al. using a single crystal Fe/MgO/FeCo(001) structure [56]. Soon after, a series of studies reported even higher TMR values in MgO-based MTJs [57–59], with a sputtered trilayer combining amorphous CoFeB and crystalline MgO(001) achieving the highest TMR value measured to date at 604% at room temperature [60]. These high TMR values were predicted on the basis of theoretical work that considered the evanescent Density of States (DOS) in the barrier [61–63]. In systems such as Fe / MgO, with nearly identical crystalline symmetries of the Bloch states in the two materials, it was found that the evanescent wave in the barrier decays much faster for certain electronic bands (specifically Δ_2 and Δ_5) than for others (Δ_1). This implies that tunneling events for Δ_1 electrons are much more probable than for Δ_2 and Δ_5 electrons. Moreover, both the majority and minority states of Δ_2 and Δ_5 have some presence at the Fermi energy, resulting in relatively low polarization. This is not the case for the Δ_1 states, which have only one spin population at the Fermi level, leading to a 100%

spin polarization. In a trilayer structure with two ferromagnets and a relatively thick tunnel barrier, all these factors can yield expected TMR values higher than 1000% at room temperature [64]. Unfortunately, such high values have never been observed, probably because of imperfections in the crystalline structure. Additionally, reducing the thickness of the tunnel barrier allows contributions from electrons with Δ_5 symmetry, which have lower spin polarization, leading to lower TMR values.

In conclusion, TMR, with its large amplitude at room temperature and resistance values compatible with CMOS electronics (MTJ resistance typically on the order of a few kilo Ohms), is one of the most widely used phenomena in spintronics, particularly in MRAM applications, as we will discuss in Section 1.2.4.

1.2.3 Magnetization dynamics

Magnetization dynamics refers to the evolution over time of the magnetization vector within a magnetic material when influenced by external factors. The dynamics and performance of most spin-based devices are commonly described using the Landau-Lifshitz-Gilbert-Slonczewski (LLGS) equation. This equation dictates how the magnetization vector ($\mathbf{M}$) within a monodomain nanomagnet changes over time due to the effects of magnetic fields, spin-transfer torque (STT), and thermal fluctuations [4,65–68]. In 1935, Landau and Lifshitz established a formal framework to describe magnetization dynamics, which was later refined by Gilbert in 1955 with an improved formulation [69,70]. This equation depicts the magnetization's precessional motion around an effective field while accounting for energy dissipation in a manner reminiscent of viscosity.

The first term in the equation signifies a conservative, perpetual motion of the magnetization that never reaches a stable state. The second term accounts for dissipation, which occurs in proportion to the rate of change in magnetization over time [71].

The Spin transfer torque (STT) effect, predicted in 1996 by Slonczewski and Berger [4,5], describes the interaction between a spin-polarized current and local magnetization in a material. This effect is based on the conservation of total angular momentum, where electronic spins and local magnetizations exert reciprocal torques in opposite directions. As we will explore in the following section, this effect is commonly utilized in the trilayer structures mentioned above in the context of GMR and TMR.

The main idea of spin transfer torque theory is that the angular momentum must be conserved. If a spin-polarized electrical current passes through a magnetic layer whose magnetization is non-collinear with the current's polarization, electrons will be polarized in the direction of magnetization. The conservation of angular momentum implies the existence of a torque acting on the magnetic layer, which tends to align the magnetization in the direction of the initial polarization. This torque can be expressed as follows:

$$\tau_{\mathrm{STT}} = -\gamma a_j \mathbf{M} \times (\mathbf{M} \times \mathbf{P}) + \gamma b_j (\mathbf{M} \times \mathbf{P}) \tag{1.20}$$

Here, $\mathbf{M}$ is the magnetization of the magnetic layer, and $\mathbf{P}$ is the spin polarization of the electrons. The terms a_j and b_j are the spin transfer torque and the effective field coupling coefficients induced by the current, respectively. Typically, b_j is weaker than a_j, so the exerted torque tends to align the magnetization with the direction of polarization of the electron. The dynamics of

magnetization under spin-polarized current can be calculated using the Landau-Lifshitz-Gilbert (LLG) equation:

$$\frac{d\mathbf{M}}{dt} = -\gamma\left(\mathbf{M} \times \mu_0 \mathbf{H}_{\text{eff}}\right) + \frac{\alpha}{M_S}\left(\mathbf{M} \times \frac{d\mathbf{M}}{dt}\right) + \tau_{\text{STT}} \tag{1.21}$$

The first term describes the precession of magnetization $\mathbf{M}$ around the effective field $\mathbf{H}_{\text{eff}}$ (comprising the applied field, dipolar field, and magnetic layer's anisotropy field), with γ being the electron's gyromagnetic ratio. The second term phenomenologically represents the damping term (divided by the magnetization saturation M_S) that tends to bring the magnetization back in the direction of the effective field, where α is the Gilbert damping parameter. Depending on the sign of a_j, the term τ_{STT} can oppose or enhance the damping effect (see Fig. 1.18). a_j, being proportional to the current density, leads to a critical current J_C for which the spin transfer torque becomes greater than the damping, allowing the reversal of the magnetization of a material [72].

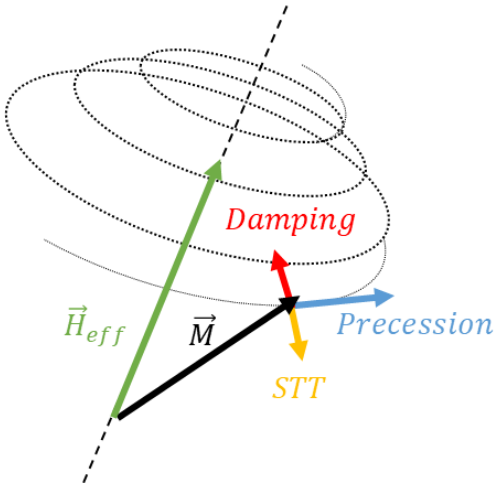

Fig. 1.6: Magnetization dynamics | Trajectories of the magnetization induced by the LLG equation as in 1.21 with the adiabatic term of spin transfer torque.

1.2.4 Magnetoresistive random-access memory (MRAM)

As we mentioned in the introduction chapter, magnetoresistive random-access memory (MRAM) is an innovative and promising technology that has the potential to revolutionize the world of computer memory. MRAM combines the advantages of both traditional volatile and nonvolatile memories, offering a unique set of characteristics that make it a compelling choice for various applications in the field of electronics and computing.

In a computer system's memory, there are billions of bits, each capable of holding either a 0 or a 1, forming the basis of digital data storage. MRAM operates by harnessing magnetoresistance principles to efficiently encode and retrieve data. Instead of relying on the charge stored in capacitors like traditional DRAM, MRAM stores information using magnetic states within individual memory cells.

The core element of MRAM is the magnetic tunnel junction, as discussed in Section 1.2.2. This junction consists of two ferromagnetic layers separated by a thin oxide layer. The relative

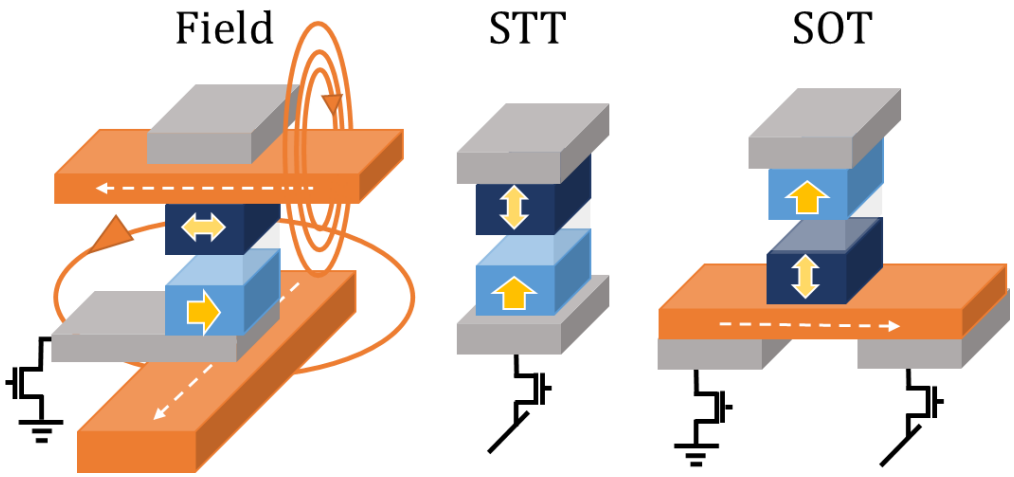

Fig. 1.7: MRAM | Writing mechanisms in MTJ-based devices. From left to right: Oersted field, thermally asistend/ spin transfer torque and, spin–orbit torque. Adapted from [15]

magnetization orientation of these ferromagnetic layers results in two distinct resistance states that represent a single bit of data. To store information (write), it is necessary to control the alignment of these layers, and reading the information involves a straightforward check of the resistance.

Regarding the writing mechanism in MRAM, various approaches have been explored over the years in different MRAM generations, as summarized below:

1. **Stoner Wolfarth MRAM**: In the first generation, each MTJ was placed between two perpendicular current lines (bit and word lines) as shown in Fig. 1.7. The switching mechanism relied on a field-driven effect generated by the current passing through these lines. Synchronized fields from both lines were necessary to switch the MTJ's magnetization. However, this approach had high writing error rates due to dot-to-dot variability and did not reach the market.

2. **Toggle MRAM**: The Toggle MRAM, introduced later, incorporated a synthetic antiferromagnet as the free layer and used a rotating field created by properly designed current pulses to switch the magnetization. This technology was the first to be commercialized, but it required relatively large currents, resulting in high power consumption and limitations in downsize scalability.

3. **Thermally assisted MRAM (TA-MRAM)**: TA MRAM featured a free layer with a high energy barrier in standby mode, reduced during writing by Joule heating generated by an injected current through the MTJ. It offered good power consumption, selectivity, and high retention time but was eventually replaced by current-induced switching MRAM technology.

4. **Spin transfer torque MRAM (STT-MRAM)**: STT-MRAM, the most advanced technology, employs the Spin Transfer Torque effect for writing (as described in Section 1.2.3). It offers low power consumption and high integration density since the same current path is used for both writing and reading, as shown in Fig. 1.7. This technology is now commercially available and has been adopted by major microelectronics companies, including Samsung, Sony, Avalanche Technologies, Everspin Technologies, TSMC, and IBM. These major players have already introduced or released MRAM products using manufacturing nodes of 40 nm, 28 nm, and/or 22 nm. In particular, TSMC was the first to unveil MRAM devices based on the 22 nm node, and subsequently Avalanche Technologies, Everspin Technologies and Samsung are planning to follow suit [73].

5. **Spin orbit torque MRAM (SOT-MRAM)**: A more recent MRAM generation utilizes

spin orbit torque switching, as shown in Fig. 1.7. Although it has a larger cell size due to the integration of a three-terminal device, it offers shorter switching times and higher endurance, making it suitable for L1 or L2 cache applications.

These methods have facilitated the scaling of magnetic devices to sub-nanometer dimensions and large-scale integration with capacities reaching gigabytes.

1.2.5 Performance metrics of MRAM

When evaluating the performance of MRAM memory, it is crucial to consider four key functionalities simultaneously. These functionalities include ensuring **high retention**, **writing speed**, **high readability**, and **low writing energy**.

The ability of memory cells to retain information over time is tied to its thermal stability factor, denoted as Δ. This factor represents the ratio of the activation energy required for state switching to the available thermal energy and is mathematically expressed as:

$$\Delta = \frac{E_b}{k_b T} \tag{1.22}$$

Here, E_b represents the energy barrier needed for transitioning between AP-to-P or P-to-AP states, and k_b is the Boltzmann constant. It is important to emphasize that Δ is determined at operating temperatures. Effective non-volatile operation requires $\Delta > 60$ for a 10-year retention in a 1 Gbit memory chip at room temperature.

Moving forward, **writing speed** is a vital metric that measures how quickly data can be written into the MRAM. Faster writing speeds contribute to improved overall system performance and responsiveness.

Additionally, **high readability** is imperative, indicating the ease with which data can be retrieved from the memory cells. High TMR values ensure enough resistance difference between high and low states, thus avoiding reading errors. A memory technology with high readability ensures swift and reliable access to stored information.

Lastly, **low writing energy** is another critical aspect of MRAM performance. This refers to the amount of energy required to write data into the memory cells. Minimizing the writing energy is essential for energy-efficient operation and overall performance optimization.

Balancing these four functionalities is essential for achieving optimal MRAM performance in various applications. However, the fastest magnetic switching involving spin precession, where an electric current stimulus must persist for at least one-quarter of the precession period, sets lower limits on switching speed and energy consumption.

In fact, according to the principles of angular momentum conservation and the macrospin model, the switching current is related to the switching time (τ or the duration of the current pulse) as follows:

$$I(\tau) = I_{c0}(1 + \frac{t_{c0}}{\tau}) \tag{1.23}$$

where t_{c0} represents the characteristic time scale of switching dynamics, and I_{c0} is the static switching current. The energy required for switching can be calculated using the following formula:

$$U(\tau) = I^2 R\tau = U_{c0}\left(2 + \frac{\tau}{t_{c0}} + \frac{t_{c0}}{\tau}\right) \tag{1.24}$$

where $U_{c0} = I_{c0}^2 R t_{c0}$ is the static switching energy. This expression reveals that the switching energy ($U(\tau)$) exhibits different scaling behaviors with time in fast and slow regimes characterized by the time constant t_{c0}. On significantly longer timescales than t_{c0}, the switching energy increases proportionally with the switching time τ, while on much shorter timescales, it becomes inversely proportional to τ. Fig. 1.8 presents data sourced from Kimel and Li's research [3], which compiles findings from various studies on switching MTJs and spin valves. This graphical representation effectively shows the connection between switching time and energy, highlighting that electrical switching faster than 1 nanosecond results in a high energy cost.

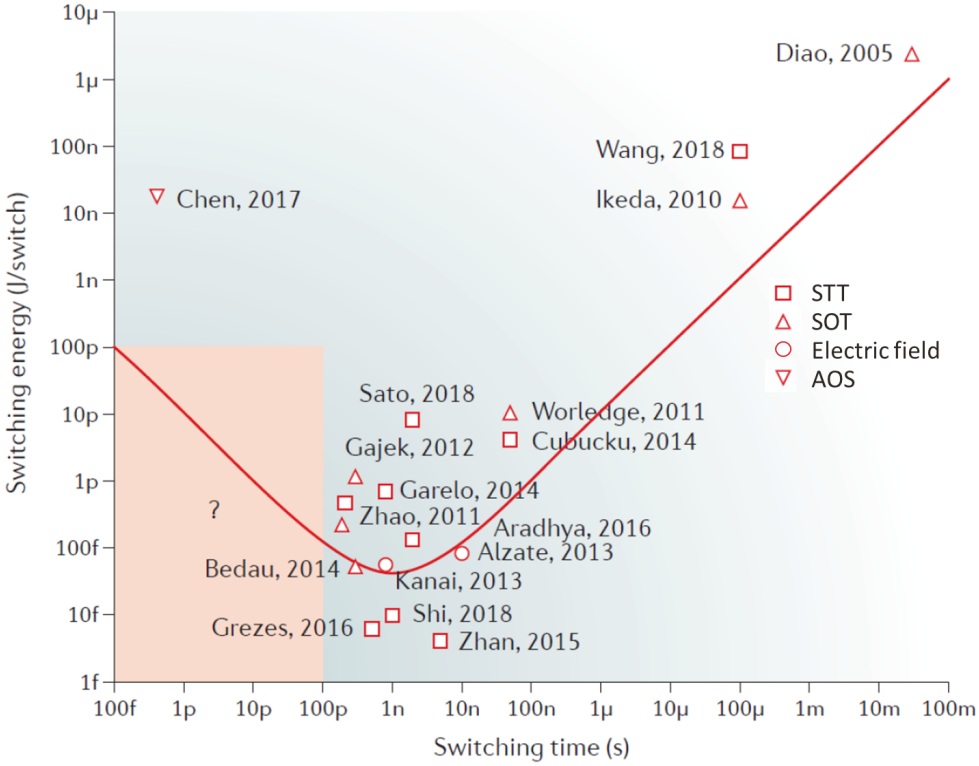

Fig. 1.8: MTJ spin transfer switching energy and time | Summary of switching energy and time of magnetic tunnel junction (MTJ) memory devices and spin valves using mechanisms of spin-torque transfer (squares) [74–77], spin-orbit torque (SOT) (triangles) [78–83], and electric-field-induced switching (circles) [84–86]. The red line the plot of equation (1) with t_{c0} = 1 ns and U_{c0} = 10 fJ. The shaded area indicates the specifications targeted by future technologies. Fig. from [3].

This suggests that to create faster and more energy-efficient memory systems, a fundamental change in the writing mechanism is necessary. An exceptionally promising approach that could help us attain this objective is the concept of all-optical magnetization switching.

1.3 Ultrafast all-optical switching

In 1996, a groundbreaking discovery by Beaurepaire et al. [87] unveiled a remarkable timescale for manipulating magnetic order. The researchers observed the rapid reduction of magnetization in a thin nickel film within picoseconds, achieved through laser pulses lasting only 60 femtoseconds. This extraordinary finding sparked extensive discussions and debates concerning the underlying mechanism responsible for this ultra-fast demagnetization process. It implied the transfer of energy

and momentum to magnetic spins on a timescale significantly shorter than those associated with spin-orbit interaction (1 - 10 picoseconds) or magnetic precession (100 - 1000 picoseconds) [88].

These processes are described by the longitudinal spin dynamics, where the magnitudes of the magnetic moments are not conserved [87]. This ultrafast demagnetization is explained within a phenomenological three-temperature model, wherein laser energy is initially absorbed by electrons, leading to an instantaneous excitation of the electrons within the timescale of the laser pulse. Subsequently, there is an exchange of energy and angular momentum among the electron, phonon, and spin reservoirs, characterized by electron-phonon and spin-lattice relaxation parameters.

Various mechanisms for transferring angular momentum to the surrounding environment have been explored, ranging from phenomenological descriptions [89] to first-principles calculations [90]. These demagnetization rates have been observed to scale inversely with the magnetic moment and are influenced by the spin-lattice coupling [91–93]. In multi-sublattice systems, the demagnetization rate can also be affected by the nature of sublattice exchange [94]. This means that the same magnetic moment can exhibit different demagnetization rates depending on whether it is coupled ferromagnetically or antiferromagnetically to another moment, as confirmed experimentally [93].

Following the initial discovery of subpicosecond demagnetization in nickel, researchers observed similar ultrafast demagnetization phenomena in various other systems. However, it wasn't until 2007 that scientists made a significant observation in the ferrimagnetic multi-sublattice Rare Earth Transition Metal (RE-TM) alloy GdFeCo [16]. They achieved a remarkable outcome: the complete reversal of magnetization and its stable maintenance in the opposite magnetic orientation using a single 40 fs circularly polarized laser pulse.

The laser pulse rapidly excited the electrons into highly non-equilibrium states within a few hundred femtoseconds. Interestingly, it seemed that the helicity of light played a pivotal role in determining the subsequent magnetization direction, leading to all-Optical Switching (AOS). At the time, there was a prevailing belief that circular polarization of light was crucial for achieving AOS because it disrupted time-reversal symmetry due to the inverse Faraday effect.

However, a surprising revelation challenged this previously held belief: All-Optical Switching in GdFeCo was achieved using a linearly polarized femtosecond laser pulse [17]. To decipher this AOS phenomenon, researchers delved into the ultrafast dynamics of individual magnetic sublattices, namely Gd and Fe, using the element-specific technique of X-ray magnetic circular dichroism.

Initially, when pumped with a linearly polarized 60 fs laser pulse, GdFeCo experienced rapid excitation, resulting in swift but distinct decreases in magnetizations for both sublattices. Fe magnetization collapsed within a mere 0.2 ps, while the Gd demagnetization process extended to approximately 1.5 ps (as illustrated in Fig. 1.9). This noticeable discrepancy in demagnetization timescales between the two sublattices could be attributed to the fact that the Gd moment, primarily contributed by 4f spins, is roughly four times larger than that of Fe.

Subsequently, as the electronic environment cooled down, the antiferromagnetic exchange interaction between the two sublattices became influential. This led to the continued gradual demagnetization of Gd, accompanied by the growth of the Fe moment in the opposite direction, thereby conserving the total angular momentum. This gave rise to a transient state resembling ferromagnetism, characterized by parallel Fe and Gd magnetizations, occurring between 0.2 ps and 1.5 ps after the initial excitation.

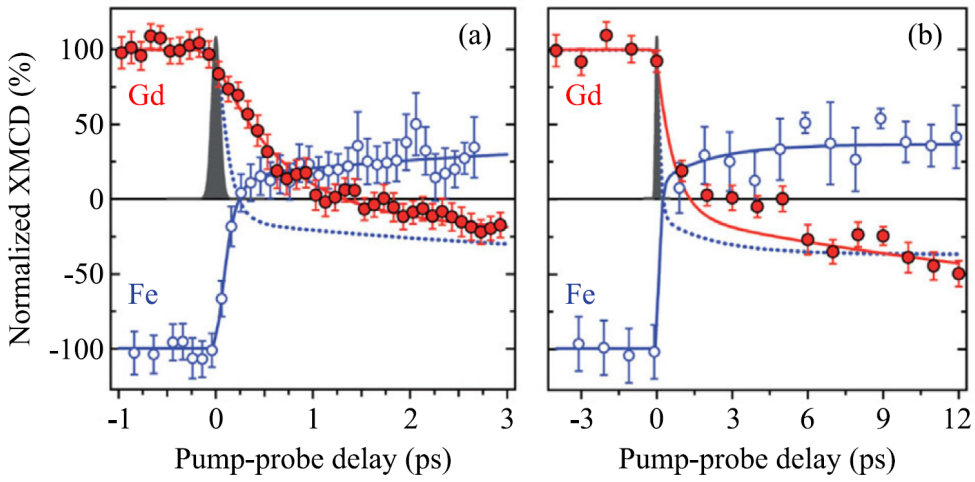

Fig. 1.9: All-Optical Magnetization Switching of GdFeCo Using Linearly Polarized Light – This figure displays the transient evolution of magnetic moments in Fe and Gd for the first 3 picoseconds (a) and over a 12 picosecond timeframe (b). We investigated the element-specific behavior of Fe (depicted as open circles) and Gd (depicted as filled circles) magnetic moments in GdFeCo when subjected to a femtosecond laser pulse with linear polarization. These measurements were conducted using time-resolved X-ray magnetic circular dichroism (XMCD), and the error bars indicate the statistical standard error. The figure is reproduced from [17].

Ultimately, following the complete demagnetization of the Gd sublattice in the presence of a finite reversed Fe magnetization, the antiferromagnetic exchange interaction prompted the Gd sublattice to align antiparallel to the Fe magnetization over a longer timescale. This completed the All-Optical Switching of GdFeCo using a linearly polarized laser pulse, a phenomenon known as helicity-independent all-optical switching (HI-AOS) or light-induced toggle-switching. This discovery underscores the pivotal role that distinct sublattices play in the achievement of AOS with linearly polarized light. It should be noted that the described AOS mechanism is not applicable to antiferromagnetic materials composed of identical magnetic atoms [95]. Also, keep in mind that a laser pulse primarily excites TM 3d and RE 5d spins, not RE 4f spins, and the ultrafast demagnetization of TM 3d spins is transferred to RE 4f spins through the intermediary RE 5d spins. This contributes to the relatively slower demagnetization of RE 4f moments. Moreover, the antiferromagnetic alignment between RE 5d and TM 3d spins at the Fermi level allows non-equilibrium conduction electron spins to move through an effective antiferromagnetic order, characterized by exchange fields with varying magnitudes and alternating signs on an atomic scale [95].

Therefore, ultrafast laser-induced heating of electrons in GdFeCo is capable of initiating magnetization reversal without the need for internal or external magnetic fields. In this mechanism, the helicity-dependent nature of the switching seen in the previously mentioned experiment may also be attributed to the reliance of laser-induced heating on optical absorption. Due to magnetic circular dichroism (MCD), the absorption of circularly polarized light is contingent upon the polarization helicity and the magnetization polarity. This helicity-dependent absorption, known as dichroism, results in helicity-dependent laser heating and consequently leads to helicity-dependent all-optical switching (HD-AOS). To comprehend the contributions of the inverse Faraday effect and MCD to AOS in GdFeCo, investigations into the spectral dependence of the efficiency of laser-induced magnetization reversal needed to be compared with the spectra of the inverse Faraday effect and MCD.

Initial attempts at these studies did not confirm or refute these two mechanisms due to the presence of large error bars in the measurements [96]. These significant error bars might have originated from the fact that the switching was not performed with a single pulse, but rather with multiple pulses. Subsequent spectral studies [97] of the probability of magnetic switching in GdFeCo induced by a single femtosecond laser pulse demonstrated that the switching probability correlates with MCD, and the helicity dependence is a result of laser-induced heating dependent on the helicity [3].

Although HD-AOS will be preferred for recording application, for many materials the switching occurs only after a large number of pulses, thus slowing down the process.

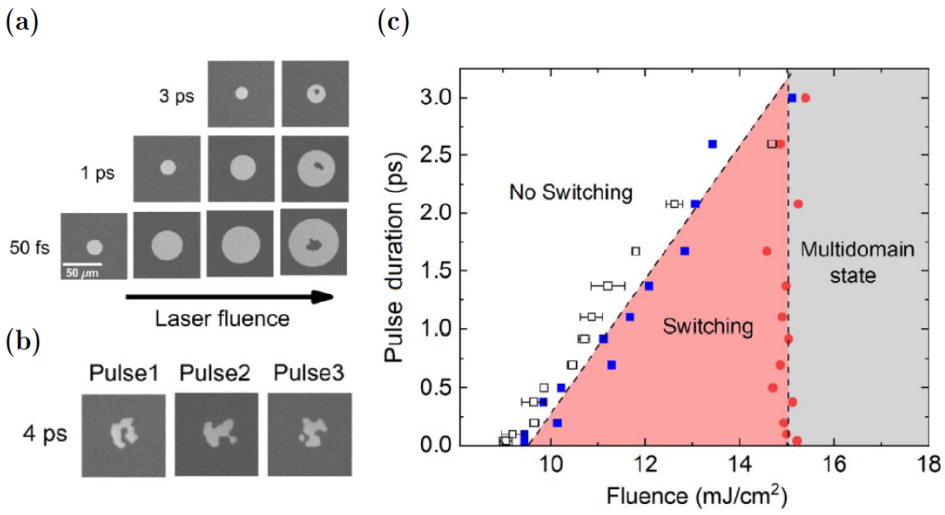

Fig. 1.10: Magneto-optical images and all-optical helicity-independent switching state diagram for a 20-nm $Gd_{24}(FeCo)_{76}$ film. MOKE images after exposure to a single linearly polarized laser pulse with pulse durations of 50 fs, 1 ps, 3 ps (a) and 4 ps (b) at various fluences. (c) HI-AOS state diagram showing the switching fluence (F_{switch}) and multidomain fluence (F_{multi}) as a function of pulse duration. Fig. from [98]

On the other hand, HI-AOS requires one single laser shot making it much more energy efficient and fast. Extensive research has been done on Gd-based systems to fully understand the nature of this reversal. Wei et al. studied the state diagram for GdFeCo, which plots the HI-AOS laser threshold fluences against its pulse duration. It is shown in Fig. 1.10, single-shot switching was observed for short pulse durations, but the fluence range decreases as the pulse duration increases. This maximum pulse duration for single switching is approximately 3 ps for the GdFeCo alloy.

In 2020, Banerjee and colleagues (Banerjee et al. [99]) achieved single-shot toggle switching in Mn_2Ru_xGa half-metallic ferrimagnetic Heusler alloys of Mn $_2$ Ru $_x$ Ga. This achievement marked a significant advance by overcoming the previous limitation of achieving single-pulse reversal exclusively within Gd-based materials. This limitation had persisted for more than a decade since the initial observation of HI-AOS.

High-density data storage applications encounter significant challenges when utilizing materials from the TM-Gd system. These challenges arise primarily due to the low perpendicular magnetic anisotropy (PMA) of both the Gd and the transition metal (TM) systems, which is essential for stabilizing relatively small data storage domains.

In the quest for materials with enhanced magnetic anisotropy, there has been considerable in-

terest in compounds containing the rare-earth (RE) element terbium (Tb). However, achieving complete magnetization reversal with a single laser pulse in TbCo alloy has been challenging because of the significant spin-orbit coupling in Tb. Although this increased anisotropy is beneficial for increasing storage density capacity, it has been observed that it leads to a considerably faster demagnetization of the $4f$ orbitals compared to that of Gd. Frietsch et al. explained this phenomenon by highlighting the transfer of angular momentum from the $4f$ moments to the magnon and phonon systems, which is only feasible in the presence of spin–orbit coupling [100].

During approximately the same timeframe as Banerjee, Avilés-Félix et al. also documented Gd-free single-shot switching. They accomplished this using femtosecond and picosecond laser pulses, particularly in systems based on Tb/Co multilayers [20,21]. The utilization of a multilayer structure produced encouraging outcomes in achieving efficient switching, which was somewhat unexpected.

The majority of this thesis is a continuation of this research, with the primary objective of uncovering the components, behaviors, and mechanisms involved in switching within multilayer structures. We focus specifically on the phenomenon known as "single-shot helicity-independent all-optical switching" (HI-AOS).

1.4 Opto-spintronics state-of-the-art

Although ongoing exploration of novel materials for AOS persists together with discussions on the details of each mechanism, it is evident that the application of ultra-short light pulses to manipulate magnetism has demonstrated its effectiveness in a range of magnetic materials [101].

AOS presents promising prospects for magnetic devices that can be controlled through light, thereby bridging the gap between photonics and spintronics.

The initial efforts to integrate AOS materials into spintronic devices took advantage of electrical readout via the anomalous Hall effect. This was demonstrated during optical switching in a GdFeCo film patterned with Hall cross structure [102]. Here, a near-infrared pulse lasting 200 fs effectively switched the magnetization of the junction area, resulting in a subsequent reduction of the Hall resistance after each pulse. Similar accomplishments were achieved in ferromagnetic Pt/Co/Pt heterostructures [103], showcasing HD-AOS with multiple pulses.

The logical application of AOS in the realm of spintronics involves its utilization as a writing mechanism in magnetic random access memory. Replacing the free layer in a conventional MTJ with a layer of AOS material enables switching of the MTJ using light.

However, as mentioned in the introduction, Chen et al. [104] performed the first successful demonstration of the functionality of AOS in a micrometer-sized p-MTJ cell using a storage layer of a GdFeCo alloy, showing only a modest TMR ratio of 0.6%.

Subsequent advances by Wang et al. [105] enabled switching in Co/Gd bilayer tunnel junctions with cell sizes as small as 3 μm, achieving an improved TMR ratio of 34.7%. This progress was made possible through a clever design pioneered by Avilés-Félix et al. [20,21], involving the magnetic coupling of an optically switchable material to the FeCoB interface of the storage layer.

Initial reports on a storage layer based on [Tb/Co]N multilayers coupled to FeCoB showcased the ability to manipulate the Co/Tb composition for controlling the effective perpendicular anisotropy of magnetic tunnel junctions. Even after annealing at 250°C to achieve a 38% TMR ratio after

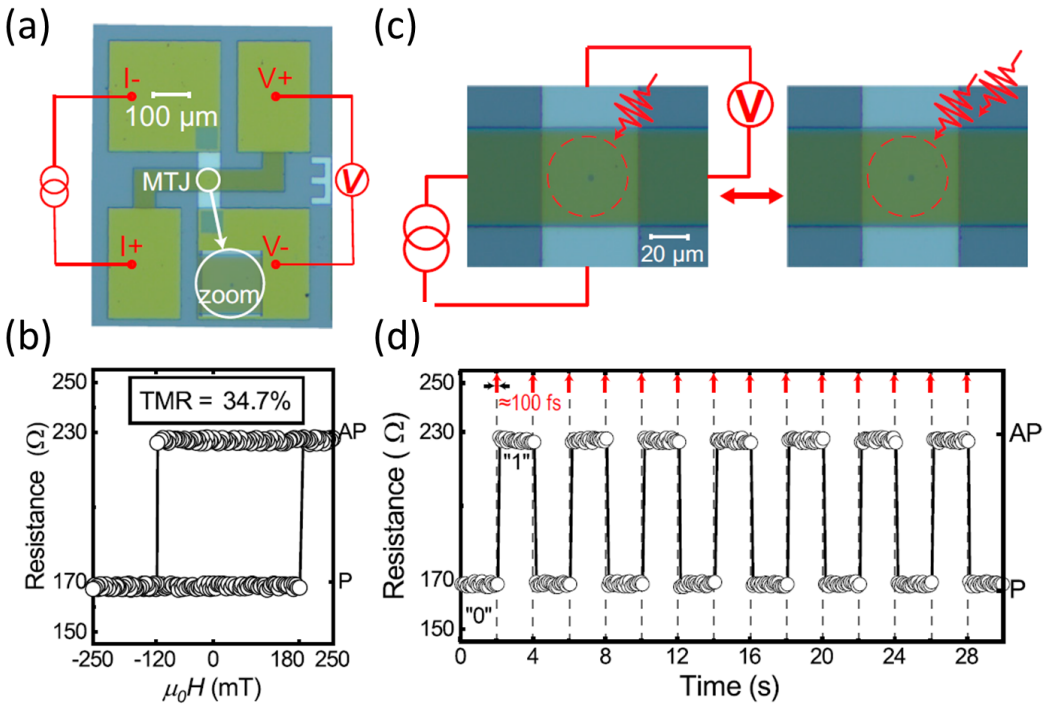

Fig. 1.11: Wang et al. results from [105]: All-Optical "Writing" and Electrical TMR Readout of a 3 μ m MTJ. (a) Microscope image of the device fabricated with a 100-nm thick transparent ITO top electrode, as well as four electrode pads to perform four-point TMR detection. (Inset) Zoom-in of the pillar. (b) R-H magnetoresistance loop measured by sweeping an out-of-plane magnetic field, showing a typical TMR ratio of 34.7%. (c) Schematic overview of the "writing" of an AOS device. A small current is applied through the device, while the resulting TMR voltage is measured in real time. The pillar is excited by a train of linearly polarized laser pulses. (d) Typical TMR measurement as a function of time upon laser-pulse excitation. The resistance toggles between P and AP state upon every laser pulse excitation. No external field was applied during the measurements.

patterning, the perpendicular anisotropy remained stable. Thin film experiments employing the same storage layer stacks confirmed HI-AOS using both 60 fs and 5 ps laser pulses, even at incident fluences as low as 3.5 mJ/cm^2. However, reliable field-free AOS demonstrations on patterned devices and a comprehensive understanding of the switching mechanism within this system are still forthcoming.

After examining the advancements in all-optical switching MTJ devices, it is crucial to shift our focus towards a broader perspective, highlighting the pivotal role played by the integration of hybrid photonic-spintronics for an ultimate memory solution.

Integrated photonic platforms, such as silicon-on-insulator (SOI) [106,107] and indium phosphide (InP) membrane on silicon (IMOS) [108,109], have made significant progress in high-bandwidth and energy-efficient data transmission.

In terms of directing light onto spintronic devices, Becker et al. [110] proposed a two-dimensional grating coupler to project light pulses vertically into all-optical switchable MTJs [111]. However, the requirement for interwafer integration presents additional challenges.

For multiplexing, Kimel and Li [3] introduced an integration scheme with AOS switchable MTJs by using cross-coupled photonic waveguides, as illustrated in Fig. 1.12. This setup allows for random access by employing optical waveguides and transistor selector circuits to address specific

elements. In a time-domain multiplexing configuration, precise control over pulse timing ensures the synchronization required for AOS switching. Alternatively, in a wavelength multiplexing approach, word and bit lines are selected based on their optical wavelength, similar to wavelength-division multiplexing (WDM) systems in communication.

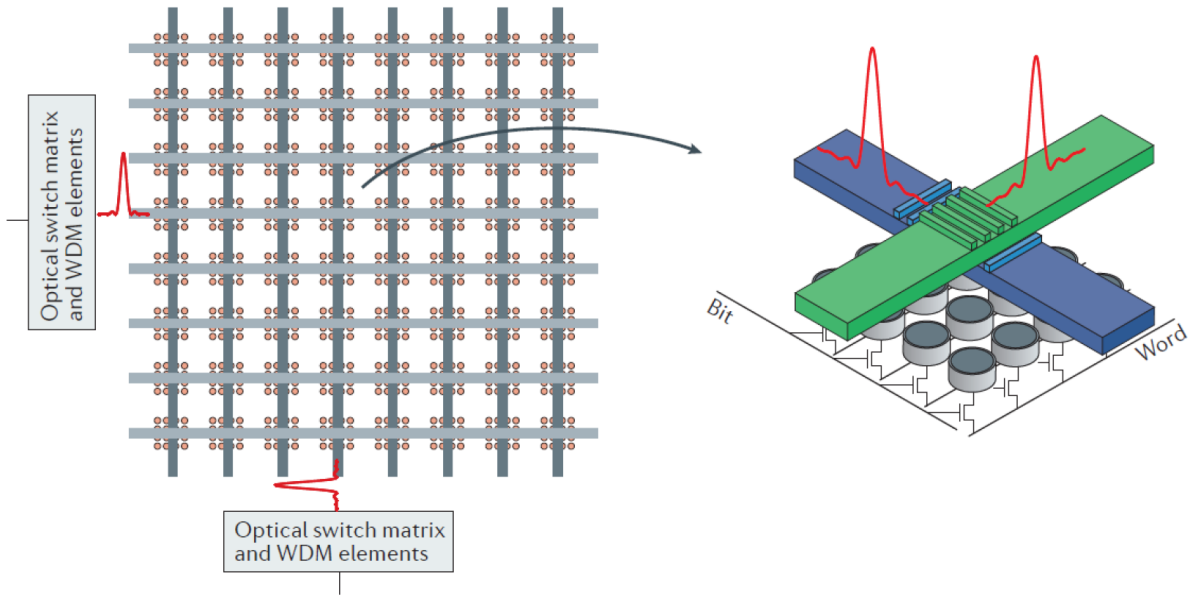

Fig. 1.12: Schematics from [3] of large-scale integration of AOS devices in an array for high-speed memory application. Random access can be achieved with a fabric of optical waveguides and transistor selector circuits to address each individual element. The coincidence of two optical pulses in the two waveguides provides enough energy to switch the AOS device at the junction. In the time-domain multiplexing scheme, the arrival time of the pulse sequence in the word and bit lines can be controlled with a tunable delay line so that two pulses arrive coincidentally only at the AOS device to be switched. In the wavelength multiplexing scheme, the word and bit lines can be selected by the optical wavelength in the same way as wavelength-division multiplexing (WDM) communication.

However, directly coupling light energy to spintronic devices suffers from inefficient interaction due to the substantial size mismatch between waveguide modes and the size of spintronic devices [1], resulting from the diffraction limit. This issue not only compromises the energy efficiency of AOS, but also poses scalability challenges for hybrid integration. Furthermore, the substantial transient power needed for AOS can introduce additional losses in the waveguide due to non-linear absorption [111].

Hence, a photonic design capable of focusing light beyond the diffraction limit while ensuring efficient energy transfer becomes imperative.

Recently, Pezeshki and colleagues have designed an integrated hybrid plasmonic-photonic device for AOS and all-optical reading of nanoscale ferrimagnet bits with perpendicular magnetic anisotropy (PMA) on an IMOS platform. They proposed a hybrid plasmonic nanoantenna (PNA) and photonic crystal (PhC) cavity to address the aforementioned challenges [112].

The requirement for femtosecond laser excitation poses a hurdle in practical applications. Implementing ultrafast magnetism principles with pulses of 10 ps or longer is more feasible, as these pulses can be generated using less sophisticated lasers, and advanced electronics can produce sub-100 ps

electric current pulses.

In conclusion, the fusion of all-optical switching with spintronics has opened exciting possibilities for the development of advanced magnetic devices controlled by ultrashort light pulses. Recent achievements in AOS materials, particularly in magnetic tunnel junctions, have demonstrated the potential to revolutionize memory solutions. However, challenges persist, such as the integration of photonic and spintronic platforms. Furthermore, advancements in hybrid photonic-spintronic devices and integrated photonic platforms offering high-bandwidth, energy-efficient data transmission and innovative multiplexing techniques, overcoming limitations, such as size mismatches and efficiency concerns, are crucial for the practical implementation of these technologies. As the field continues to evolve, the merging of photonics and spintronics holds great potential for the development of next-generation memory solutions with unprecedented capabilities.

1.5 Conclusion

In this chapter, an introduction magnetism unfolded, traversing through the historical backdrop and evolution of our understanding of magnetism from its early discoveries to its contemporary quantum description.

Within this realm, a spotlight was cast upon ferrimagnets, particularly the rare-earth transition-metal (RE-TM) systems, showcasing their significance and the complexities they introduce to this study.

Transitioning to the realm of spintronics, several pivotal concepts were presented. The discussion of spin-dependent transport phenomena, shedding light on how spin influences the behavior of electrons, where the tunnel magnetoresistance ratio (TMR) emerged as a crucial metric phenomenon.

Further exploration centered around magnetization dynamics, reporting the processes governing the behavior of magnetization in time. Magnetoresistive random-access memory (MRAM) emerged as a pivotal technology, offering promising prospects for data storage and processing.

The field of magnetoresistive random-access memory has witnessed significant advancements in recent years, with various generations of MRAM technologies offering unique features and benefits. Spin transfer torque MRAM (STT-MRAM) and spin orbit torque MRAM (SOT-MRAM) have emerged as leading contenders in the MRAM landscape, offering low power consumption, high integration density, and potential for applications in various electronic and computing devices.

One of the key challenges in MRAM technology has been optimizing the writing mechanism to achieve faster and more energy-efficient memory systems. The traditional methods of magnetic switching in MRAM, such as the spin transfer torque effect, have limitations in terms of speed and energy consumption, especially when trying to achieve sub-nanosecond switching.

The concept of all-optical magnetization switching, as demonstrated in groundbreaking research, provides a promising avenue to overcome these limitations. Ultrafast AOS has been shown to enable rapid magnetization reversal without the need for external magnetic fields. This approach has the potential to revolutionize MRAM technology by offering faster switching speeds and greater energy efficiency.

Recent studies have explored the mechanisms and materials involved in AOS, and researchers

have achieved single-shot AOS in various materials, including GdFeCo alloys and Tb/Co multilayers. These advances have paved the way for the integration of AOS into MRAM devices, offering the potential for high-speed and low-power memory solutions.

Moreover, the integration of AOS with photonic and spintronic platforms has opened up new possibilities for data storage and processing. By combining AOS with advanced photonic and spintronic technologies, the aim is to create memory solutions that provide fast and efficient data storage. This integration holds great promise for next-generation memory devices and computing systems.

In conclusion, MRAM continues to evolve, and the emergence of all-optical magnetization switching represents a significant breakthrough in the quest for faster, more energy-efficient memory solutions. As the field advances, the integration of AOS with photonic and spintronic platforms will play a crucial role in shaping the future of memory technology, offering unprecedented capabilities and performance for a wide range of applications in the field of electronics and computing.

Chapter 2

Experimental techniques

Contents

2.1 Introduction

In this chapter, I present the experimental techniques central to our research, both for the growth of the layers and their magnetic characterisation. These methods are essential for understanding the magnetic properties and dynamics of the materials under investigation. Magnetron sputtering is employed for precise material deposition, which offers control over film thickness and composition. MOKE serves as a powerful tool for exploring magnetization in thin films, allowing us to characterize in-plane and out-of-plane magnetization properties. Furthermore, TR-MOKE, a cutting-edge approach, leverages ultrafast laser technology to investigate rapid and transient magnetization dynamics, enabling the study of dynamic processes and material responses to external stimuli. In the forthcoming chapters, I will unveil the results and insights derived from the application of these techniques, shedding light on the magnetic characteristics and behaviors of our system.

2.2 Magnetron sputtering

In the studies carried out during my project, all materials were deposited using a technique known as magnetron sputtering on wafers with a diameter of 100 mm by Stéphane Auffret. The substrates were made of either thermally oxidized silicon or glass. Magnetron sputtering is a widely adopted Physical Vapor Deposition (PVD) technique both in industry and research due to its high deposition rates, efficiency, and relatively good material quality [113]. The process is based on ion bombardment of the target material to be deposited. A brief description of the process is given in the following section.

2.2.1 Sputtering process

The sputtering machine used is an Actémium tool, the process begins by injecting argon gas into the chamber at 2×10^{-3} mbar, which is then ionized and accelerated towards the target by a direct current discharge between the cathode and the anode, creating a localized plasma near the target, as one can see in Fig. 2.1(a) . The accelerated Ar^+ ions collide with the target surface atoms, causing the removal and vaporization of the target material. This vapor then condenses as a thin film on the substrate. The deposition rate of the target material depends mainly on the plasma density and the energy of the Ar^+ ions.

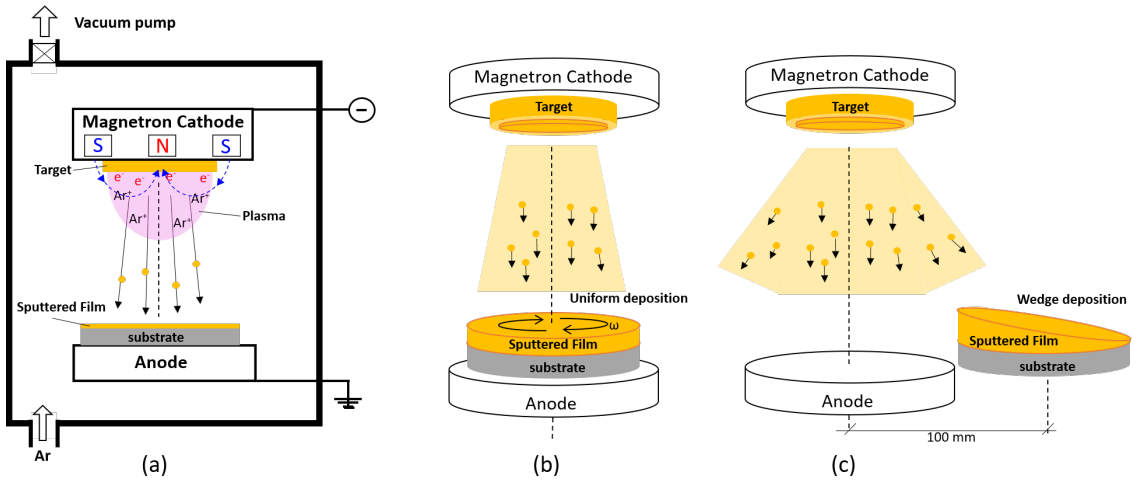

Fig. 2.1: (a) Schematic of the magnetron sputtering process with two different possible geometries : (b) on-axis deposition and (c) off-axis deposition, respectively.

A key characteristic of this technique is the use of a magnetic field parallel to the target surface, which confines the generated secondary electrons and enhances the probability of Ar ionization. As a result, highly dense plasma is created near the target surface, leading to increased target sputtering efficiency and deposition rate. To achieve this, a low chamber pressure (10^{-9} mbar) is essential before initiating the sputtering process to stabilize the Ar plasma, maximize the target sputtering process, and prevent the introduction of impurities during the growth of materials. Our magnetron sputtering system is made up of three main components: a load lock, a main deposition chamber that contains 12 different target materials, and an auxiliary chamber designed to carry out natural oxidation treatments and surface etchings [114,115]. For the MgO barrier formation, natural oxidation of metallic Mg is employed in the treatment chamber, and the magnetic stack

grows without breaking the vacuum to maintain interface properties.

2.2.2 Deposition geometries

Two geometries are available: on-axis deposition (Fig. 2.1(b)) and off-axis deposition (Fig. 2.1(c)). On-axis deposition involves rotating the substrate at 600°/s, resulting in uniform material thickness deposition, although inherent inhomogeneity between the center and edges due to the gradual reduction of the deposition rate with distance from the target will be present. Off-axis deposition induces a thickness gradient across the wafer along a specific axis direction. This effect is achieved by depositing the material without rotation and offset the substrate center by 100 mm from the target center. The ability to deposit these wedge samples is of utmost importance, as it significantly accelerates material optimization. In fact, the resulting thickness gradient facilitates the investigation of thickness-dependent properties using a reduced number of depositions.

In my research, I consistently employed double wedge samples, featuring layers with thickness gradients oriented perpendicularly. The fine adjustment of sample thickness, whether with single wedge or double wedge, proved to be crucial allowing to effectively identify the thickness region of interest. This approach accelerated the optimization of stack composition for the magnetic tunnel junctions.

2.3 Vibrating sample magnetometer (VSM)

The Vibrating sample magnetometer (VSM) serves as a crucial instrument within the spintronic community, leveraging Faraday's law as its fundamental operating principle. Faraday's law dictates that a change in magnetic flux within a circuit induces an electromotive force. The basic principle of a Vibrating Sample Magnetometer involves suspending a sample in a magnetic field and subjecting it to small amplitude vibrations. As the sample vibrates, its magnetic response is measured. By varying the magnetic field strength and direction, it is possible to gather information about the sample's magnetic properties, such as magnetization, coercivity, and susceptibility.

More precisely, the magnetized sample is situated in a constant magnetic field and subjected to vibrational motion along the z-axis at a constant frequency (see Fig. 2.2). The resultant flux variation generates a voltage in adjacent pick-up coils, which is quantified using a lock-in circuit with the vibrating frequency as a reference. Magnetic hysteresis loops are obtained by sweeping the magnetic field.

The MicroSense® VSM utilized for the measurements detailed in this manuscript has a sensitivity of 10^{-6} emu and a maximum applied field of 2 T. This technique facilitates precise determination of magnetic parameters, including saturation magnetization, anisotropy field, and coercive field. The flexibility to rotate the sample holder at various angles relative to the field direction enables the acquisition of hysteresis loops in different planes, such as out-of-plane, in-plane, and at intermediate polar and azimuthal angles.

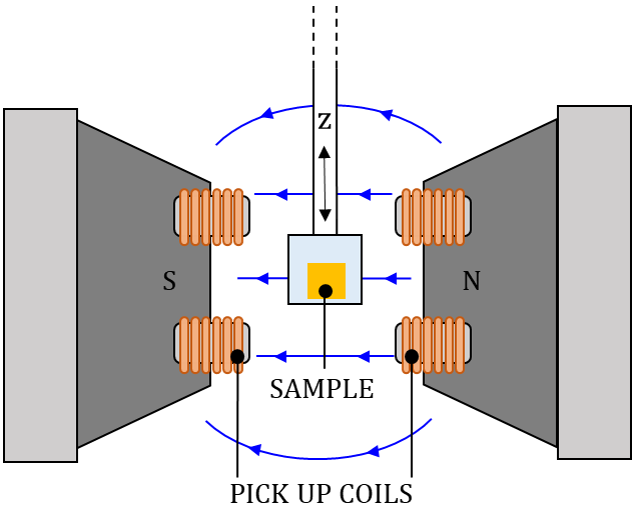

Fig. 2.2: Schematic of vibrating sample magnetometer tool | Diagram illustrating the configuration of a vibrating sample magnetometer tool.

2.4 Magneto-optic Kerr effect

In this section a description of the magneto-optic Kerr effect (MOKE) is given as both MOKE magnetometry and MOKE microscopy are key experiments of this thesis. The Kerr effect refers to the phenomenon in which the plane of polarization of incoming light changes when it reflects from a magnetically active material [116].

The rotation and ellipticity are linearly proportional to the strength of the applied magnetic field or the magnetization of the medium. These effects allow to monitor changes in magnetization in the studied sample. The microscopic description of magneto-optics involves the splitting of degeneracy between multiple spin states due to the spin-orbit interaction and exchange interaction, resulting in different transition strengths for left and right circularly polarized photons.

Based on the orientation of the magnetization vector relative to the sample surface and the plane of incidence of the light beam, three types of MOKE are observed: longitudinal, polar, and transverse MOKE. Each configuration yields distinct changes in the polarization state of light. For longitudinal and polar MOKE, the light wave vector has a non-zero projection along the magnetization direction, while the transverse Kerr effect results in a change of the reflected intensity.

In this thesis, we utilize the longitudinal and polar configurations to characterize the in-plane and out-of-plane magnetization of our samples, respectively. For an in-depth exploration of this phenomenon, a comprehensive study can be found in [117].

2.4.1 MOKE magnetometry

The MOKE magnetometry setup I used is NanoMOKE3®from Durham Magneto Optics. Its primary function is to measure hysteresis loops of the sample, providing crucial insights into magnetization behaviour, see Fig. 2.3(c).

One of the key advantages of this setup is its automation capability. By incorporating precise automated controls, the setup can systematically move the sample with finite steps of just a few millimeters in both the x and y directions. This automated scanning feature allows for efficient

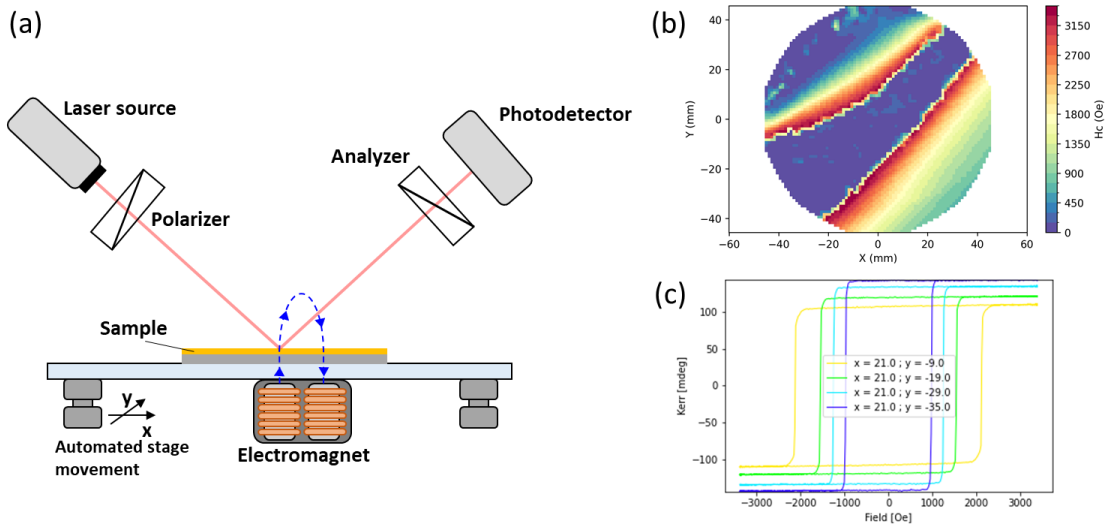

Fig. 2.3: (a) Schematics of the experimental setup of a magneto-optic Kerr effect magnetometer, including laser source, polarizers, and magnetic field generators. (b) Coercivity mapping of 100 mm wafer.(c) Kerr signal vs. applied field hysteresis loops recorded for several positions: x=21 mm and y=(-9, -19, -29, -35) mm of the map shown in (b).

mapping of the entire wafer surface. When combined with the use of wedge-deposited samples, it facilitates and accelerates the study of magnetic properties across a wide range of thicknesses.

The MOKE measurement process, depicted in Fig. 2.3(a), involves a linearly polarized light beam from a laser directed onto the magnetic sample. Upon reflection, the polarization of the light undergoes changes dependent on the magnetic properties of the material. Notably, the Kerr rotation angle (θ_K) and Kerr ellipticity (ϵ_K), as mentioned above, are linearly proportional to the magnetization.

The laser used has a wavelength of 660 nm and spot size of approximately 300 μm. The MOKE tool used in this setup has a maximum applied field limitation of 4000 Oe. Consequently, conducting measurements may encounter challenges with certain material thicknesses where reversal fields diverge, such as the central region of Fig. 2.3(b) in the MOKE setup. In this region, the apparent coercivity appear to be 0 Oe, but it is, in fact, immeasurable due to the experimental limitations. A detailed discussion on this matter is presented in Chapter 3.

Overall, MOKE magnetometry is a powerful tool that provides valuable insights into the magnetic properties of materials, enabling us to investigate magnetization behaviour efficiently.

2.4.2 MOKE microscopy with femtosecond laser pulse irradiation

The following setup is based in Nancy at the Institute Jean Lamour, thanks to our collaboration within the UltraFast Opto-magneto-spintronics (UFO) project we were able to conduct all-optical switching experiments on our samples. Below you will find a synthetic description of the setup and methods adopted, more in depth information can be found in [118].

Using MOKE microscopy, it was possible to study whether a magnetic layer undergoes magnetization reversal during single pulse irradiation and determine the threshold fluence for this process. The setup configuration is illustrated in Fig. 2.4.

The process involves sending a single pulse through a pulse picker, half wave-plate, and polariser

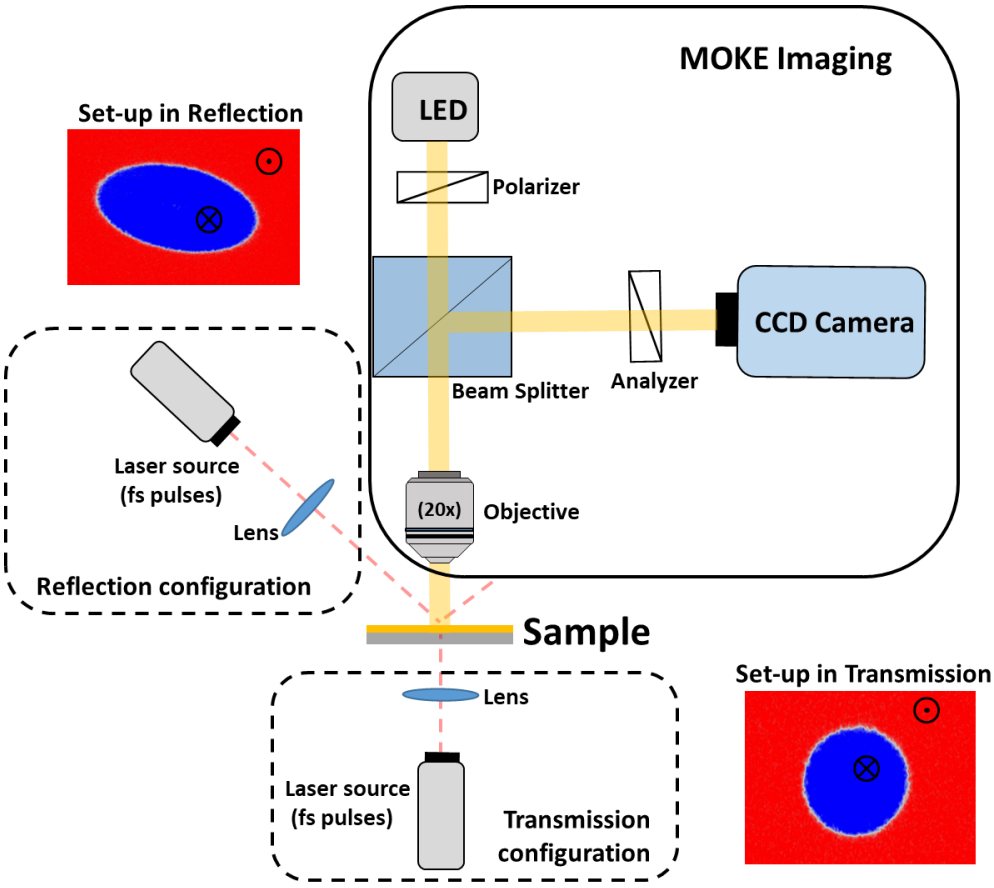

Fig. 2.4: MOKE microscopy setup with single femtosecond laser pulse irradiation.

to control the laser pulse fluence. The pulse is then focused on the sample using a lens, and microscopy imaging is performed on the other side of the sample using a light-emitting diode (LED) with a center wavelength around 628 nm. A Ti:sapphire femtosecond-laser source and regenerative amplifier were used for the pump laser beam in AOS measurement. The wavelength and repetition rate of the femtosecond laser are 800 nm and 5 kHz, respectively.

A collector (Fresnel lens) collects the light and sends it through a field diaphragm before collimating it with a lens. The collimated light is then linearly polarized by another polarizer and directed to the microscope objective with a beam splitter and lens. After reflecting off the magnetic sample, the light acquires Kerr rotation and ellipticity, which is then analyzed by passing it back through the objective and lens. To prevent laser light from reaching the Charge-Coupled Device (CCD), a filter is used, and an analyzer is placed before the filter to complete the MOKE measurement. The crossed polarizer and analyzer ensure that only the light that has undergone Kerr rotation reaches the CCD.

By computing the difference in light intensity for two opposite magnetizations at a specific pixel of the microscope image, we obtain a signal proportional to the sample's magnetization. Raw images obtained from the setup reveal valuable information about magnetization behavior under various conditions, such as applying an external magnetic field with a permanent magnet or after sending femtosecond laser pulses on specific materials.

The acquired microscope images undergo background subtraction to remove non-magnetic contributions, and image analysis is carried out using open-source software like ImageJ; see Fig. 2.5.

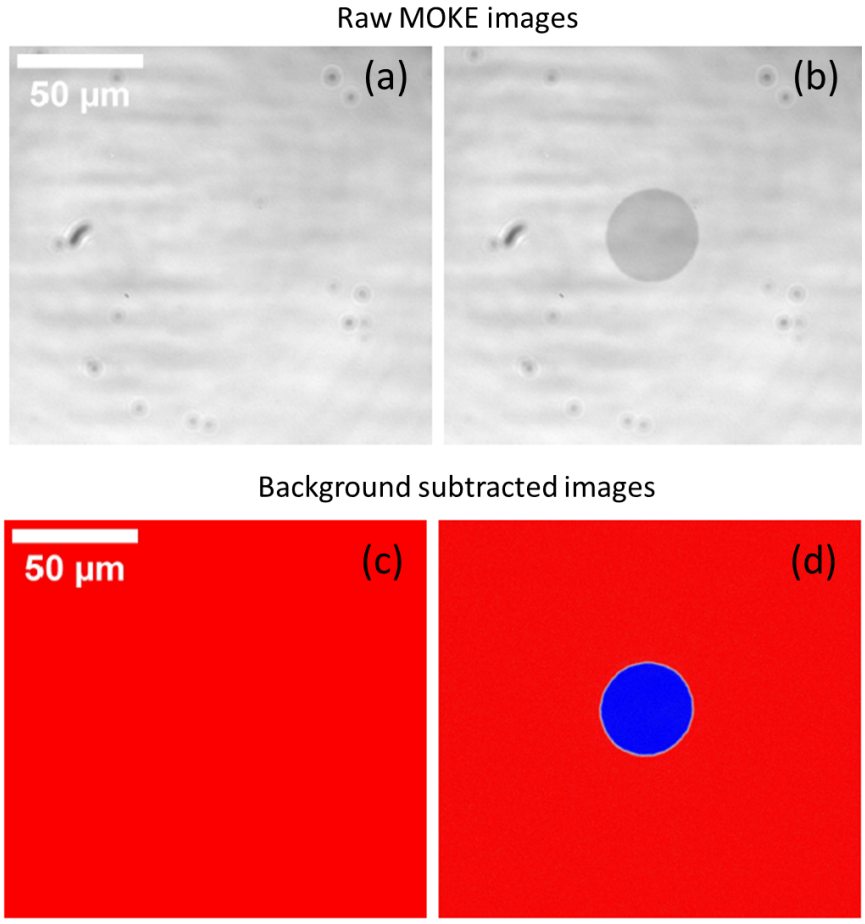

Fig. 2.5: (a-b): Raw images and (c-d): subtracted images observed by MOKE microscopy. The images are recorded after being saturated by a magnetic field (a) and thus (c), after sending the first (b) and thus (d) laser pulse reversing domain, dark gray and blue spot respectively.

Depending on the material's characteristics and external stimuli, the observed magnetic domains can exhibit various shapes and sizes, ranging from ring structures to multidomain states. Additionally, as one can see in Fig. 2.4, depending on the configuration of the setup, reflection or transmission, the blue on red processed reversal spot images will be either elliptical or circular, respectively. In the reflection configuration, utilized with silicon substrates, the images are more elliptical, while in the transmission configuration, used for glass substrates, they appear circular.

In summary, the MOKE microscopy setup with single pulse irradiation provides valuable insights into the magnetization behavior of materials, revealing threshold fluences and domain patterns during magnetization reversal processes.

2.4.3 Laser spot size determination

The Gaussian beam size was assessed through two different approaches: one involved direct observation of the beam at the focal plane of the microscope's imaging lens, and the other utilized a fitting method that correlated domain size with pulse energy.

When examining samples grown on glass substrates, it is possible to use the transmission configuration (see Fig. 2.4), in this case both of these methods yielded consistent results for determining the beam size.

For samples grown on silicon substrates, the reflection configuration (see Fig. 2.4) must be used. In this scenario, the beam size was exclusively determined by fitting the domain size to the pulse energy.

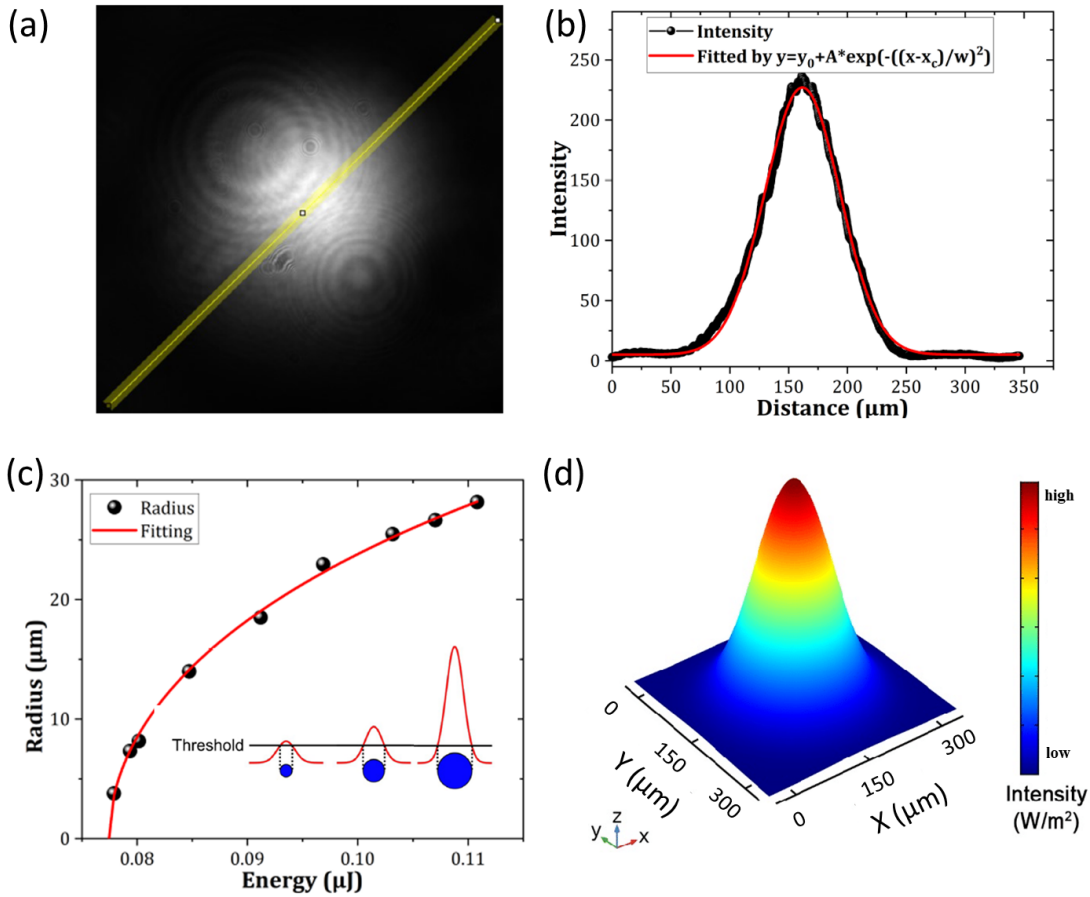

Fig. 2.6: (a) Beam spot observed with a microscope. The diffraction fringes come from dust on the optics. (b) Spatial Intensity. (c) Reversed magnetic domain radius as a function of the incident laser pulse energy. With illustration of the reversed domain above a threshold energy, when the amplitude of the Gaussian intensity profile increases. (d) two-dimensional Gaussian laser beam.

Analysis of laser spot with a microscope

Using a microscope set-up to examine a laser beam spot at a fixed distance z, the intensity of light can be extracted and depicted as a function of spatial distance, as shown in Fig. 2.6(a). This spatial intensity profile can be accurately described by a Gaussian formula.

$$y = y_0 + Ae^{-\left(\frac{x-x_c}{\sigma}\right)^2} \tag{2.1}$$

This Gaussian fitting validates the laser pulse's spatial distribution.

An ordinary two-dimensional Gaussian energy spatial distribution of an ultrafast laser pulse is typically represented by the following equation, which defines the spatial intensity profile of the laser beam:

$$I(x,y) = I_0 e^{-\left(\frac{x}{2\sigma_x}\right)^2 - \left(\frac{y}{2\sigma_y}\right)^2} \tag{2.2}$$

Here is a breakdown of the variables in this equation:

- $I(x,y)$ is the intensity at coordinates (x,y) within the beam profile. - I_0 signifies the peak intensity at the center of the beam. - σ_x and σ_y are the standard deviations that determine the width of the beam in the x and y axes, representing the long and short axes, respectively. The beam appears round when $\sigma_x = \sigma_y$, and elliptical when $\sigma_x \neq \sigma_y$.

When $\sigma_x = \sigma_y$, the energy profile can be simplified to:

$$I(x) = I_0 e^{-\left(\frac{x}{\sigma_x}\right)^2} \tag{2.3}$$

To compute the total energy of the laser pulse, you can integrate the energy distribution using the Gaussian integral formula:

$$E_{\text{total}} = \int_{-\infty}^{\infty} I_0 e^{-(\frac{x}{\sigma_x})^2} dx = I_0 \sigma_x \sqrt{\pi} \tag{2.4}$$

This equation enables us to determine the total energy contained within the laser pulse.

The width of the beam is the following.

$$\text{width} = \sigma_x \sqrt{\pi} \tag{2.5}$$

Considering a two-dimensional Gaussian profile, the area covered by the laser beam is:

$$S = \pi \sigma_x \sigma_y \tag{2.6}$$

For example, in the case of Fig. 2.6(b), the measured beam radius σ obtained from the camera data is 46.9 ± 0.4 micrometers.

Fitted threshold fluence and beam size

This method assumes that something happens once the energy is above a certain threshold fluence (or threshold energy). Because of the spatial Gaussian beam profile, the material does not receive the same amount of energy everywhere. Magnetization will only reverse where the local energy exceeds its threshold energy.

Defining $R = \sigma$ the radius of the beam spot it equals $\frac{FWHM}{2\sqrt{2\ln 2}}$, where FWHM is the *spatial* full width of the laser of half maximum. Therefore, the measured fluence $\bar{F}$ corresponds to the power of the laser divided by a factor e^2 at a distance from the center of the beam:

$$\bar{F} = \frac{P}{f\pi R^2} \tag{2.7}$$

The fluence profile has the following form:

$$F(r) = 2\bar{F}e^{-\left(\frac{r}{R}\right)^2} \tag{2.8}$$

where r is the domain radius. The peak value is then twice its measured value.

A magnetic domain appears as soon as the fluence peak value exceeds a certain threshold value F_{th}. When this happens, one would measure fluence $F = \frac{F_{th}}{2} = \bar{F}_{th}$. The domain radius must verify the following equation:

$$F(r) = F_{th} \iff r = R\sqrt{\ln\left(\frac{\bar{F}}{\bar{F}_{th}}\right)} \tag{2.9}$$

Considering equation 2.7, the threshold powers, as well as beam spot radius, can be extracted as a fitting parameter:

$$r = R\sqrt{\ln\left(\frac{P}{f\pi R^2 \cdot \bar{F}_{th}}\right)} \tag{2.10}$$

For the reflection configuration, the domains and the beam spot are elongated because of an angle of incidence of 45°. The following equation was used to extract the threshold powers and beam spot area as a fitting parameter:

$$a = S\ln\left(\frac{P}{fS\bar{F}_{th}}\right) \tag{2.11}$$

where a is the domain area, while S is the beam area.

If our only objective is to determine the threshold fluence $\bar{F}_{th}$, we can employ either the magnetic domain radius or the magnetic domain area and fit it using Equation 2.11. However, when aiming to characterize the energy distribution, to fit the spot size, the magnetic domain radius must be employed. Furthermore, in cases of an elliptical spot, such as in a reflection configuration, the Equation 2.10 can be rewritten as follows:

$$r_{x/y} = R_{x/y}\sqrt{\ln\left(\frac{P}{f\pi R_x R_y \cdot \bar{F}_{th}}\right)} \tag{2.12}$$

where $R_x = \sigma_x$, $R_y = \sigma_y$ correspond to the beam spot radius along x and y directions, respectively.

2.5 Time-resolved MOKE (TR-MOKE)

Time-resolved MOKE (TR-MOKE) is a sophisticated technique used to explore rapid and transient processes in materials. It relies on the pump-probe method, utilizing two precisely synchronized laser pulses: an initial *pump* pulse and a delayed *probe* pulse. These pulses are fundamental in studying fast changes within a sample.

TR-MOKE employs an ultra-fast laser source capable of generating both the "pump" and "probe" pulses. These pulses are exceedingly short in duration and precisely timed. The "pump" pulse is adjusted to either excite the material or trigger a specific event within it. Meanwhile, the

"probe" pulse is intentionally delayed and directed onto the material to monitor the arising changes. Detectors are employed to measure and record the modifications induced by the "pump" pulse, as detected through the "probe" pulse. It is possible to vary the time delay between the "pump" and "probe" pulses. This parameter is crucial for generating time-resolved data, allowing for an in-depth exploration of the material's dynamic response.

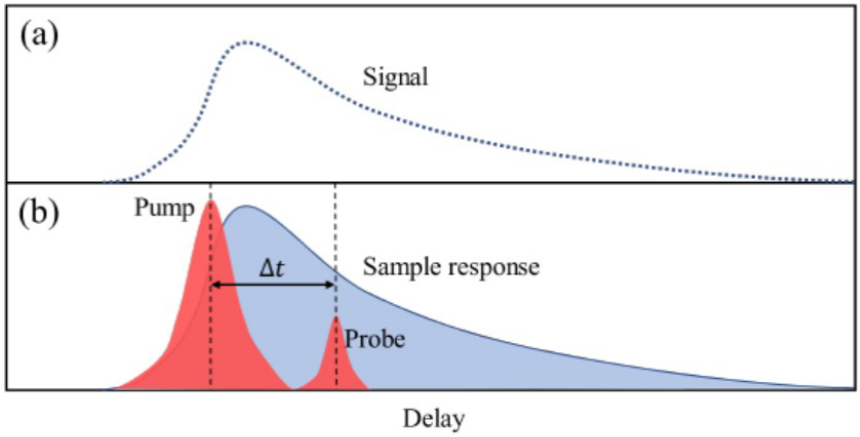

Fig. 2.7: The idea of pump-probe technique for TR-MOKE. The magnetization dynamics can be detected by changing the delay time (δt) between the "pump" pulse and "probe" pulse. Figure adopted from [118]

In TR-MOKE experiments can be described as follows:

1. **Laser Pulse Generation:** An ultrafast laser source continuously emits laser pulses at a high repetition rate, typically around 5,000 pulses per second.

2. **Beam splitting:** A beam splitter divides the laser pulses into two separate beams. One beam is directed toward the sample, while the other is manipulated to introduce a controlled time delay.

3. **Pump and probe pulses:** Laser pulses play different roles. One beam serves as the "pump" pulse, initiating dynamic changes within the material, such as altering its magnetization. The other beam functions as a "probe" pulse, capturing the evolving states of the material.

4. **Optical control:** Optical elements, including a half-wave plate and a polarizer, are utilized to manage the power of both the "pump" and "probe" beams. The "probe" power remains constant, while the "pump" power can be adjusted as needed.

5. **Focused irradiation:** Both beams are focused on the sample at almost normal incidence using spherical mirrors. The "pump" beam has a much higher intensity than the "probe" beam to ensure uniform excitation across the probed area.

6. **Signal detection and separation:** The "probe" signal is collected, collimated and directed onto a balanced photodiode with the help of lenses and a Wollaston prism. A half-wave plate is employed to balance the signal on the photodiodes.

7. **Data collection:** The output signal, after frequency-selective filtering through a lock-in amplifier, is converted to a digital signal and collected for in-depth analysis using a computer.

This setup allows us to investigate the rapid magnetization dynamics in materials with precision and control, making it a valuable tool for studying fast processes in various scientific and technological contexts.

2.6 Conclusion

In this chapter, I have outlined the experimental techniques employed in this thesis, focusing on magnetron sputtering, vibrating sample magnetometry, the Magneto-optic Kerr effect, and Time-resolved MOKE. These techniques play a crucial role in characterizing the magnetic properties and dynamics of the materials under investigation.

Magnetron sputtering is utilized for material deposition, providing a versatile and efficient method for growing thin films with precise control over thickness and composition. The use of different deposition geometries, such as on- and off-axis, allows for tailored film properties and thickness profiles, enabling the optimization of material characteristics.

The Magneto-optic Kerr effect is a powerful tool for studying magnetization in thin films. By measuring changes in the polarization of light reflected from a magnetic sample, we analyzed in-plane and out-of-plane magnetization properties. MOKE magnetometry and MOKE microscopy provide valuable insight into the magnetic behavior of materials, enabling the characterization of hysteresis loops and domain patterns.

TR-MOKE is a cutting-edge technique that combines MOKE with ultra-fast laser technology. By using synchronized pump and probe pulses, TR-MOKE can capture rapid and transient magnetization dynamics on femtosecond and nanosecond timescales. This technique is invaluable for studying dynamic processes and exploring the response of magnetic materials to external stimuli.

In the following sections, I will show the results and findings applying these experimental methods to prove insight on the magnetic properties and behavior of the materials studied.

Chapter 3

All-optical switching in Tb/Co multilayer

Contents

3.1 Introduction

This chapter the results of helicity-indepentent all-optical switching (HI-AOS) in Tb/Co multilayer systems are summarized. As discussed in Chapter 1 (Section 1.3), all-optical switching involves manipulating the magnetization of a material using ultra-fast laser pulses. It has been observed in ferrimagnetic materials in particular RE-TM systems, which include alloys and multilayers, where "RE" stands for rare-earth elements such as terbium (Tb) or gadolinium (Gd), and "TM" stands

for transition metals like cobalt (Co), Iron (Fe) or Nickel (Ni). The combination of these elements in alloys and multilayers results in intriguing magnetic properties that are crucial for understanding all-optical switching phenomena. Before discussing the results, it is essential to briefly cover the fundamental properties of these systems to facilitate a better understanding of the upcoming discussions.

3.1.1 Terbium vs. gadolinium for AOS applications

Although they have a similar electronic configuration, gadolinium and terbium exhibit significantly different magnetic properties. In fact, terbium has a high magnetic anisotropy, whereas the magnetic anisotropy of gadolinium is smaller by two orders of magnitude. This difference is due to the singularities of the electronic structures of terbium and gadolinium. While the trivalent gadolinium ion is characterized by being in the S state (with L = 0) and having a spherical 4f electron arrangement, the trivalent terbium ion, having an additional 4f electron, exhibits an oblate electron configuration. This is the result of the extra electron added to the spherical 4f subshell of the gadolinium ion, leading to the development of an orbital angular momentum of L=3. As a result, Gd has a much weaker spin-orbit coupling compared to that of Tb. This weaker coupling contributes to substantially smaller perpendicular magnetic anisotropy, Gilbert damping, and spin-lattice coupling in Gd compared to Tb. Although successful integration into perpendicular MTJs was demonstrated using Gd-based storage layers [104,105], the favorable anisotropic properties make Tb-based systems more suitable for storage applications. In fact, due to the inherently magnetically soft nature of Gd, the lateral size achieved for MTJs was limited to a minimum of 3 µm [105], as stated in Chapter 1. In another study, stable switched domains in Gd were shown to reach a minimum size of 200 nm (not in MTJ devices) [119–121]. However, in a continuous TbFeCo alloy film, stable domains as small as 50 nm were switched, with the help of a two-wire plasmonic nanoantenna [122]. Moreover, variations can be observed in the laser-induced demagnetization between elemental Gd and Tb, as investigated by Wietstruk et al. in their study [92]. This variation, as outlined in Chapter 1, is explained by a greater transfer of angular momentum from the $4f$ moments to the magnon and phonon systems, which is only feasible in the presence of spin–orbit coupling [100].

3.1.2 Sperimagnets

One aspect often overlooked is the influence of amorphous or polycrystalline systems, as well as the presence of defects. In one of his research, Coey investigated systems consisting of 3d and 4f elements within amorphous solids and distinguished two magnetic sublattices based on their chemical composition [25,123].

In such systems, the $d-d$ exchange exhibits strong ferromagnetic characteristics, defining a 3d ferromagnetic sublattice. Consequently, $3d-4f$ interactions tend to align the 4f sublattice spins antiparallel to the 3d sublattice. This results in parallel alignment of sublattice moments for heavy rare-earths and antiparallel alignment for the light rare-earths. As a result, it is possible to have an amorphous ($a-$) ferrimagnet where the RE and TM subsystems are distinguished on the basis of their chemical properties. For example, consider the case of $a-Gd_{25}Co_{75}$. In some instances, there may be a magnetization compensation point at a temperature where $M_{4f} > M_{3d}$, similar to that of crystalline ferrimagnets.

However, for rare earths with strong uniaxial anisotropy and weak exchange coupling to the 3d sublattice, such as Tb or Dy, their local easy axes are primarily defined by the local crystal-field interaction. These local easy axes are random, resulting in the formation of sperimagnetic structures, as illustrated in Fig. 3.1.

S

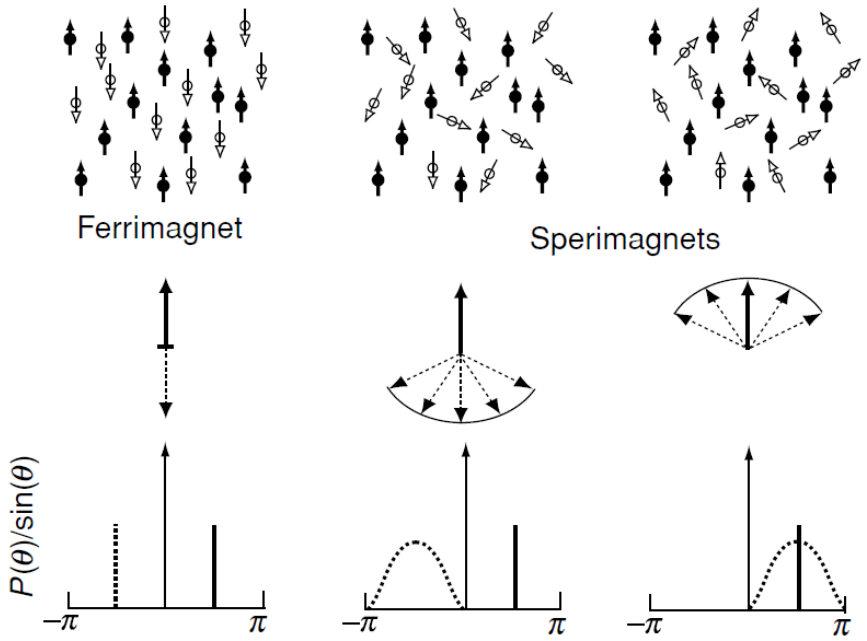

Fig. 3.1: Possible two-sublattice magnetic structures in amorphous binary alloys. At the top Ferrimagnet and sperimagnet atomic spin illustration (RE empty/white spins, TM filled/black spins); at the bottom distribution of local easy axes direction for each sublattice (RE dashed line, TM continuous line). Schematics from [25].

Our systems, although not strictly amorphous, can still possess defects and may exhibit polycrystalline characteristics. In fact, RE-TM alloys are known to be amorphous, but ferromagnets are instead polycrystalline or textured when deposited at room temperature on amorphous layers, with typical grain sizes of 20 to 30 nm. As our Tb/Co multilayer system is composed of a repetition of these layers with intermixed interfaces, this implies that at the grain level, the uniaxial anisotropy can vary depending on the local crystal-field interaction.

3.1.3 Alloys and multilayers

We will now compare multilayers to alloys in order to understand the key differences between them and the reasons to have chosen one with respect to the other.

For MRAM applications, it is essential to control the annealing resiliance of the magnetic layers of the MTJs [124]. This because in order to obtain high TMR values, well-textured MgO barriers are required. They can be grown either by molecular beam epitaxy (MBE) on bcc CoFe or Fe magnetic electrodes or on amorphous CoFeB electrodes followed by annealing to recrystallize the electrode with the same texture as the crystalline barrier. Therefore, by growing multilayers instead of alloys, a surface anisotropy is introduced at each interface of the multilayer. This helps to maintain perpendicular anisotropy and generally improves annealing resistance [20,21]. Our multilayer systems consist of layers of Tb and Co atoms stacked on top of each other. When the deposited layers are thin, interdiffusion mixes the species, and the obtained deposit is an amorphous alloy [125]. If they are thick enough, the obtained system is a multilayer with diffuse interfaces. In this second case, for [Tb / Co] multilayers, Ertl et al. [126] measured an interface anisotropy of approximately 0.5

erg/cm^2.

In general in amorphous RE-TM alloys, by adjusting the RE and TM composition it is possible to tune magnetic properties such as the T_{Comp}, T_{Curie}, total saturation magnetization $M_{S,tot}$ and the coercive field H_C. Similarly, in multilayers, one can tune the same properties by varying the thicknesses of the RE and TM layers.

The primary distinction between alloys and multilayers, related to the anisotropy previously mentioned, arises from the antiferromagnetic exchange coupling. In alloys, it is distributed homogeneously across the entire film; in multilayers, the coupling exists only at the interface between the RE and TM layers.

Ertl et al. in addition to the measurement of the interface anisotropy, also reported an interesting aspect. As the thickness of each layer increases, the behavior tends to resemble that of bulk material. It is possible that for RE like Tb, which has a bulk Curie temperature much lower than the room temperature, the layers located farther from the interfaces might exhibit paramagnetic characteristics. This could result in the 'effective' magnetic thickness of the layer being less than its actual physical thickness. However, this phenomenon was shown to occur in the Tb / Co multilayer, for thicknesses exceeding 3.0 nm for Tb [126], which is not a concern in our study, since the layer thicknesses that we investigate are smaller.

3.1.4 Integration of Tb/Co multilayers in magnetic tunnel junctions

The research outlined in this thesis is an extension of a preliminary study conducted by Sébastien Bandiera [125], followed by a more comprehensive investigation carried out by Luis Avilés-Félix [20,21]. Both researchers explored the potential of Tb/Co multilayers to enhance the performance of Magnetic Tunnel Junctions.

In 2012, Bandiera focused on advancing MRAM through thermally assisted spin transfer torque writing in perpendicular magnetic tunnel junctions [127]. The study demonstrated the benefits of Tb-Co systems for use in magnetic tunnel junctions, owing to their distinctive properties such as high coercivity and the capacity to create low magnetization structures. The authors also emphasized the need for careful control of the composition based on the annealing conditions and total thickness to counteract terbium diffusion and oxidation effects. Moreover, Tb-Co alloys and multilayers were found to be less suitable for spin-transfer torque switching applications because of the high Gilbert damping resulting from the strong spin-orbit coupling of heavy-terbium atoms. The critical writing current is proportional to the Gilbert damping, therefore the higher the damping the higher current density required to switch.

Instead, Avilés-Félix and colleagues were pioneers in exploring Tb/Co multilayers for all-optical switching MRAM applications, publishing two relevant papers [20,21], see Fig. 3.2. The work was carried out by L. Avilés-Félix, A. Olivier, G. Li, C. S. Davies, L. Álvaro-Gómez, M. Rubio-Roy, S. Auffret, A. Kirilyuk, A. V. Kimel, Th. Rasing, L. D. Buda-Prejbeanu, R. C . Sousa, B. Dieny and I. L. Prejbeanu under the SPICE project (FET-Open Grant Agreement No. 713481, European Union's Horizon 2020 research and innovation program). They developed a multilayer stack based on $[\text{Tb/Co}]_N$, coupled to a CoFeB layer, and examined how the annealing temperature affects the magnetic properties of the multilayer. The thermal stability of [Tb/Co] multilayers was found to be highly dependent on the thickness ratio of Tb / Co, and perpendicular magnetic anisotropy was

preserved to annealing temperatures up to 275°C in [Tb(0.9 nm)/Co(1.3 nm)]$_5$ or a Co/Tb ratio of 1.44, (Fig. 3.2a).

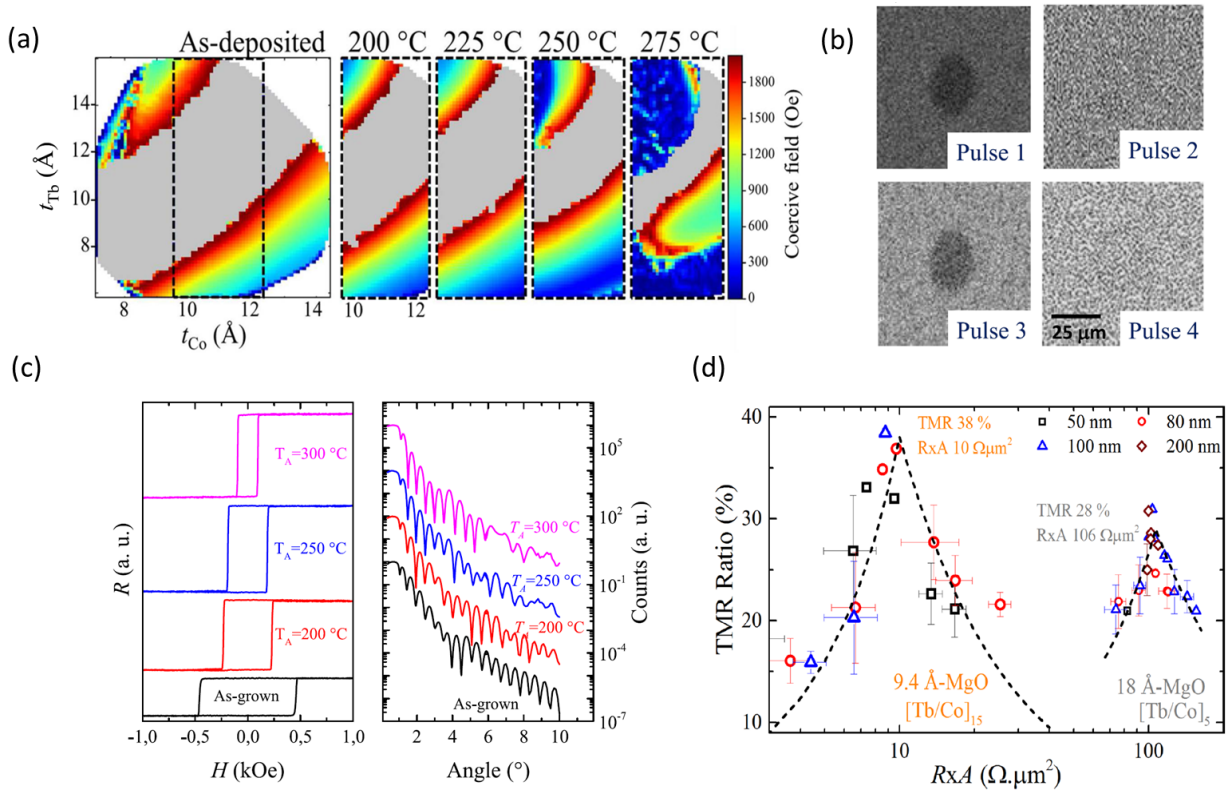

Fig. 3.2: Summary of the main findings presented in [20,21]: (a) Evolution of the coercivity mappings of the CoFeB(13 Å)/[Tb(t_{Tb})/Co(t_{Co})]5 electrode after annealing at different temperatures from 200°C to 275°C. (b) Single-shot AOS of the electrode after consecutive 5ps-long laser pulses with an incident fluence of 4.7 mJ/cm^2. (c) $R(H)$ obtained from EHE experiments and x-ray reflectivity measurements of [Tb(10 Å)/Co(12 Å)]5 samples as-deposited and annealed at temperatures T_A = 200, 250°C, and 300°C as indicated. (d) TMR versus RxA of nanopatterned junctions for stacks with different repetition numbers N of the [Tb/Co]N stacks as indicated, with 9.4 Å and 18 Å MgO barriers. The wafer-level TMR potential for optimal processing is 38% and 28%, respectively. For detailed information, please refer to the original papers [20,21].

.

They also investigated the impact of the number of [Tb/Co]$_N$ bilayer repetitions, performing current-in-plane tunneling measurements on full-sheet film samples with 5 and 15 repetitions following annealing at 250°C. They found through X-ray reflectivity measurements that the amplitude of the oscillating peaks, which are related to the interfaces of the multilayer, decreases with an increase in the annealing temperature, eventually disappearing completely after annealing at 300°C, as shown in Fig. 3.2c. This trend suggests that the post-deposition annealing process affects both the interfacial roughness and the long-range order within the multilayer. The degradation of these characteristics correlates with a decrease in the coercive field and may explain the observed loss of PMA.

The team showed for the first time ultra-fast all-optical switching of the FeCoB(13)/Ta(2)/[Tb/Co]$_5$ sample after annealing at 250°C, utilizing 5-picosecond and 60-femtosecond laser pulses. AOS was observed exclusively in the Co-rich compositions of the storage electrode [20], (Fig. 3.2b).

They have managed to fabricate nanopatterned magnetic tunnel junctions, employing optically

switchable FeCoB/Ta/$[Tb/Co]_N$ multilayers as the storage electrode. Impressive TMR values of approximately 38% and 28% have been achieved for repetitions of [Tb / Co] of 15 and 5, respectively [21], see Fig. 3.2(d).

The work demonstrated that the multilayer system held promise for integration into spintronics devices that allow optical switching. However, even with notable progress, achieving consistent and field-free validation of AOS in patterned devices remained a persistent challenge. Additionally, a comprehensive understanding of the underlying switching mechanism that governed this process remained unclear, highlighting a goal that was yet to be achieved.

In the forthcoming sections and chapters, we will go deeper into the specific aspects of all-optical switching in Tb/Co multilayers.

3.2 Magnetic and all-optical switching thin film characterization

3.2.1 Experimental Approach: investigating physical phenomenon and application-oriented experiments

The approach undertaken in our study is focused on systematically exploring the underlying physical mechanisms of HI-AOS in our system while simultaneously conducting experiments with a focus on the application aspect. In other words, our experimental approach aims to understand the fundamental physical phenomena and extrapolate these findings for MRAM applications.

In our efforts to understand how our type of reversal works, we performed a series of experiments that focused on the physical mechanisms responsible for this process. Different approaches, such as changing the laser fluence and pulse duration in a systematic way were tested and conducted. These experiments helped us gather important information that led us to create a well-thought-out hypothesis about the magnetization reversal.

In parallel, our study extends beyond fundamental understanding, embracing a pragmatic perspective by conducting experiments tailored to the MRAM application. We performed thin film experiments on MTJ-focused stacks and then, as shown in Chapter 5, developed and tested AOS on nanopatterned devices. By considering these application-driven experiments, we aimed to establish a robust foundation for potential technological implementation.

3.2.2 Detailed thicknesses for AOS and reliability

Collaborative efforts with the Institut Jean Lamour at the *Université de Lorraine*, in partnership with PhD student, now Dr. Yi Peng and the colleagues Michel Hehn, Gregory Malinowski and Stéphane Mangin, in the frame of UFO project (ANR-17-CE24-0007), allowed systematic AOS measurements in our samples. The first goal aimed to delineate the optimal thickness range for AOS while investigating its behavior and verify that the switching occurs also without the coupled FeCoB. Our exploration is centred around crossed-wedge samples, where both the thicknesses of the Tb and Co layers vary throughout the wafer; details on the deposition technique were presented in Chapter 2. Specifically, the initial stack investigated was Ta(30)/$[Tb(t_{Tb})/Co(t_{Co})]_5$/Ta(20)/Pt(20), referred as **Sample 0** see Fig. 3.3(a), where all the thicknesses in brackets are expressed in the ranges Å, and wedges of t_{Tb} and t_{Co} are shown in Fig. 3.3(b).

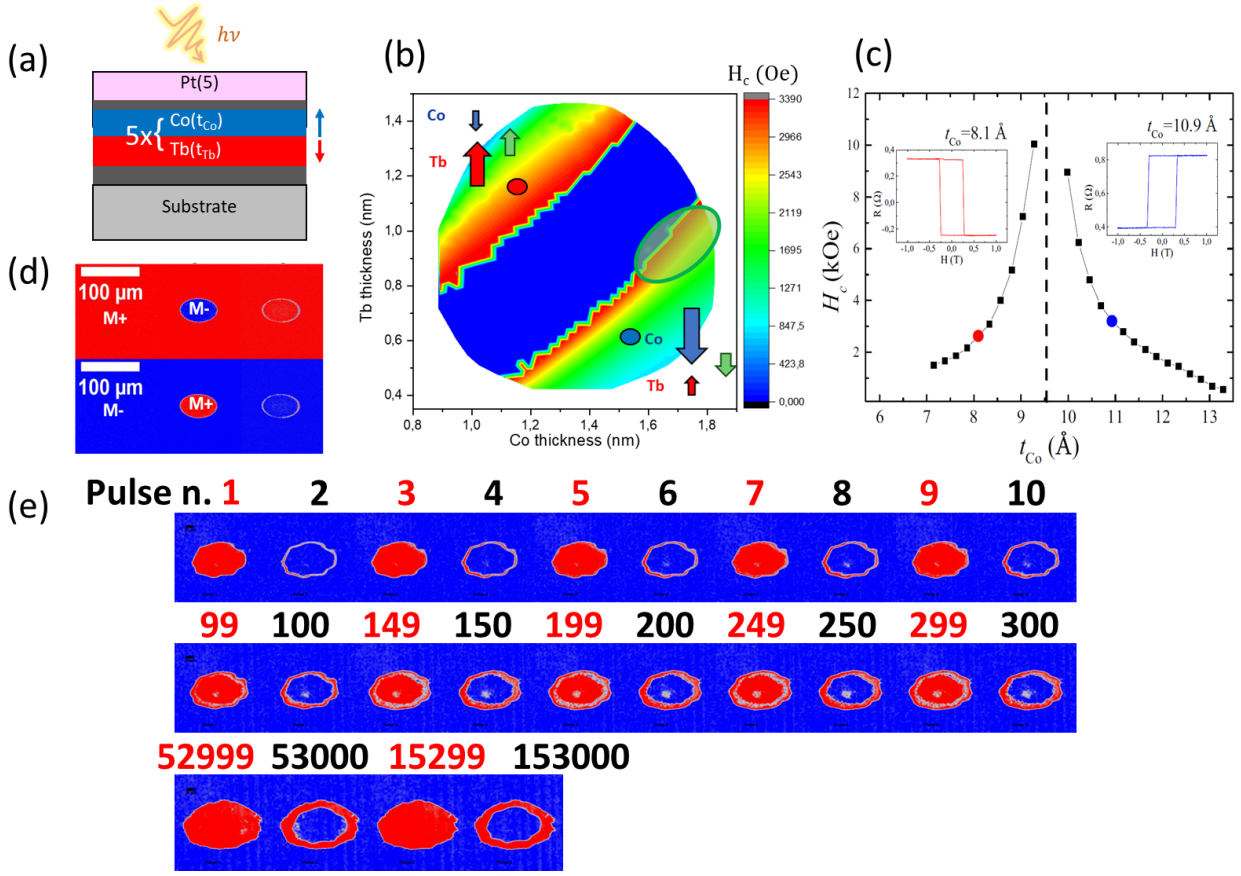

Fig. 3.3: Single shot switching in $[\mathrm{Tb}(1.06\ \mathrm{nm})/\mathrm{Co}(1.78\ \mathrm{nm})]_5$ multilayer (sample AV39- 05): (a) $\mathrm{Ta}(30)[\mathrm{Tb}(t_{Tb})/\mathrm{Co}(t_{Co})]_5/\mathrm{Ta}(20)/\mathrm{Pt}(20)$ investigated stack schematic. (b) Coercive field map of $[\mathrm{Tb}(t_{\mathrm{Tb}})/\mathrm{Co}(t_{\mathrm{Co}})]_5$. The coercive field values were obtained from the $M(H)$ loops measured with H applied perpendicular to the plane of the film. The superimposed blue region in the center indicates the region in which H was not sufficient to saturate the stack. (c) Coercive field of the multilayer $[\mathrm{Tb}/\mathrm{Co}]_5$ as a function of the Co thickness t_{Co}: $7-13$, Åwith the thickness of the Tb layers fixed at $t_{\mathrm{Tb}} = 10$, Å. Insets: $R(H)$ for $t_{\mathrm{Co}} = 8.1$, Åand $t_{\mathrm{Co}} = 10.9$, Åas indicated, panel from [21]. (d-e) Background subtracted images after each single pulse at 5.1 mJ/cm^2 laser pulse at 50 fs.

Our findings confirmed what Avilés-Félix et al. showed, namely the critical role of specific thickness and ratios between the Tb and Co layers for HI-AOS. In Figs. 3.3(d) and (e), we show background subtract MOKE images after 50 fs laser pulse irradiation at a fluence of 5.1 $\mathrm{mJ/cm^2}$. Recall that the fluence is calculated using $F = P/fS$ where P is the measured power in repetition mode, f is the repetition rate of the laser and S is the beam spot area. The setup, described in Chapter 2, in this case is in a reflection configuration, as one can infer by the elongated reversal spots. In Fig. 3.3(d) the out-of-plane magnetization is saturated by applying a strong magnetic field either up (red) or down (blue) background, regardless of the initial direction, the reversal is obtained, and a domain with opposite magnetization direction is created. The resultant AOS region, for the "as deposited" sample mentioned above, was identified as follows:

$$1.35\,\text{nm} \leq t_{Co} \leq 1.9\,\text{nm}$$
$$0.8\,\text{nm} \leq t_{Tb} \leq 1.2\,\text{nm}$$
$$0.59\,\text{nm} \leq \frac{t_{Tb}}{t_{Co}} \leq 0.63\,\text{nm}$$

In Fig. 3.3(e), we show that the observed reversal continues up to 153,000 pulses when the measurement was stopped. There is no clear indication of switching degradation within this range, implying that the toggle switching exhibits high endurance and repeatability for the specified thickness ranges. The outside ring visible on the MOKE images after a large number of pulses is due to the vibrations of the laser beam, over time the laser does not hit the sample in the exact same position every time.

Similar to the previous research, the AOS behavior appears exclusively in the cobalt-rich region. It is important to note that the regions "rich" in terbium and cobalt are temperature dependent. When we mention the cobalt-rich region, we are usually referring to room-temperature conditions (300 K). Put differently, our systems allow for ultra-fast reversal only when the initial temperature (usually RT) is slightly above the compensation temperature (T_{Comp}). In such cases, the total magnetization increases as the temperature increases. This phenomenon is evident in Fig. 1.3 and was also measured in our system using VSM by Mishra et al. [128] Fig. 3.4(a) where the black curve for Tb rich sample shows a decrease of magnetic moment with increase temperature and the opposite is true for the blue, red and green curves where Co is dominating. Fig. 3.4(b) shows the hysteresis loops both out-of-plane and in-plane evidencing a clear reorientation towards the in-plane, this measurement is coherent with what observed in the VSM measurements in section 3.4.

Although this aspect will be thoroughly discussed in Chapter 4, we will see that it plays a significant role in the reversal process.

3.2.3 Complete study on AOS properties: ring patterns and state diagrams

After identifying the region for the complete and reliable reversal region at lower fluences, our investigation expanded to observing the response of HI-AOS under higher fluence conditions and across different pulse durations.

When dealing with materials like GdFeCo alloy, when AOS is observed, typically as the fluence increases, the diameter of the reversed spot also increases, this is due to the Gaussian shape of the laser spot. However, there is a threshold fluence above which the central area of the spot shows the creation of multiple domains with non-uniform magnetization, known as "multidomain" [98], see Fig. 1.10 of Section 1.3 . This phenomenon occurs because the temperature induced by the laser becomes excessively high for HI-AOS, the TM sublattice remains demagnetized for too long, and no transient ferromagnetic state can be observed, leading to a random-like remagnetization.

Interestingly, in our system something different is happening. When subjected to fluences greater than 11 mJ/cm^2, in addition to the increase in diameter, the reversed domains show a distinct pattern of concentric rings with opposite magnetic orientations. This pattern can be observed in

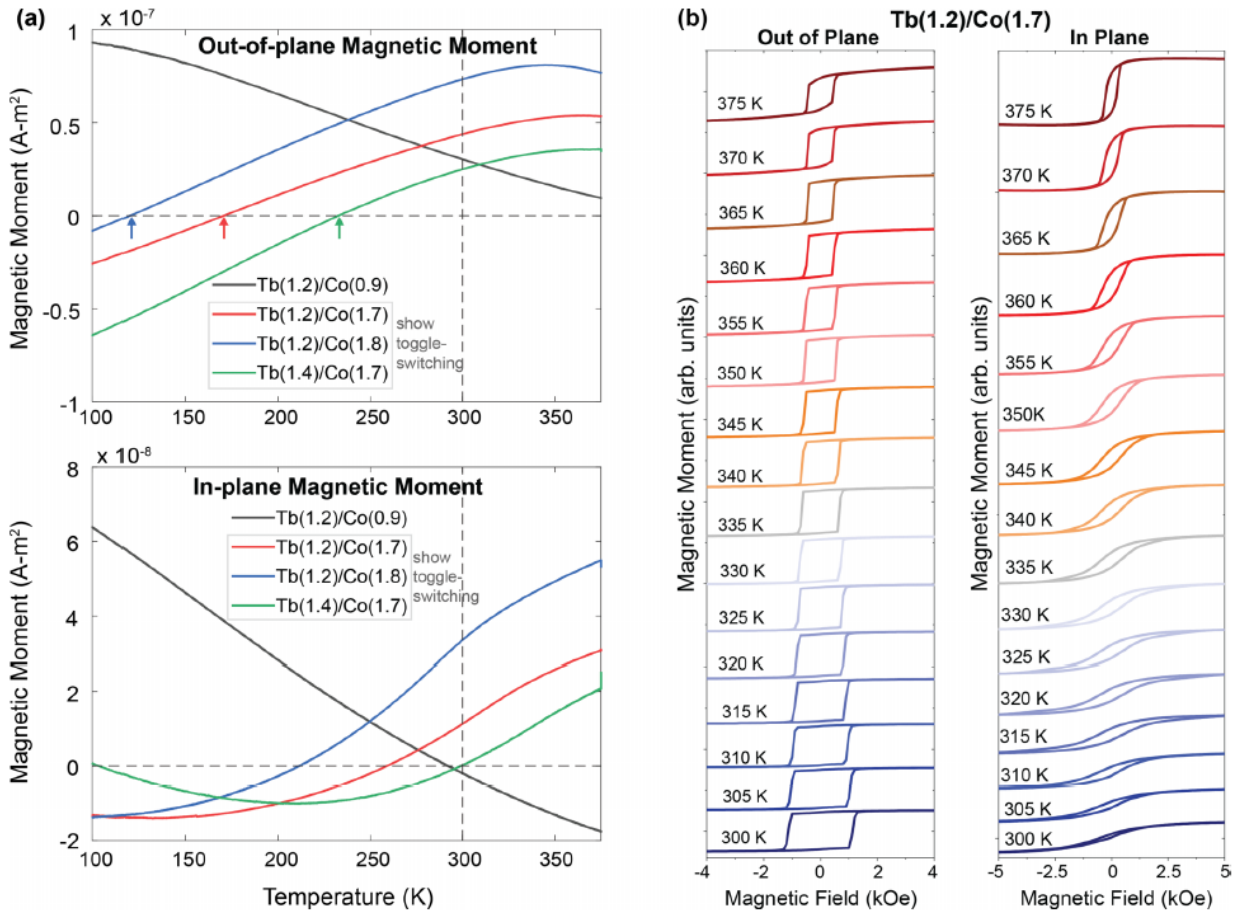

Fig. 3.4: Figure from [128]: (a) Temperature dependence of the out-of-plane magnetic moment measured under 200 mT applied field (top panel) and in-plane magnetic moment measured under 1 T applied field (bottom panel) for different compositions of the Tb/Co multilayers, measured using a superconducting quantum interference device vibrating sample magnetometer (SQUID-VSM). The colored arrows in the top panel indicate the compensation temperatures (T_{comp}) of each composition. (b) Evolution of the out-of-plane and in-plane magnetic hysteresis loops with increasing temperature from 300 K (loops at the bottom of the plots) to 375 K (loops at the top of the plots) for the composition Tb(1.2 nm)/Co(1.7 nm), showing an increasing in-plane component that emerges upon heating.

both Fig. 3.5 and Fig. 3.6. In Section 3.5, we explore how this phenomenon can be replicated in other materials by adjusting their properties and thicknesses, leading to a varying number of rings. From the outside inward fluence thresholds (TF1-TF4...), for the reversal or non-reversal, can be identified taking into account the Gaussian profile of the laser spot.

The observed phenomenon has not been reported in gadolinium-based samples so far. And, more importantly, the commonly accepted explanation for the reversal mechanism in Gd samples does not seem to apply in this case. It is worth noting that the demagnetization rate of Tb is significantly higher than that of Gd, as shown by Wietstruk et al. [92], and is comparable to that of Co. Even if we overlook this detail, if the magnetization reversal is attributed to differences in demagnetization rates [93], it is puzzling how an increasing fluence value can result in a repeating pattern of reversed and non-reversed domains.

One could speculate that there might be a competition between the demagnetization rate switch-

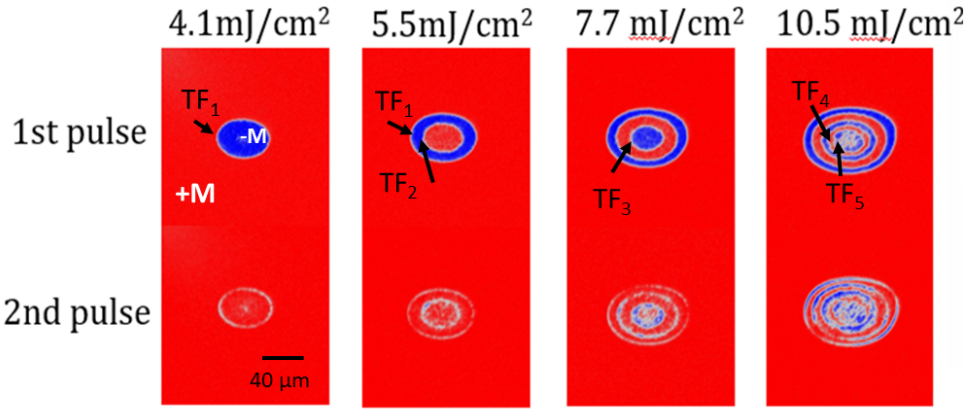

Fig. 3.5: All-optical switching in [Tb(1.06 nm)/Co(1.78 nm)]5 multilayer (sample AV39-05). Background subtracted images after first single with 50 fs laser pulse of different fluence.

ing and some influence of hot electrons or spin currents [129] that could be driving the switching in the opposite direction. Perhaps the observed ring patterns are the outcome of the "winner" in this competition of effects. However, as we will see, this hypothesis does not hold when considering the dependence on pulse duration.

Instead, an intriguing parallel can be drawn with a study conducted by Davies et al. [130] involving iron garnet. Although the systems under investigation differ, and an in-plane bias is applied in their study, a similar reversal pattern of magnetization is evident. Their work revealed that the reversal process involves a precession of magnetization, which is triggered by transient thermal modification of the growth-induced crystalline anisotropy in the presence of a fixed perpendicular magnetic field. While a precession-like mechanism could account for the observed rings, it appeared improbable at first because it cannot occur on an ultrafast time scale, such as subpicosecond, which seemed to contradict our observations of switching with 50 fs laser pulses.

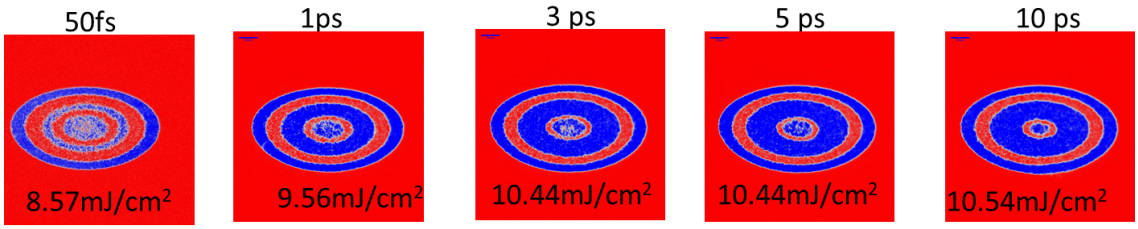

Fig. 3.6: All-optical switching in $[Tb(1.06\ nm)/Co(1.78\ nm)]_5$ multilayer (sample AV39-05). Background subtracted images after each single laser pulse with fluence between 8.57 mJ/cm_2 and 10.54 mJ/cm_2, pulse duration: 50 fs, 1 ps, 3 ps, 5 ps and 10 ps.

Yet, the other main finding that differs from previously reported HI-AOS studies is the fact that the fluences required to reverse and stabilize a given number of rings depend little or not at all on the duration of the laser pulses investigated, see Fig. 3.6. In fact, single-pulse reversals have been obtained for long pulse durations, up to 12 ps (the maximum pulse duration available on our measurement lasers), and the threshold fluences for each transition remain mostly constant. This finding already helped to realize that the reversal was occurring on a longer time scale and to reevaluate the precession comparison to explain the reversal. On the basis of the MOKE observation

upon varying the laser pulse duration, it was possible to draw a complete state diagram of pulse duration versus fluence, as reported in Fig. 3.7.

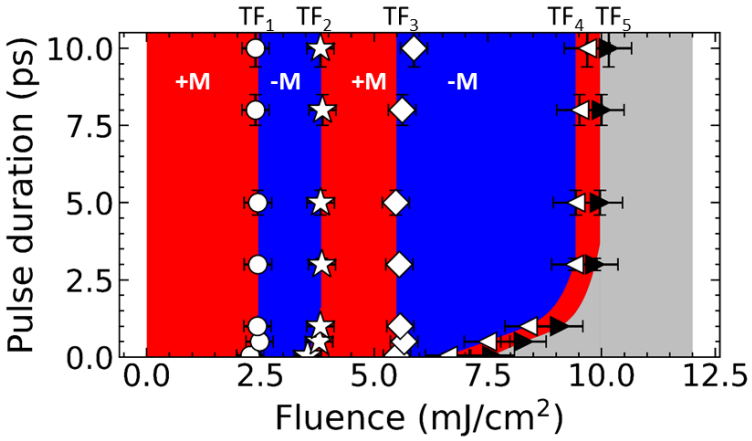

Fig. 3.7: All-optical switching and state diagram in [Tb(1.06 nm)/Co(1.78 nm)]5 multilayer (sample AV39-05). State diagram pulse duration versus laser fluence. TF1 is the border for switching; TF2 is the border to two domains state, one ring; TF3 is the border to three domains state, two rings; TF4 is the border to four domains state, three rings;TF5 is the border to demagnetized state at the center and four rings. Red filling refers to unchanged magnetization direction compared to the initial saturated one, blue opposite magnetization direction, and grey is the multidomain state.

The state diagram serves as a clever method to comprehend the overall system behavior. It compiles data from the previous measurements conducted at varying pulse durations and plots them relative to corresponding threshold fluences. These measurements are static, allowing sufficient time for magnetization to fully recover after the laser pulse stimulus. To aid readers in identifying the threshold fluences and establishing a connection to the reversed spots in Fig. 3.6, a color code has been implemented. Red signifies an unchanged magnetization direction compared to the initial one, blue indicates the opposite magnetization direction (AOS magnetization reversal), and grey represents the multidomain state. The state diagram is evidently different from the state diagrams shown in the case of HI-AOS in GdFeCo, Fig. 1.10 [98] and of multiple pulse HD-AOS [131]. This must be evidenced by the fact that in our system the magnetization reversal process is different with respect to the GdFeCo or Mn_2Ru_xGa alloys.

3.2.4 AOS with ITO and SAF for MTJ development

Alongside our investigation into the mechanism of the HI-AOS, we also took a practical approach by carrying out experiments to combine all-optical switching with MRAM technology. We replicated the AOS experiments described earlier, this time focusing on MTJ structures within thin-film stacks. In Chapter 5, we further advanced this by developing and testing AOS on nanopatterned devices. Avilés-Félix and his colleagues have successfully developed and demonstrated the implementation of all-optical switching on a $[Tb/Co]_N$ multilayer stack that is coupled to a FeCoB storage layer, as described in their work [20,21]. Now, to create a fully functional MTJ memory device, the establishment of a stable reference state is crucial. This is often achieved using a synthetic antiferromagnet structure (SAF), which not only enhances stability but also reduces magnetostatic stray fields. Moreover, for the purpose of both optical access to the device and simultaneous reading of the junction resistance, the integration of a transparent and conductive electrode (TCE) is necessary. In Chapter 5, a detailed description of the fabrication process with the material chosen for this TCE is provided: Indium Tin Oxide (ITO) has been selected for this role. The experimental investigations were then carried out with the aim of understanding how the all-optical switching behavior varies when 1. FeCoB is present (referred to as half-MTJ stack with and without ITO), and 2. with a reference layer incorporating a SAF structure.

Sample 1 (half-MTJ stack)

Ta(30)/FeCoB(3)/MgO(22.8)/FeCoB(13)/Ta(2)/[Tb/Co(14)] × 5/Ta(20)/Pt(20)(/ITO(1500)).

Sample 2 (full-MTJ stack)

Ta(30)/Pt(250)/[Co(5)/Pt(2.5)] × 5/Co(5)/Ru(9)/[Co(5)/Pt(2.5)] × 2/
Co(5)/W(3)/FeCoB(10)/MgO/FeCoB(14)/W(2)/[Tb/Co(14)] × 5/W(20)/Pt(50).

The numbers within parentheses represent the respective layer thicknesses in angstroms (Å), comprising the entire stack. The samples were annealed at 250°C, a necessary step to enhance TMR in the final MTJ application. A MOKE mapping for the half-MTJ stack is shown in Fig. 3.8.

The results are presented in the following figures. In the case of the half-MTJ sample, see Fig. 3.8(a), we have included the results with the ITO capping layer, as we did not observe significant differences, except for a slight increase in fluence due to the absorption of the TCE. This outcome was anticipated, as it had been thoroughly investigated by Sobolewska et al. in their study, which will be discussed in Chapter 5.

As depicted in Fig. 3.8(b), a notable observation is the slight shift towards lower values in the thickness range for HI-AOS compared to the previously reported sample:

$$1.19\,\text{nm} \leq t_{Co} \leq 1.69\,\text{nm}$$
$$0.61\,\text{nm} \leq t_{Tb} \leq 1.06\,\text{nm}$$
$$0.51 \leq \frac{t_{Tb}}{t_{Co}} \leq 0.62$$

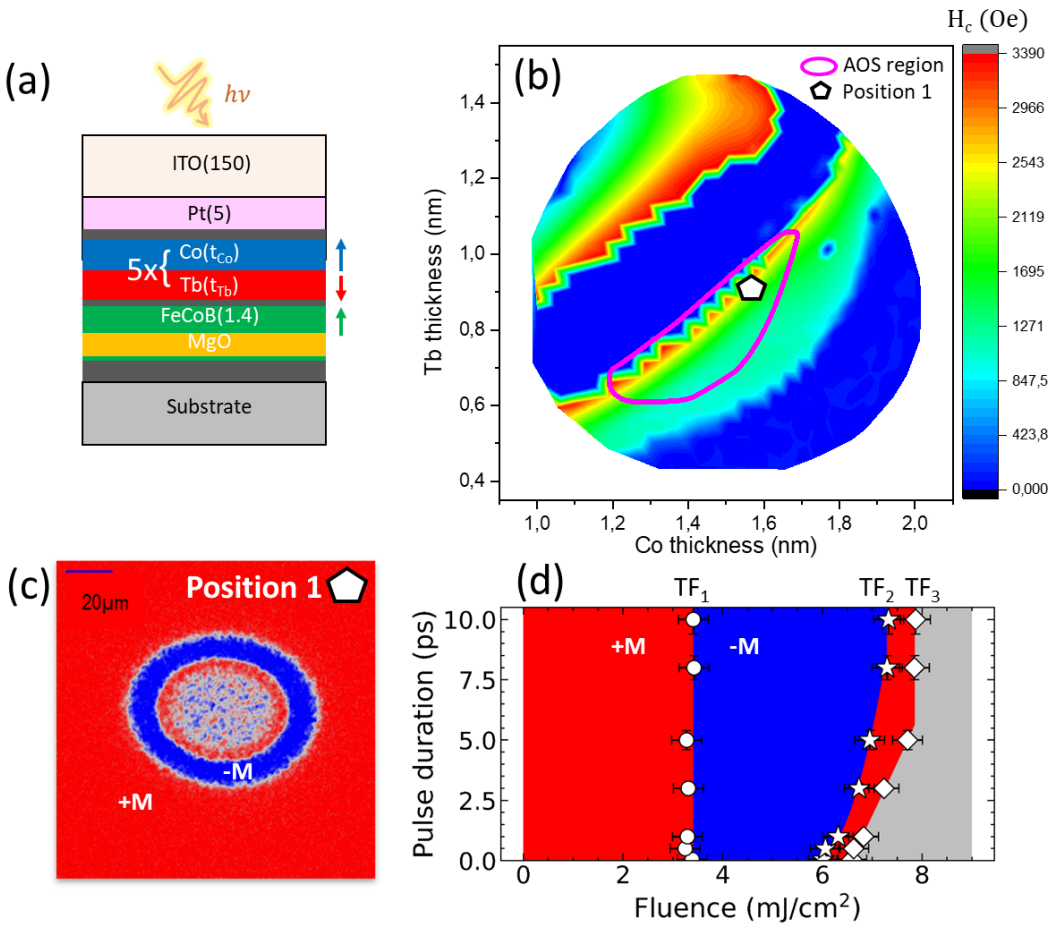

Fig. 3.8: All-optical switching in half-MTJ with ITO stack annealed at 250°C for 10 min (sample AV39_ 09): (a) half-MTJ with ITO investigated stack schematic. (b) Coercive field map of $[\mathrm{Tb}(t_{\mathrm{Tb}})/\mathrm{Co}(t_{\mathrm{Co}})]_5$. The coercive field values were obtained from the $M(H)$ loops measured with H applied perpendicular to the plane of the film. The superimposed blue region in the center indicates the region in which H was not sufficient to saturate the stack. (c) Background subtracted images after each single pulse at 9.62 mJ/cm^2 laser pulse at 50 fs, in Position 1 $[\mathrm{Tb}(0.9nm)/\mathrm{Co}(1.56nm)]_5$. (d) State diagram pulse duration versus laser fluence in Position 1. Red filling refers to unchanged magnetization direction compared to the initial saturated one, blue opposite magnetization direction, and grey is the multidomain state.

This shift in the thickness range may be attributed to the new presence of the coupled FeCoB. The FeCoB layer is antiferromagnetically coupled to the Tb sublattice, thus helping the Co sublattice; as a result, the HI-AOS switching region has shifted to lower values of Co. The HI-AOS region seems to be very sensitive to the balance of magnetic moments of the sublattices. A second aspect important to mention is the effect of annealing, and as can be seen from MOKE mappings in Figs. 3.3(b) and 3.8(b), the sample's anisotropy is reduced. This is evident by looking at the reduction of the compensation region and from the appearance of in-plane magnetization regions and low Tb and high Co thicknesses. Both Bandiera and Avilés-Félix reported that Tb diffusion occurs during the annealing process. Still, PMA is mostly preserved because of the additional anisotropy coming from the MgO/FeCoB interface that counterbalances the loss due to the interdiffusion just mentioned.

Note that the thermal conductivity of the sample might be affected by the MgO barrier, which could consequently alter the temperature distribution when laser heating. Despite these alterations,

it appears that the core switching mechanism remains unchanged. In Fig. 3.8(c) the magnetization reversal spot appears to maintain the external ring (TF1-TF2), however, the threshold for transitioning to a multidomain state is lowered to smaller energy levels, as if the barrier is more proficient in retaining heat, making it easier to get to the Curie temperature (T_C). The pulse duration dependency also remained the same, as shown in Fig. 3.8(d); this is of extreme importance for the application point of view, as having a large pulse duration window allows for much easier integration with laser technology. As discussed in Chapter 1, ps lasers are far more simpler than fs lasers, thus for the short term, being able to switch with ps pulses makes future integration to complete memories less complex.

Moving to the results for the sample containing the SAF structure, we see in Fig. 3.9 and Fig. 3.10 that the reversed domain shows again multiple rings but at higher fluences. The variations from the half-MTJ stack are mainly two:

1. the metallic volume is much greater in this case; the increase metallic volume will increase the heat capacity of the system and thus allowing to withstand higher fluences.

2. The second is a possible increased roughness; this impact was observed mainly in the Tb-rich region, where no perpendicular anisotropy was seen after annealing. Despite this loss of anisotropy coming from both the roughness and the annealing, it was concluded that the switching region is the same as for the half-MTJ stack, where strong PMA is still kept.

To further understand what are the ingredients for AOS, namely anisotropy and magnetization, the coercive field vs net magnetization are reported in Fig. 3.10(a) with a colorcode on the Tb/Co thickness ratio. To calculate the net magnetization, we used the thickness of deposited Tb and Co layers and $M_{S,\,Co}$ = 760 kA/m, $M_{S,\,Tb}$ = 1350 kA/m from references [132,133]. MOKE mappings were used for the calculations, which allowed to pinpoint the magnetization compensation point and address possible fluctuations in the deposition rate and disparities from established M_S values from sources in the literature. In the figure it is highlighted the region where AOS occurs (gray area).

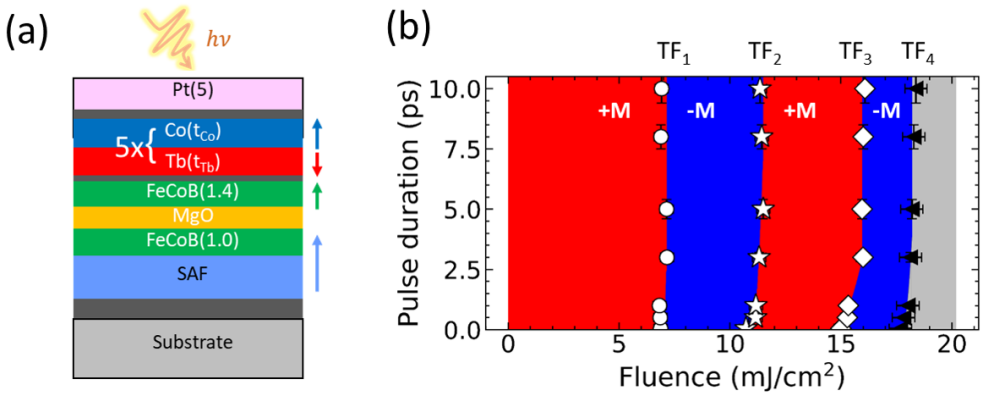

Fig. 3.9: All-optical switching in bottom-pinned AOS-MTJ stack annealed at 250°C for 10 min (sample AV68-23): (a) AOS-MTJ stack with bottom-pinned and [Tb/Co]ML storage layer schematic. (b) Pulse duration vs fluence experimental state diagram of the magnetization reversal. Threshold (ring) boundaries: TF1 outer-border red to blue; TF2 blue to red border; TF3 second red to blue border; TF4 center demagnetized multidomain. Red filling refers to unchanged magnetization direction compared to the initial saturated one, blue opposite magnetization direction, and grey is the multidomain state.

In order to have HI-AOS, the system needs to be close to the compensation point where the net magnetization is relatively low and anisotropy, which is proportional to the coercive field, is high. In this AOS thickness region we expect a strong reduction of anisotropy and a slight increase of net magnetization with temperature [128].

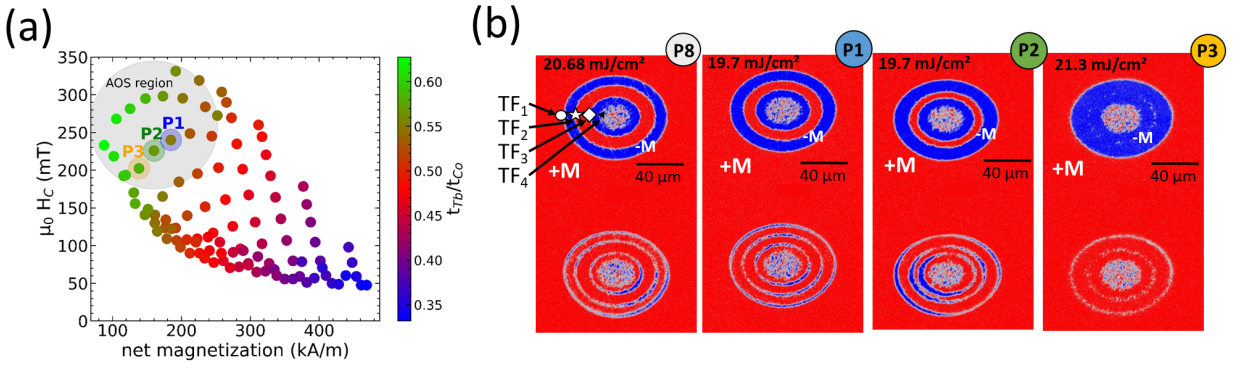

Fig. 3.10: All-optical switching in bottom-pinned AOS-MTJ stack annealed at 250°C for 10 min (sample AV68-23): (a) MOKE magnetometer measured coercive field vs net magnetization, $M_{S,\,Co}$ = 760 kA/m, $M_{S,\,Tb}$ = 1350 kA/m [132,133]. (b) Background subtracted images after first single with 50 fs laser pulse of different fluence.

The observations of Fig. 3.10(b) highlight that different thicknesses within the same sample's HI-AOS region can show different reversal patterns, for almost identical fluence values. This means that there must be some physical parameters that influence the final outcome. For positions P8, P1, and P2, the threshold fluences TF2 and TF3 are present defining the second ring having the same magnetization as the initial state (red contrast). The dependency of the threshold fluences is illustrated in Fig. 3.11 as both Tb and Co layer thicknesses increase. This data is the elaboration of the reversals shown in Fig. 3.10(b) plus the additional positions that were measured. As the thickness of Tb and Co increases, these thresholds converge, progressively nearing each other. At P3, with Tb: 0.86 nm / Co: 1.45 nm, they merge to create a unified reversed domain. In the next chapter we correlate this behavior to a possible increase in Gilbert damping due to the increased Tb content [134,135].

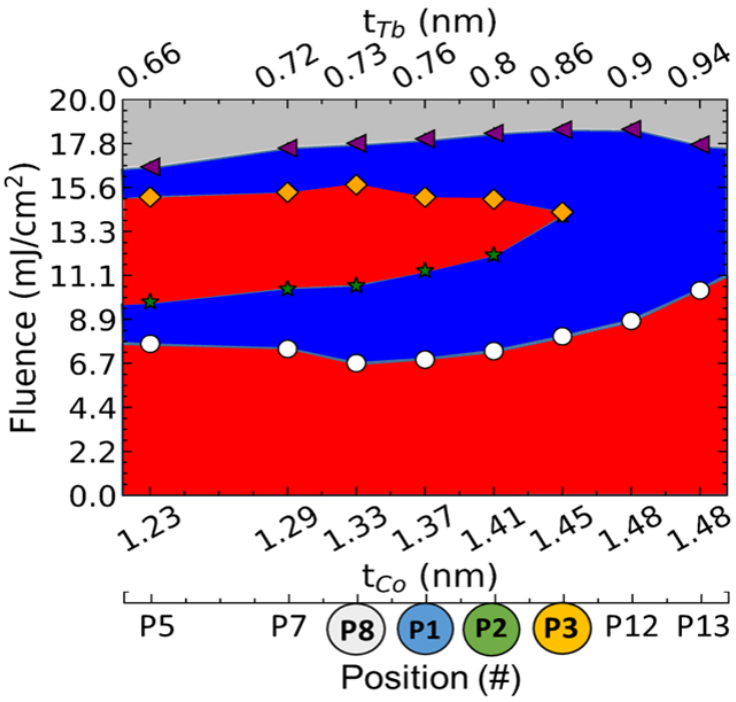

Fig. 3.11: All-optical switching in bottom-pinned AOS-MTJ stack annealed at 250°C for 10 min (sample AV68- 23): Tb and Co layers thickness vs Threshold fluence state diagram of the magnetization reversal. Red filling refers to unchanged magnetization direction compared to the initial saturated one, blue opposite magnetization direction, and grey is the multidomain state, P1 (t_{Co}: 1.37nm,t_{Tb}: 0.76 nm), P2 (t_{Co}: 1.41 nm,t_{Tb}: 0.80 nm) and P3(t_{Co}: 1.45 nm,t_{Tb}: 0.86 nm).

3.2.5 HI-AOS dynamics in Tb/Co multilayers

In this section, we present the work on the Tb/Co multilayer dynamics conducted by Kshiti Mishra from our collaboration with the *Radboud University* of Nijmegen. The effort on the sample from Avilés-Félix et al. [21] resulted in the publication entitle "Dynamics of all-optical single-shot switching of magnetization in Tb/Co multilayers" published in Physical Review Research (June 2023) [128].

The analysing of magnetization dynamics give key insights to better understand the mechanism at play during a reversal process. Using pump-probe MOKE spectroscopy, it was possible to examine the spatio-temporal aspects of the HI-AOS process, also known as toggle-switching, shown in Fig. 3.12.

The magnetization dynamics of the multilayers was analyzed for both Tb- and Co-rich compositions. In Fig. 3.12 (c)-(e) the magnetization dynamics are shown on a timescale of 200 ps for three distinct compositions, where the Tb thickness is fixed and the Co layer thickness varies. Common to all compositions is the ultrafast demagnetization occurring within 1 ps, succeeded by a also fast partial recovery of magnetization within the subsequent 10 ps. However, beyond this point, the magnetization dynamics diverges for the Tb- and Co-rich compositions. In the case of the Tb-rich composition [Tb(1.2 nm)/Co(0.9 nm)] shown in Fig. 3.12(c), the magnetization eventually stabilizes to a constant positive value, representing a partially demagnetized state. On the contrary, for the Co-rich compositions, namely Tb(1.2 nm)/Co(1.7 nm) in Fig. 3.12(d) and Tb(1.2 nm)/Co(1.8 nm) in Fig. 3.12(e), the rapid partial recovery of magnetization is followed by a slower reorientation

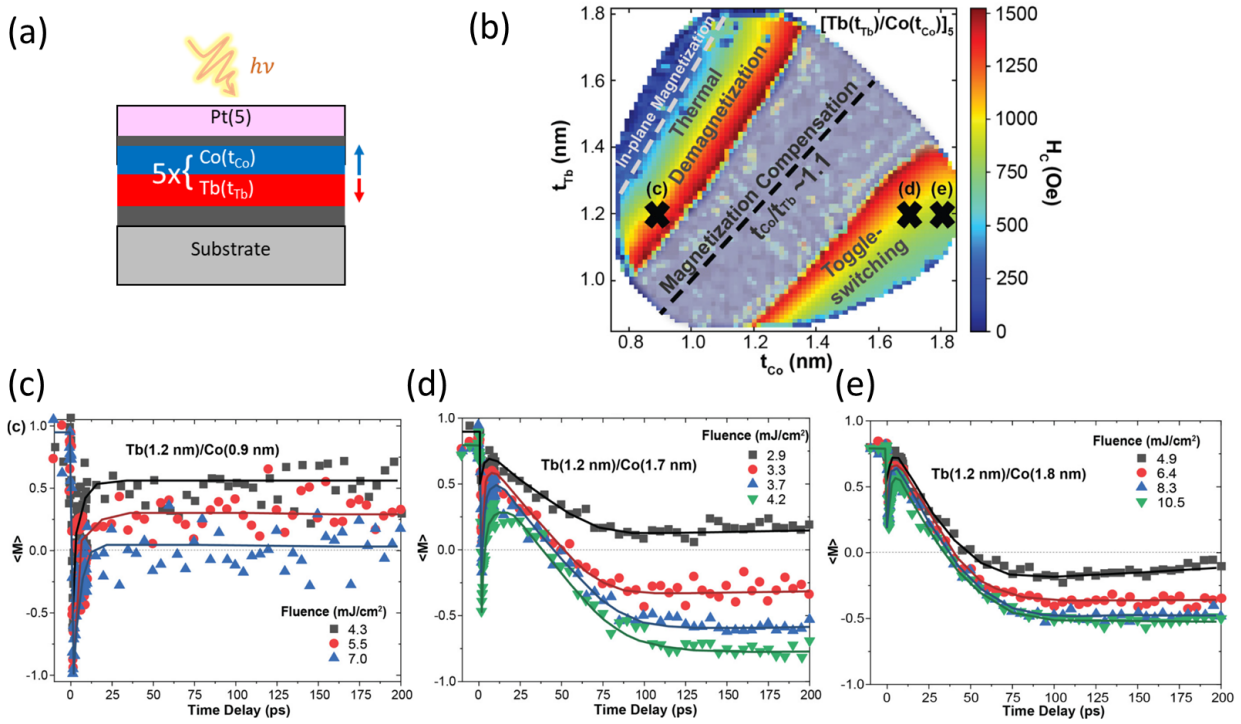

Fig. 3.12: Tb/Co magnetization dynamics [128]. The figure highlights (a) Magnetic stack schematics; (b) Coercive field Hc mapping of the Tb/Co multilayered sample. The Tb-rich region shows thermal demagnetization in response to a laser pulse, whereas the Co-rich region shows HI-AOS; (c)-(e) Calibrated magnetization dynamics measured for (c) $[\mathrm{Tb}(1.2\ \mathrm{nm})/\mathrm{Co}(0.9\ \mathrm{nm})]_5$ showing laser-induced thermal demagnetization; (d) $[\mathrm{Tb}(1.2\ \mathrm{nm})/\mathrm{Co}(1.7\ \mathrm{nm})]_5$ showing HI-AOS; and (e) $[\mathrm{Tb}(1.2\ \mathrm{nm})/\mathrm{Co}(1.8\ \mathrm{nm})]_5$ with a thicker Co layer, also showing HI-AOS. The different points were measured with different incident pump fluences as indicated, and the solid lines are a guide to the eye.

step, ultimately stabilizing at a constant negative value after approximately 75-100 ps (depending on composition). This final value corresponds to a homogeneously switched magnetic state, which tends to stabilize more rapidly for multilayer configurations with thicker Co layers.

Upon increasing the pump fluence, both the degree of ultra-fast demagnetization and the final magnetization value show an increase.

Given that the probe spot has a radius of approximately 20 µm, the measured signal integrates over spatially varying magnetization dynamics, that takes into account the whole Gaussian spot, thus all the distribution of fluence. This may result in trends that do not correspond to the local behavior at each fluence value, and we will come back to this point in Section 3.5.

Nevertheless, it seems natural to categorize the magnetization dynamics during HI-AOS into three steps: (i) ultrafast demagnetization, (ii) rapid partial magnetization recovery, characterized by an upturn in the detected signal, and (iii) a slower magnetization reorientation leading to eventual stabilization in the switched state. Notably, compared to the switching dynamics observed in GdFeCo alloys and Gd/Fe bi-/multilayers, the distinctive feature for the Tb/Co multilayer dynamics is the observed upturn in step (ii), regardless of what happens in the ultrafast step (i), where for some fluences a complete reversal is measured temporarily and for others not.

As anticipated from the state diagrams results, indeed the reversal of Tb/Co multilayer is slower than the sub-picosecond timescale, more specifically depending on composition and fluence, the reversal occurs between 50 and 120 ps.

3.3 Description of the magnetization reversal mechanism

The data we have presented thus far have enabled us to formulate a hypothesis regarding the underlying mechanism responsible for the optically induced reversal in our system. This mechanism appears to differ from what is observed in GdFeCo. Several key observations have led us to this hypothesis:

1. **Multilayer structure**: When terbium-cobalt (Tb-Co) forms an alloy, it does not exhibit the single-shot helicity-independent all-optical switching (HI-AOS) phenomenon. However, when Tb-Co is deposited as a multilayer structure, this unique phenomenon becomes evident.

2. **Resemblance to precessional driven domains**: The type of reversed rings we observe in our system bears a striking resemblance to the precession-driven domains seen in iron garnet [130]. However, in our case, there is no external field around which precession can occur. Thus, we need to identify the source of an effective field that breaks the symmetry and enables the switching process.

3. **TR-MOKE measurements**: Time-resolved magneto-optical Kerr effect (TR-MOKE) measurements reveal a clear magnetization reorientation following the initial ultrafast response, suggesting a slower dynamics that supports a precessional-type switching.

4. **Sperimagnetic behaviour**: As discussed in section 3.1.2, it is expected that Tb in combination with Co exhibits sperimagnetic behavior. Therefore, our system, compared to Co/Gd (which does not exhibit ring formations, as reported in [136]), is expected to have a uniaxial anisotropy that varies depending on local crystal-field interactions within the polycrystalline grains. This local anisotropy could be the missing element that breaks the symmetry and enables this type of reversal.

According to our hypothesis, the magnetization reversal is induced by a rapid decrease in the

local anisotropy due to the temperature rise caused by the laser pulse. This temperature increase creates an imbalance between the demagnetization field and the uniaxial anisotropy. Before the pulse, the uniaxial anisotropy dominates; however, at high temperatures, the demagnetization field becomes dominant. As the system cools down, the uniaxial anisotropy gradually reestablishes itself. The high Curie temperature of cobalt is crucial in maintaining magnetization and enabling it to precess around this ever-changing effective field.

It is important to note that the precession occurs for a duration determined by the cooling time and, thus, the energy absorbed, which is related to the laser fluence and not on the pulse duration. As the fluence increases, more time is needed to re-establish the anisotropy, and consequently, the number of rotations made by the magnetization during precession increases. Depending on whether the number of half-rotations is odd or even, the magnetization will end up either reversed or not reversed, resulting in the formation of concentric rings.

A more detailed analysis of this mechanism is presented in chapter 4. In the following section, we provide an overview of the experiments that have contributed significantly to our understanding of this process, further supporting the mechanism described above.

3.4 In-plane remanence and temperature dependent hysteresis loops

The magnetic properties of our systems were investigated through vibrating sample magnetormetry (VSM). The goal of these measurements was to evidence the high temperature dependency of the anisotropy in Tb/Co multilayers and investigate the presence of in-plane anisotropies originating from the sperimagnet nature of the system.

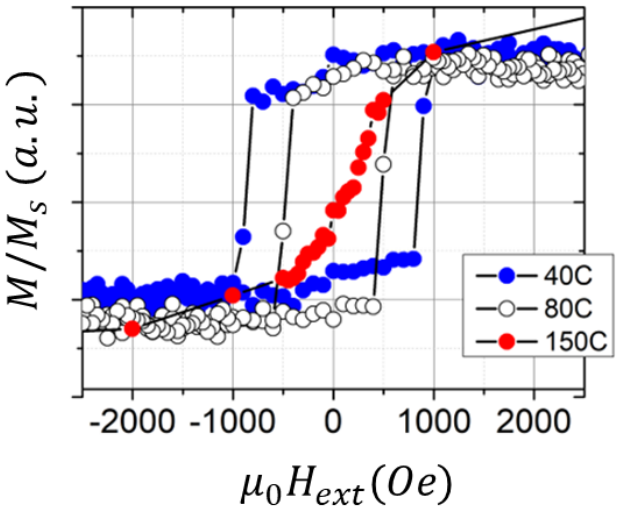

Fig. 3.13: Out-of-plane VSM hysteresis loops vs temperature of $[Tb(1.0\ nm)/Co(2.0\ nm)]_5$ multilayer.

In Fig. 3.13 it is shown the out-of-plane hysteresis loop at three different temperatures of Tb/Co multilayer sample in the Co rich region, in particular, the thicknesses of each layers are Tb 1.0 nm, Co 2.0 nm. As you can see the square loops for 40°C and 80°C with high coercivity are typical of out-of-plane magnetization, however, at 150°C the hysteresis loop shows a hard-axis behaviour

evidencing an in-plane magnetization, thus a magnetization reorientation has occurred within less than a hundred degrees.

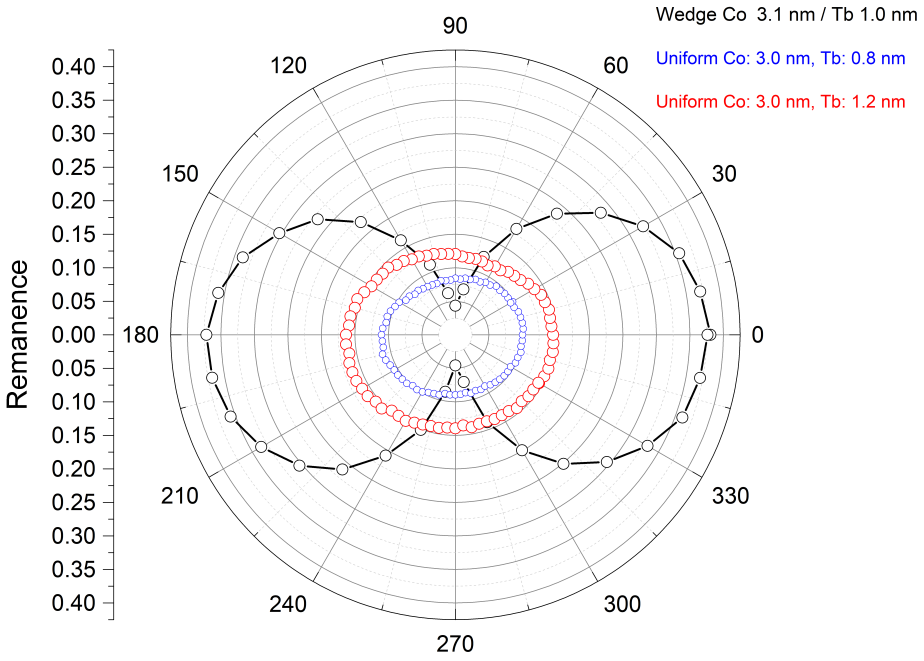

Fig. 3.14: Remenance magnetization extracted from VSM measurements of $[Tb/Co]_5$ multilayers. In black the sample deposited off-axis without rotation (wedge sample) at thicknesses $[Tb(1.0\ nm)/Co(3.1\ nm)]_5$, the red line and blue line for samples grown uniformly (on-axis with rotation) for thickness of $[Tb(1.2\ nm)/Co(3.0\ nm)]_5$ red points and $[Tb(0.8\ nm)/Co(3.0\ nm)]_5$ the blue points.

Instead, Fig. 3.14 represents the in-plane angular remanence of Tb/Co multilayer samples with thicker Co layers. In this case the out-of-plane anisotropy is not sufficient to overcome the demagnetization field and the magnetization of the sample is in-plane at room temperature. In the graph there are three distinct samples: the black line show the sample grown throw the wedge technique (off-axis without rotation) with thickness of Co and Tb of 3.1 nm and 1.0 nm respectively, the red line and blue line for samples grown uniformly (on-axis with rotation) for thickness of Co 3.0 nm and Tb 1.2 nm and the blue Co 3.0 nm and Tb 0.8 nm. It is evident that the type growth is influencing the in-plane anisotropy. The sample when grown off-axis shows a strong uniaxial remanence. However, what is remarkable is the fact that even for the samples uniformly deposited large remanence is observed with a small preferential direction. Indeed for pure Co layer no anisotropy is present and the observed remanence is 0 regardless of the angle of the applied field, but the presence of Tb drastically changes this aspect. However, the origin of this preferential direction is not fully understood.

3.5 Generalizing HI-AOS in RE-TM multilayers

This section presents the previously seen single-shot HI-AOS switching generalizing it to various multilayer, bilayer, and trilayer systems. We found that the helicity-independent switching is a

general phenomenon in Tb- and Dy-based multilayers, which have sperimagnetic properties coupled with transient metals. These results have been possible thanks to ANR (ANR-17-CE24-0007 UFO project) and the work of Yi Peng and colleagues; a thorough description of all the measurements and detailed stacks investigated (including more than 200 samples) can be found in her thesis [118] and in our published article: Peng et al., "In-plane reorientation induced single laser pulse magnetization reversal", Nature Communications 14(1):5000, 2023 [137]. The samples were deposited and measured at the *Institut Jean Lamour*, in Nancy.

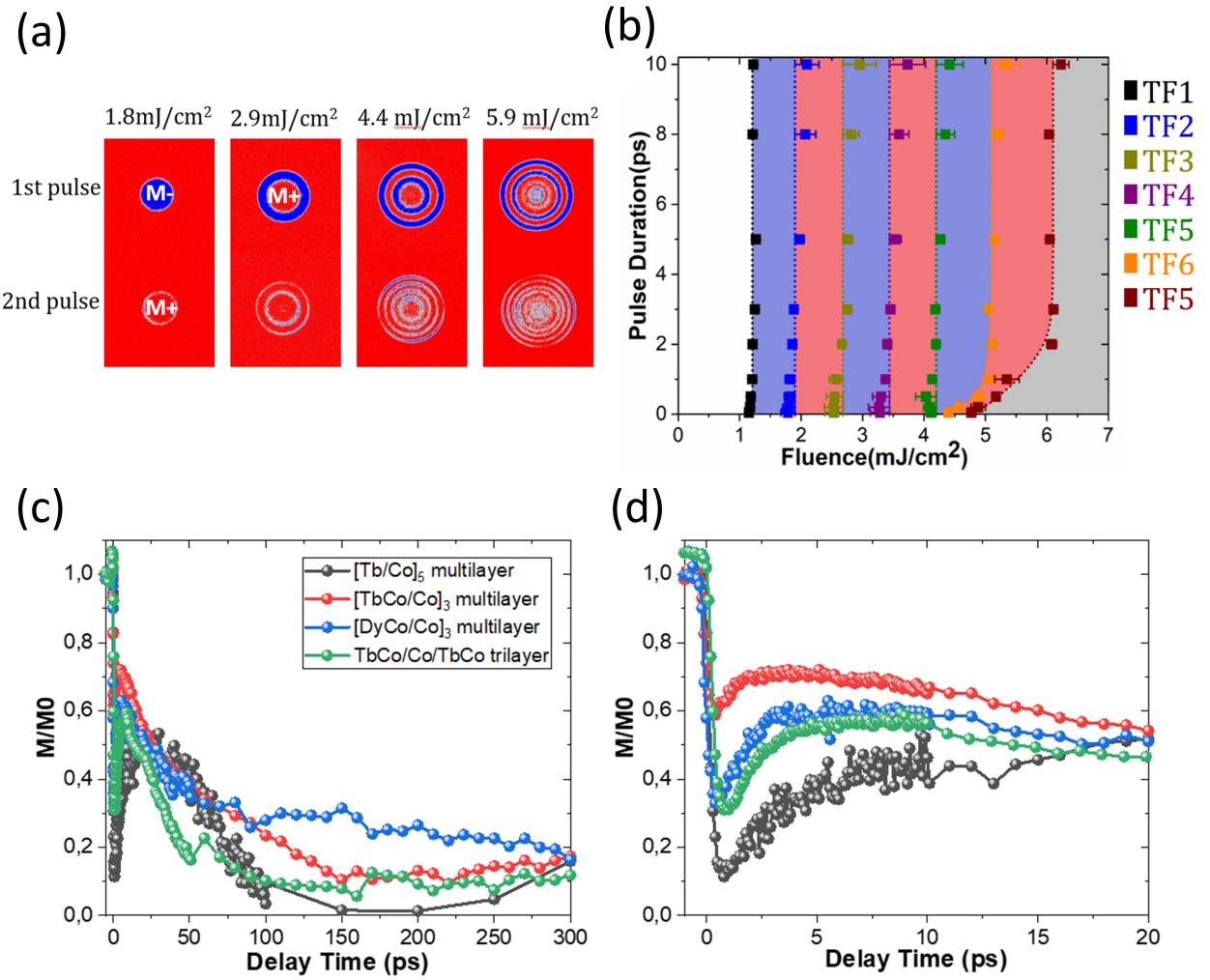

Fig. 3.15: Single pulse reversal in Tb32Co68(4)/Co(1.52nm)/Tb32Co68(4) trilayer. (a) Background subtracted images after first and second pulses with 50 fs laser pulse with different fluences; (b) State diagram which is plotted by pulse duration as a function of fluences. TF1 is the border for switching; TF2 is the border to two domains state, one ring; TF3 is the border to three domains state, two rings; etc. . . .TF7 is the border to demagnetized state at the center. The dotted lines are guide for the eyes. TR-MOKE measurements performed on the different multilayers showing single pulse reversal. (c) 300 ps time scale; (d) zoom-in of the first 20 ps time scale. The description of the stacks and conditions for TR-MOKE measurements have been show in Fig. 3.1. [137]

We limit ourselves to the main findings that were essential to verify the explanation and the model used to describe the observed phenomena in Tb/Co multilayers, details can be found in Peng's dissertation [118]. As HI-AOS switching was observed with Tb/Co multilayers, the first reasonable system to be investigated was Tb/Fe multilayers as Co and Fe have similar properties. Where the

exact same switching was achieved for a specific thicknesses with pulse-duration independent state diagrams and rings reversals. The investigation continued undergoing the path of analyzing the interfaces. A diffused interface is expected in our system, this means that somehow our multilayers could be seen as a RE/RE-TM alloy/TM where the RE-TM alloy is the interface between the layers. What happens if we expand this "interface" and shine a system composed of RE-TM alloy/ TM layer? The findings, as depicted in Fig. 3.15, confirmed that the reversal previously observed in Tb / Co multilayers extended to these new systems, exhibiting even more distinct rings and threshold fluences. In another experiment, Tb was replaced with Dy, a rare-earth element with with atomic number of 66 (compared to Tb's 65) which shares similar electronic configuration and thus similar properties, including high SOC, low Curie temperature, sperimagnet behavior. The results showed the same reversal features.

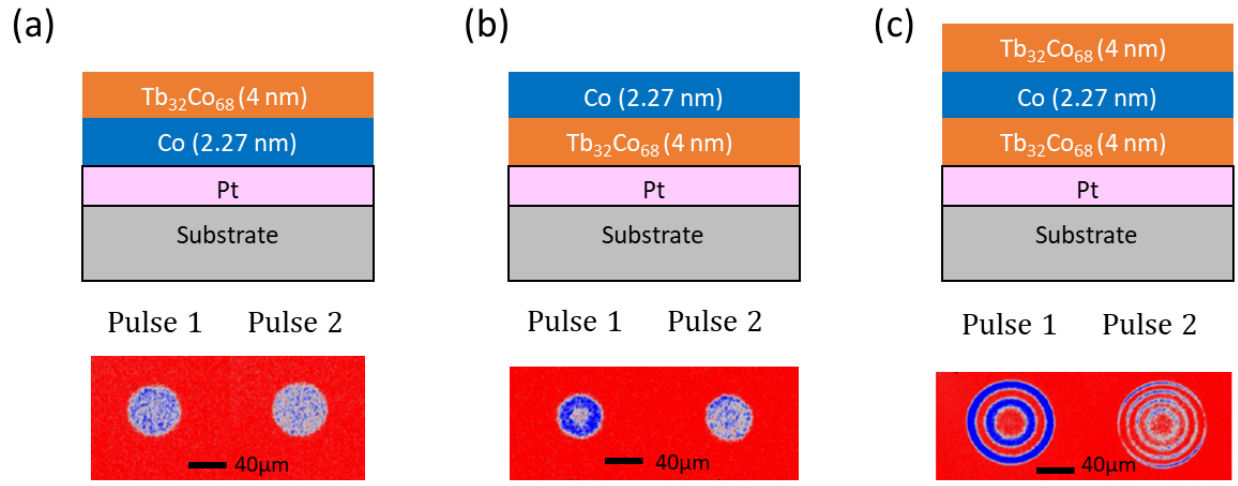

Fig. 3.16: Single laser pulse measurements in: (a) Pt/Co(2.27 nm)/$Tb_{32}Co_{68}$ bilayer, PMA from Pt/Co interface leads to only demagnetization; (b) Pt/$Tb_{32}Co_{68}$ (4 nm) /Co(2.27 nm) bilayer, AOS starting appearing; (c) Pt/$Tb_{32}Co_{68}$ (4 nm) /Co(2.27 nm)/$Tb_{32}Co_{68}$ trilayer, ring pattern AOS. [137]

The pivotal experiment that illustrates the significance of anisotropy in these systems is presented in Fig. 3.16. This experiment investigates the response to laser pulses in three distinct systems comprising Pt, Co, and $Tb_{32}Co_{68}$ alloy, with carefully adjusted layer configurations. In panel (a), we observe that Co is directly grown on Pt, a known setup that gives perpendicular magnetic anisotropy to Co. However, this anisotropy persists at higher temperatures, preventing the system from undergoing precession reorientation. The only result that can be obtained is the formation of a multidomain state when the sample is fully demagnetized.

On the contrary, in panel (b), we witness a different scenario where the anisotropy of the Co layer is induced by its interface with $Tb_{32}Co_{68}$ alloy. In this configuration, the reversal starts to manifest itself. The most favorable situation occurs when both interfaces are with $Tb_{32}Co_{68}$ alloy, facilitating the rapid reduction of anisotropy, panel (c).

This experiment underscores the critical role of anisotropy in these systems and highlights the conditions necessary for achieving the desired all-optical switching behavior.

Fig. 3.1 provides a comprehensive overview of the samples studied in the investigation, including their thickness variations, and highlights the specific thickness range where HI-AOS was

	Stacks		
1	[Tb(wedge)/Fe(wedge)]*4		
2	[Tb(wedge)/Co(wedge)]*5 (Cross wedge)		
3	$[Tb_{40}Co_{60}(x)/Co(wedge)]*3$	x = 1	
4		x = 2	
5		x = 3	
6		x = 4	
7		x = 5	
8		x = 7,5	
9	$[Dy_yCo_{100-y}$ (4) /Co(wedge)]*3	y = 25	
10		y = 30	
11		y = 35	
12	$Pt(5)/Co(wedge)/Tb_{32}Co_{68}$ (4)		
13	$Pt(5)/Co(wedge)/Tb_{32}Co_{68}$ (8)		
14	$Pt(5)/Co(wedge)/Tb_{32}Co_{68}$ (16)		
15	$Dy_{35}Co_{65}$ (4) /Co(wedge)/ $Dy_{35}Co_{65}$ (4)		
16	$Tb_{55}Fe_{45}$ (4) /Co(wedge)/ $Tb_{55}Fe_{45}$ (4)		
17	$Tb_{32}Co_{68}$ (4) /Co(wedge)/ $Tb_{32}Co_{68}$ (4)		
18	$Tb_{32}Co_{68}$ (4) /CoFeB(wedge)/ $Tb_{32}Co_{68}$ (4)		
	Thickness of the TM layer	0.8 nm 1.2 nm 1.6nm 2.0 nm 2.4 nm 2.8 nm 3.2 nm	
19	$Tb_{32}Co_{68}$ (4) /Permalloy (wedge)/ $Tb_{32}Co_{68}$ (4)		
		2.0 nm 2,6nm 3,2nm 3,8nm 4,4nm 5,0nm 5,6nm	

Table 3.1: Stacks that have been studied in this paper. 1-11 are multilayers, 12-14 are bilayers and 15-19 are trilayers. Light pink color shows the TM layer (including Co, Fe, CoFeB, Permalloy) thickness range that have been studied in this paper, while blue color shows the region of TM thickness where single shot switching occurs in different stacks. Note that stack 1 is a double wedge-sample in the same direction, while stack 2 is a cross-wedge sample. Numbers in parenthesis are the layer thicknesses in nanometers. [137]

observed. The investigation extended to trilayer structures like TbCo/X/TbCo (with X being Co, Py, and CoFeB), all of which exhibited the intriguing single-pulse magnetization reversal behavior. The presence of in-plane reorientation in these structures was identified as a crucial contributing factor. The study delved into exploring how film thickness, material composition, and anisotropy characteristics influenced the HI-AOS behavior.

This extensive study revealed that all these multilayer combinations exhibited a similar behavior when subjected to femtosecond to picosecond laser pulses, resulting in a magnetization reversal with a distinct ring-shaped pattern triggered by a single laser pulse. The perpendicular anisotropy in materials such as TbCo, DyCo, or TbFe alloys diminishes as the lattice temperature increases after the laser pulse. Consequently, the easiest multilayers to investigate were the TbCo/X/TbCo (X = Co, Py, CoFeB) and Y/Co/Y (Y = DyCo, TbFe) trilayers, where the perpendicular magnetic anisotropy was induced by the proximity to TbCo, DyCo, or TbFe alloys.

The key ingredient for the reversal is the persistence of the magnetization of the ferromagnetic (FM) layer due to its high Curie temperature (T_C), which arises from being composed of pure Co, Fe, Py, or CoFeB materials. In a scenario where magnetic grains or a couple of grains (identified as "magnetic" grains) behave independently, the magnetization exhibits precession around the local anisotropy axis, which is distributed from grain to grain.

To verify the presence of these grains, and thus a local distribution of easy axis orientations, a Magnetic Force Microscopy (MFM) image was recorded in the region of the layer that had been saturated before the experiments (see Fig. 3.17). A detailed examination of a magnetic force microscopy image (Fig. 3.17 a) shows how the ring-shaped structures form. To understand this process, we need to look at it on a smaller scale, focusing on a few grains in the TM layer.

First, the rings in the image do not have clear, sharp boundaries like in Fig. 5.25b. Instead, the separation between the domains in the rings is made up of many small domains that are tightly packed together, especially near the center of the separation (as shown in Fig. 3.17e). If we compare this with a domain wall in the middle of Fig. 3.17a, which existed before laser treatment, it has a much clearer and well-defined boundary (Fig. 3.17c).

Second, within the rings, we can see the presence of small domains, which range in size from 100 to 300 nm (as indicated by red circles in Fig. 3.17b and 3.17c). The number of these small domains increases as we move toward the center of the spot, especially when we increase the fluence (Fig. 3.17e). The rapid decrease and subsequent recovery of anisotropy within the transition metal-rare earth alloy (TM-RE), attributed to the notably low Curie temperature (T_C) of the rare earth component, led to reorientation of the magnetization of the FM layer in the plane and its subsequent precession.

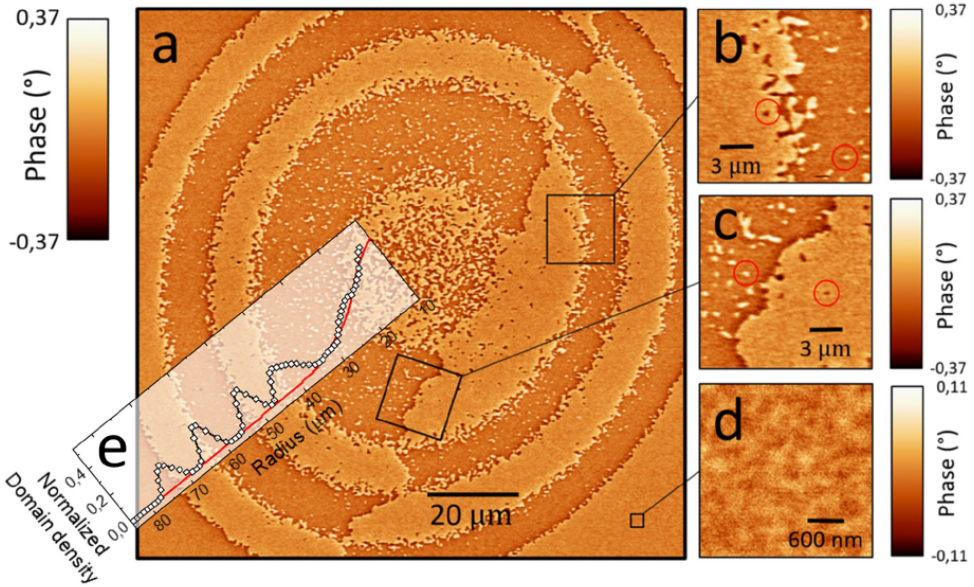

Fig. 3.17: Magnetic force microscopy investigation of a characteristic ring structure. (a) A ring structure observed by MFM. (b) Zoom on the region that separates two rings. (c) Zoom on a domain wall. (d) Zoom on a region outside the laser spot that has been saturated before the experiment. (e) Annular analysis of the small domain density. [137].

To eliminate the possibility that dipolar coupling is the cause of the reversed rings, we conducted

a straightforward test by slightly shifting two consecutive pulses. As illustrated in Fig. 3.18, it becomes evident that the magnetic state at a local level remains unaffected by the arrangement of neighboring initial domains and is solely determined by the distance from the central spot, specifically the local laser fluence.

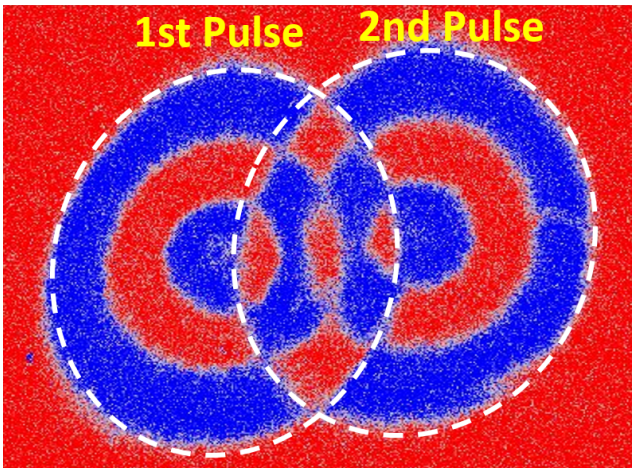

Fig. 3.18: Domain pattern obtained by sending 2 successive pulses: a first one and then, after moving the laser at a distance smaller than the spot size, a second one. The two spots are then over lapping. Experiment done on [Tb(1.31 nm)]/Fe(1.89 nm)]4 multilayer. The color scale corresponds to magnetization pointing out of plane: M+ (respectively M-) along the perpendicular to the film plane, along +z (resp. -z) in red (resp. in blue). The sample is initially saturated along the M+ direction. The laser pulse has a fluence of 4.4 mJ/cm2 and a duration of 50fs. [137]

3.6 Optimization of annealing resilience

This section presents the results of our efforts to enhance the resilience of the annealing temperature for our Tb/Co multilayer system.

Annealing is a crucial process in the development of magnetic tunnel junctions (MTJs), as discussed in Chapter 1. In conventional STT-MTJs, the efficiency of spin polarization plays a major role in determining the final tunnel magnetoresistance ratio (TMR) and spin-torque efficiency. These factors directly impact the readability of memory cells and the critical current required to switch the magnetization of the storage layer.

One key to optimizing the properties of MTJs is achieving an epitaxial texture on magnetic electrodes that matches the crystalline bcc (001) structure of the MgO barrier, as highlighted by Yuasa et al [138]. A significant breakthrough in sputtered MTJs was achieved by incorporating boron into the composition of the MTJ electrodes. Typically, CoFe-based magnetic electrodes grow naturally with fcc (111) structures. However, when a CoFeB target is sputtered, the deposited electrodes initially remain amorphous on both sides of the tunnel barrier. Subsequently, the MgO barrier grows with a rough (001) bcc texture on top of the amorphous CoFeB magnetic electrode. To crystallize the electrodes and improve the crystallinity of the MgO barrier, the electrode/MgO/electrode stack undergoes annealing within the temperature range of 250°C to 400°C.

In our specific case, all magnetic electrodes in the MTJ stacks consist of an iron-rich $Fe_{72}Co_8B_{20}$ alloy [139]. During annealing, boron atoms diffuse out of the FeCoB alloy and form boride com-

pounds with the nonmagnetic layers in contact with the amorphous FeCoB electrodes [140]. These non-magnetic layers typically consist of metals such as Ta, Mo, or W [141–144]. The already-textured MgO barrier further crystallizes during this process, acting as a seed layer for the crystalline growth of FeCo.

In our standard MTJ process, annealing involves maintaining the structure at 300°C for 10 minutes under a pressure of 10^{-6} mbar, without the application of an external magnetic field. To enhance the annealing temperature resilience in our Tb/Co-based MTJ, we introduced a capping MgO layer above the multilayer. This modification provided sufficient anisotropy to withstand subsequent annealing steps, each lasting 10 minutes, at temperatures of 250°C, 275°C, and 300°C, as illustrated in Fig. 3.19.

This approach allowed us to increase the resilience of the annealing process of our Tb/Co-based MTJ system while still keeping the HI-AOS properties.

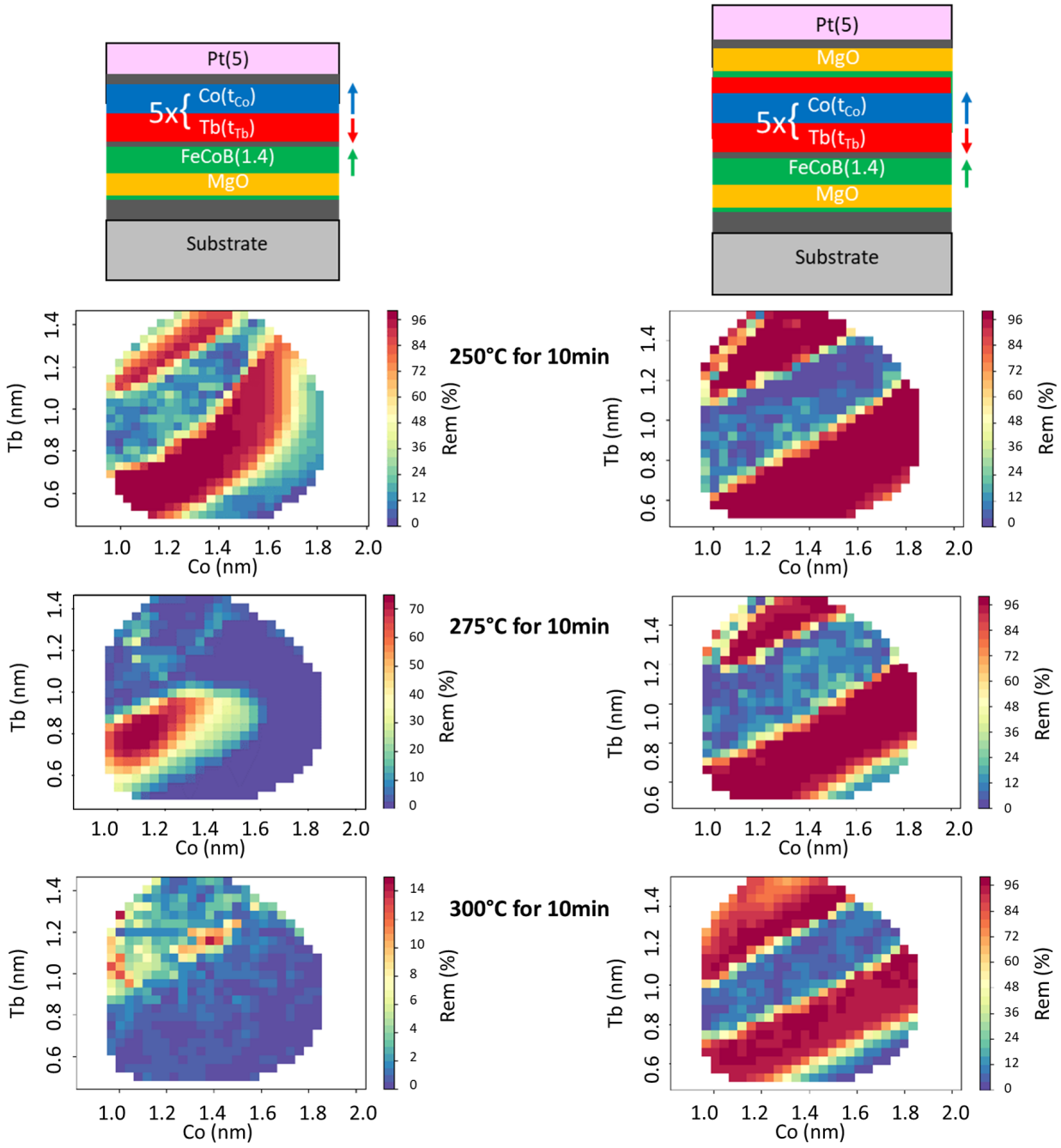

Fig. 3.19: MOKE mapping showing the perpendicular remanence magnetization of half-MTJ stack (top row) and MgO-capping Stack (bottom) after subsequent annealing steps each of 10 min at 250°C, 275°C and 300°C.

3.7 Conclusion

This chapter showed a comprehensive exploration of the phenomenon of HI-AOS in RE-TM multilayer systems. Through a series of experiments and analyzes, several key insights regarding the mechanism and generalizability of HI-AOS in these unique multilayer structures were gained.

In conclusion, the investigation of the behavior of AOS in the $[Tb/Co]_5$ multilayer system has revealed some intriguing and unexpected findings. The study began by focusing on identifying the region for complete and reliable magnetization reversal at lower fluences, but it expanded to explore the response of this system under higher fluence conditions and across different pulse durations. Here are the key takeaways from the research:

1. **Distinct reversal phenomenon**: At high fluences, the reversed domains exhibit a unique pattern of concentric rings with opposite magnetic orientations. This intriguing phenomenon is not observed in gadolinium-based samples, and the commonly accepted explanation for magnetization reversal in Gd samples does not apply to this case.

2. **Pulse duration independence**: Perhaps the most significant finding is that the fluences required to reverse and stabilize a specific number of rings showed little to no dependence on the duration of the laser pulses. This indicates that the magnetization reversal process occurs on a longer time scale.

The investigation began by proposing a hypothesis to explain the underlying mechanism behind HI-AOS in RE-TM multilayers. This hypothesis pointed to the significance of the local anisotropy in these systems, which rapidly decreases as a result of the temperature increases caused by the laser pulse. The subsequent reduction in the anisotropy compared to the demagnetization field enables the magnetization of the ferromagnetic layer to reorient and precess, ultimately leading to the formation of concentric rings in the magnetization pattern. This mechanism was supported by various experiments, TR-MOKE measurements, and MFM images, all of which provided essential insights into the behavior of these systems.

The exploration expanded to a broad range of multilayer configurations, including different RE-TM alloys, bilayers, trilayers, and interfaces, to investigate the generality of HI-AOS. The results consistently showed that the phenomenon extended to various multilayer combinations, highlighting the role of anisotropy and the presence of a high Curie temperature in the ferromagnetic layers. Furthermore, it was observed that these rings of magnetization domains were not primarily influenced by dipolar coupling but were solely determined by the distance from the central laser spot.

In the quest to develop magnetic tunnel junctions, annealing is a crucial step. The challenge was to optimize the annealing process while preserving the HI-AOS properties of the Tb/Co multilayer system. A layer of MgO capping was introduced above the multilayer, allowing it to withstand subsequent annealing at temperatures ranging from 250°C to 300°C. This innovation successfully increased the annealing temperature resistance of the Tb/Co-based MTJ, enhancing its performance while retaining the unique HI-AOS characteristics. Moreover, complete MTJ stacks were studied, comprising the reference layer and the ITO (transparent conductive electrode), showing the same laser induced phenomenon.

This chapter has provided an overview of the mechanism of HI-AOS in RE-TM multilayers,

its applicability to various configurations, and the issue of annealing resistance in the development of RE-TM-based magnetic tunnel junctions. These findings not only deepen our understanding of these special systems, but also create new opportunities for their use in the development of new technologies and devices.

Chapter 4

Modelling of HI-AOS in multilayer systems

Contents

4.1 Introduction

In this chapter, we present the different theoretical approaches that have been used to understand the various physical phenomena presented in this thesis. Starting by exposing a theory of laser pulse absorption which is approximated as a simple heating effect in the two temperature model

(2TM). Then the developed model that couples the 2TM to a macrospin algorithm is presented. It was utilized to phenomenologically simulate the optically driven magnetization reversal. After showing the obtained results a second investigation based on an atomistic spin approach is shown to complement the study.

4.2 Laser absorption and numerical implementation of the two-temperature model (2TM)

The two-temperature model is employed to simulate the rapid reaction of a metallic materials to ultrafast laser pulses that cause heating. This model characterizes the system by dividing it into two reservoirs: one for the electrons, referred to as the electron bath, and the other for the lattice, known as the phonon bath, schematics in Fig. 4.1. More particularly, it involves rate equations to describe how the temperatures of both electrons and phonons change over time. The semiclassical two-temperature model was derived by Chen et al., based on the Boltzmann transport equation, offering a proper description of non-equilibrium electron effects [145]. The usual method for ultrafast magnetization dynamics involves integrating this model into atomistic spin models [146] or Landau-Lifshitz-Bloch (LLB) simulations [147,148], thereby facilitating the simulation of the rapid magnetic response when materials are heated by femtosecond laser excitation. However, as we will discuss, our approach will diverge slightly as we leverage certain approximations made possible by the unique characteristics of our studied phenomenon.

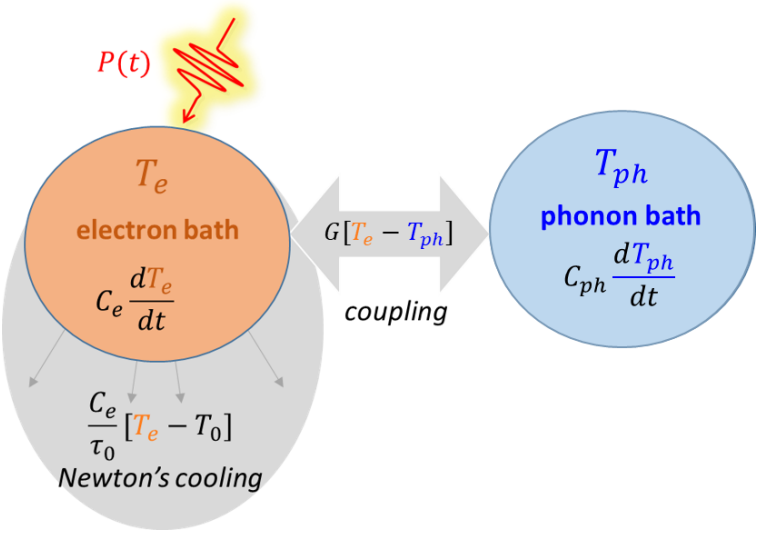

Fig. 4.1: Two temperature model schematics.

Each bath has its own heat capacity C_i $(i = e, ph)$ and exchanges energy through the coupling parameter G, where e and ph stand for electron and phonon respectively. The laser pulse excitation heats the electron bath and, neglecting thermal diffusion, the equations of the two temperature model used to describe the ultrafast laser heating are:

$$C_e \frac{dT_e(t)}{dt} = -G[T_e(t) - T_{ph}(t)] + P(t) - \frac{1}{t_0}[T_e(t) - T_0(t)] \tag{4.1}$$

$$C_{ph} \frac{dT_{ph}(t)}{dt} = G[T_e(t) - T_{ph}(t)] \tag{4.2}$$

$$P(t) = P_0 \cdot \exp - \frac{(t - t_0)^2}{\tau_L^2/(4ln2)} \tag{4.3}$$

$$P_0 = \frac{F\mu_a}{t_{FM}\tau_L} \tag{4.4}$$

Here, $P(t)$ represents the external power injected by the laser pulses, with key parameters such as μ_a, F, t_{FM}, and τ_L signifying the absorption coefficient, laser fluence, layer thickness, and pulse duration, respectively. Equation (4.1) also incorporate a Newton's cooling term, responsible for returning the system to room temperature following the laser pulse, characterized by the characteristic cooling time t_0 [149].

4.3 Analysing laser pulse duration effects and implications

Assuming that all-optical switching occurs due to a rapid temperature increase exceeding a specific threshold, we can elucidate some intriguing insights. In fact, the unique characteristics of the experimental state diagrams can be comprehended considering solely the framework of the 2TM.

In Fig. 4.2 it is shown the time evolution of the electron temperature T_e and phonon temperature T_{ph} upon varying the laser fluence and/or pulse duration. As expected, increasing fluence rises both electron and phonon temperatures, Fig. 4.2(a) but, interestingly, with constant fluence the electron temperature peak reduces drastically upon increasing the pulse duration, e.g. from 100 fs to 1 ps at F = 5.0 mJ/cm^2 the T_e peak drops of ∼500K. The HI-AOS mechanism in GdFeCo alloy, as mentioned, has been related to a difference in the characteristic demagnetization time of the two sublattices (Gd and Fe/Co) that have to demagnetize almost completely in order to switch. Because the TM sub-lattice has the higher T_C and its magnetic properties come from the 3d electrons, it makes sense that, to switch, the electron temperature T_e needs to approach T_C and thus due to dependency on the pulse duration shown in Fig. 4.2, the resulting state diagram has a triangular shape Fig. 1.10 [98], where longer pulse duration need higher fluences to reach the same temperatures. In contrast, for a precessional switching, it is not required to completely demagnetize the TM, or at least it is not crucial. What seems to be important is the cooling time as we will discuss in the following.

As outlined in the preceding chapter, the fluence required to reverse and stabilize a specific number of rings in [Tb/Co] multilayers shows little to no dependence on the laser pulse duration. Single-pulse reversals was achieved for pulse durations ranging from 50 fs up to 12 ps, the maximum available pulse duration on our laser setup. The possible origin of these peculiar AOS properties point to an in-plane magnetization reorientation with a precessional switching mechanism and similarities between the state diagrams observed in Tb/Fe, and $Tb_{32}Co_{68}$/Co/ $Tb_{32}Co_{68}$ trilayer [137] and those of [Tb/Co] multilayers indicate a common magnetization reversal process.

Considering the two temperature model described earlier, at the short time scale up to a few ps the behaviour of the electron temperature T_e is highly dependent on the laser pulse duration, see Fig. 4.2. Within few ps the T_e relaxes to the phonon temperature T_{ph} and, from there on, the time evolution of the two becomes indistinguishable. For longer times, in the order of tens/hundreds of ps, the temperatures evolution are mainly influenced by the absorbed laser fluence and cooling of the system to the thermal bath. Based on the experimental results, we understand that the key dynamics for the reversal occur during this second time phase. This interpretation is based on the

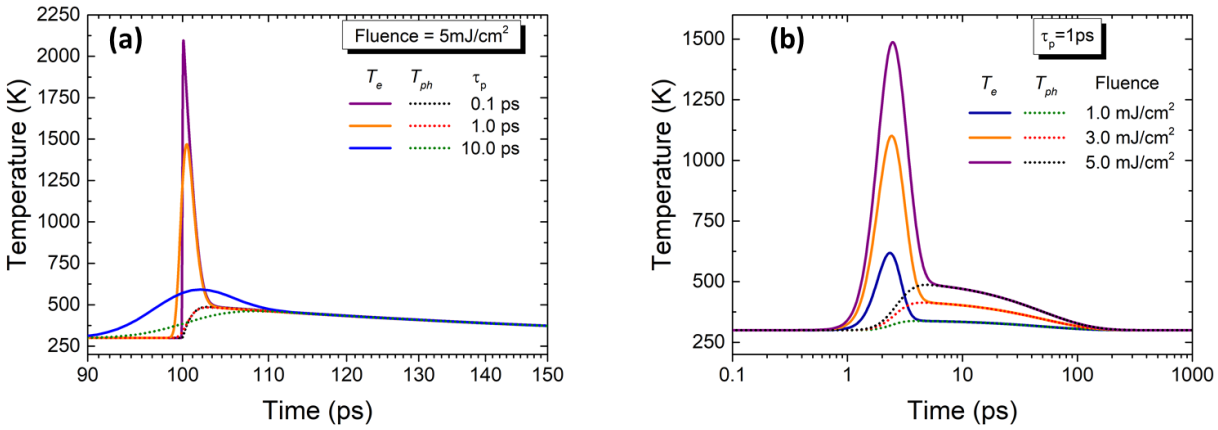

Fig. 4.2: Time evolution of the T_e and T_{ph}, according with 2T model a) for constant pulse duration of 1 ps and variable fluence and b) constant fluence of 5.0 mJ/cm^2 and variable pulse duration respectively. Simulation parameters: t_{FM}=100 nm, T_0=300 K, G $= 2.5 \cdot 10^{17}\ W \cdot m^{-3}K^{-1}$, $C_e = \gamma T_e = 225\ Jm^{-3}K^{-2}$ Te and $C_{ph} = 2.6 \cdot 10^6\ Jm^{-3}K^{-1}$ [100,150].

fact that super-diffusive spin currents [129], hot electrons and ultrafast demagnetization are effects highly dependent on pulse duration. This is contrary to our experimental observations where the final reversed state is essentially independent of the laser pulse length up to 12 ps and probably beyond. The initial fast response phase certainly plays a role at the beginning of the reversal, and may be more important for fs pulses, but does not determine the end-state. Hence, we developed a phenomenological macrospin model based on the Landau-Lifshitz-Gilbert equation coupled to the two temperature model to assess whether the above assumptions are consistent with the main features of our observations, providing an insight into the underlying reversal process taking place at the ps timescale.

4.4 Macrospin study of Tb-Dy based multilayers HI-AOS

In this section, we present the theoretical framework used to simulate the precession-driven switching observed in our samples after the application of a short laser pulse.

Our systems is expected to have a distribution of uniaxal anisotropy directions between what are referred as magnetic grains. We assume that they respond independently to the laser heating based on the MFM images (Fig. 3.17) where different outcomes are seen for neighbouring grains. With these assumptions, each magnetic grain was simulated separately having a uniform magnetization with its own uniaxial anisotropy. The magnetization dynamics of each grain is not influenced by the other grains, they are independent (or isolated), see Fig. 4.3.

The model incorporates two essential features that are crucial for retrieving the physical phenomena observed experimentally:

1. **Temperature-dependent uniaxial anisotropy (K_u):** The uniaxial anisotropy, denoted as K_u, exhibits a rapid decrease with temperature. This effect is taken into account to capture the temperature-induced changes in the material.

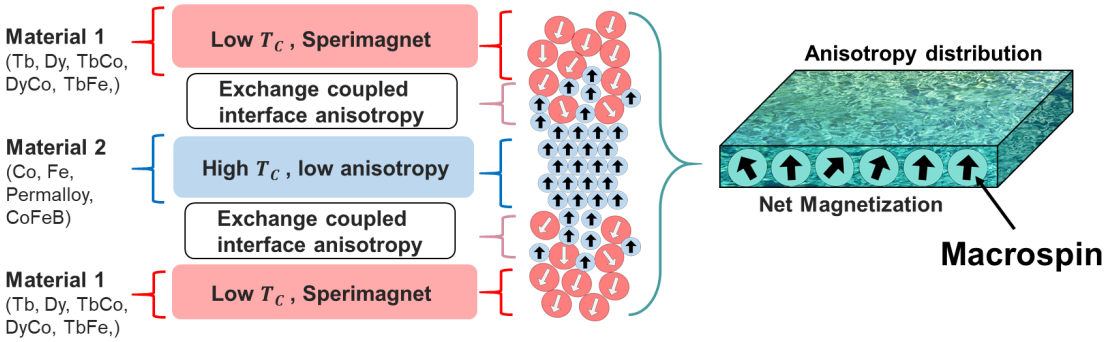

Fig. 4.3: Schematics of the system composed of individual grains. Each grain is simulated as a individual isolated macrospin.

2. **Tilted uniaxial anisotropy axis:** The uniaxial anisotropy axis is slightly tilted relative to the out-of-plane direction. This tilt is characterized by the unit vector $\mathbf{u}_k = (\sin\theta_u, 0, \cos\theta_u)$, where θ_u is greater than 0°. Note that selecting the direction of the tilt along x was done by convention, changing it does not affect the results. From grain to grain this direction is expected to vary.

4.4.1 Model and material parameters

The dynamics of the unitary vector of the magnetization ($\mathbf{m}$) are described by the Landau-Lifshitz-Gilbert (LLG) equation, see 1.21 in chapter 1. Defining the reduced time as $\tau = \frac{\mu_0\gamma}{1+\alpha^2}t$, the equation 1.21 for $\mathbf{m}$ becomes:

$$\frac{d\mathbf{m}}{d\tau} = -(\mathbf{m}\times\mathbf{H}_{\text{eff}}) + \alpha\left[\mathbf{m}\times(\mathbf{m}\times\mathbf{H}_{\text{eff}})\right] \tag{4.5}$$

Here, α represents the Gilbert damping constant, γ is the gyromagnetic ratio, and t denotes time.

The effective magnetic field ($\mathbf{H}_{\text{eff}}$) is derived as the functional derivative of the Gibbs' free energy density (E_{tot}) with respect to the magnetization ($\mathbf{m}$):

$$\mathbf{H}_{\text{eff}} = -\frac{\mathbf{1}}{\mu_0 M_S}\frac{\delta E_{\text{tot}}}{\delta \mathbf{m}} \tag{4.6}$$

The total Gibbs' free energy density (E_{tot}) in our case is composed of three main contributions:

1. **Demagnetizing energy density:** This term incorporates the effects of the demagnetization tensor (N_x, N_y, N_z) and the magnetization components:

$$E_d = \frac{1}{2}\mu_0 M_s^2\left(N_x m_x^2 + N_y m_y^2 + N_z m_z^2\right) \tag{4.7}$$

Here, μ_0 represents the vacuum magnetic permeability and note that $N_x + N_y + N_z = 1$.

2. **Anisotropy energy density**: This term accounts for the tilted magnetocrystalline anisotropy (MCA) axis and the temperature-dependent uniaxial anisotropy ($K_u(T)$):

$$E_{ani} = -K_u\left(\mathbf{u_k}\cdot\mathbf{m}\right)^2 \tag{4.8}$$

Here, $\mathbf{u_k}$ is the unit vector representing the tilt of the MCA axis.

3. **Zeeman energy density**: The Zeeman energy density, accounting for the externally applied magnetic field $\mathbf{H}_{\text{ext}}$, is expressed as:

$$E_{\text{Zeeman}} = -\mu_0 M_S(\mathbf{m} \cdot \mathbf{H}_{\text{ext}}) \tag{4.9}$$

The total energy density will read:

$$E_{\text{tot}} = -K_u \left(\mathbf{u_k} \cdot \mathbf{m}\right)^2 + \frac{1}{2}\mu_0 M_s^2 \left(N_x m_x^2 + N_y m_y^2 + N_z m_z^2\right) - \mu_0 M_S(\mathbf{m} \cdot \mathbf{H}_{\text{ext}}) \tag{4.10}$$

taking the tilt of the anisotropy along x we have $\mathbf{u_k} = \begin{pmatrix} u_x & 0 & u_z \end{pmatrix}$ and $u_x^2 + u_z^2 = 1$

$$\begin{aligned} E_{\text{tot}} = &- K_u \left(u_x^2 m_x^2 + u_z^2 m_z^2 + 2u_x u_z m_x m_z\right) \\ &+ K_d \left[\left(N_x - N_y\right) m_x^2 + \left(N_z - N_y\right) m_z^2 + N_y\right] \\ &- \mu_0 M_S(\mathbf{m} \cdot \mathbf{H}_{\text{ext}}) \end{aligned} \tag{4.11}$$

With $K_d = \frac{1}{2}\mu_0 M_s^2$.

4.4.1.1 Continuous film approximation

In a specific case where $N_x = N_y = 0$ and $N_z = 1$, the energy E_{tot} and the effective field $\mathbf{H}_{\text{eff}}$ undergo simplifications. The energy density of the system, assuming this continuous film approximation, is given by,

$$E_{tot} = -K_u(\mathbf{u_k} \cdot \mathbf{m})^2 + \frac{1}{2}\mu_0 M_S^2 m_z^2 - \mu_0 M_S(\mathbf{m} \cdot \mathbf{H}_{\text{ext}}) \tag{4.12}$$

$$E_{tot} = -K_u u_x^2 m_x^2 - K_{eff,z} m_z^2 - 2K_u u_x u_z m_x m_z - \mu_0 M_S(\mathbf{m} \cdot \mathbf{H}_{\text{ext}}) \tag{4.13}$$

$$\mathbf{H}_{\text{eff}} = \frac{2}{\mu_0 M_S} \begin{pmatrix} K_u u_x^2 m_x + K_u u_x u_z m_z \\ 0 \\ K_u u_x u_z m_x + K_{eff,z} m_z \end{pmatrix} + \mathbf{H}_{\text{ext}} \tag{4.14}$$

With $K_{eff,z}$ defined as $K_{eff,z} = \left[K_u u_z^2 - K_d \left(N_z - N_y\right)\right]$.

According to the reference [151], the phenomenological relation used in our model for the anisotropy temperature dependency is:

$$K_u(T) = K_{u,RT}\left[1 - \left(\frac{T}{T_{Crit}}\right)^{1.73}\right]^2 \tag{4.15}$$

where $K_{u,RT}$ is the uniaxial-anisotropy at room temperature (300 K) and $T_{Crit} = 450$ K is a critical temperature that was determined both by the measured blocking temperature, and supported by VSM measurement of Chapter 3. As a first approximation the simulations were performed with M_s independent of temperature, and consequently constant shape anisotropy. This strong approximation is backed up by the atomistic spin simulations shown in the following, where net magnetization

is shown as a function of temperature. For the specific Co rich region where AOS is observed, we see that the magnetization is not reducing but actually increasing, see Fig. 3.4, but as this increase is not pronounced in the simulated temperature range this seems to be a reasonable approximation for the model. Furthermore, the fact that the Co rich region is expected to increase M_s with temperature would further promote the in-plane reorientation. This instead is not true for the Tb rich region where the M_s is expected to drop fast with temperature, and no AOS is observed.

It's crucial to emphasize that the simulation simplifies the system by representing it as an effective single macrospin. While this simplification is quite strong and may raise questions, the simulation's primary aim is to elucidate the reversal dynamics of transition metals undergoing rapid changes in anisotropy. These changes occur due to the interface between RE and TM and the low Curie temperature of the RE. Unlike the RE, the TM has a high Curie temperature. As the temperature increases, the anisotropy diminishes and then begins to recover during the cooling phase. During this process, the TM, which has not fully demagnetized, undergoes a reorientation driven by the evolving balance between the demagnetizing field and the anisotropy field. This results in precessional dynamics that ultimately lead to magnetization reversal, depending on the energy of the laser pulse. The parameters used during the simulations are reported in Table 4.1.

Table 4.1: Material parameters used in macrospin simulations

Description	**Parameter**	**Standard Value**	**Range**
Uniaxial anisotropy tilt angle from z	θ_u	5°	(0° - 45°)
Magnetization saturation	M_s	760 kA/m [133]	-
Q factor $= K_u/K_d = 2K_u/\mu_0 M_S^2$	Q	1.1	1.0 - 1.3
Uniaxial Anisotropy	$K_{u,RT}$	$K_{u,RT} = 1.1K_d$	$K_{u,RT} = \mathrm{Q}(300K)K_d$
Temperature	T_0	300 K	-
Critical temperature	T_{Crit}	450 K	-
Bohr magneton	μ_B	9.274×10^{-24} J/T	-
Permeability constant	μ_0	1.2566×10^{-6} Tm/A	-
Demagnetizing tensor	(N_x, N_y, N_y)	(0,0,1)	-
Gyromagnetic ratio	γ	1.760859×10^{11} 1/Ts	-
Electron-phonon coupling	G	$2.5 \cdot 10^{17}\ W \cdot m^{-3}K^{-1}$	-
Phonon heat capacity	C_{ph}	$2.6 \cdot 10^{6}\ Jm^{-3}K^{-1}$	-
Electron heat capacity (at 300K)	C_e	$225T_e\ Jm^{-3}K^{-1}$	-
Characteristic cooling time	t_0	50 ps	$20 - 50$ ps
Pulse duration	τ_L	1 ps	$0.1 - 10$ ps
Absorption	μ_a	0.2	-
Gilbert damping	α	0.1	0.05 - 0.2

4.4.2 Simulation results

4.4.2.1 Magnetization reversal dynamics and critical threshold fluences

Simulations were performed investigating the impact of a the laser fluence, and the corresponding anisotropy drop, to a system with perfectly out-of-plane anisotropy, hence axis along z. The results are shown in Fig. 4.4. Furthermore, we introduce the the Q factor (Q factor $= \frac{K_u}{K_d} = \frac{2K_u}{\mu_0 M_S^2}$) that value will determine if the systems uniaxial anisotropy is dominating the demagnetizing field or not. The results show that after the laser pulse, the demagnetizing field overcomes the anisotropy, the magnetization starts precessing towards the plane. If $\theta_u = 0°$ the precession occurs only around the z axis and no crossing of the x,y plane is possible.

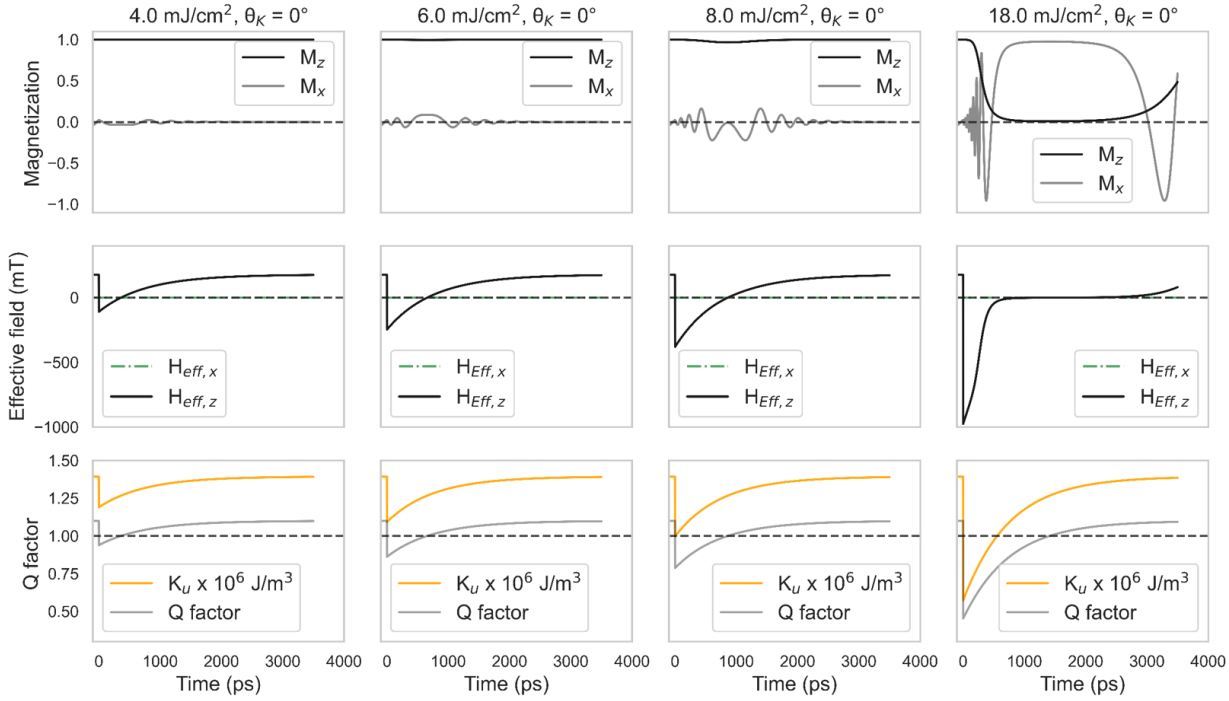

Fig. 4.4: Time traces of m_x, m_z, $H_{eff,\,x}$, $H_{eff,\,z}$ and K_u for $\theta_u = 0^o$ fluences 4.0 mJ/cm^2, 6.0 mJ/cm^2, 8.0 mJ/cm^2, 18.0 mJ/cm^2. Simulations performed with $M_s = 760$ kA/m and $K_{u,300K} = 1.1 \cdot K_d$, Gilbert damping $\alpha = 0.1$. [152]

The picture changes when a non-zero anisotropy axis angle with respect to the z direction is present. In Fig. 4.5 the macropsin calculation for the same four fluence values are illustrated. This time, a $\theta_u = 5°$ was chosen for the simulations to compare to Fig. 4.4, both cases were using a Gilbert damping $\alpha = 0.1$. The small tilt introduces a x component in the effective field ($H_{eff,\,x}$) that strongly affects the trajectory of the magnetization and drives the reversal. The precession occurs for a time that depends on the energy absorbed, i.e. the laser fluence. The anisotropy field recovers during the precession due to cooling ($K_d < K_u$). As the fluence increases, the number of rotations made by the magnetization during precession increases, as you can see by the x component of the magnetization in the last column of Fig. 4.5. Depending whether the number of half-rotations is odd or even, the magnetization will end up as reversed or not reversed. As the laser spot has a Gaussian profile, with lower fluence outside and increasing moving towards the inside, the resulting reversed pattern will show concentric rings, as shown in Chapter 3.

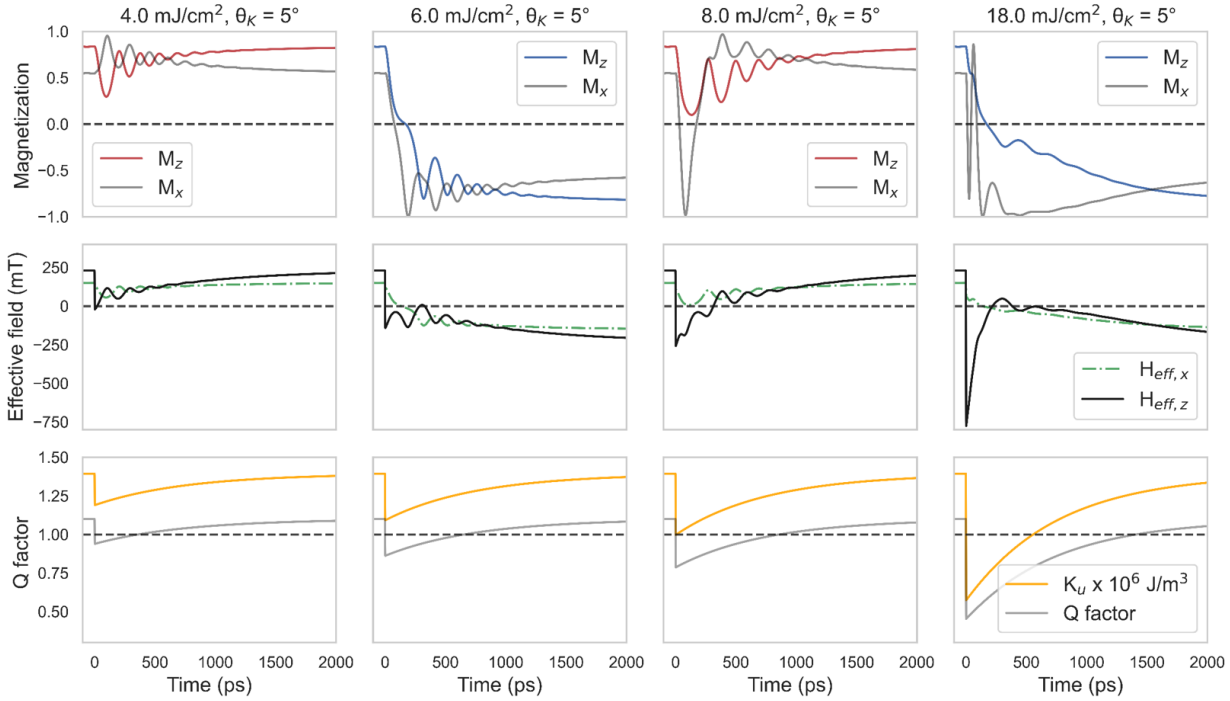

Fig. 4.5: Time traces of m_x, m_z, $H_{eff,\,x}$, $H_{eff,\,z}$ and K_u for $\theta_u = 5^o$ fluences 4.0 mJ/cm^2, 6.0 mJ/cm^2, 8.0 mJ/cm^2, 18.0 mJ/cm^2. Simulations performed with $M_s = 760$ kA/m and $K_{u,300K} = 1.1 \cdot K_d$, Gilbert damping $\alpha = 0.1$.

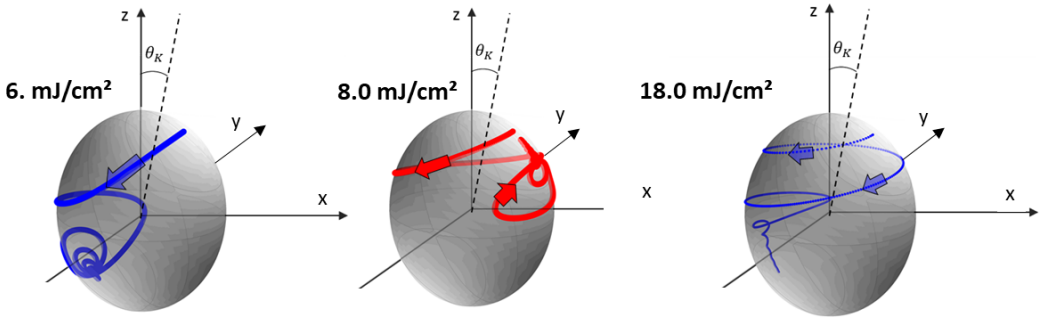

Fig. 4.6: 3D trajectories of increasing fluences for $\theta_u = 5^o$ fluences 6.0 mJ/cm^2, 8.0 mJ/cm^2, 18.0 mJ/cm^2. Simulations performed with $M_s = 760$ kA/m and $K_{u,300K} = 1.1 \cdot K_d$, Gilbert damping $\alpha = 0.1$. [152]

To assist the reader in visualizing the trajectory of reversal, we provide a three-dimensional representation in Fig. 4.6(a). The energy landscape of the system is also depicted for different values of the Q factor in Fig. 4.7(a) with the corresponding time evolution of the Q factor, the T_e and T_{ph} upon 40.0 mJ/cm^2 laser pulse. This includes the equilibrium state with a Q factor of 1.1, where an axial energy minimum exists, as well as lower values corresponding to higher temperatures induced by laser heating. The magnetization trajectories follow a precession towards the local energy minimum, which transitions from an "easy-plane" state (Q factor less than 1) to an "easy-axis" state (Q factor greater than 1). The rings, and thus the reversal dependency on fluence, are related to the point at which the anisotropy field recovers during a precession cycle.

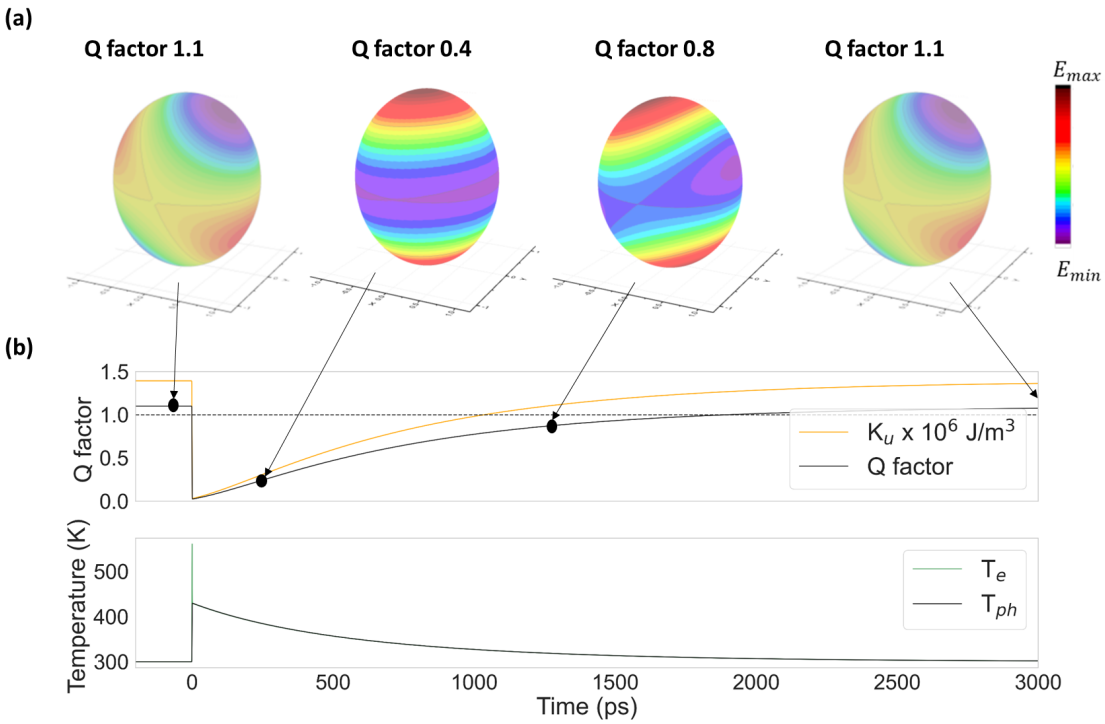

Fig. 4.7: (a) Energy landscape for Q factor of 1.1, 0.4, 0.8 and 1.1; (b) Q factor, electron temperature T_e and phonon temperature T_{ph} evolution in time upon 40.0 mJ/cm^2 laser pulse.

When changing the Gilbert damping to $\alpha = 0.05$ more ringing occur half-cycles occur, as shown in 4.8, and the switching fluence thresholds get closer. In this case fluences 6.0 mJ/cm^2 and 8.0 mJ/cm^2 are already of two different fluence bands (or rings). A detailed damping analysis is shown in Fig. 4.11(a).

To further understand the results and be able to compare them to the experimental measured reversal spots, we perform calculations of the reversal dynamics as a function of fluence, Fig. 4.9(a). Subsequently, these results were visualized by plotting them in accordance with the anticipated Gaussian distribution of the laser pulse in the x-y plane. This visualization approach, as shown in Fig. 4.9(b), will be consistently used moving forward.

In Fig. 4.10(a,b,d), we illustrate how varying the parameters of the Gaussian laser pulse in the simulation — specifically, pulse duration and power, and consequently fluence — aligns exceptionally well with the observed ring-shaped spots. It's worth noting that when dealing with very short pulse durations, on the order of hundreds of femtoseconds, the model exhibits certain limitations and does not entirely replicate the experimental dependency. In cases with such short timescales, an LLB or atomistic spin model is indeed necessary, as demagnetization and other phenomena may prove to be influencing factors making the reversal faster.

The time required for magnetization reversal in this simple model is on the order of hundreds of picoseconds, as demonstrated in Fig. 4.5. This value is slightly greater than what we presented in Chapter 3. Once again, this discrepancy can be attributed to the basic nature of the simulation and the approximations that were adopted (constant M_S). However, we anticipate that by integrating our hypothesis into an atomistic spin model, this understanding of the reversal was verified and

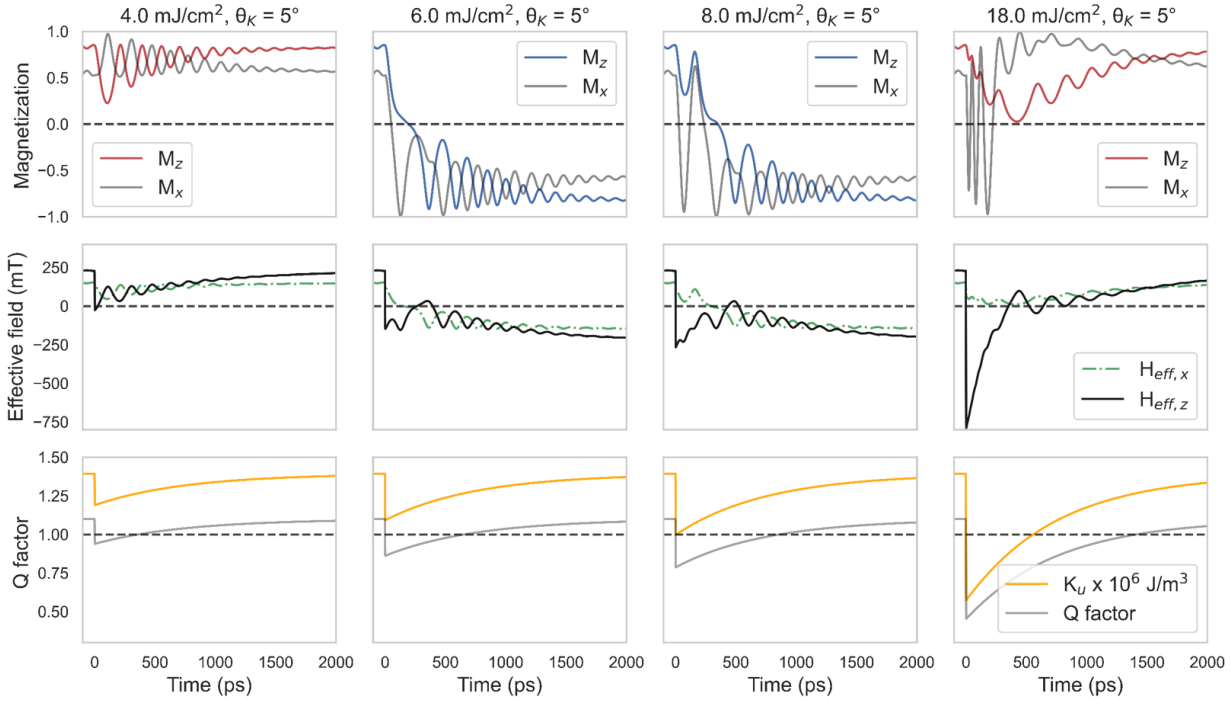

Fig. 4.8: Time traces of m_x, m_z, $H_{eff,\,x}$, $H_{eff,\,z}$ and K_u for $\theta_u = 5^o$ fluences 4.0 mJ/cm^2, 6.0 mJ/cm^2, 8.0 mJ/cm^2, 18.0 mJ/cm^2. Simulations performed with $M_s = 760$ kA/m and $K_{u,300K} = 1.1 \cdot K_d$, Gilbert damping $\alpha = 0.05$.

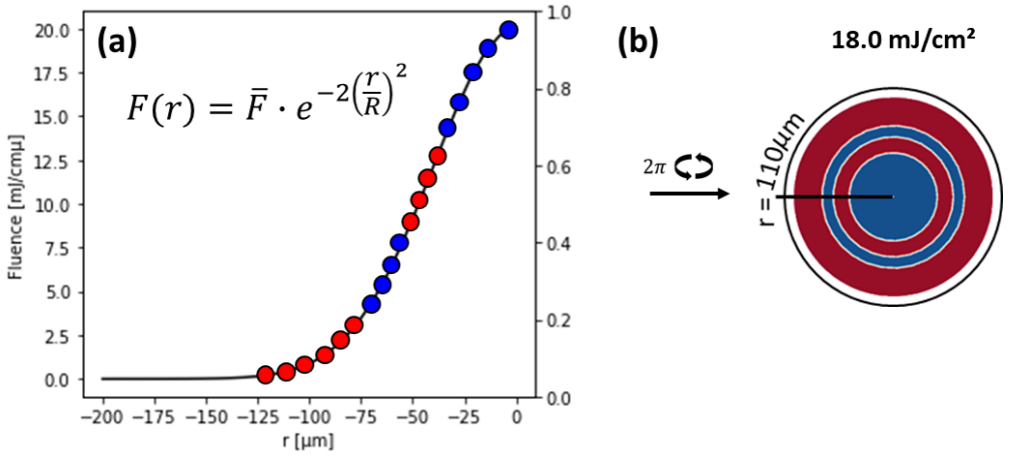

Fig. 4.9: (a) Gaussian fluence profile each blue (reversed) and red (not reversed) point representing the final state of the simulation at that fluence; (b) 2D visualization of the reversed spot calculated in (a).

alignment in reversal times was achieved. Furthermore, the most striking property of the reversal state diagram, showing no dependency on pulse duration is seen also in the simulation, Fig. 4.10(c).

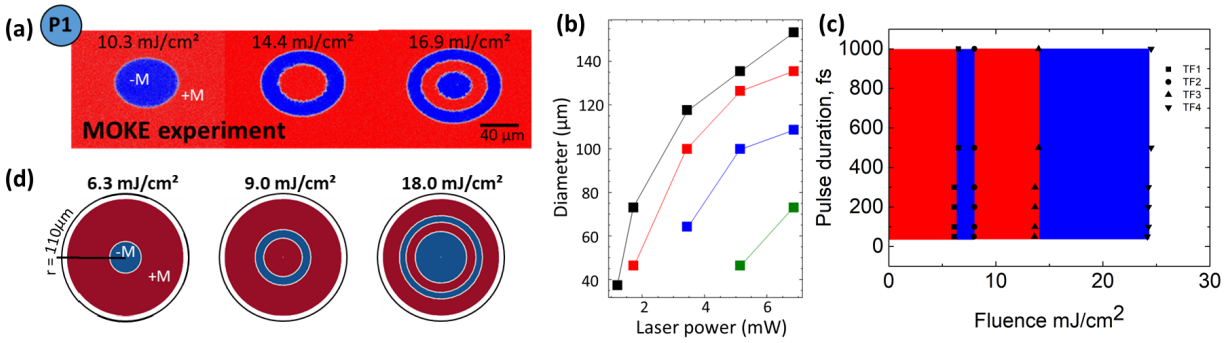

Fig. 4.10: (a) Experimental spot observations when increasing fluence/power; (b) Simulated diameters of each threshold fluence when increasing power; (c) Simulated state diagram, no pulse duration dependency; (d) Visualization of the increased diameter as calculated in (b).

4.4.2.2 Influence of parameters on threshold fluences

In this section, we dive into the influence of parameters on threshold fluences, including damping, uniaxial-anisotropy angle, and the Q factor at equilibrium.

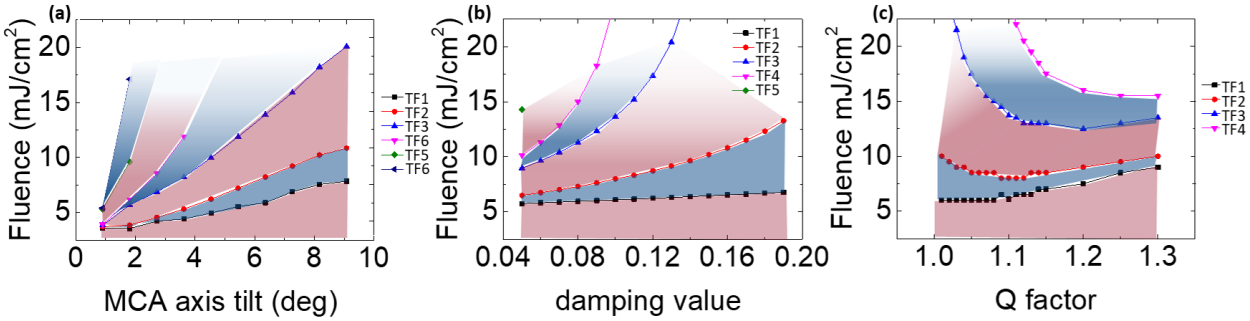

Fig. 4.11: Threshold fluences as a function of: (a) Angle of the uniaxial anisotropy; (b) Gilbert damping parameter; (c) Q factor at equilibrium, 300 K.

Specifically, we observed the distinct behaviour of the regions in the state diagram: switching (blue) and non-switching (red) regions, depicted in Fig. 4.11. These regions align directly with the switching 'rings,' or areas of the sample illuminated by a Gaussian-shaped laser pulse with varying fluence, as previously illustrated.

The data clearly shows that increasing the tilt angle and having higher damping consistently leads to a separation of the switching rings/bands along with an increase of threshold fluences. The first threshold, TF1, varies linearly with MCA acis tilt and damping while the following thresholds have a more complected dependency arising from the non-trivial magnetization trajectories. This increase in fluences in turn expands also the width of these switching bands/rings. Although, even at small angles, a reversal is expected, achieving the necessary fluence must be extremely precise. The same applies to low damping, where the range of fluences that allow for AOS is very narrow and could pose experimental challenges. In contrast, the Q factor exerts a different influence on threshold fluences. Initially, there is a decline from values of 1 to 1.1, where a minimum is observed, followed by an increase.

These findings underscore the impact of each material parameter on the characteristics of mag-

netization reversal. Furthermore they point out the requirements needed to achieve this type of reversal, revealing why it happens in systems with Tb and Dy based systems and not with Gd ones. Indeed Tb and Dy with TM, as we said, behave as sperimagnets but also, very importantly, they are known to increase drastically damping when introduced as doping in other materials [153,154], contrary to Gd where the effect is less significant. This makes Tb and Dy ideal, as the have low T_C, high damping and their local easy axes are primarily defined by the local crystal-field interaction.

4.4.2.3 Influence of applied external magnetic field on threshold fluences

Another adjustable factor in the AOS is the presence an external field, which can vary in direction with respect to the tilted anisotropy axis. Our objectives encompassed two key aspects: firstly, elucidating past laser switching measurements under external fields, showcasing shifts in switching bands and a substantial influence of in-plane fields; and secondly, enabling a more accurate representation of the material system, acknowledging a non-uniform anisotropy axis distribution among different grains.

Three magnetic field orientations were studied: in-plane and parallel to the anisotropy tilt ($H_{ext,x}$), in-plane and perpendicular to the tilt ($H_{ext,y}$), and out-of-plane ($H_{ext,z}$). The results for the in-plane parallel field are shown in Fig.4.12(a). Clearly, a positive x-field caused a squeezing of the switching bands and an increase in the first fluence threshold (black line), while a negative field resulted in band expansion and a lower first threshold. Additionally, the dependence on the in-plane component was pronounced, exhibiting a significant preference towards $+m_y$ ($-m_y$) for $H_{ext,x} > 0$ ($H_{ext,x} < 0$). The in-plane field influenced the moment when m_y switches to positive, with a large negative parallel field favoring switching and a positive field hindering it by pulling m_x towards -1.

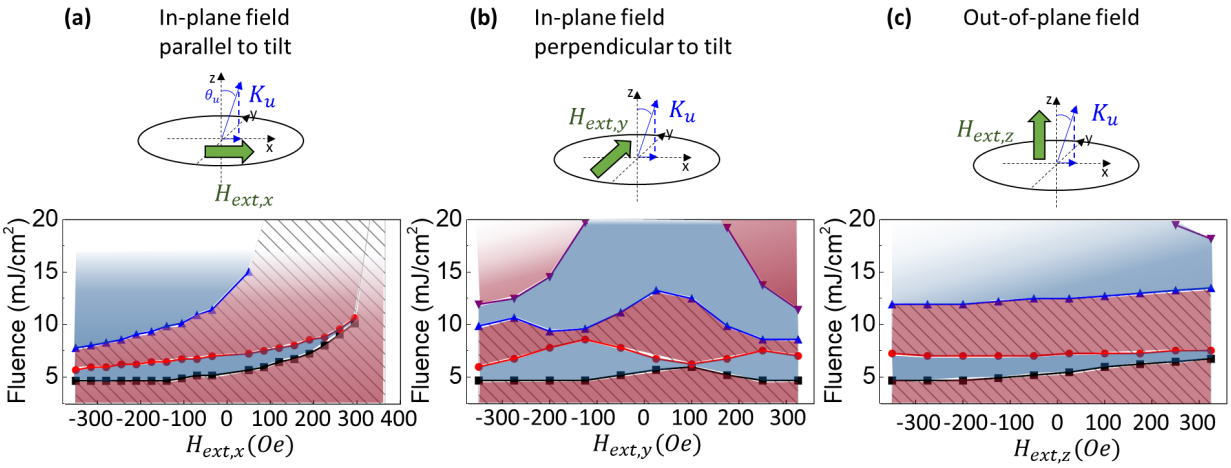

Fig. 4.12: Threshold fluences as a function of applied magnetic field: (a) In-plane parallel to the tilt anisotropy axis direction; (b) In-plane perpendicular to the tilt anisotropy axis direction; (c) Out-of-plane direction.

Regarding the perpendicular in-plane direction, Fig.4.12(b) displays a reduction of the higher thresholds when increasing the magnitude of the filed and an oscillating-type of effect on the first switching band, reducing and increasing its fluence range. These results are difficult to interpret. Meanwhile, the out-of-plane field $H_{ext,z}$ affected switching in a more symmetric manner, opening

the first switching band at negative fields. However, this effect was less pronounced compared to the impact of the $H_{ext,x}$ field, as shown in Fig.4.12(c).

These findings underscore that because this mechanism involves a slower reversal, external fields exert a significant influence on its behavior. This aspect is crucial from an application standpoint as stray fields at the device level might influence the overall junction behavior. But also this might be an interesting opportunity to exploit, indeed haveing to different threshold fluences may open the possibility to move from toggle to deterministic switching.

Presently, this model offers a robust understanding of observed magnetization reversal behaviors, even without accounting for rapid partial demagnetization due to sudden rises in electron temperature. Addressing this necessitates more detailed atomistic or Landau-Lifshitz-Bloch (LLB) models, as explored in Section 4.6.

4.5 Distribution of anisotropy axis

In this section, we explore the influence of a distribution of the anisotropy axis between grains in the x,y plane on the expected reversal pattern in magnetic grains. Previously, our results demonstrated how the anisotropy angle and damping affects HI-AOS in grains with uniform magnetization.

Starting from the calculated expected threshold fluences as a function of the tilt angle of Fig. 4.11(a), we investigate the reversal rings of an ensemble of independent grains varying their dimensions. The square grain dimension was calculated by dividing the FWHM of the Gaussian by the number of grains to visualize. This was done in order to keep the radius of the expected reversal pattern the same and study what impact does the grain size have on the end result. The angle θ_u was randomly varied between grains following a Gaussian distribution. It's worth noting that the azimuth angle remains constant since the grains are independent, meaning they don't affect each other's orientations. This lack of interaction ensures that the final outcome isn't influenced by changes in the azimuth angle. In Fig. 4.13 the results for 1.7 µm, 343 nm and 69 nm are shown for a $\theta_u = 5° \pm 1°$. The reversal pattern is highly influence by the tilt and the distribution, but in Fig. 4.13 it is already clear that to have experimental matching the grains must be at least below 400 nm.

Taking from now on the grain size as 70 nm with a normal distribution of tilted angles, the results for different angles and standard deviations are presented in Fig. 4.14 and 4.15.

Fig. 4.14 illustrates the distribution of tilted anisotropy angles centred around 7° with different standard deviations. The resulting reversal pattern, shown in the bottom row, closely aligns with the experimental observations, as for $5° \pm 1°$.

Conversely, Fig. 4.15 shows a distribution centered around 0° with varying standard deviations. The resulting reversal pattern, while exhibiting a sort of probabilistic helicity-independent all optical switching, it may resemble more a multidomain state rather than complete switching.

In Section 3.4, we saw that the remanence of a in-plane magnetized multilayer has an angular dependency when deposited as a wedge but interestingly also when the sample was deposited in rotation. Although, this is not a proof of an off-centred distribution, it indeed suggest an overall slight preference along one specific direction. These results suggesting that the distribution can not be much disperse and a preferential tilt must be present.

In summary, our investigation into the influence of anisotropy axis distribution on magnetic grains has provided valuable insights into HI-AOS. The specific distribution of tilted anisotropy angles significantly impacts magnetic behaviour, with non-zero centred distribution demonstrating good agreement with experimental observations, while the 0° distribution yields a pattern resembling multidomain states.

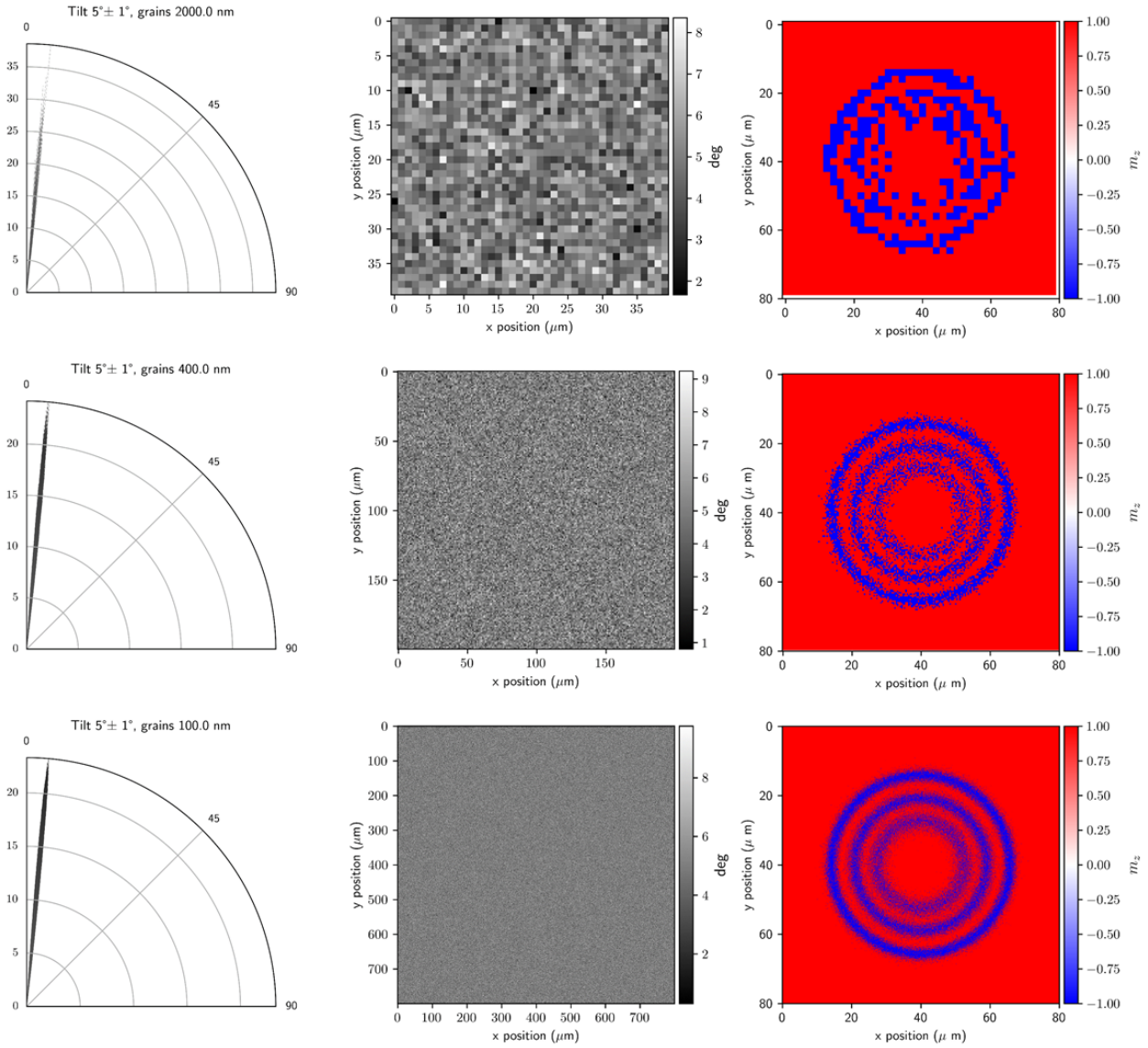

Fig. 4.13: Normal distribution of tilted anisotropy around 5° with standard deviations of 1° for grains of 2000 nm, 400 nm and 100 nm. (Left column) angular histogram of the tilted axis distribution; (center column) visualization of the distribution of grains tilted axis in x,y position, with color code for the tilted axis angle θ_u; (right column) expected HI-AOS reversal pattern for a Gaussian pulse, 5 mJ/cm^2 and $\sigma = 0.2$ [137]

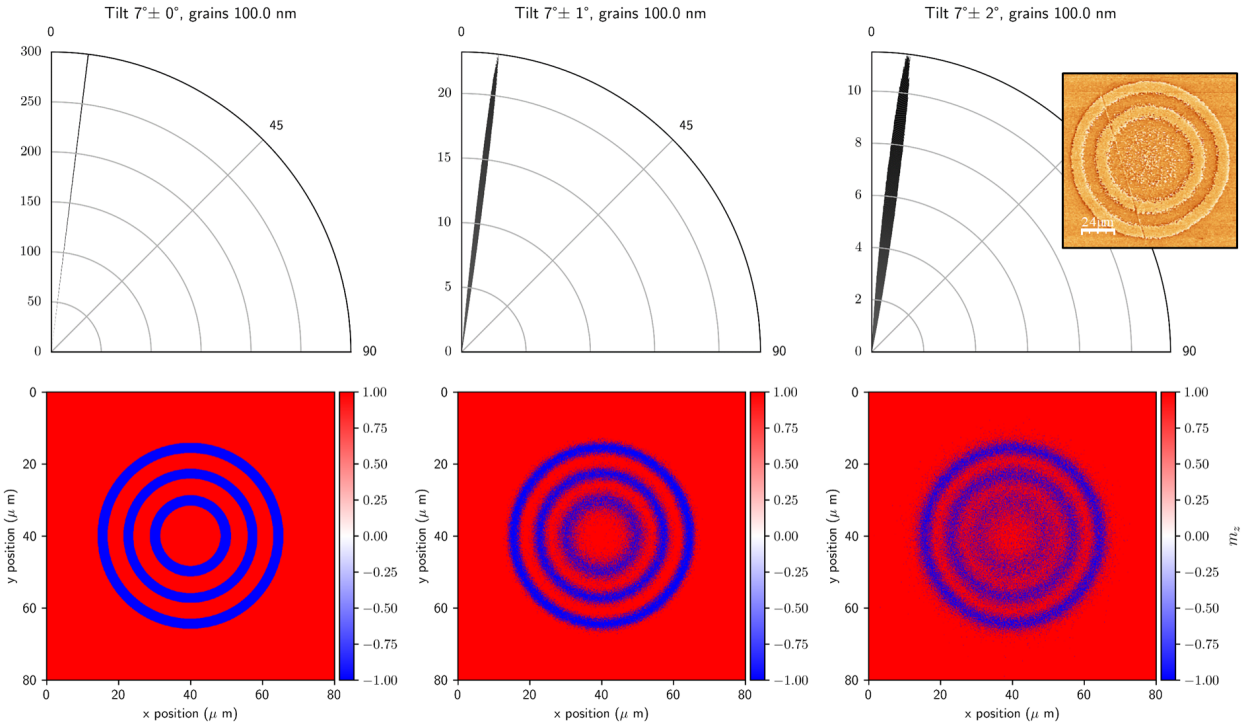

Fig. 4.14: Expected HI-AOS reversal pattern (bottom row) for a normal distribution of tilted anisotropy around 7° with standard deviations of 0°, 1°, and 2° (top row) with a grain size of 23 nm. Inset of MFM measurements [137]

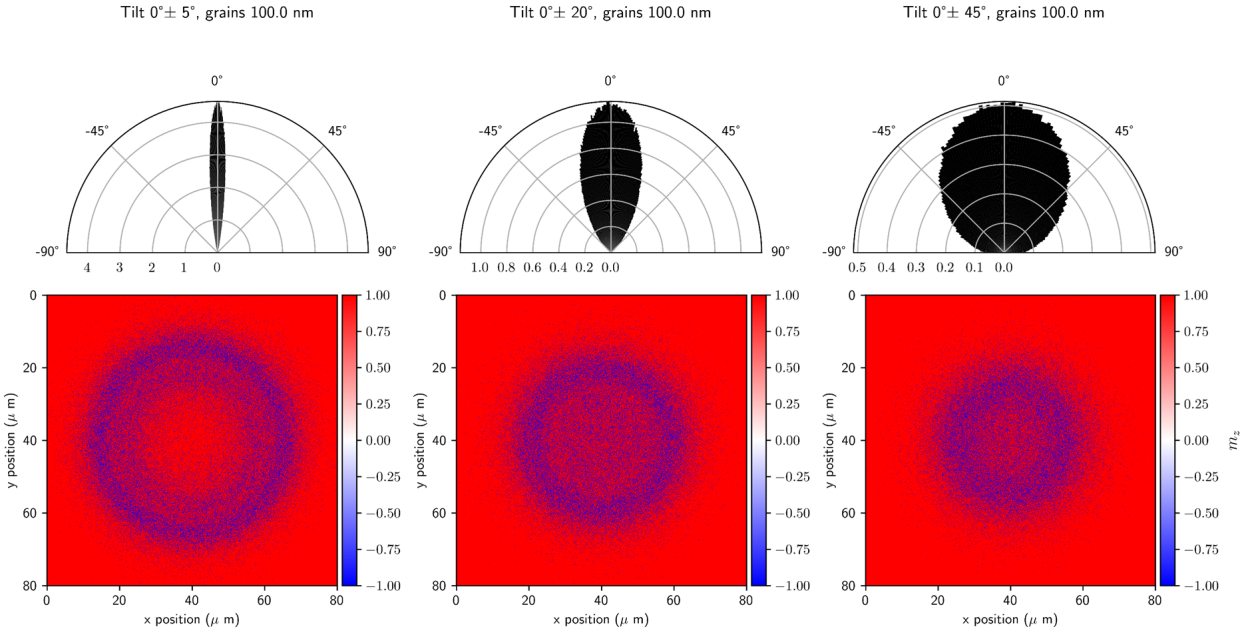

Fig. 4.15: Expected HI-AOS reversal pattern (bottom row) for a normal distribution of tilted anisotropy around 0° with standard deviations of 5°, 20°, and 45° (top row) with a grain size of 23 nm.

4.6 Atomistic spin simulations

Elizaveta Tremsina, a PhD student from *Massachusetts Institute of Technology* during a three-month secondment at Spintec helped to validate the results obtained from our macrospin model. Our joint efforts aimed to implement the AOS hypothesis in VAMPIRE [146], a fully atomistic spin model. VAMPIRE was chosen for several reasons, including its increasing popularity in the magnetism research community and its built-in support for laser pulses and a two-temperature model with cooling mechanisms.

It's worth noting that the macrospin model for simulations was chosen for its simplicity, speed, and ease of conducting simulations. In contrast, atomistic spin models are highly time-consuming, and given the slower nature of the magnetization reversal process we were investigating, the atomistic spin simulations were mainly employed to provide additional evidence for the validity of the significant approximations made in the macrospin model.

4.6.1 Simulation overview

4.6.1.1 Model and material parameters

The atomistic spin model is crucial in studying the behavior of magnets at the atomic scale. As thoroughly explained in [146], it utilizes the extended Heisenberg spin model to describe the atomic-level physics of magnetic materials with the spin Hamiltonian, denoted as H. The Hamiltonian encompassing exchange interaction (H_{exc}), magnetic anisotropy (H_{ani}), and external magnetic fields (H_{app}) as follows:

$$H = H_{\text{exc}} + H_{\text{ani}} + H_{\text{app}} \tag{4.16}$$

The exchange energy (H_{exc}) for interacting atomic moments originates from electron wavefunction symmetry and the Pauli exclusion principle. It is the most dominant term and is expressed as:

$$H_{\text{exc}} = -\sum_{i \neq j} J_{ij} \mathbf{S}_i \cdot \mathbf{S}_j \tag{4.17}$$

Here, J_{ij} represents the exchange interaction between atomic sites i and j, $\mathbf{S}_i$ is the unit vector indicating the local spin moment direction, and $\mathbf{S}_j$ represents the spin moment direction of neighboring atoms. The unit vectors are taken from the atomic moment $\mathbf{S}$ and given by $\mathbf{S}_i = \mu_{\mathbf{s}}/|\mu_{\mathbf{s}}|$. For ferromagnetic materials ($J_{ij} > 0$), neighboring spins align in parallel, while for antiferromagnetic materials ($J_{ij} < 0$), spins tend to align antiparallel.

The exchange interaction diminishes with distance, often involving only nearest neighbors due to its strong distance dependence, although it can extend across several atomic spacings.

Magnetic anisotropy plays a crucial role in a material's thermal stability, arising from various physical effects, predominantly magnetocrystalline anisotropy. This preference for atomic moments to align along specific crystallographic axes originates from atomic electron orbitals interacting with the local crystal environment.

Uniaxial single-ion anisotropy represents the simplest form, where magnetic moments prefer aligning along a single axis, **e**, often termed the *easy-axis*:

$$H_{\text{uni-ani}} = -k_u \sum_i (\mathbf{S}_i \cdot \mathbf{e})^2 \tag{4.18}$$

For out-of-plane (PMA) anisotopry **e** corresponds to $\hat{z}$, in our case for Tb the easy-axis has a tilt with respect to $\hat{z}$, as discussed later.

Another form of anisotropy is the Néel anisotropy, it describes the surface anisotropy:

$$H_{\text{Néel}} = -\sum_{i \neq j} \frac{k_s}{2} (\mathbf{S}_i \cdot \mathbf{r_{ij}})^2 \tag{4.19}$$

where, k_s is the surface anisotropy constant between atoms i and j, and $\mathbf{r_{ij}}$ is a unit vector between sites i and j.

The interactions between the system and external applied fields, denoted as H_{ext} is given by:

$$H_{\text{ext}} = -\sum_i \mu_s \mathbf{S}_i \cdot \mathbf{H}_{\text{ext}} \tag{4.20}$$

where μ_s is the atomic magnetic moment.

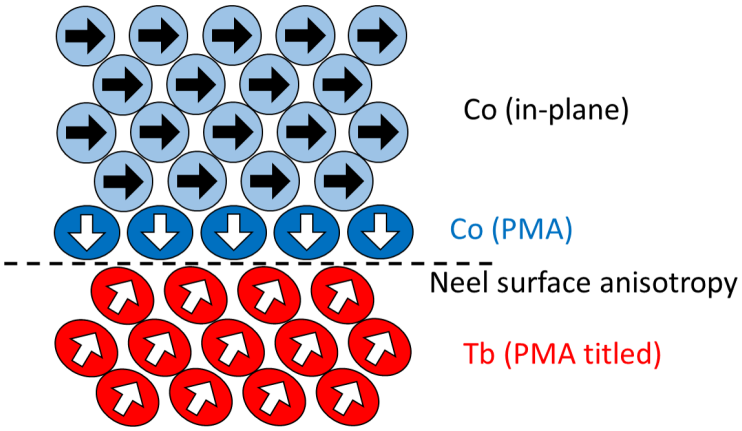

Fig. 4.16: Schematic of modeled material system, showing the three separate magnetic regions and anisotropy terms, with periodic boundary conditions in all three directions.

To describe the system in our atomistic spin simulations, several features into the system's structure were incorporated. Fig.4.16 provides a schematic of the structure simulated, with an FCC unit cell of magnetic lattice sites and a global lattice constant of 2.5Å (note that this is not a full representation of the crystal structure of the material, but an approximation). A total of three magnetic material layers were used, of various thickness: Tb, and Co, separated by an *interfacial PMA* Co layer, the justification for which is provided below. The number of monolayers of each material type was chosen to mimic a Co-rich system, which has been shown experimentally to display AOS, unlike Tb-rich stacks. Periodic boundary conditions were used along all three directions, thus, the bottom Tb layer also has an interface with the top Co. The atomistic input parameters for the system are listed in Table 4.2 [149].

Table 4.2: Material parameters used in VAMPIRE simulations of [Tb/Co] multilayers [149]

Description	Parameter	Value
Exchange	j_{Tb-Tb}	8.2×10^{-22} J
Exchange	j_{Co-Co}	5.9×10^{-21} J
Exchange	j_{Tb-Co}	-1.0×10^{-21} J
Magnetic Moment	μ_{Tb}	$9.34\mu_B$
Magnetic Moment	μ_{Co^i}	$2.0\mu_B$
Magnetic Moment	μ_{Co}	$1.72\mu_B$
Uniaxial Anisotropy Constant	k_U^{Tb}	2.16×10^{-22} J
Uniaxial Anisotropy Axis Tilt from $\hat{z}$	θ_{Co}	15°
Uniaxial 'Interface' Anisotropy	$k_U^{Co^i}$	8.00×10^{-23} J
Néel Surface Anisotropy	$k_S^{Co^i}$	8.00×10^{-23} J
In-Plane Anisotropy	k_p^{Co}	-1.00×10^{-23} J
Fractional Height	h_{Tb}	0.375
Fractional Height	h_{Co^i}	0.125
Fractional Height	h_{Co}	0.5
Number of unit cells	n_{Tb}	3
Number of unit cells	n_{Co^i}	1
Number of unit cells	n_{Co}	5
Temperature Rescaling Coefficient	All materials	2.37
System Dimensions	-	$4 \times 4 \times 2$ nm^3
Unit Cell Size	-	2.5Å

4.6.2 Magnetisation vs temperature, anisotropy and role of interfaces

The *Curie Temperature* program was used to model magnetisation as a function of temperature, using the Monte Carlo algorithm to equilibrate the system at each temperature point and then extract statistics over a certain number of time steps. The modeled system shows magnetization compensation around 250K, just below room temperature, with a transition from Tb to Co-rich state. The normalized net magnetisation magnitude is given by $|m| = |\sum_i \mu_i \mathbf{S}_i| / \sum_i \mu_i$ and is reported as a function of temperature in Fig. 4.17. It shows a decrease until the compensation point in the Tb-rich regime, and then slightly increase in the Co-rich. These results are in good agreement with previously extracted values of saturation magnetisation versus temperature from MOKE measurements [128].

The anisotropy energy is the most crucial component of the observed AOS process, as shown by experiment and macrospin simulations. For this reason, it was necessary to replicate the temperature dependence of effective anisotropy of the system, but instead of the phenomelogical law used in the macrospin study (4.15), here the anisotropy had to be encoded intrinsically in the system, the temperature fluctuations given by the stochastic temperature behavior itself, resulting in effective parameters. Based on previous work and past evidence of the critical role of interface anisotropy, this interfacial anisotropy causes the system to have net PMA at lower tempeatures. Above a threshold temperature a spin reorientation transition occurs due to thermal fluctuations. Evans *et al.* [146] applied MC simulations to a system with uniaxial bulk anisotropy, and Néel surface anisotropy perpendicular to the thin-film plane, to model temperature-dependent spin reorientation transition (SRT). Furthermore [155] modelled interfacial effects using a fictitious interfacial Fe layer, with a higher magnetic moment, and perpendicular anisotropy axis.

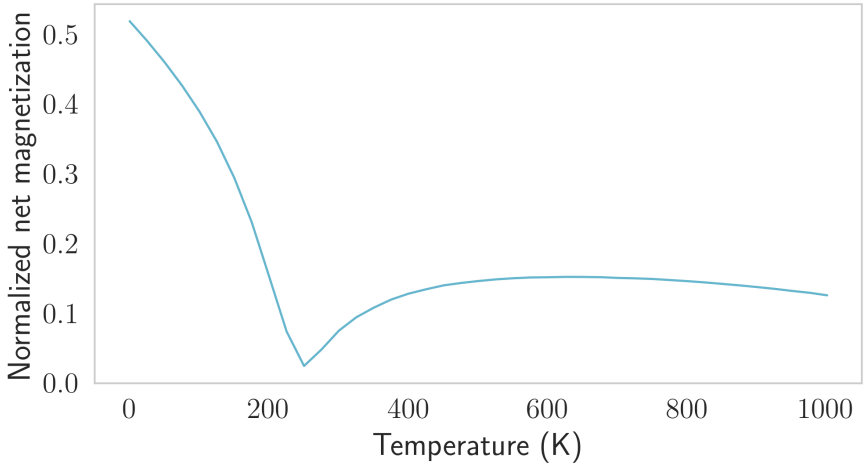

Fig. 4.17: Monte Carlo simulations of temperature-dependent net magnetisation length of Tb/Co multilayer stack. The compensation point occurs below room temperature, where there is a transition from Tb to Co regime.

Thus, based on both these studies, we chose the *interface Co* layer having PMA, and also included Néel surface anisotropy of same magnitude in the *bulk Co* layer as well. The *bulk Co* layer has easy-plane anisotropy, effectively providing the demagnetisation field. Note that this treatment of the demagnetizing field, instead of performing the dipole-dipole calculations, was chosen due to limitations of computational power and accuracy with this small system size, however, also supported by the fact that the net M_S does not change significantly in the regime of interest during the switching process, in which the main precessional dynamics takes place, according to the macrospin model.

A sweep over different values of the interfacial anisotropy values, varying both the Néel surface anisotropy constant k_S, as well as the uniaixial PMA constant k_u^i of the interfacial Co layer, while maintaining the Co in-plane value constant at $k_{IP} = -1 \times 10^{-23} J$. Fig.4.18 shows that depending on the value of the interfacial anisotropies, the net m_z shows different behavior with temperature. The value of $k_S = 8 \times 10^{-23} J$ was chosen for optical switching modelling, due to the fact that the expected precessional switching occurs during the cooling phase, as the system temperature drops to 300K, as opposed to during the pulse itself (high temperature regime).

4.6.2.1 Anisotropy extraction from constrained Monte Carlo method

In addition to normal Monte Carlo, the hybrid constrained Monte Carlo (HCMC) method [146,156] allowed the explicit extraction of macroscopic quantities such as temperature-dependent magnetic effective anisotropy, by performing a constrained number of Monte Carlo steps. In this procedure, the system is initialized at various angles with respect to the easy axes (in this case, the PMA easy axis), and then evolved according to the Monte Carlo steps and compute an average torque value to then reconstruct an anisotropy value from the angle-dependent torque.

For the case of PMA, Fig. 4.19 illustrates the effective anisotropy scaled by the value at 0K (K_0). Notably, this anisotropy demonstrates a linear reduction with rising temperatures. In Section 5.5 temperature dependent measurements will demonstrate a parallel linear relationship of coercivity on temperature for patterned junctions. Considering that coercivity is proportional to the effective

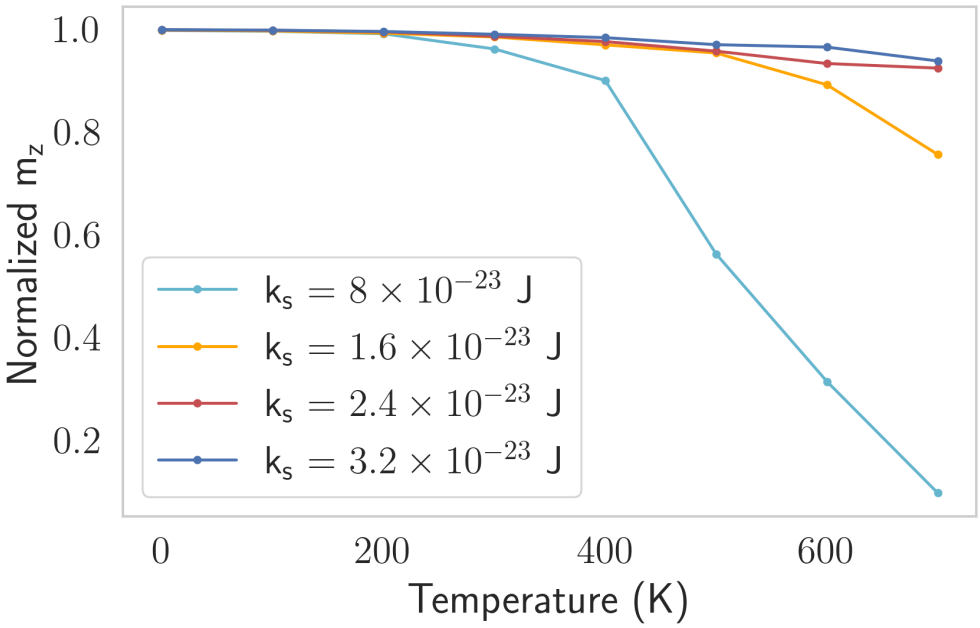

Fig. 4.18: Monte Carlo simulations of temperature-dependent net out-of-plane magnetisation component

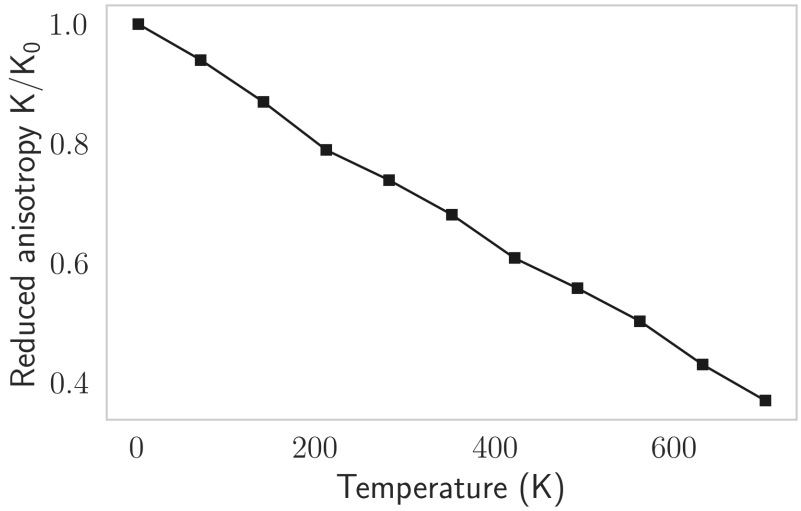

Fig. 4.19: Hybrid constrained Monte Carlo (HCMC) method extracted effective anisotropy versus temperature, normalized by K_0, the effective anisotropy at 0 K.

anisotropy, this comparison offers an intriguing correlation deserving attention. Such consistency provides another compelling reason to support the validity of the model's predictions in this context.

4.6.3 Laser pulse modeling and switching of multilayer stack

The *laser-pulse* program with the two-temperature model, including a cooling term with effective time constant, are used to model the all-optical switching of the multilayer structure. First, the system is equilibrated, then the laser pulse is applied starting at $t = 0$ps. Ultrafast demagnetization occurs up to around 18.0 mJ/cm^2 for 100 fs laser pulses, higher than what observed in the macrospin model. Magnetization dynamics for 16.0 mJ/cm^2 are reported in Fig. 4.20. The simulation shows a clear ultrafast demagnetization and then recovery in less than 10 ps. Up to around 25 ps the the non-

zero in-plane components show a start of reorientation but not sufficient to drive the magnetization reversal.

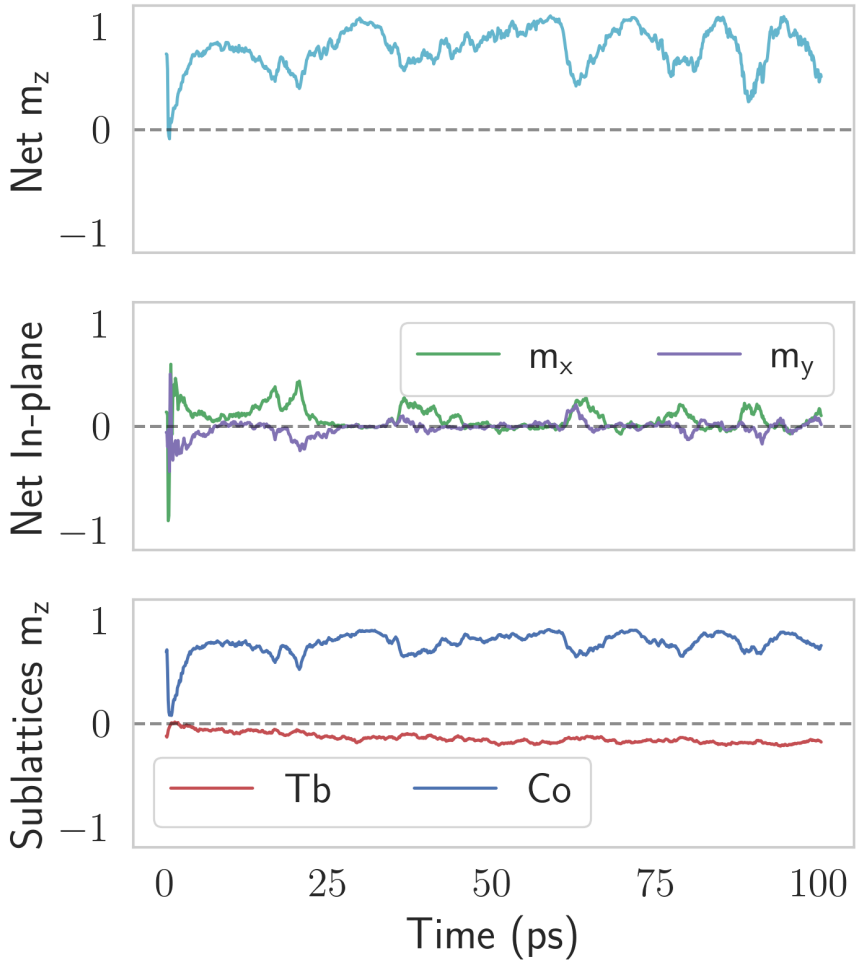

Fig. 4.20: Atomistic simulation results showing magnetisation evolution during and after the application of a laser pulse with fluence of 16.0 mJ/cm^2, and pulse duration of 100 fs, starting at t=0 ps according to the two-temperature model. Time evolution plots of: Net m_z the total magnetisation component m_z; Net m_x and Net m_y total in-plane magnetisation components; individual material perpendicular magnetisation components m_z;

Fig.4.21 shows a magnetisation switching from the *up* to *down* state for fluence $f = 18.5\ mJ/cm^2$, showing a spike in the total m_z in few ps, and return to the $m_z \approx 0.5$ state and subsequent zero-crossing at around 30 ps and switching to the *down* state. The total in-plane components are shown as well, evidencing the precessional type of reversal as in the macrospin model. The net magnetisation of Co (the dominant magnetic material at room temperature), shows a huge drop in magnetisation, following the spike in electron temperature during the pulse, and then a restoring to the original value, as seen in Fig.4.22. The Tb magnetisation remains low in this regime. This quantity represents the uniformity of the magnetisation, and is highly dependent on electron temperature, through the stochastic temperature term. These simulations show that the short-term dynamics which occurs during the laser pulse and the temperature spike, notably the demagnetisation, is followed by a cooling of the system, during which the Co moments go in-plane (as seen by the increase in the m_x and m_y components and restoring of the Co magnetisation), followed by switching to $m_z < 0$.

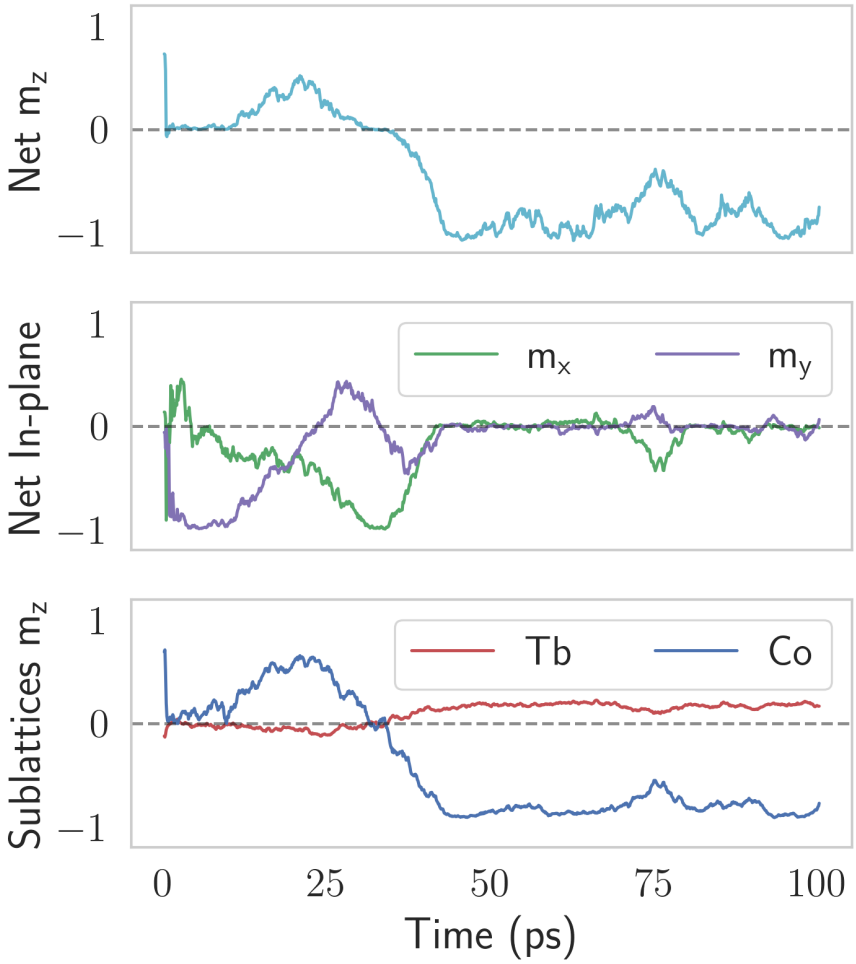

Fig. 4.21: Atomistic simulation results showing magnetisation evolution during and after the application of a laser pulse with fluence $f = 18.5\ mJ/cm^2$, and pulse duration of 100 fs, starting at t=0 ps according to the two-temperature model. Time evolution plots of: Net m_z the total magnetisation component m_z; Net m_x and Net m_y total in-plane magnetisation components; individual material perpendicular magnetisation components m_z;

Fig. 4.22 displays both switching and non-switching events resulting from laser pulses with varying fluence values. The net out-of-plane magnetization relates to the signal detected via MOKE measurements, although the precise sensitivity of MOKE measurements to different magnetizations—whether it primarily captures the total magnetization or predominantly reflects contributions from the Co or Tb sublattices—is not fully comprehended. In a study by Mishra et al. [128] concerning a 600 nm wavelength, it was concluded that the signal correlates with a linear combination of the two sublattices.

Notably, these findings align well with the three-step process observed in Chapter 3. Moreover, the initial dip in the signal immediately following the laser pulse is observed here, contrary to the macrospin simulations. Additionally, we have good correlation between the simulated reversal time and the TR-MOKE measurements.

These preliminary results validate the hypothesis of our macrospin model, showing that it is indeed possible to obtain the similar type of fluence dependent reversal with a more accurate an extensive model that takes into account the ultrafast response of the system. Although, HI-AOS simulations using the atomistic spin model, we note that the Co sublattice appears to undergo complete

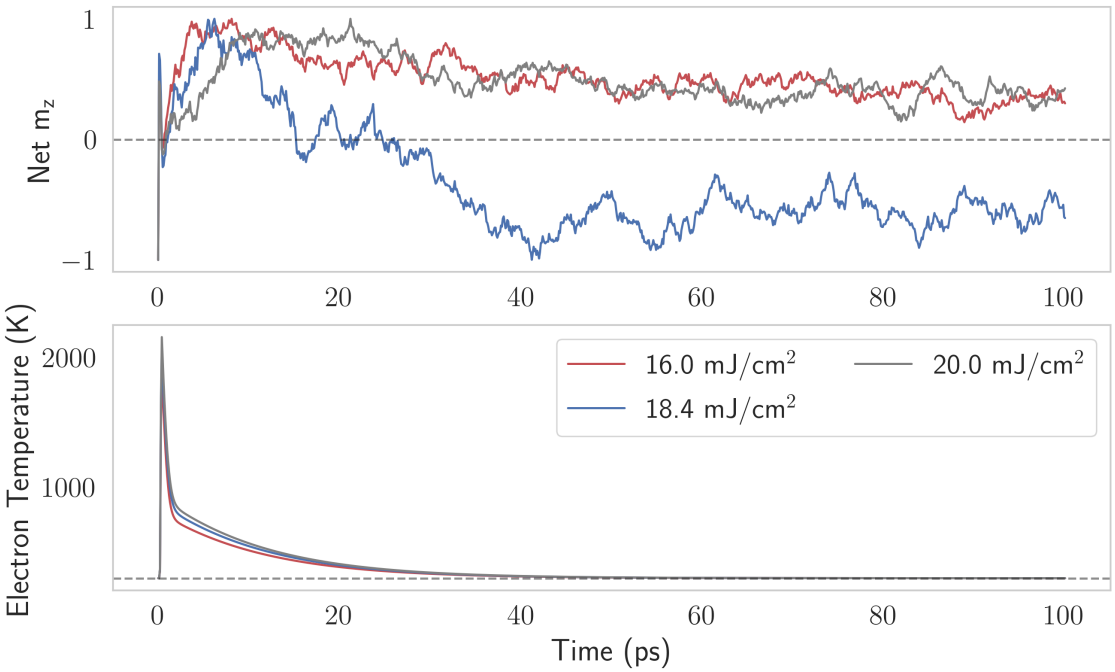

Fig. 4.22: Atomistic simulation results showing magnetisation evolution during and after the application of a laser pulse of various fluences 16.0 mJ/cm^2, 18.4 mJ/cm^2, 20.0 mJ/cm^2, and pulse duration of 100 fs, starting at t=0 ps according to the two-temperature model. (a) Time evolution of normalized net perpendicular magnetisation component m_z showing both switching and non-switching cases. The initial state is $m_z \approx 1$; (b) Time evolution of temperature electron (T_e)

demagnetization during the ultrafast response (step 1). This aspect is not entirely comprehended and deviates slightly from the macrospin representation of the phenomenon. This deviation impacts the complete mapping of the fluence-pulse duration phase diagram, where the switching thresholds are expected to be unaffected by pulse duration. It is hypothesized that adjusting material parameters like anisotropy values and structure thickness might resolve this discrepancy. Consequently, further investigation is needed to assess the system's behavior in contrast to macrospin dynamics.

4.7 Conclusion

In this chapter, we embarked on a comprehensive exploration of the two-temperature model and its pivotal role in understanding the phenomenon of HI-AOS in multilayer systems. The 2TM served as a foundational framework for our investigations, allowing us to simulate the rapid response of our system to ultrafast laser pulses and gain valuable insights into the underlying physics.

One of the central findings of our study is the remarkable independence of HI-AOS from the pulse duration, a characteristic that was consistently observed experimentally and can be attributed to the unique dynamics of the system. This independence implies that the core mechanisms driving the reversal process occur over longer timescales, primarily influenced by the absorbed laser fluence and the subsequent cooling of the system to its thermal equilibrium.

Furthermore, we introduced a phenomenological macrospin model that incorporates the principles of the 2TM. This macrospin model enabled us to delve deeper into the precession-driven switching observed in our samples after the application of short laser pulses. It considered vari-

ous parameters such as temperature-dependent uniaxial anisotropy and the tilted anisotropy axis, shedding light on the intricacies of the reversal mechanisms within the system.

Our simulations have demonstrated how parameters like damping, anisotropy angles, and the Q factor at equilibrium influence the threshold fluences necessary for HI-AOS.

While the 2TM provided the foundational knowledge, it is clear that the full complexity of HI-AOS requires further investigation. The integration of detailed atomistic or LLB models will be essential for a more comprehensive understanding, especially when considering intricate interactions such as rapid partial demagnetization.

In conclusion, the macrospin model, building upon the 2TM, has illuminated the nuanced mechanisms behind precessional HI-AOS. Together, these models provide a solid foundation for future research and applications in the realm of ultrafast magnetization control, making HI-AOS an exciting avenue in the field of magnetics and spintronics.

We conducted atomistic spin simulations to validate the results obtained from our macrospin model, particularly focusing on the AOS hypothesis in multilayer systems. We employed the VAMPIRE simulation tool, which offered built-in support for laser pulses and a two-temperature model with cooling mechanisms, making it suitable for our investigation.

The atomistic simulations involved a system with a three-layer structure, incorporating different magnetic materials and anisotropy terms. These simulations were carried out with careful consideration of material parameters, including exchange interactions, magnetic moments, anisotropy constants, and more.

We found that the temperature-dependent magnetization behaviour in the multilayer stack agreed well with experimental measurements, particularly in the vicinity of the compensation point, which is crucial for the AOS phenomenon. The role of interfacial anisotropy was highlighted, showing its significance in influencing the system's behaviour at different temperatures. These results were instrumental in our understanding of the interplay between various anisotropy effects and temperature-dependent magnetization.

Overall, the atomistic simulations provided valuable insights into the AOS phenomenon in multilayer systems. The results supported the validity of our macrospin model and shed light on the complex interplay of anisotropy effects and temperature in the switching process. These findings contribute to our understanding of magnetism and offer a solid foundation for future research in this field.

Chapter 5

Nano-patterned all-optical switching spintronics devices

Contents

5.1 Introduction

The integration of all-optical switching into magnetoresistive random access memory technology presents an exciting opportunity to greatly improve writing speeds, surpassing conventional electrical methods by more than a hundredfold. Furthermore, this innovation promises to significantly reduce energy consumption, with an anticipated level of less than 16 fJ per bit as predicted by Kimel and Li in [3]. To make this approach feasible, the memory elements must be accessible both optically and electrically, allowing for optical writing and electrical read-out. Therefore, the incorporation of a top electrode that is both transparent and conductive becomes crucial.

Early explorations into AOS-MTJs were pioneered by Chen et al. [104] who successfully demonstrated the operation of micrometer-sized p-MTJ employing a GdFeCo alloy storage layer. Although

their initial attempt yielded a modest TMR of 0. 6%, Wang et al. [105] achieved subsequent refinements. Their work involved manipulating Co / Gd bilayer-based tunnel junctions, resulting in a good TMR ratio of 34.7% for cell dimensions of 3 µm in diameter. In particular, this substantial improvement of TMR was facilitated by the innovative design concept introduced by Avilés-Félix and his team [20,21]. As we said previously, the approach focused on magnetically coupling an optically switchable material to the standard CoFeB free layer, effectively amplifying the TMR ratio.

This chapter serves a dual purpose: first, to provide an overview of the nano-fabrication processes central to the creation of these MTJ devices, encompassing the fabrication of magnetic pillars and the definition of the transparent and conductive electrodes; second, to explore critical aspects of device characterization. Particularly TMR, coercivity mappings, and the exciting potential of femtosecond laser pulse irradiation in achieving all-optical switching in nano-patterned spintronics devices.

5.2 Nano-fabrication process

The nano-fabrication methodology utilized in this thesis was developed by the Spintec MRAM group and has undergone continuous refinement and adaptation to align with advances in cleaning tool capabilities [114,115,157]. This standard process involves four distinct lithography steps: an initial e-beam lithography step followed by three subsequent optical lithography steps. The primary objective of this process is to create an array of nano-sized pillars, connecting them both at their upper and lower ends to larger metallic electrodes, which serve as points for external connections. The entire fabrication process takes place within the *Plateforme Technologique Amont* (PTA).

To enable the integration of all-optical switching capabilities with magnetic tunnel junctions, Olivier et al. have explored the incorporation of indium tin oxide (ITO) as a transparent top electrode [111,158]. Fig. 5.1 provides a visual representation of the main steps involved in the process, highlighted in red indicating the modifications that were made to the standard MRAM process to accommodate ITO integration.

In the upcoming section, you will find a step-by-step explanation of the process. To keep things concise, note that all lithography steps involve standard procedures like resist spin coating, hot plate baking, manual mask alignment using SUSS MicroTec MJB4 for UV-insulation, development, and resist removal. These steps are assumed in the following description.

5.2.1 MTJ patterning

The fabrication process begins with the deposition of the bottom contact material onto a 2" or 4" SiO_2 wafer, usually around 25 nm of Pt or Ta, and then the complete magnetic stack. Subsequently, the sample undergoes annealing under optimized conditions to enhance its magnetic properties. A hard mask (HM) layer deposition is essential for nano-patterning and later contact with the pillars. For standard MRAM, the tipical HM is 150 nm thick layer of Ta, the integration of a transparent electrode begins already at this step with the replacement of Ta with ITO [111,158], as shown in Fig. 5.1 (a).

The initial lithographic step aims to define the shape of the nano-sized pillars. The diameters range from 20 to 300 nm, depending on specific requirements. These small features are patterned using an e-beam tool, resulting in an array of 168 pillars per die, on 163 dies per 100 mm wafer. A 20 nm thick layer of Cr is deposited, followed by a lift-off process that creates a Cr pattern on the ITO layer. This pattern serves as a mask for the subsequent reactive ion etching (RIE) step, where an Induced Coupled Plasma (ICP) etching (Oxford Plasma Lab) based on CH_4/H_2 chemistry, etches the ITO layer [159]. This process leads to the formation of nano-sized ITO pillars, as observed in Fig. 5.1(b). The precise shape of these pillars is crucial, as they serve as physical masks in the subsequent ion beam etching (IBE) step. The IBE tool employs an Ar-based plasma to physically etch the magnetic stack. The angle at which the ion beam impinges on the substrate is critical for achieving the desired shape, preventing the re-deposition of etched materials on the pillar walls, and preserving the magnetic properties of the stack. Consequently, the recipe for this step is continuously refined to optimize the results based on the specific magnetic stack under consideration. The etching process, monitored by a secondary ion mass spectrometer (SIMS), halts when the bottom contact material is reached, as shown in Fig. 5.1(c).

5.2.2 Bottom electrode definition

A second lithographic step is used to create a 150 µm side plate for the bottom contact. In this process, a UV lithographic tool is employed along with a positive AZ positive resist to define the desired shape. Subsequently, the bottom contact undergoes etching in a subsequent RIE step, resulting in the configuration depicted in Fig. 5.1(d). It is worth noting that the scale of this figure is intentionally unrealistic, as the pad's size is significantly larger than that of the pillars, as one can see in the scanning electron microscopy (SEM) image of the completed device in Fig. 5.1(l).

5.2.3 Accuflo isolating layer

At this stage of the process, a protective insulating polymer called Accuflo is spincoated onto the sample, as shown in Fig. 5.1(e). This polymer serves a dual purpose: it safeguards the pillars from external damage and oxidation while also isolating the bottom contact from the top one. To shape the polymer, two successive RIE etching steps are employed.

The first etching step defines a square shape around each pillar, as illustrated in Fig. 5.1(f). The second step is critical to establish contact between the pillar and the top electrode. In this RIE step, the polymer is thinned to achieve the desired configuration depicted in Fig. 5.1(g), where only a portion of the top ITO layer is exposed. Precision is essential in this step, as over-etching of the polymer could lead to a short circuit between the top and bottom electrodes, while under-etching could result in an open circuit. The optimal thinned thickness target is approximately 100 nm. To achieve this, the etching rate, that can fluctuate between 2.0 nm/s and 2.5 nm/s, is carefully calculated based on profilometer measurements from the previous RIE step enabling precise control over the amount of polymer to be selectively removed.

5.2.4 Indium tin oxide transparent conductive top electrode definition

The main deviation from the standard process [114,115,157] lies in the definition of the top transparent conductive electrode.

To assess the feasibility of indium tin oxide (ITO) films, Olivier et al. conducted an extensive examination of its optical and electrical properties. For more comprehensive information, please refer to the work by Olivier et al. in [111,158]. Following the earlier Accuflo thinning step, a 150 nm ITO deposition is performed, followed by a lithography step and RIE etching to define the top and bottom pads. At this stage, the junction is already operational. However, the contact between the probe tip and the ITO pads during electrical measurements is not as efficient as that achieved with standard aluminum pads. Typically, Al leads to lower series resistance and greater durability. For this reason, few final steps are taken to ensure standard contact levels.

In the final stages, a final UV lithography step is employed, using a negative resist to define the shape of the top electrode, which covers the magnetic pillar, as illustrated in Fig. 5.2(b-c). Following this, a deposition of 10 nm of Cr and 150 nm of Al using an evaporation process is carried out, and a subsequent lift-off procedure yields the final device. The resulting configuration can be observed in Fig. 5.1(k-l). As you can see in Fig. 5.2 (b-c), the Al pads are intentionally designed not to cover the ITO above the pillar. Moreover, from the detailed view in Fig. 5.2(b) it is possible to glimpse the underlying 300 nm pillar, thanks to the transparency of the ITO layer. In contrast,

in the SEM image (c), the pillar remains concealed as a result of the conductive properties of the ITO.

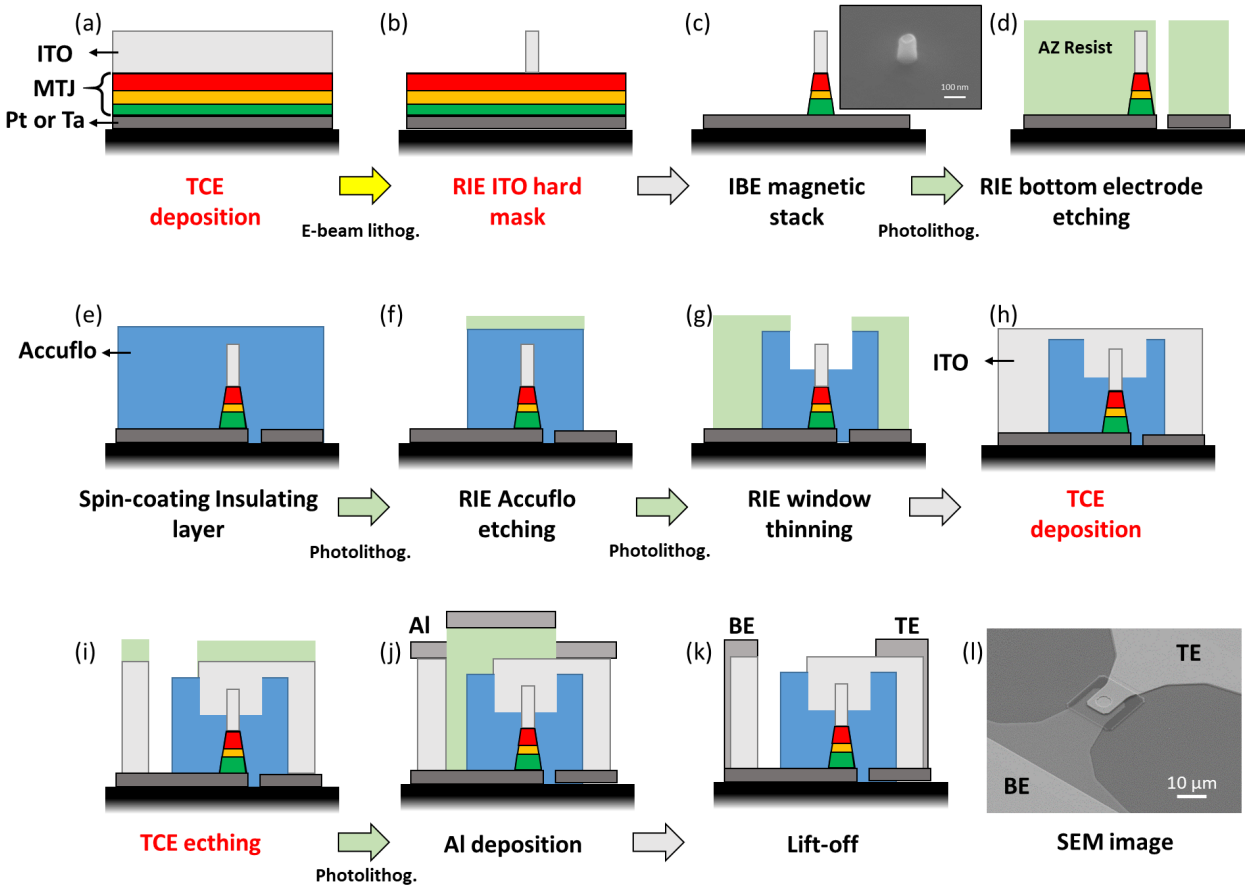

Fig. 5.1: Nano-fabrication process steps: (a) Deposition of ITO Transparent Conductive Electrode (TCE) on top of the magnetic stack, marking the beginning of the fabrication process. (b) E-beam lithography followed by reactive ion etching (RIE) after development, defining the shape and position of nano-sized pillars. (c) Ion beam etching (IBE) of the magnetic stack, removing excess material to form the pillars. (d) Etching of the bottom electrode of the RIE, shaping the bottom contact. (e) Accuflo deposition, serving as a protective and isolating layer. (f) RIE Accuflo window etching, further defining the Accuflo layer. (g) Thinning of the RIE Accuflo window, creating openings in the Accuflo layer. (h) TCE (ITO) deposition as the top electrode, enabling optical access and electrical connections. (i) TCE etching, defining the shape of the top electrode. (j) Cr electrodeposition and (k) Cr lift-off, creating a pattern for further better contact. (l) Final result, ready for electrical characterization, showcasing the completed device.

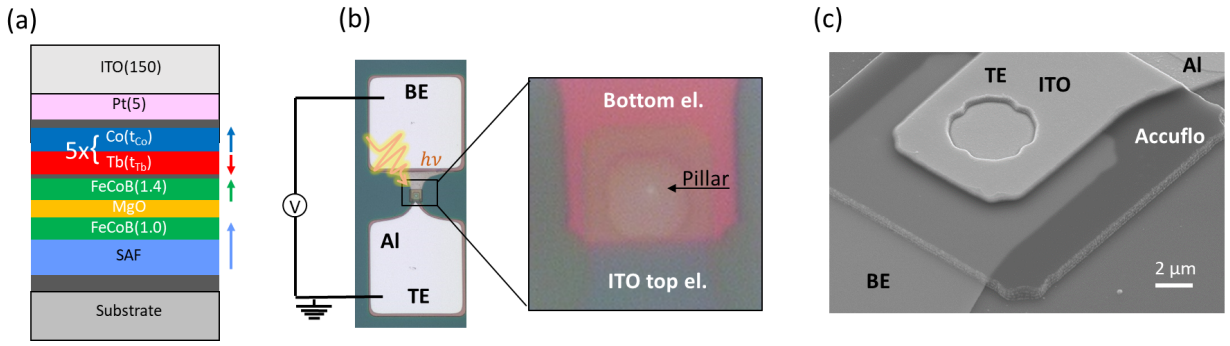

Fig. 5.2: (a) Schematic representation of the AOS-MTJ stack with bottom-pinned configuration. (b) Microscope image of the final device with a close-up view of the transparent ITO layer, revealing the underlying pillar. (c) SEM image providing a closer look at the Accuflo layer and ITO, with the underlying pillar not visible due to the conductive nature of ITO.

5.3 Electrical characterization setup

We will now detail the steps and equipment used for gathering and analyzing measurement data, setting the stage for the main findings of our study.

The electrical characterization of the wafer was performed by using an electrical prober, which has undergone optimization over several years at SPINTEC. This characterization process involves the application of a magnetic field to the wafer from an electromagnet equipped with two coils linked to a KEPCO generator. For generating hysteresis loops, we employed a waveform generator - the Agilent 33500B - to control the magnetic field sweeping, which was synchronized with the KEPCO power supply.

To determine the resistance states of the Magnetic Tunnel Junction device, we employed a Keithley 2401 current generator to direct a current through an RF probe onto the contact pads. At the same time, a digital multimeter, the Agilent 34411A, was employed to measure the resulting voltage. This voltage measurement enables the direct calculation of the MTJ's resistance in accordance with Ohm's law.

Fig. 5.3 shows a simple drawing of our experimental setup, highlighting the important parts of the electrical prober configuration. For a clearer understanding of the setup and how it works, interested readers can refer to the detailed explanation provided in the references [114,115,157].

The assessment of wafer yield is made easier through the use of automated stage movement, which additionally provides the capability to regulate the sample temperature. A screening procedure has been put in place to detect and skip devices with short or open circuits, which may result from potential manufacturing flaws. This is a crucial step in identifying issues associated with specific critical stages during fabrication. As outlined in Section 5.2, short circuits could arise from excessive polymer window thinning prior to top electrode deposition, while open circuits could result from pillar losses during patterning or insufficent polymer window thinning before top electrode contact.

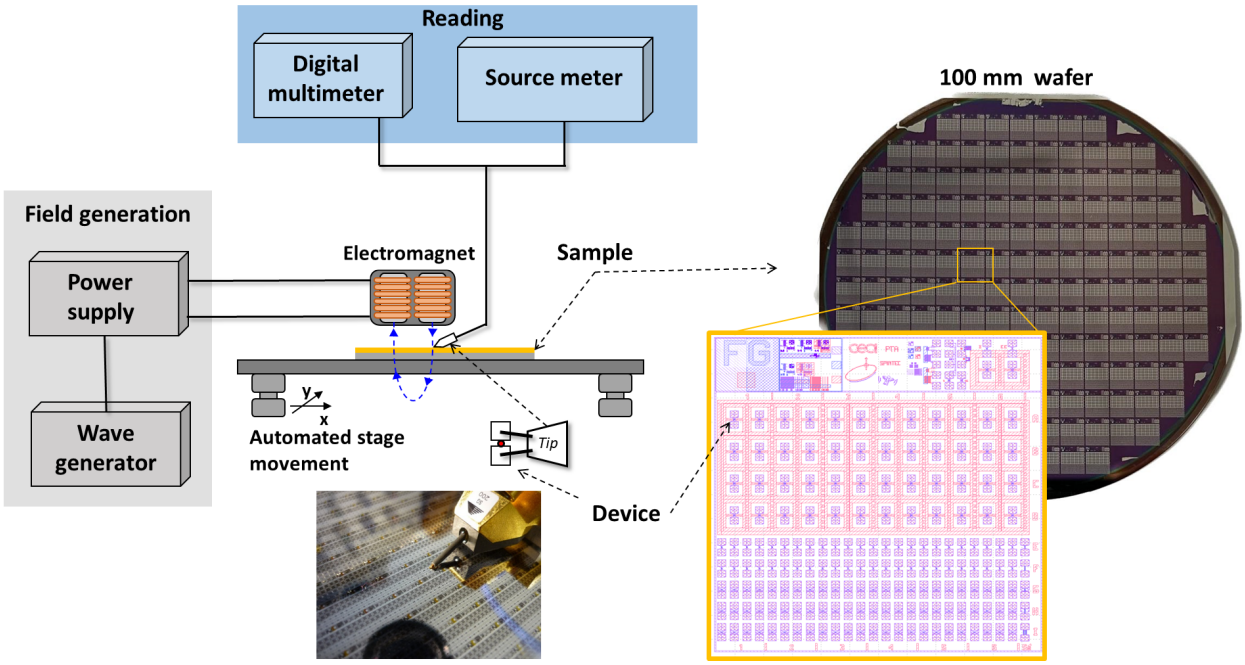

Fig. 5.3: Electrical prober setup schematic on the top left, photo of electrical probe at the bottom for contacting the devices. On the right a photo of 100 mm wafer after nano-fabrication process with a zoom in schematic of a die.

5.4 MTJ nano-patterned devices based on [Tb/Co] multilayer: yield and TMR measurements

In this section, we will investigate the results obtained from our nano-patterned MTJ devices, which were fabricated as previously explained. Our experimental approach started creating two distinct samples: one featuring a noncompensated soft reference layer, and the other incorporating a synthetic antiferromagnet to stabilize and compensate the reference layer. The structures are as follows:

Stack 1

$$\text{Ta(30)/Pt(250)/W(3)/FeCoB(10)/MgO/FeCoB(14)/W(2)/[Tb/Co(14)]} \times 5\text{/W(20)/Pt(50)}.$$

Stack 2

$$\text{Ta(30)/Pt(250)/[Co(5)/Pt(2.5)]} \times 5\text{/Co(5)/Ru(9)/[Co(5)/Pt(2.5)]} \times 2\text{/}$$
$$\text{Co(5)/W(3)/FeCoB(10)/MgO/FeCoB(14)/W(2)/[Tb/Co(14)]} \times 5\text{/W(20)/Pt(50)}.$$

The numbers in parentheses represent the respective layer thicknesses in angstroms (Å), comprising the entire stack.

Knowing the properties of AOS at the thin film level, as discussed in Chapter 3, our strategy was designed to maximize our chances of achieving the desired thickness region of AOS at as many junctions as possible. To achieve this, we reevaluated the composition of the double wedge formed by the Tb and Co layers. Given that most of the investigated stacks exhibited AOS characteristics with a Co thickness around 1.4 nm, and considering the stability of the Co deposition rate in our

sputtering equipment, a decision was made to maintain a fixed Co thickness at this value. Instead, we opted to implement the wedge solely on the Tb layers, which varied from 0.4 to 1.1 nm, as its deposition rate could exhibit slight fluctuations. This modification allowed us to adjust to any minor shift in the deposition rate, ensuring a higher likelihood of obtaining complete sets of dies with the desired AOS characteristics.

Simultaneously, a perpendicular wedge of the MgO barrier layer was deposited on the sample, with its thickness ranging from 1.1 nm to 3.0 nm. This was done to determine the optimal natural oxidation thickness of the Mg layer, which would yield the highest Tunnel Magnetoresistance ratio. The TMR ratio is a critical parameter for magnetic tunnel junction devices, as it significantly influences their performance.

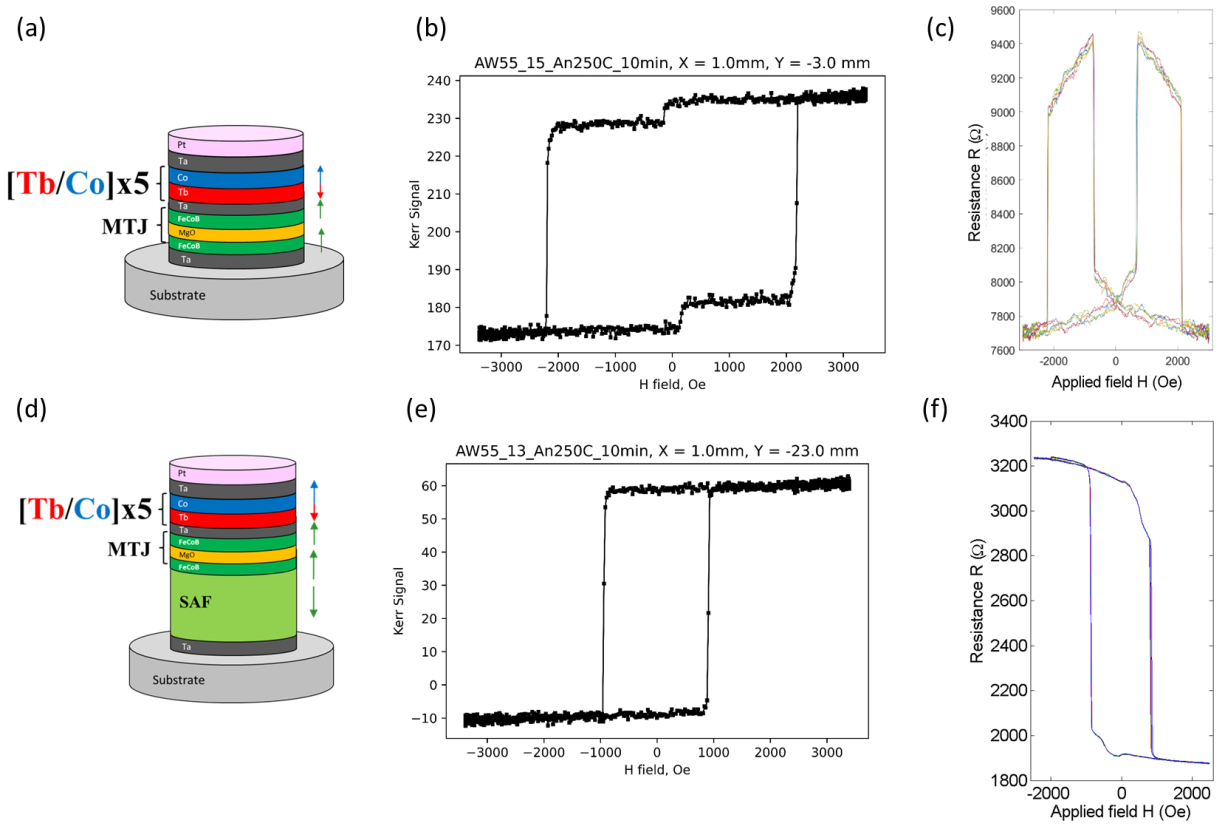

Fig. 5.4: Stack 1 and **Stack 2**: a) The device average TMR versus naturally oxidized MgO thickness for nominal diameter between 100 nm to 300 nm and thicknesses t_{Tb} from 0.5 nm to 0.75 nm and t_{Co}=1.4 nm, respectively compared to literature values [21,104,105,158]. b) Coercive field vs Tb thickness comparison between thin film sample and nano-patterned devices.

In Fig. 5.4, the hysteresis loops are presented at two points of the two samples, before and after the fabrication process. The measurements for the thin-film samples were conducted using MOKE interferometry, followed by a fabrication process, and then the measurements with the prober. Notably, the sample featuring a soft "reference" layer exhibits two distinct transitions, indicating that the magnetic field has the capacity to switch the two layers. On the contrary, in the second sample, the coercive field of the reference layer is higher than the maximum field attainable in both experimental setups. Consequently, this results in an observed hysteresis loop solely for the storage

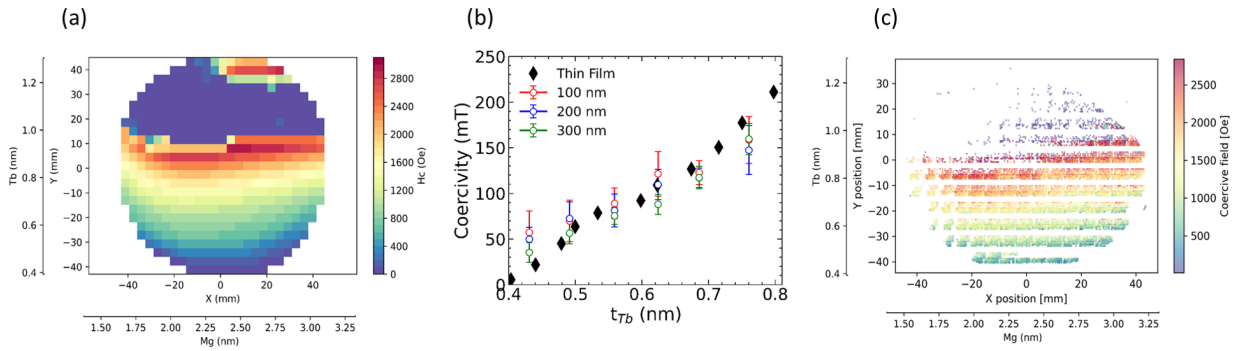

Fig. 5.5: Stack 2: (a) thin film double wedge coercivity map of full stack MTJ; (b) processed wafer TMR in function of position. [152]

FeCoB layer, which is closely coupled with the Tb/Co multilayer. Fig. 5.5 shows the same measured loops that show coercive field values across the whole wafer. From these mappings one can see the evident dependence of the coervicity with the Tb thickness. As shown already in Chapter 3 in this Co rich region, the thicker the Tb layer, the closer we move to the compensation point and thus the higher the coercive field. Above the 20 mm Y position in the wafer, we can see that the field is too low to be able to measure the hysteresis loop, showing 0 Oe as an artifact.

The fabricated MTJ devices had a range of diameters from 80 to 300 nm. Crucially, the nano-patterning process did not compromise the expected properties of the AOS stack. This underscores the robustness of perpendicular magnetic anisotropy at the film level, which was preserved even after the intricate nano-patterning process, as demonstrated in the coercivity measurements illustrated in Fig. 5.5. As we said, coercivity was found to depend on the thickness of the Tb/Co but remained comparable before and after patterning, with no significant dependence on the diameter size of the pillars.

The quasi-static hysteresis loops are significantly affected by the system's anisotropy. When the anisotropy axis aligns precisely with the applied magnetic field, the resulting loops exhibit a square shape, representing an easy axis configuration. Conversely, when there is an angle between these axes, as seen when approaching the hard axis, the hysteresis loop adopts a more rounded form. This roundness indicates a gradual alignment of the magnetization direction with the direction of the applied field.

Our measurements, depicted in Fig. 5.4 and carried out using MOKE and prober techniques, involved applying the magnetic field perpendicular to the system. We can observe a difference in the loop shapes before and after patterning. In the latter case, the rounded loop we observe suggests that the anisotropy is not perfectly oriented out of the plane, particularly noticeable in the soft reference layer sample. Determining which of the two FeCoB layers has experienced a loss of anisotropy is a challenging task, since the measured resistance depends on their mutual orientation. However, it appears that the reference layer is mostly affected, since the coercivity of the Tb/Co layer remained largely unchanged, as previously mentioned. Moreover, in the uncompensated sample, a greater "slope" compared to the SAF sample suggests that it may indeed be this layer undergoing the gradual magnetization realignment to the field direction.

The stability of the reference layer also influences the spin polarization of the current, which, in turn, impacts the TMR. In general, we observed that the TMR in uncompensated samples is lower

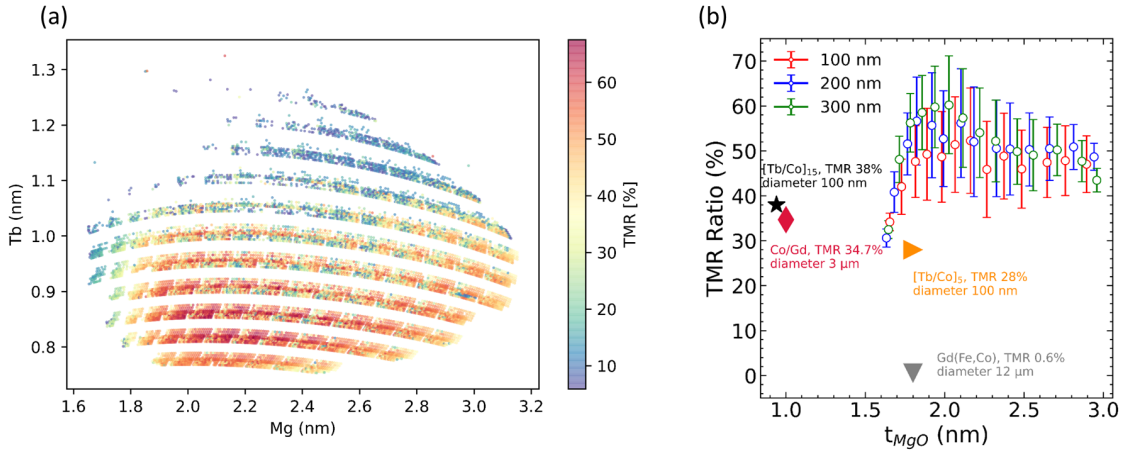

Fig. 5.6: Stack 2: a) The device average TMR versus naturally oxidized MgO thickness for nominal diameter between 100 nm to 300 nm and thicknesses t_{Tb} from 0.5 nm to 0.75 nm and t_{Co}=1.4 nm, respectively compared to literature values [21,104,105,158]. b) Coercive field vs Tb thickness comparison between thin film sample and nano-patterned devices. [152]

compared to samples with a SAF.

The highest TMR was achieved for the SAF sample on the low side of the Tb and Mg thickness wedges, as can be seen in Fig. 5.6(a).

Instead, in Fig. 5.6(b), we examined devices with nominal diameters ranging from 80 to 300 nm. We measured the device-average TMR regarding the naturally oxidized MgO thickness while maintaining a Tb thickness from 0.5 to 0.75 nm. The natural oxidation process followed a standard procedure that involved two steps of 10 seconds each at 150 mbar. We found that the optimal Mg thickness was 2 nm. Below this value, the tunnel barrier tended to be excessively oxidized, leading to a decrease in TMR values.

The yield of the SAF sample, as illustrated in Fig. 5.5(c), is approximately 75%. This yield is considered quite good, especially for a non-optimized process. Furthermore, this stable reference layer, combined with the optimized natural oxidation thickness of Mg, allowed us to achieve the highest TMR values, reaching impressive 74%. This represents a significant two-fold improvement compared to the highest AOS-MTJ values reported in the literature [20,21,104,105,158], achieved with MTJs featuring a diameter at least 30 times smaller.

5.5 Coercivity vs temperature

This section serves as a complement to our discussion on AOS magnetic reversal presented in Chapter 3. We examine the dependence of the coercivity on temperature, which is closely related to the multilayer's anisotropy and magnetization. A magnetic field sweep was applied and resistance loops were taken at temperatures between 30°C and 80°C

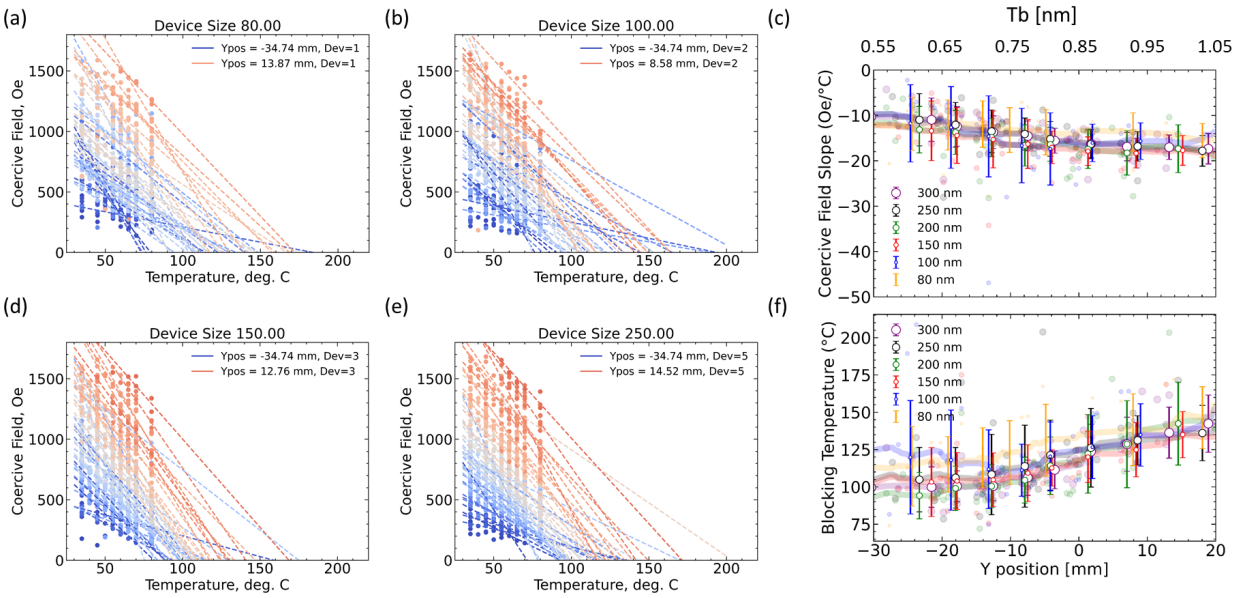

Fig. 5.7: Stack 2:(a-b-d-e) Coercivity vs temperature for junction nominal diameter sizes of 80 nm, 100 nm, 150 nm, and 250 nm respectively; (c) Average linear fitted extracted slope. (f) Average linear fitted extracted Blocking temperature.

The panels (a, b, d, and e) in Fig. 5.7, illustrate the evolution of coercivity with increasing temperature for different diameter sizes, along with the calculated corresponding slope (Fig. 5.7 (c)) and blocking temperature (Fig. 5.7 (f)) obtained from the data fitting for each junction. Despite the observed data dispersion and significant variability from one junction to another, it is apparent that the junction dimensions have a minimal impact on both the slope and the blocking temperature.

In general, a trend emerges of a slight increase in steepness and a non-negligible rise in the blocking temperature as we move towards higher Y positions. This shift is associated with higher coercive field positions and thicker Tb layers, spanning from 100°C to 150°C.

This sharp phase transition is coherent with the in-plane reorientation-driven reversal discussed earlier. The increase in temperature resulting from an applied laser pulse dramatically reduces the anisotropy while increasing the total magnetization. Because this transition happens at relatively low temperatures compared to the Curie temperature of bulk Co (1388 K), one can expect that the Co layers will remain magnetized. However, without anisotropy, they are forced to reorient towards the easy-plane due to the demagnetizing field.

5.6 Femto-second laser pulse device irradiation and electrical readout: all-optical switching demonstration

Investigating the all-optical switching properties of nano-sized MTJ pillars was conducted through collaborations with two prestigious institutions: the *Lawrence Berkeley National Laboratory* and the *Institute Jean Lamour, Nancy*. Both experiments followed similar procedures, utilizing linearly polarized femtosecond laser pulses to irradiate the MTJ pillars while simultaneously measuring their resistance, as depicted in the schematics of Fig. 5.2(b) and Fig. 5.9(a). The electrical readout was achieved by connecting a digital multimeter to the top and bottom electrodes of the device using wire bonding, with a continuous reading voltage of 10 mV applied to measure the resistance.

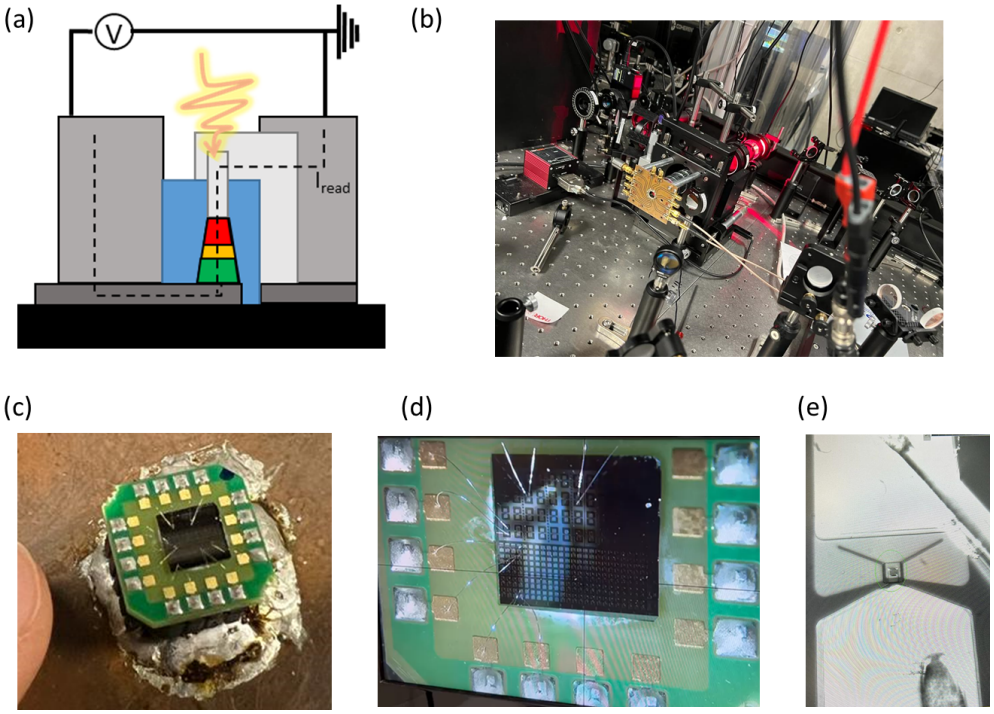

Fig. 5.8: Electrical detected AOS measurement setup. (a) Schematic of the setup; (b) Photo of the sample holder, notice the cables for the electrical measurement; (c-d) Die cut from the wafer with wire-bonding; (e) Microscope image of a device wire-bonded.

Our initial attempts to achieve all-optical switching in Tb/Co-based MTJs at the nano-scale were carried out at the University of California, Berkeley, led by S. Mondal. These efforts, detailed in [160], focus primarily on MTJs with a soft reference layer.

In this context, the larger anisotropy of the FeCoB/Ta/$[Tb/Co]_5$ layer, compared to the reference FeCoB layer, and the nano-scale size of the MTJ, make magnetostatic coupling and magnetic anisotropy critical factors influencing the equilibrium state and the switching rate. Our experiments demonstrated for the first time the feasibility of optically driven switching operations in these devices. However, it became evident that to at least approach 100% switching probability, a pinning field larger than the saturation field of the reference layer was required. Without this applied field, the reversal process exhibited stochastic behavior, as illustrated in 5.9(b).

The probabilistic nature of this switching was attributed to the stray magnetic field originating

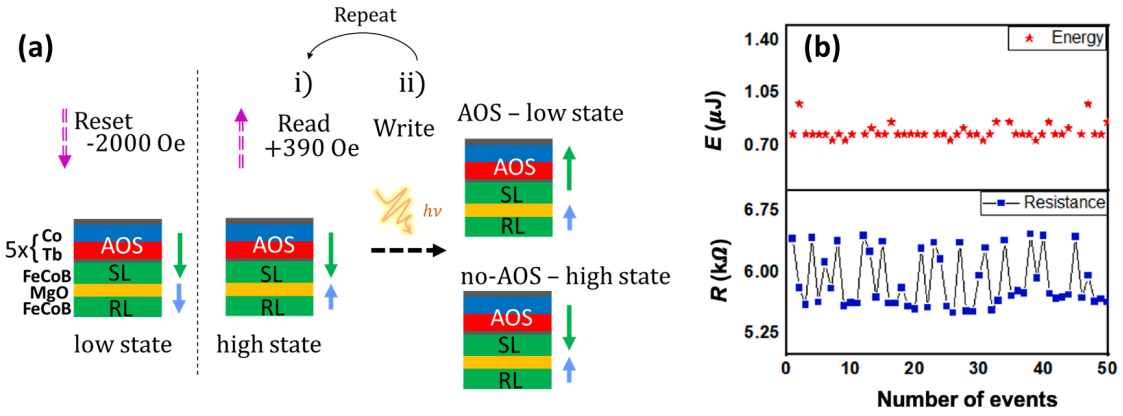

Fig. 5.9: [160] **Stack 1**: (a) For an MTJ cell of 300 nm diameter, the sequence of reading the magnetic state electrically and switching the state optically in presence of the pinning field is depicted. The *high* and *low* stand for high and low resistance states, respectively. The drawings represent the final configuration at each stage of the write/read process. (b) The change in the magnetoresistance value (R) recorded after the approach of each optical pulse with fluence $\gtrsim 50$ mJ/cm^2. The energy of the pulse (E) was also recorded simultaneously. The magnetic field sequence is plotted as a reference with the number of events.

from the soft reference layer. As mentioned earlier, the reversal in our system [137,161] is slower compared to the Gd samples [17], indicating that an external field could significantly influence the switching process.

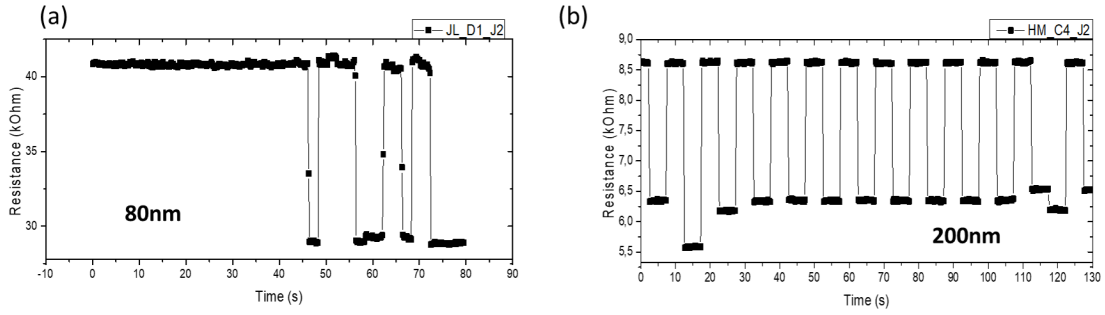

Fig. 5.10: Stack 2: Without external field, TMR measurement as a function of time upon laser-pulse excitation for (a) 80 nm junction, (b) 200 nm junction.

5.10(b) shows a significant improvement in performance when using a stack with a compensated reference layer. These experiments were carried out in Nancy by the writer with the help of Yi Peng, without the need for an external magnetic field on a 200 nm junction. Although one can see that an incomplete reversal is taking place evidencing the presence of magnetic domains. Instead, at 80 nm in diameter 5.10(a) it appears that the junction reversal is still affected by stray field despite having an SAF.

However, in 5.11(b) we see how at 100 nm the junction appears to be small enough to switch uniformly and large enough to reduce stray fields. In this case, the AOS-MTJ exhibited repeatable toggling between parallel (P) and antiparallel (AP) states, displaying the 50% TMR resistance change observed by the R-H loop, shown in Fig. 5.11(a).

To further investigate the behavior of these devices, we compared the fluence write levels between

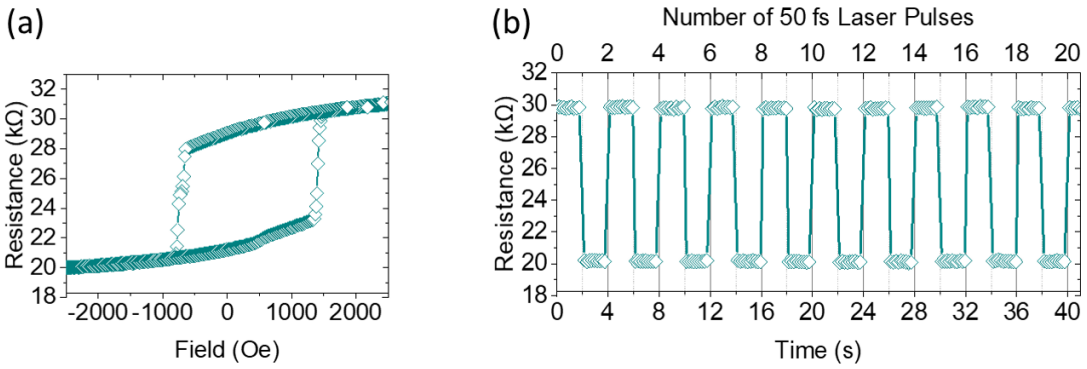

Fig. 5.11: Stack 2: Measurements of 100 nm AOS-MTJ: (a) AOS-MTJ hysteresis R-H loop, field applied out-of-plane. (b) TMR measurement as a function of time upon laser-pulse excitation. [152]

the patterned tunnel junction and the equivalent AOS stack at the thin film level, as shown in Fig. 5.12. The dependence of switching on fluence was preserved after patterning. During this experiment, the laser was fired repeatedly at a 1 Hz frequency, incrementally increasing the laser power every second by 0.01 mW. This allowed us to determine the minimum fluence required for the reversal. At low fluence, no switching was observed, with switching events starting at 4 mJ/cm^2. In the region between 5-6 mJ/cm^2, the switching probability reached 100%, as highlighted in blue in Fig. 5.11.

However, at even higher fluences, represented by the red region, switching was no longer observed, and then a last random switching region occurred before eventual device degradation. This established device phase diagram closely correlated with the thin film phase diagram presented in Fig. 3.9 in Chapter 3, indicating a similar mechanism governing the reversal process. In the framework of our model, the same precessional switching reversal process determines the AOS properties of the patterned device, despite the fact that some small stray field from the reference layer is acting on the storage layer.

In this way, we elucidated the complex interplay of factors influencing the optical switching behavior of nano-sized MTJ pillars, shedding light on the critical role of magnetic anisotropy and stray fields in achieving reliable and efficient all-optical switching.

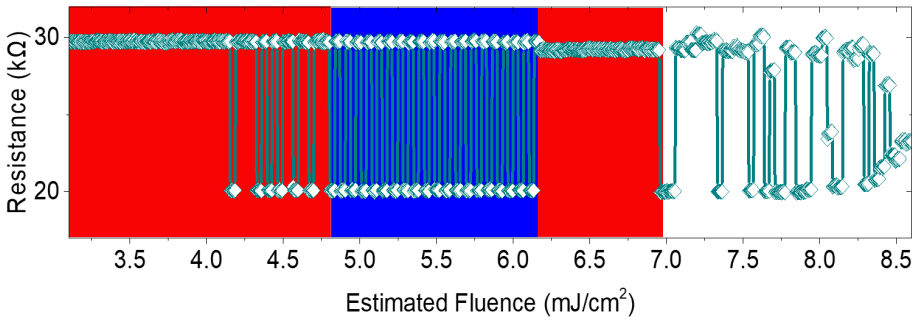

Fig. 5.12: Stack 2: TMR measurement using constant 1 Hz laser frequency and incremental laser power for each pulse. [152]

Another experiment was performed on a larger device (250 nm) in order to verify the presence

of different magnetic domain. Shown in 5.13 the usual TMR measurement with applied pulses was carried out but this time "resetting" the junction with an external magnetic field. As you can see, the resistance values of the AOS toggle switching varies upon exposure to field, but the overall TMR remains lower than what observed during an R(H) loop (57%). This means that the grains within the junction have different threshold fluences and each pulse is not able to revers the whole storage layer.

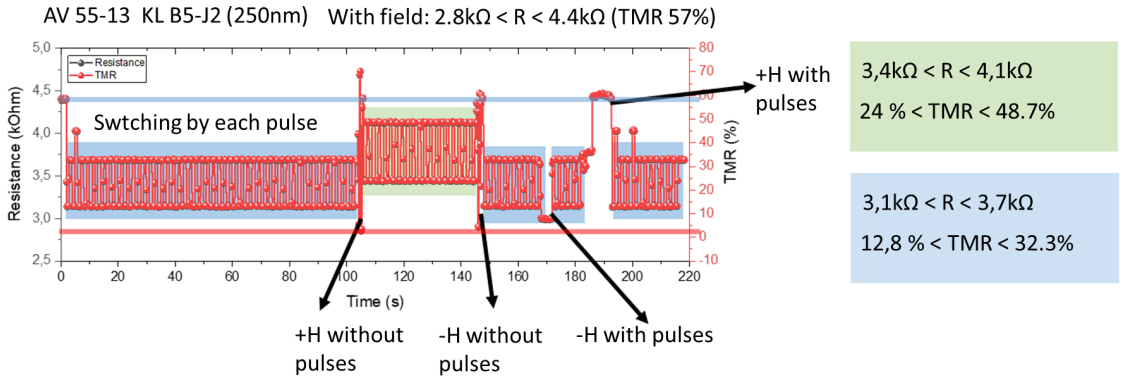

Fig. 5.13: Stack 2: TMR measurement as a function of time upon laser-pulse excitation for 250 nm junction while applying magnetic field rest pulses.

5.7 Energy consumption: significance and findings

As we said in the Introduction, in today's rapidly evolving technological landscape, the quest for energy-efficient solutions is paramount. One of the goals of merging AOS to MRAM, alongside the speed potential, is to lower the energy needed to write data.

In this context of AOS, Sobolewska et al. conducted a pioneering study [111], investigating the light absorption properties of full-sheet films within our unique ITO-Tb/Co stack configuration.

Employing ellipsometry, they explored the stack's properties both before and after annealing. Subsequently, these parameters were incorporated into a theoretical Finite Difference Time Domain (FDTD) model, enabling them to calculate absorption in fullsheet films and estimate the effective absorption within the pillar. In particular, the results showed a remarkable convergence between simulations and experiments, unveiling a maximum absorption of 17.5% at 1550 nm for MTJs with a diameter of 300 nm.

On the basis of their insights, we calculated the energy consumption required for our AOS demonstration experiments. By assuming a 17.5% absorption of the laser fluence (as reported in [111]), and scaling this by the area of the pillar, we derived an estimated energy consumption of 68.6 fJ/bit. Importantly, this figure already puts our technology well below the energy dissipation levels of established technologies like hard disk drives (10-100 nJ) [162], FLASH memory (10 nJ) [**?**], and cutting-edge STT-RAM (450 pJ-100 fJ) [3,163].

Furthermore, for pillars with a diameter as small as 40 nm, our energy consumption would fall to just 11 fJ/bit. This represents a substantial 45% reduction compared to previous predictions [3], marking a significant leap forward in the pursuit of energy-efficient data storage solutions. In Fig. 5.14 we re-present the data shown in Chapter 1 but adding the expected properties of our device;

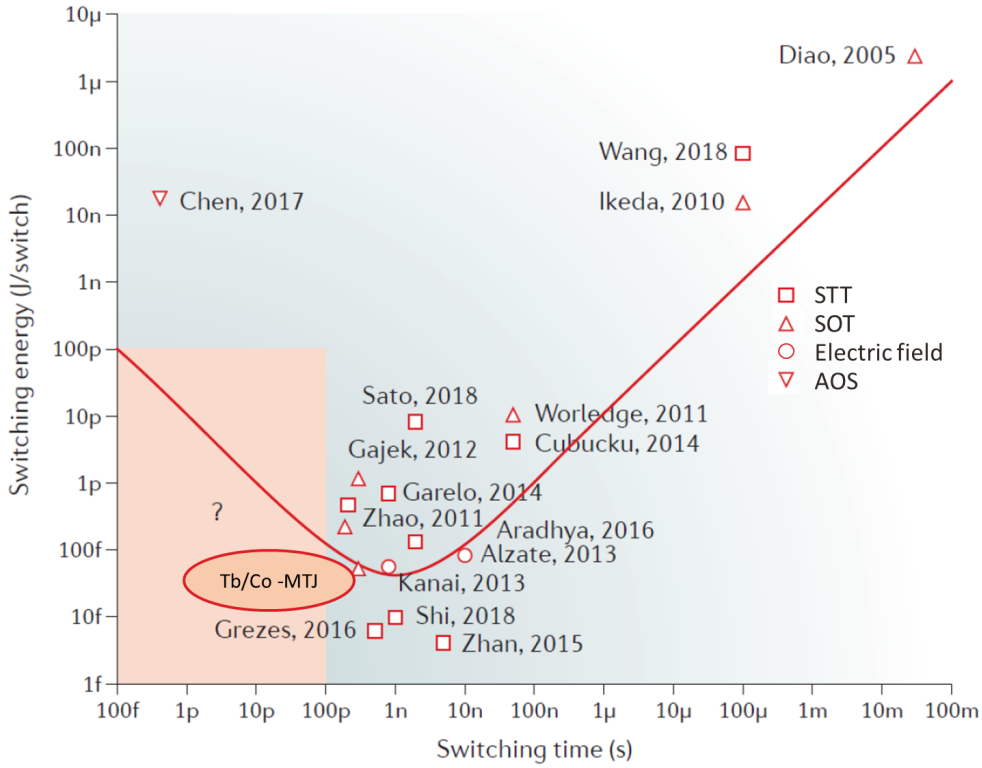

Fig. 5.14: Spin transfer vs AOS switching energy and time | Summary of switching energy and time of magnetic tunnel junction (MTJ) memory devices and spin valves using mechanisms of spin-torque transfer (squares) [74–77], spin-orbit torque (SOT) (triangles) [78–83], and electric-field-induced switching (circles) [84–86]. The red line the plot of equation (1) with $t_{c0} = 1$ ns and $U_{c0} = 10$ fJ. The shaded area indicates the specifications targeted by future technologies. Figure from [3].

indeed we are only able to give and estimate as no time-resolved measurements were performed on patterned devices, but if one considers the reversal time scale as that of thin-film switching we can expect somewhere around 50 to 100 ps, making the device extremely competitive.

5.8 Conclusion

In this chapter, I described in detail the fabrication of magnetic tunnel junction devices, concentrating on their electrical and optical properties at the nano-scale. The fabrication process consists in a careful sequence of steps, beginning with the deposition of the initial material and ending with the definition and patterning of the electrodes. The fabricated MTJ devices with top ITO electrodes that are both transparent and conductive, forming the basis for a functional AOS-MTJ.

I then moved on to electrical characterization, methodically outlining our experimental setup and procedures. The measurements focused on MTJ devices featuring a multilayer structure of [Tb/Co], with particular attention to the influence of the Tb and MgO layer thicknesses on the TMR ratios and coercivity. Our findings not only confirmed the robustness of nano-patterned devices, but also revealed that the implementation of a stable reference layer and optimization of natural MgO oxidation allowed for TMR values of 74%, the highest reported so far for AOS-MTJs.

Additionally, the temperature-dependent coercivity behaviors within were explored on nano-scale MTJ devices of varying dimensions. This in-depth analysis sheds light on the relationship

between coercivity in response to temperature for different device sizes, offering critical insights into the dynamic nature of the reversal discussed in Chapter 4.

Our scientific investigation reached its pinnacle with an exploration of all-optical switching in nano-patterned junctions. By subjecting MTJ pillars to ultra-fast laser pulses, we probed the prospects of achieving non-volatile data storage and energy-efficient computation. Field-free helicity-independent all-optical toggle switching was demonstrated on 100 nm patterned [Tb/Co] p-MTJ devices, driven by 50 fs laser pulses for an estimated absorbed energy of 68.6 fJ/bit.

In conclusion, our thorough investigation has not only deepened the knowledge of these devices, but has also furthered the quest for more efficient and sustainable data storage solutions. Investigation into nano-scale MTJ devices has laid the groundwork for further scientific investigation, stimulating the development of spintronic devices that could potentially create a new form of storage technology.

Chapter 6

Conclusion and future research directions

Key findings and contributions

This thesis illustrates an extensive and insightful study of helicity-independent all-optical switching in multilayer systems. The work carried out was aimed to gain a more comprehensive understanding of this physical phenomenon in Tb/Co multilayers and to develop a fully functional nanometer-sized AOS-MTJ.

Across the thesis, we have revealed its mechanisms, exploring its dependence on fluence and pulse duration in different samples and validating our findings through numerical simulations. Moreover, we have applied this knowledge to the creation of functional Magnetic Tunnel Junction devices, opening new horizons for non-volatile data storage and energy-efficient computation at the nanoscale.

Chapter 3 laid the foundation for our exploration by investigating HI-AOS on thin films of rare-earth transition-metal multilayer systems. The study identified the region for complete and reliable magnetization toggle reversal and explored the response across different pulse durations and fluences. The key takeaways from the observations were that, depending on the layers thicknesses, the reversed domains exhibit a unique pattern of concentric rings with opposite magnetic orientations and that the fluences required to reverse and stabilize a specific number of rings showed little to no dependence on the duration of the laser pulses. This indicates that the magnetization reversal process is distinct from previously seen single shot AOS and occurs on a slightly longer time scale.

The investigation lead to the hypothesis explaining the underlying mechanism behind HI-AOS in (Tb or Dy)-TM based multilayers. This hypothesis pointed to the significance of the magnetic grains local anisotropy of these systems, which rapidly decreases due to temperature increases caused by the laser pulse and the low Curie temperatures of Tb and Dy.

In terms of model, our work challenges existing paradigms surrounding HI-AOS by demonstrating the unique dynamics of the Tb/Co-based multilayer system. In fact, Chapter 4 focused on the numerical investigation of HI-AOS. We developed a macrospin model that incorporated the 2TM principles, providing a deeper understanding of the precession-driven switching observed in our samples. The model incorporates two essential features that are crucial for retrieving the phys-

ical phenomena observed experimentally: the first is a temperature-dependent uniaxial anisotropy exhibiting a rapidly decrease with temperature thus temporarily "loosing" to the demagnetization energy after laser irradiation; the second a slightly angled axis relative to the out-of-plane direction of the anisotropy, this is assumed to be due to local crystal-field interaction given the sperimagnet nature of Tb and Dy.

As temperature increases, the anisotropy decreases and then begins to recover during the cooling phase. Throughout this process, the partially demagnetized TM undergoes reorientation, influenced by the changing balance between the demagnetizing field and the anisotropy field. These dynamics result in precession, and due to the high damping, ultimately lead to magnetization reversal depending on the energy absorbed from the laser pulse.

The simulations show how parameters like Gilbert damping, tilt angle and Q factor influence the reversal patterns. Atomistic spin simulations further validated our findings, emphasizing the significance of temperature-dependent magnetization and anisotropy effects in the HI-AOS process.

Additionally, our research addresses a practical challenge of enhancing annealing resilience. The introduction of a capping MgO layer improved the annealing resistance of Tb/Co-based MTJs to a temperature of 300°C, while preserving HI-AOS characteristics, has clear implications for the development of reliable and robust AOS-devices. This is particularly pertinent in the quest for MTJs, which are fundamental components in various applications, including MRAM, sensors, and spintronic devices.

Chapter 5 brought our exploration to the practical realm by detailing the fabrication and electrical characterization of MTJ devices. The optimization of TMR values, a key factor in data storage efficiency, is a significant contribution of our work. Achieving TMR values as high as 74%, the highest reported thus far for AOS-MTJs, opens the door to more efficient and reliable data storage devices. Our scientific inquiry reached its peak by demonstrating all-optical switching within nanopatterned junctions. Through the exposure of MTJ pillars to ultrafast laser pulses, we explored the potential for non-volatile data storage and energy-efficient computation. The experiment showcased field-free, helicity-independent all-optical toggle switching on 100 nm in diameter patterned [Tb/Co] p-MTJ devices. This was achieved using 50 fs laser pulses, with an approximate absorbed energy of 68.6 fJ per bit.

Our research methodology combines both experimental and simulation approaches, which, we believe, allowed us to gain valuable insights into the phenomenon of HI-AOS. The blend of real-world experiments and computational simulations was crucial in providing a comprehensive understanding of the complex dynamics at play in HI-AOS. It is important, though, to acknowledge the boundaries of our study. While our research provides valuable insights into HI-AOS, it does not provide a complete and exhaustive investigation for all the different systems where the phenomenon was observed. Moreover, HI-AOS is a multifaceted process with many physical processes and interacting variables. The reversal due to femtosecond laser pulse may be a combination of several physical processes, as a dependency on pulse duration can be found at high fluences. The complexities and intricacies of HI-AOS may require further investigation, potentially involving more detailed studies with atomistic models or Landau-Lifshitz-Bloch (LLB) models to capture the intricate interactions at play.

Regarding MTJ devices, the characterization for AOS, needs still substantial work. Currently,

there is no efficient measurement setup in place, as a result, the measurements necessitated wire-bonding becoming time-consuming, thus leading to a lack of statistical data. While the groundbreaking achievement of demonstrating fs pulse-driven switching is highly significant, it is crucial for AOS-MTJs to transition from toggle switching to deterministic switching. If it is necessary to read the current state before writing to a memory cell, the advantages of speed will be lost. Therefore, further technological advancements are needed.

Moreover, since the reversal process depends on the anisotropy axis of each grain, there is an expected variability from junction to junction due to the inherent randomness of the system's sperimagnet nature. However, this variability may be addressed through material optimization.

The most challenging aspect in achieving AOS-MRAM remains the integration of photonic and spintronic elements. Research in this field needs to advance to accurately predict the performance of the final memory devices. However with this work we presented a new type of reversal that allows for longer laser pulse duration that require laser technology much more feasible compared to femtosecond laser pulses.

Future Directions

While our research has yielded significant insights, it has also illuminated several promising avenues for future exploration:

- **Atomistic and LLB models:** Given the complexity of HI-AOS, future research can delve into more intricate atomistic models or potentially explore the application of Landau-Lifshitz-Bloch (LLB) models, offering an exhaustive understanding.
- **Exploring alternative materials:** Our research predominantly focused on Tb/Co-multilayer based MTJ devices. However, thanks to the collaboration with Yi Peng, we now know there are many alternative systems with similar properties. Additionally, the understanding of the phenomenon may open a door to new engineered materials that do not require RE elements.
- **Deterministic HI-AOS with spin transfer torque (STT):** An important ongoing study is the possibility of combining Spin Transfer Torque (STT) with AOS to achieve deterministic switching. This exploration takes advantage of the slower dynamics of the system and may open new horizons for controlled switching in memory devices.
- **Device variability:** The development of an advanced setup that seamlessly integrates automated probing with AOS experiments holds the potential to significantly enhance our understanding of HI-AOS at the device level.
- **Low-temperature applications:** The investigation into harnessing Ohmic heating at low temperatures presents a interesting prospect. It may enable the picosecond switching with current pulses, potentially obviating the need for laser pulses and offering novel possibilities for device applications.

In summary, this thesis has provided a comprehensive exploration of helicity-independent all-optical switching (HI-AOS) in multilayer systems, uncovering the intricate mechanisms underpin-

ning this phenomenon, its applications in data storage, and its transformative potential for nanoscale technology. Our research has not only deepened our comprehension of HI-AOS but has also laid the groundwork for innovative applications in non-volatile data storage and energy-efficient computation. As we continue to chart this uncharted territory, the integration of photonic and spintronic elements holds the promise of revolutionizing memory technology. With this work, we have set the stage for further investigation and innovation, shaping the future of HI-AOS and its profound impact on the landscape of data storage and computation.

References

[1] Dieny B., Prejbeanu I. L., Garello K., Gambardella P., Freitas P., Lehndorff R., Raberg W., Ebels U., Demokritov S. O., Akerman J. *et al. Opportunities and challenges for spintronics in the microelectronics industry.* Nature Electronics **3**, 446–459 (2020). [pp. 1, 2, 29]

[2] Kim J., Paul A., Crowell P. A., Koester S. J., Sapatnekar S. S., Wang J.-P. & Kim C. H. *Spin-based computing: Device concepts, current status, and a case study on a high-performance microprocessor.* Proceedings of the IEEE **103**, 106–130 (2014). [p. 1]

[3] Kimel A. V. & Li M. *Writing magnetic memory with ultrashort light pulses.* Nature Reviews Materials **4**, 189–200 (2019). [pp. 1, 2, 23, 26, 28, 29, 103, 117, 118]

[4] Slonczewski J. C. *Current-driven excitation of magnetic multilayers.* Journal of Magnetism and Magnetic Materials **159**, L1–L7 (1996). [pp. 2, 19]

[5] Berger L. *Emission of spin waves by a magnetic multilayer traversed by a current.* Physical Review B **54**, 9353 (1996). [pp. 2, 19]

[6] Ralph D. C. & Stiles M. D. *Spin transfer torques.* Journal of Magnetism and Magnetic Materials **320**, 1190–1216 (2008). [p. 2]

[7] Yuasa S., Nagahama T., Fukushima A., Suzuki Y. & Ando K. *Giant room-temperature magnetoresistance in single-crystal fe/mgo/fe magnetic tunnel junctions.* Nature materials **3**, 868–871 (2004). [p. 2]

[8] Parkin S. S., Kaiser C., Panchula A., Rice P. M., Hughes B., Samant M. & Yang S.-H. *Giant tunnelling magnetoresistance at room temperature with mgo (100) tunnel barriers.* Nature materials **3**, 862–867 (2004). [p. 2]

[9] Brataas A., Kent A. D. & Ohno H. *Current-induced torques in magnetic materials.* Nature materials **11**, 372–381 (2012). [p. 2]

[10] Brataas A., Kent A. D. & Ohno H. *Current-induced torques in magnetic materials.* Nature materials **11**, 372–381 (2012). [p. 2]

[11] Ando K., Fujita S., Ito J., Yuasa S., Suzuki Y., Nakatani Y., Miyazaki T. & Yoda H. *Spin-transfer torque magnetoresistive random-access memory technologies for normally off computing.* Journal of Applied Physics **115**, 172607 (2014). [p. 2]

[12] Khvalkovskiy A., Apalkov D., Watts S., Chepulskii R., Beach R., Ong A., Tang X., Driskill-Smith A., Butler W., Visscher P. *et al. Basic principles of stt-mram cell operation in memory arrays.* Journal of Physics D: Applied Physics **46**, 074001 (2013). [p. 2]

[13] Manchon A., Železnỳ J., Miron I. M., Jungwirth T., Sinova J., Thiaville A., Garello K. & Gambardella P. *Current-induced spin-orbit torques in ferromagnetic and antiferromagnetic systems.* Reviews of Modern Physics **91**, 035004 (2019). [p. 2]

[14] Miron I. M., Garello K., Gaudin G., Zermatten P.-J., Costache M. V., Auffret S., Bandiera S., Rodmacq B., Schuhl A. & Gambardella P. *Perpendicular switching of a single ferromagnetic layer induced by in-plane current injection.* Nature **476**, 189–193 (2011). [p. 2]

[15] Krizakova V., Perumkunnil M., Couet S., Gambardella P. & Garello K. *Spin-orbit torque switching of magnetic tunnel junctions for memory applications.* Journal of Magnetism and Magnetic Materials **562**, 169692 (2022). [pp. 2, 3, 21]

[16] Stanciu C. D., Hansteen F., Kimel A. V., Kirilyuk A., Tsukamoto A., Itoh A. & Rasing T. *All-optical magnetic recording with circularly polarized light.* Physical review letters **99**, 047601 (2007). [pp. 2, 24]

[17] Radu I., Vahaplar K., Stamm C., Kachel T., Pontius N., Dürr H., Ostler T., Barker J., Evans R., Chantrell R. *et al. Transient ferromagnetic-like state mediating ultrafast reversal of antiferromagnetically coupled spins.* Nature **472**, 205–208 (2011). [pp. 2, 24, 25, 115]

[18] Ostler T., Barker J., Evans R., Chantrell R., Atxitia U., Chubykalo-Fesenko O., El Moussaoui S., Le Guyader L., Mengotti E., Heyderman L. *et al. Ultrafast heating as a sufficient stimulus for magnetization reversal in a ferrimagnet.* Nature communications **3**, 666 (2012). [p. 2]

[19] Vedmedenko E. Y., Kawakami R. K., Sheka D. D., Gambardella P., Kirilyuk A., Hirohata A., Binek C., Chubykalo-Fesenko O., Sanvito S., Kirby B. J. *et al. The 2020 magnetism roadmap.* Journal of Physics D: Applied Physics **53**, 453001 (2020). [p. 2]

[20] Avilés-Félix L., Álvaro-Gómez L., Li G., Davies C., Olivier A., Rubio-Roy M., Auffret S., Kirilyuk A., Kimel A., Rasing T. *et al. Integration of tb/co multilayers within optically switchable perpendicular magnetic tunnel junctions.* Aip Advances **9**, 125328 (2019). [pp. 2, 27, 48, 49, 50, 57, 104, 112]

[21] Avilés-Félix L., Olivier A., Li G., Davies C. S., Álvaro-Gómez L., Rubio-Roy M., Auffret S., Kirilyuk A., Kimel A., Rasing T. *et al. Single-shot all-optical switching of magnetization in tb/co multilayer-based electrodes.* Scientific reports **10**, 5211 (2020). [pp. 2, 27, 48, 49, 50, 51, 52, 57, 61, 104, 110, 112]

[22] *History of chinese invention - invention of the magnetic compass.* [p. 8]

[23] Oersted H. C. *Experiments on the effect of a current of electricity on the magnetic needle.* Annals of Philosophy **16**, 273–276 (1820). [p. 8]

[24] Maxwell J. C. *A Treatise on Electricity and Magnetism* (1873). [p. 8]

[25] Coey J. M. *Magnetism and magnetic materials* (Cambridge university press, 2010). [pp. 8, 47, 48]

[26] Hund F. *Linienspektren: Und Periodisches System der Elemente*, vol. 4 (Springer, 1927). [p. 9]

[27] Heisenberg W. *Erweiterungen des h ilbert-raums in der quantentheorie der wellenfelder*. Original Scientific Papers/Wissenschaftliche Originalarbeiten 241–248 (1993). [p. 10]

[28] Stoner E. C. *Collective electron ferromagnetism II. Energy and specific heat*. Proceedings of the Royal Society of London. Series A. Mathematical and Physical Sciences **169**, 339–371 (1939). [p. 11]

[29] Stoner E. C. *Collective electron ferronmagnetism*. Proceedings of the Royal Society of London. Series A. Mathematical and Physical Sciences **165**, 372–414 (1938). [p. 11]

[30] Néel L. *Anisotropie magnétique superficielle et surstructures d'orientation*. J. phys. radium **15**, 225–239 (1954). [p. 13]

[31] Engel B. N., England C. D., Van Leeuwen R. A., Wiedmann M. H. & Falco C. M. *Interface magnetic anisotropy in epitaxial superlattices*. Physical review letters **67**, 1910 (1991). [p. 13]

[32] Johnson M., Bloemen P., Den Broeder F. & De Vries J. *Magnetic anisotropy in metallic multilayers*. Reports on Progress in Physics **59**, 1409 (1996). [p. 13]

[33] Nakajima N., Koide T., Shidara T., Miyauchi H., Fukutani H., Fujimori A., Iio K., Katayama T., Nỳvlt M. & Suzuki Y. *Perpendicular magnetic anisotropy caused by interfacial hybridization via enhanced orbital moment in co/pt multilayers: Magnetic circular x-ray dichroism study*. Physical Review Letters **81**, 5229 (1998). [p. 13]

[34] Zeper W., Greidanus F., Carcia P. & Fincher C. *Perpendicular magnetic anisotropy and magneto-optical kerr effect of vapor-deposited co/pt-layered structures*. Journal of Applied Physics **65**, 4971–4975 (1989). [p. 13]

[35] Den Broeder F., Kuiper D., Van de Mosselaer A. & Hoving W. *Perpendicular magnetic anisotropy of co-au multilayers induced by interface sharpening*. Physical review letters **60**, 2769 (1988). [p. 13]

[36] Yang H., Chshiev M., Dieny B., Lee J., Manchon A. & Shin K. *First-principles investigation of the very large perpendicular magnetic anisotropy at fe— mgo and co— mgo interfaces*. Physical Review B **84**, 054401 (2011). [p. 13]

[37] Dieny B. & Chshiev M. *Perpendicular magnetic anisotropy at transition metal/oxide interfaces and applications*. Reviews of Modern Physics **89**, 025008 (2017). [p. 13]

[38] Skomski R. *Simple models of magnetism* (Oxford university press, 2008). [p. 14]

[39] Drovosekov A., Kholin D. & Kreinies N. *Magnetic properties of layered ferrimagnetic structures based on gd and transition 3 d metals*. Journal of Experimental and Theoretical Physics **131**, 149–159 (2020). [p. 15]

[40] Kittel C. *Theory of ferromagnetic resonance in rare earth garnets. i. g values.* Phys. Rev. **115**, 1587–1590 (1959). [p. 15]

[41] Mott N. F. *The electrical conductivity of transition metals.* Proceedings of the Royal Society of London. Series A-Mathematical and Physical Sciences **153**, 699–717 (1936). [p. 16]

[42] Sommerfeld A. *Zur elektronentheorie der metalle auf grund der fermischen statistik: I. teil: Allgemeines, strömungs-und austrittsvorgänge.* Zeitschrift für Physik **47**, 1–32 (1928). [p. 16]

[43] Fert A. & Campbell I. *Two-current conduction in nickel.* Physical Review Letters **21**, 1190 (1968). [p. 17]

[44] Fert A. & Campbell I. *Transport properties of ferromagnetic transition metals.* Le Journal de Physique Colloques **32**, C1–46 (1971). [p. 17]

[45] Fert A. & Campbell I. *Electrical resistivity of ferromagnetic nickel and iron based alloys.* Journal of Physics F: Metal Physics **6**, 849 (1976). [p. 17]

[46] Thomson W. *Xix. on the electro-dynamic qualities of metals:—effects of magnetization on the electric conductivity of nickel and of iron.* Proceedings of the Royal Society of London 546–550 (1857). [p. 17]

[47] Ramirez A. *Colossal magnetoresistance.* Journal of Physics: Condensed Matter **9**, 8171 (1997). [p. 17]

[48] Solin S., Thio T., Hines D. & Heremans J. *Enhanced room-temperature geometric magnetoresistance in inhomogeneous narrow-gap semiconductors.* science **289**, 1530–1532 (2000). [p. 17]

[49] Julliere M. *Tunneling between ferromagnetic films.* Physics letters A **54**, 225–226 (1975). [p. 17]

[50] Miyazaki T. & Tezuka N. *Giant magnetic tunneling effect in fe/al2o3/fe junction.* Journal of magnetism and magnetic materials **139**, L231–L234 (1995). [p. 17]

[51] Moodera J. S., Kinder L. R., Wong T. M. & Meservey R. *Large magnetoresistance at room temperature in ferromagnetic thin film tunnel junctions.* Physical review letters **74**, 3273 (1995). [p. 17]

[52] Tsunoda M., Nishikawa K., Ogata S. & Takahashi M. *60% magnetoresistance at room temperature in co–fe/al–o/co–fe tunnel junctions oxidized with kr–o 2 plasma.* Applied physics letters **80**, 3135–3137 (2002). [p. 18]

[53] Wang D., Nordman C., Daughton J. M., Qian Z. & Fink J. *70% tmr at room temperature for sdt sandwich junctions with cofeb as free and reference layers.* IEEE Transactions on Magnetics **40**, 2269–2271 (2004). [p. 18]

[54] Sousa R., Sun J., Soares V., Freitas P., Kling A., Da Silva M. & Soares J. *Large tunneling magnetoresistance enhancement by thermal anneal.* Applied physics letters **73**, 3288–3290 (1998). [p. 18]

[55] De Teresa J. M., Barthelemy A., Fert A., Contour J. P., Montaigne F. & Seneor P. *Role of metal-oxide interface in determining the spin polarization of magnetic tunnel junctions.* Science **286**, 507–509 (1999). [p. 18]

[56] Bowen M., Bibes M., Barthélémy A., Contour J.-P., Anane A., Lemaıtre Y. & Fert A. *Nearly total spin polarization in la 2/3 sr 1/3 mno 3 from tunneling experiments.* Applied Physics Letters **82**, 233–235 (2003). [p. 18]

[57] Faure-Vincent J., Tiusan C., Jouguelet E., Canet F., Sajieddine M., Bellouard C., Popova E., Hehn M., Montaigne F. & Schuhl A. *High tunnel magnetoresistance in epitaxial fe/mgo/fe tunnel junctions.* Applied Physics Letters **82**, 4507–4509 (2003). [p. 18]

[58] Parkin S. S., Kaiser C., Panchula A., Rice P. M., Hughes B., Samant M. & Yang S.-H. *Giant tunnelling magnetoresistance at room temperature with mgo (100) tunnel barriers.* Nature materials **3**, 862–867 (2004). [p. 18]

[59] Djayaprawira D. D., Tsunekawa K., Nagai M., Maehara H., Yamagata S., Watanabe N., Yuasa S., Suzuki Y. & Ando K. *230% room-temperature magnetoresistance in cofeb/ mgo/ cofeb magnetic tunnel junctions.* Applied physics letters **86** (2005). [p. 18]

[60] Ikeda S., Hayakawa J., Ashizawa Y., Lee Y., Miura K., Hasegawa H., Tsunoda M., Matsukura F. & Ohno H. *Tunnel magnetoresistance of 604% at 300k by suppression of ta diffusion in cofeb/ mgo/ cofeb pseudo-spin-valves annealed at high temperature.* Applied Physics Letters **93** (2008). [p. 18]

[61] Mavropoulos P., Papanikolaou N. & Dederichs P. *Complex band structure and tunneling through ferromagnet/insulator/ferromagnet junctions.* Physical review letters **85**, 1088 (2000). [p. 18]

[62] Mathon J. & Umerski A. *Theory of tunneling magnetoresistance in a junction with a non-magnetic metallic interlayer.* Physical Review B **60**, 1117 (1999). [p. 18]

[63] Butler W., Zhang X.-G., Schulthess T. & MacLaren J. *Spin-dependent tunneling conductance of fe— mgo— fe sandwiches.* Physical Review B **63**, 054416 (2001). [p. 18]

[64] Mathon J. & Umerski A. *Theory of tunneling magnetoresistance of an epitaxial fe/mgo/fe (001) junction.* Physical Review B **63**, 220403 (2001). [p. 19]

[65] Ralph D. C. & Stiles M. D. *Spin transfer torques.* Journal of Magnetism and Magnetic Materials **320**, 1190–1216 (2008). [p. 19]

[66] Stiles M. D. & Zangwill A. *Anatomy of spin-transfer torque.* Physical Review B **66**, 014407 (2002). [p. 19]

[67] Li Z. & Zhang S. *Magnetization dynamics with a spin-transfer torque.* Physical Review B **68**, 024404 (2003). [p. 19]

[68] Stiles M. D. & Miltat J. *Spin-transfer torque and dynamics.* Spin dynamics in confined magnetic structures III 225–308 (2006). [p. 19]

[69] Landau L. & Lifshitz E. *On the theory of the dispersion of magnetic permeability in ferromagnetic bodies.* In *Perspectives in Theoretical Physics*, 51–65 (Elsevier, 1992). [p. 19]

[70] Gilbert T. L. *A phenomenological theory of damping in ferromagnetic materials.* IEEE transactions on magnetics **40**, 3443–3449 (2004). [p. 19]

[71] Azzawi S., Hindmarch A. & Atkinson D. *Magnetic damping phenomena in ferromagnetic thin-films and multilayers.* Journal of Physics D: Applied Physics **50**, 473001 (2017). [p. 19]

[72] Ament S., Rangarajan N., Parthasarathy A. & Rakheja S. *Solving the stochastic landau-lifshitz-gilbert-slonczewski equation for monodomain nanomagnets: A survey and analysis of numerical techniques.* arXiv preprint arXiv:1607.04596 (2016). [p. 20]

[73] Choe J. *Recent technology insights on stt-mram: Structure, materials, and process integration.* In *2023 IEEE International Memory Workshop (IMW)*, 1–4 (IEEE, 2023). [p. 21]

[74] Bedau D., Liu H., Bouzaglou J.-J., Kent A., Sun J., Katine J., Fullerton E. E. & Mangin S. *Ultrafast spin-transfer switching in spin valve nanopillars with perpendicular anisotropy.* Applied Physics Letters **96** (2010). [pp. 23, 118]

[75] Diao Z., Apalkov D., Pakala M., Ding Y., Panchula A. & Huai Y. *Spin transfer switching and spin polarization in magnetic tunnel junctions with mgo and alox barriers.* Applied Physics Letters **87** (2005). [pp. 23, 118]

[76] Zhao H., Glass B., Amiri P. K., Lyle A., Zhang Y., Chen Y.-J., Rowlands G., Upadhyaya P., Zeng Z., Katine J. *et al. Sub-200 ps spin transfer torque switching in in-plane magnetic tunnel junctions with interface perpendicular anisotropy.* Journal of Physics D: Applied Physics **45**, 025001 (2011). [pp. 23, 118]

[77] Ikeda S., Miura K., Yamamoto H., Mizunuma K., Gan H., Endo M., Kanai S., Hayakawa J., Matsukura F. & Ohno H. *A perpendicular-anisotropy cofeb–mgo magnetic tunnel junction.* Nature materials **9**, 721–724 (2010). [pp. 23, 118]

[78] Gajek M., Nowak J., Sun J., Trouilloud P., O'sullivan E., Abraham D., Gaidis M., Hu G., Brown S., Zhu Y. *et al. Spin torque switching of 20 nm magnetic tunnel junctions with perpendicular anisotropy.* Applied Physics Letters **100** (2012). [pp. 23, 118]

[79] Garello K., Avci C. O., Miron I. M., Baumgartner M., Ghosh A., Auffret S., Boulle O., Gaudin G. & Gambardella P. *Ultrafast magnetization switching by spin-orbit torques.* Applied Physics Letters **105** (2014). [pp. 23, 118]

[80] Aradhya S. V., Rowlands G. E., Oh J., Ralph D. C. & Buhrman R. A. *Nanosecond-timescale low energy switching of in-plane magnetic tunnel junctions through dynamic oersted-field-assisted spin hall effect.* Nano letters **16**, 5987–5992 (2016). [pp. 23, 118]

[81] Wang M., Cai W., Cao K., Zhou J., Wrona J., Peng S., Yang H., Wei J., Kang W., Zhang Y. *et al. Current-induced magnetization switching in atom-thick tungsten engineered perpendicular magnetic tunnel junctions with large tunnel magnetoresistance.* Nature communications **9**, 671 (2018). [pp. 23, 118]

[82] Shi S., Ou Y., Aradhya S., Ralph D. & Buhrman R. *Fast low-current spin-orbit-torque switching of magnetic tunnel junctions through atomic modifications of the free-layer interfaces.* Physical Review Applied **9**, 011002 (2018). [pp. 23, 118]

[83] Sato N., Xue F., White R. M., Bi C. & Wang S. X. *Two-terminal spin–orbit torque magnetoresistive random access memory.* Nature Electronics **1**, 508–511 (2018). [pp. 23, 118]

[84] Grezes C., Ebrahimi F., Alzate J., Cai X., Katine J., Langer J., Ocker B., Khalili Amiri P. & Wang K. *Ultra-low switching energy and scaling in electric-field-controlled nanoscale magnetic tunnel junctions with high resistance-area product.* Applied Physics Letters **108** (2016). [pp. 23, 118]

[85] Wang H., Yu L., Lee Y., Fang W., Hsu A., Herring P., Chin M., Dubey M., Li L., Kong J. *et al. Electron devices meeting (iedm), 2012 ieee international.* San Francisco, CA (2012). [pp. 23, 118]

[86] Kanai S., Nakatani Y., Yamanouchi M., Ikeda S., Matsukura F. & Ohno H. *In-plane magnetic field dependence of electric field-induced magnetization switching.* Applied Physics Letters **103** (2013). [pp. 23, 118]

[87] Beaurepaire E., Merle J.-C., Daunois A. & Bigot J.-Y. *Ultrafast spin dynamics in ferromagnetic nickel.* Physical review letters **76**, 4250 (1996). [pp. 23, 24]

[88] Kirilyuk A., Kimel A. V. & Rasing T. *Ultrafast optical manipulation of magnetic order.* Reviews of Modern Physics **82**, 2731 (2010). [p. 24]

[89] Koopmans B., Ruigrok J., Dalla Longa F. & De Jonge W. *Unifying ultrafast magnetization dynamics.* Physical review letters **95**, 267207 (2005). [p. 24]

[90] Singh N., Elliott P., Dewhurst J. K., Gross E. & Sharma S. *Ab-initio real-time magnon dynamics in ferromagnetic and ferrimagnetic systems.* physica status solidi (b) **257**, 1900654 (2020). [p. 24]

[91] Koopmans B., Malinowski G., Dalla Longa F., Steiauf D., Fähnle M., Roth T., Cinchetti M. & Aeschlimann M. *Explaining the paradoxical diversity of ultrafast laser-induced demagnetization.* Nature materials **9**, 259–265 (2010). [p. 24]

[92] Wietstruk M., Melnikov A., Stamm C., Kachel T., Pontius N., Sultan M., Gahl C., Weinelt M., Dürr H. A. & Bovensiepen U. *Hot-electron-driven enhancement of spin-lattice coupling in gd and tb 4 f ferromagnets observed by femtosecond x-ray magnetic circular dichroism.* Physical Review Letters **106**, 127401 (2011). [pp. 24, 47, 54]

[93] Radu I., Stamm C., Eschenlohr A., Radu F., Abrudan R., Vahaplar K., Kachel T., Pontius N., Mitzner R., Holldack K. *et al. Ultrafast and distinct spin dynamics in magnetic alloys.* In *Spin*, vol. 5, 1550004 (World Scientific, 2015). [pp. 24, 54]

[94] Mentink J. H. *Magnetism on the timescale of the exchange interaction: explanations and predictions* ([Sl]:[Sn], 2012). [p. 24]

[95] Kim S. K., Beach G. S., Lee K.-J., Ono T., Rasing T. & Yang H. *Ferrimagnetic spintronics.* Nature materials **21**, 24–34 (2022). [p. 25]

[96] Steil D., Alebrand S., Hassdenteufel A., Cinchetti M. & Aeschlimann M. *All-optical magnetization recording by tailoring optical excitation parameters.* Physical Review B **84**, 224408 (2011). [p. 26]

[97] Khorsand A., Savoini M., Kirilyuk A., Kimel A., Tsukamoto A., Itoh A. & Rasing T. *Role of magnetic circular dichroism in all-optical magnetic recording.* Physical review letters **108**, 127205 (2012). [p. 26]

[98] Wei J., Zhang B., Hehn M., Zhang W., Malinowski G., Xu Y., Zhao W. & Mangin S. *All-optical helicity-independent switching state diagram in gd-fe-co alloys.* Physical Review Applied **15**, 054065 (2021). [pp. 26, 53, 56, 78]

[99] Banerjee C., Teichert N., Siewierska K., Gercsi Z., Atcheson G., Stamenov P., Rode K., Coey J. & Besbas J. *Single pulse all-optical toggle switching of magnetization without gadolinium in the ferrimagnet mn2ruxga.* Nature communications **11**, 4444 (2020). [p. 26]

[100] Frietsch B., Donges A., Carley R., Teichmann M., Bowlan J., Döbrich K., Carva K., Legut D., Oppeneer P. M., Nowak U. *et al. The role of ultrafast magnon generation in the magnetization dynamics of rare-earth metals.* Science advances **6**, eabb1601 (2020). [pp. 27, 47, 79]

[101] Mangin S., Gottwald M., Lambert C., Steil D., Uhlíř V., Pang L., Hehn M., Alebrand S., Cinchetti M., Malinowski G. *et al. Engineered materials for all-optical helicity-dependent magnetic switching.* Nature materials **13**, 286–292 (2014). [p. 27]

[102] He L., Chen J.-Y., Wang J.-P. & Li M. *All-optical switching of magnetoresistive devices using telecom-band femtosecond laser.* Applied Physics Letters **107** (2015). [p. 27]

[103] El Hadri M., Pirro P., Lambert C.-H., Bergeard N., Petit-Watelot S., Hehn M., Malinowski G., Montaigne F., Quessab Y., Medapalli R. *et al. Electrical characterization of all-optical helicity-dependent switching in ferromagnetic hall crosses.* Applied Physics Letters **108** (2016). [p. 27]

[104] Chen J.-Y., He L., Wang J.-P. & Li M. *All-optical switching of magnetic tunnel junctions with single subpicosecond laser pulses.* Physical Review Applied **7**, 021001 (2017). [pp. 27, 47, 103, 110, 112]

[105] Wang L., Cheng H., Li P., van Hees Y. L., Liu Y., Cao K., Lavrijsen R., Lin X., Koopmans B. & Zhao W. *Picosecond optospintronic tunnel junctions.* Proceedings of the National Academy of Sciences **119**, e2204732119 (2022). [pp. 27, 28, 47, 104, 110, 112]

[106] Bogaerts W., Baets R., Dumon P., Wiaux V., Beckx S., Taillaert D., Luyssaert B., Van Campenhout J., Bienstman P. & Van Thourhout D. *Nanophotonic waveguides in silicon-on-insulator fabricated with cmos technology.* Journal of Lightwave Technology **23**, 401 (2005). [p. 28]

[107] Bogaerts W., De Heyn P., Van Vaerenbergh T., De Vos K., Kumar Selvaraja S., Claes T., Dumon P., Bienstman P., Van Thourhout D. & Baets R. *Silicon microring resonators.* Laser & Photonics Reviews **6**, 47–73 (2012). [p. 28]

[108] van der Tol J. J., Jiao Y., Van Engelen J. P., Pogoretskiy V., Kashi A. A. & Williams K. *Inp membrane on silicon (imos) photonics.* IEEE Journal of Quantum Electronics **56**, 1–7 (2019). [p. 28]

[109] Jiao Y., van der Tol J., Pogoretskii V., van Engelen J., Kashi A. A., Reniers S., Wang Y., Zhao X., Yao W., Liu T. *et al. Indium phosphide membrane nanophotonic integrated circuits on silicon.* physica status solidi (a) **217**, 1900606 (2020). [p. 28]

[110] Becker H., Krückel C. J., Van Thourhout D. & Heck M. J. R. *Out-of-plane focusing grating couplers for silicon photonics integration with optical mram technology.* IEEE Journal of Selected Topics in Quantum Electronics **26**, 1–8 (2020). [p. 28]

[111] Sobolewska E. K., Pelloux-Prayer J., Becker H., Li G., Davies C. S., Krückel C., Félix L. A., Olivier A., Sousa R. C., Prejbeanu I.-L. *et al. Integration platform for optical switching of magnetic elements.* In *Active Photonic Platforms XII*, vol. 11461, 54–72 (SPIE, 2020). [pp. 28, 29, 105, 106, 117]

[112] Pezeshki H., Li P., Lavrijsen R., Heck M., Bente E., van der Tol J. & Koopmans B. *Integrated hybrid plasmonic-photonic device for all-optical switching and reading of spintronic memory.* Phys. Rev. Appl. **19**, 054036 (2023). [p. 29]

[113] Kelly P. & Arnell R. *Magnetron sputtering: a review of recent developments and applications.* Vacuum **56**, 159–172 (2000). [p. 34]

[114] Sanchez Hazen D. *Engineering and evaluation of double magnetic tunnel junctions with a switchable assistance layer for high performance spin transfer torque magnetic memory.* Theses Université Grenoble Alpes [2020-....] (2022). [pp. 34, 105, 106, 108]

[115] Palomino A. *Scalable spintronics devices with reduced Pt and Ru content.* Theses Université Grenoble Alpes [2020-....] (2022). [pp. 34, 105, 106, 108]

[116] Parker M. *The kerr magneto-optic effect (1876–1976).* Physica B+ C **86**, 1171–1176 (1977). [p. 36]

[117] Hamrle J. *Magneto-optical determination of the in-depth magnetization profile in magnetic multilayers.* Ph.D. thesis Université Paris Sud-Paris XI (2003). [p. 36]

[118] Peng Y. *Commutation de l'aimantation à l'aide d'une impulsion laser unique dans des multicouches à base de RE sans Gd.* Ph.D. thesis Université de Lorraine (2023). [pp. 37, 43, 66]

[119] Le Guyader L., El Moussaoui S., Buzzi M., Chopdekar R., Heyderman L., Tsukamoto A., Itoh A., Kirilyuk A., Rasing T., Kimel A. *et al. Demonstration of laser induced magnetization reversal in gdfeco nanostructures.* Applied Physics Letters **101** (2012). [p. 47]

[120] Le Guyader L., Savoini M., El Moussaoui S., Buzzi M., Tsukamoto A., Itoh A., Kirilyuk A., Rasing T., Kimel A. V. & Nolting F. *Nanoscale sub-100 picosecond all-optical magnetization switching in gdfeco microstructures.* Nature communications **6**, 5839 (2015). [p. 47]

[121] El-Ghazaly A., Tran B., Ceballos A., Lambert C.-H., Pattabi A., Salahuddin S., Hellman F. & Bokor J. *Ultrafast magnetization switching in nanoscale magnetic dots.* Applied Physics Letters **114** (2019). [p. 47]

[122] Ciuciulkaite A., Mishra K., Moro M. V., Chioar I.-A., Rowan-Robinson R. M., Parchenko S., Kleibert A., Lindgren B., Andersson G., Davies C. S. *et al. Magnetic and all-optical switching properties of amorphous tb x co 100- x alloys.* Physical Review Materials **4**, 104418 (2020). [p. 47]

[123] Coey J. *Amorphous magnetic order.* Journal of Applied Physics **49**, 1646–1652 (1978). [p. 47]

[124] Kang S. & Lee K. *Emerging materials and devices in spintronic integrated circuits for energy-smart mobile computing and connectivity.* Acta Materialia **61**, 952–973 (2013). [p. 48]

[125] Bandiera S. *Jonctions tunnel magnétiques à anisotropie perpendiculaire et écriture assistée thermiquement.* Ph.D. thesis Université de Grenoble (2011). [pp. 48, 49]

[126] Ertl L., Endl G. & Hoffmann H. *Structure and magnetic properties of sputtered tb/co multilayers.* Journal of magnetism and magnetic materials **113**, 227–237 (1992). [pp. 48, 49]

[127] Abraham D. W. & Trouilloud P. L. *Thermally-assisted magnetic random access memory (mram)* (2002). US Patent 6,385,082. [p. 49]

[128] Mishra K., Blank T. G., Davies C., Avilés-Félix L., Salomoni D., Buda-Prejbeanu L., Sousa R., Prejbeanu I., Koopmans B., Rasing T. *et al. Dynamics of all-optical single-shot switching of magnetization in tb/co multilayers.* Physical Review Research **5**, 023163 (2023). [pp. 53, 54, 60, 61, 62, 95, 99]

[129] Choi G.-M., Min B.-C., Lee K.-J. & Cahill D. G. *Spin current generated by thermally driven ultrafast demagnetization.* Nature communications **5**, 4334 (2014). [pp. 55, 79]

[130] Davies C., Prabhakara K., Davydova M., Zvezdin K., Shapaeva T., Wang S., Zvezdin A., Kirilyuk A., Rasing T. & Kimel A. *Anomalously damped heat-assisted route for precessional magnetization reversal in an iron garnet.* Physical review letters **122**, 027202 (2019). [pp. 55, 63]

[131] Kichin G., Hehn M., Gorchon J., Malinowski G., Hohlfeld J. & Mangin S. *From multiple-to single-pulse all-optical helicity-dependent switching in ferromagnetic co/pt multilayers.* Physical Review Applied **12**, 024019 (2019). [p. 56]

[132] Dumas-Bouchiat F., Nagaraja H., Rossignol F., Champeaux C., Trolliard G., Catherinot A. & Givord D. *Cobalt cluster-assembled thin films deposited by low energy cluster beam deposition: Structural and magnetic investigations of deposited layers.* Journal of applied physics **100** (2006). [pp. 59, 60]

[133] Darnell F. *Lattice parameters of terbium and erbium at low temperatures.* Physical Review **132**, 1098 (1963). [pp. 59, 60, 82]

[134] Yue J., Jiang S., Zhang D., Yuan H., Wang Y., Lin L., Zhai Y., Du J. & Zhai H. *The influence of interface on spin pumping effect in ni80fe20/tb bilayer.* AIP Advances **6** (2016). [p. 60]

[135] Rebei A. & Hohlfeld J. *Origin of increase of damping in transition metals with rare-earth-metal impurities.* Physical review letters **97**, 117601 (2006). [p. 60]

[136] Lalieu M., Peeters M., Haenen S., Lavrijsen R. & Koopmans B. *Deterministic all-optical switching of synthetic ferrimagnets using single femtosecond laser pulses.* Physical review B **96**, 220411 (2017). [p. 63]

[137] Peng Y., Salomoni D., Malinowski G., Zhang W., Hohlfeld J., Buda-Prejbeanu L., Gorchon J., Vergès M., Lin J., Lacour D. *et al. In-plane reorientation induced single laser pulse magnetization reversal.* Nature Communications **14**, 5000 (2023). [pp. 66, 67, 68, 69, 70, 78, 91, 92, 115]

[138] Yuasa S., Nagahama T., Fukushima A., Suzuki Y. & Ando K. *Giant room-temperature magnetoresistance in single-crystal fe/mgo/fe magnetic tunnel junctions.* Nature materials **3**, 868–871 (2004). [p. 70]

[139] Cuchet L. *Propriétés de transport et d'anisotropie de jonctions tunnel magnétiques perpendiculaires avec simple ou double barrière.* Ph.D. thesis Université Grenoble Alpes (ComUE) (2015). [p. 70]

[140] Schreiber D. K., Choi Y.-s., Liu Y., Chiaramonti A. N., Seidman D. N. & Petford-Long A. K. *Effects of elemental distributions on the behavior of MgO-based magnetic tunnel junctions.* Journal of Applied Physics **109**, 103909 (2011). https://pubs.aip.org/aip/jap/article-pdf/doi/10.1063/1.3583569/15081169/103909_1_online.pdf. [p. 71]

[141] Choi Y., Nagamine Y., Tsunekawa K., Maehara H., Djayaprawira D., Yuasa S. & Ando K. *Effect of ta getter on the quality of mgo tunnel barrier in the polycrystalline cofeb/ mgo/ cofeb magnetic tunnel junction.* Applied physics letters **90** (2007). [p. 71]

[142] Honjo H., Ikeda S., Sato H., Nishioka K., Watanabe T., Miura S., Nasuno T., Noguchi Y., Yasuhira M., Tanigawa T. *et al. Impact of tungsten sputtering condition on magnetic and transport properties of double-mgo magnetic tunneling junction with cofeb/w/cofeb free layer.* IEEE Transactions on Magnetics **53**, 1–4 (2017). [p. 71]

[143] Lee D.-Y., Hong S.-H., Lee S.-E. & Park J.-G. *Dependency of tunneling-magnetoresistance ratio on nanoscale spacer thickness and material for double mgo based perpendicular-magnetic-tunneling-junction.* Scientific Reports **6**, 38125 (2016). [p. 71]

[144] Liu T., Zhang Y., Cai J. & Pan H. *Thermally robust mo/cofeb/mgo trilayers with strong perpendicular magnetic anisotropy.* Scientific reports **4**, 5895 (2014). [p. 71]

[145] Chen J., Tzou D. & Beraun J. *A semiclassical two-temperature model for ultrafast laser heating.* International journal of heat and mass transfer **49**, 307–316 (2006). [p. 77]

[146] Evans R. F., Fan W. J., Chureemart P., Ostler T. A., Ellis M. O. & Chantrell R. W. *Atomistic spin model simulations of magnetic nanomaterials.* Journal of Physics: Condensed Matter **26**, 103202 (2014). [pp. 77, 93, 95, 96]

[147] Atxitia U., Chubykalo-Fesenko O., Kazantseva N., Hinzke D., Nowak U. & Chantrell R. W. *Micromagnetic modeling of laser-induced magnetization dynamics using the landau-lifshitz-bloch equation.* Applied physics letters **91** (2007). [p. 77]

[148] Atxitia U., Hinzke D. & Nowak U. *Fundamentals and applications of the landau–lifshitz–bloch equation.* Journal of Physics D: Applied Physics **50**, 033003 (2016). [p. 77]

[149] Avilés-Félix L., Farcis L., Jin Z., Álvaro-Gómez L., Li G., Yamada K. T., Kirilyuk A., Kimel A. V., Rasing T., Dieny B. *et al. All-optical spin switching probability in [tb/co] multilayers.* Scientific Reports **11**, 6576 (2021). [pp. 78, 94, 95]

[150] Moreno R., Ostler T. A., Chantrell R. W. & Chubykalo-Fesenko O. *Conditions for thermally induced all-optical switching in ferrimagnetic alloys: Modeling of tbco.* Phys. Rev. B **96**, 014409 (2017). [p. 79]

[151] Hazen D. S., Auffret S., Joumard I., Vila L., Buda-Prejbeanu L. D., Sousa R. C., Prejbeanu L. & Dieny B. *Double magnetic tunnel junctions with a switchable assistance layer for improved spin transfer torque magnetic memory performance.* Nanoscale **13**, 14096–14109 (2021). [p. 81]

[152] Salomoni D., Peng Y., Farcis L., Auffret S., Hehn M., Malinowski G., Mangin S., Dieny B., Buda-Prejbeanu L., Sousa R. & Prejbeanu I. *Field-free all-optical switching and electrical readout of* Tb/Co*-based magnetic tunnel junctions.* Phys. Rev. Appl. **20**, 034070 (2023). [pp. 83, 84, 111, 112, 116]

[153] Russek S. E., Kabos P., McMichael R., Lee C., Bailey W. E., Ewasko R. & Sanders S. C. *Magnetostriction and angular dependence of ferromagnetic resonance linewidth in tb-doped ni 0.8 fe 0.2 thin films.* Journal of applied physics **91**, 8659–8661 (2002). [p. 88]

[154] Reidy S., Cheng L. & Bailey W. *Dopants for independent control of precessional frequency and damping in ni 81 fe 19 (50 nm) thin films.* Applied Physics Letters **82**, 1254–1256 (2003). [p. 88]

[155] Ibrahim F., Hallal A., Kalitsov A., Stewart D., Dieny B. & Chshiev M. *Unveiling temperature-dependence mechanisms of perpendicular magnetic anisotropy at* Fe/MgO *interfaces.* Phys. Rev. Appl. **17**, 054041 (2022). [p. 95]

[156] Asselin P., Evans R. F. L., Barker J., Chantrell R. W., Yanes R., Chubykalo-Fesenko O., Hinzke D. & Nowak U. *Constrained monte carlo method and calculation of the temperature dependence of magnetic anisotropy.* Physical Review B **82**, 054415 (2010). [p. 96]

[157] Mansueto M. *Mémoire magnétique memristive pour synapses spintroniques.* Ph.D. thesis Université Grenoble Alpes (2020). [pp. 105, 106, 108]

[158] Olivier A., Avilés-Félix L., Chavent A., Álvaro-Goémez L., Rubio-Roy M., Auffret S., Vila L., Dieny B., Sousa R. C. & Prejbeanu I. *Indium tin oxide optical access for magnetic tunnel junctions in hybrid spintronic–photonic circuits.* Nanotechnology **31**, 425302 (2020). [pp. 105, 106, 110, 112]

[159] Kim D., Ko J., Park M. & Lee N.-E. *Infinitely high etch selectivity during ch4/h2/ar inductively coupled plasma (icp) etching of indium tin oxide (ito) with photoresist mask.* Thin Solid Films **516**, 3512–3516 (2008). [p. 105]

[160] Mondal S., Polley D., Pattabi A., Chatterjee J., Salomoni D., Aviles-Felix L., Olivier A., Rubio-Roy M., Diény B., Prejbeanu L. D. B., Sousa R., Prejbeanu I. L. & Bokor J. *Single-shot switching in tb/co-multilayer based nanoscale magnetic tunnel junctions.* Journal of Magnetism and Magnetic Materials **581**, 170960 (2023). [pp. 114, 115]

[161] Mishra K., Blank T. G. H., Davies C. S., Avilés-Félix L., Salomoni D., Buda-Prejbeanu L. D., Sousa R. C., Prejbeanu I. L., Koopmans B., Rasing T., Kimel A. V. & Kirilyuk A. *Dynamics of all-optical single-shot switching of magnetization in tb/co multilayers.* Phys. Rev. Res. **5**, 023163 (2023). [p. 115]

[162] Hylick A., Sohan R., Rice A. & Jones B. *An analysis of hard drive energy consumption.* In *2008 IEEE International Symposium on Modeling, Analysis and Simulation of Computers and Telecommunication Systems*, 1–10 (IEEE, 2008). [p. 117]

[163] Wang K., Alzate J. & Amiri P. K. *Low-power non-volatile spintronic memory: Stt-ram and beyond.* Journal of Physics D: Applied Physics **46**, 074003 (2013). [p. 117]